DEPARTAMENT D'ASTRONOMIA I METEOROLOGIA

UNIVERSITAT DE BARCELONA

X-ray emission from classical novae

Memòria presentada per
Glòria Sala Cladellas
per optar al grau de Doctora per la Universitat de Barcelona

Barcelona, 9 de Juliol de 2004

PROGRAMA DE DOCTORAT D'ASTRONOMIA I METEOROLOGIA

BIENNI 1999-2001

Memòria presentada per **Glòria Sala Cladellas** per optar al
Grau de Doctora per la Universitat de Barcelona

DIRECTORA

Dra. Margarida Hernanz Carbó
(Investidagora Científica, CSIC)

PONENT

Dr. Ramon Canal Masgoret
(Catedràtic d'Universitat, UB)

... als meus pares, al meu germà
...i al Luis Carlos.

"Some think it necessary that noise should arise when so great bodies are in motion, since sound does arise from bodies among us which are not so large and do not move so swiftly; and from the sun and moon and from the stars in so great number, and of so great size, moving so swiftly, there must necessarily arise a sound inconceivably great. Assuming these things and that the swiftness has the principle of harmony by reason of the intervals, they say that the sound of the stars moving on in a circle becomes musical. And since it seems unreasonable that we also do not hear this sound, they say that the reason for this is that the noise exists in the very nature of things, so as not to be distinguishable from the opposite silence; for the distinction of sound and silence lies in their contrast with each other, so that as blacksmiths think there is no difference between them because they are accustomed to the sound, so the same thing happens to men."

Aristotle, *De caelo,* II.9; 290 b 15 (refering to the Pythagoreans)
(Translation by Fairbanks (1898))

Agraïments/Acknowledgements

La meva dedicació a aquest treball ha estat possible gràcies a una beca de Formació de Personal Investigador del Ministeri de Ciencia i Tecnologia, vinculada a l'Institut de Ciències de l'Espai del Consell Superior d'Investigacions Científiques (CSIC). He d'agraïr també el finançament concedit per l'Institut d'Estudis Espacials de Catalunya (IEEC) durant els darrers mesos.

La principal persona que mereix un agraïment especial és la Dra. Margarida Hernanz, investigadora científica del CSIC i directora d'aquesta tesi, que ha seguit amb entusiasme el treball presentat en aquesta memòria. Gràcies per la gran dedicació i il·lusió, per tota la paciència, les converses i discussions, tant en persona, com a distància quan ha calgut, sense les quals aquest treball no seria el que és; gràcies per compartir projectes i idees, i nervis i presses si fa falta.

Els meus agraïments al Dr. Jordi Isern, professor d'investigació del CSIC i director de l'IEEC, pel seu suport i les facilitats que m'ha proporcionat per desenvolupar aquest treball a l'Institut d'Estudis Espacials de Catalunya, tant a nivell de mitjans materials, com d'un bon ambient de treball.

Agraeixo al Departament d'Astronomia i Meteorologia de la Universitat de Barcelona la formació que m'ha proporcionat en astrofísica, tant en els anys de llicenciatura com en els cursos de doctorat. Els meus agraïments també pel Dr. Ramon Canal, catedràtic del Departament d'Astronomia i Meteorologia i ponent d'aquesta tesi.

I thank Dr. Jochen Greiner for his guidance in my first steps in X-ray data analysis during my stage in the Astrophysikalisches Institut Potsdam (AIP) in October 2000. My acknowledgements also to the AIP for the hospitality offered during my stage.

My acknowledgments to Dr. Jim MacDonald, from the University of Delaware, for gently providing his white dwarf atmosphere models. My thanks also to Dr. Frederic Daigne from the Institut d'Astrophysique de Paris, for sending us the routine to solve the Saha equation used in this work. I must thank Dr. Tim Kallman, from the Laboratory for High Energy Astrophysics (NASA) for his useful comments on the XSTAR photoionization code.

I gratefully acknowledge Dr. Steve Shore for his kind invitation to the University of Pisa, and for interesting conversations on classical novae.

Els meus agraïments també al Dr. Jordi José, de la Universitat Politècnica de Catalunya, pels comentaris sobre aquest treball i per proporcionar-me sovint un altre punt de vista. Però gràcies especialment pel suport i el companyerisme. Gràcies per tot.

Vull agraïr també el suport i els ànims de tots els membres de l'IEEC, entre ells els Drs. Eduard Bravo, Enrique Garcia-Berro, Chema Torrelles, José-Luis Gòmez, Gabriel Martínez i Domingo Garcia. Els meus agraïments a les noies d'administració, la Pilar, l'Anna, la Mireia i l'Eva, pels múltiples mal de caps que us puc haver portat, especialment durant l'enrenou mediàtic de la tardor del 2002 i els últims dies de preparació d'aquesta memòria. Gràcies també a l'Isabel per la seva atenció, trucades i gestions.

Una abraçada per tots els companys de cafès i dinars de l'IEEC, l'Alina, la Sílvia, el Pep

i el José, i a tots els altres, pels moments de descans indispensables per seguir endavant. Una salutació també per la Pilar, amb qui vaig compartir el primer viatge relacionat amb la tesi, i que encomana el seu entusiasme per la ciència, i pel Fermin, companys de tesi des dels primers temps. Mil gràcies al Josep, sense qui molts dels que som a l'IEEC estariem absolutament perduts en els misteris del linux, per tota l'atenció i ajuda sempre que m'ha calgut. Una menció especial per dos amics que espero no perdre en el futur: el Nico, company a més d'alguns viatges i excursions també fora de la feina (queda pendent el Marroc...), i el Carles, amb qui hem compartit despatx, nervis, cafès i sopars durant aquests anys de tesis paral·leles. Gràcies a tots dos per donar-me suport i ànims quan més m'ha fet falta.

Fora de l'ambient científic, una menció molt especial pel Luis Carlos, a qui dedico aquesta tesi, per ser sempre al meu costat, amb paciència i comprensió, i per compartir amb mi tantes coses. Finalment, un agraïment molt especial als meus pares, per despertar en mi la curiositat i l'empenta suficients com per ficar-me en una aventura com aquesta, i per donar sempre suport a les meves il·lusions i expectatives.

Contents

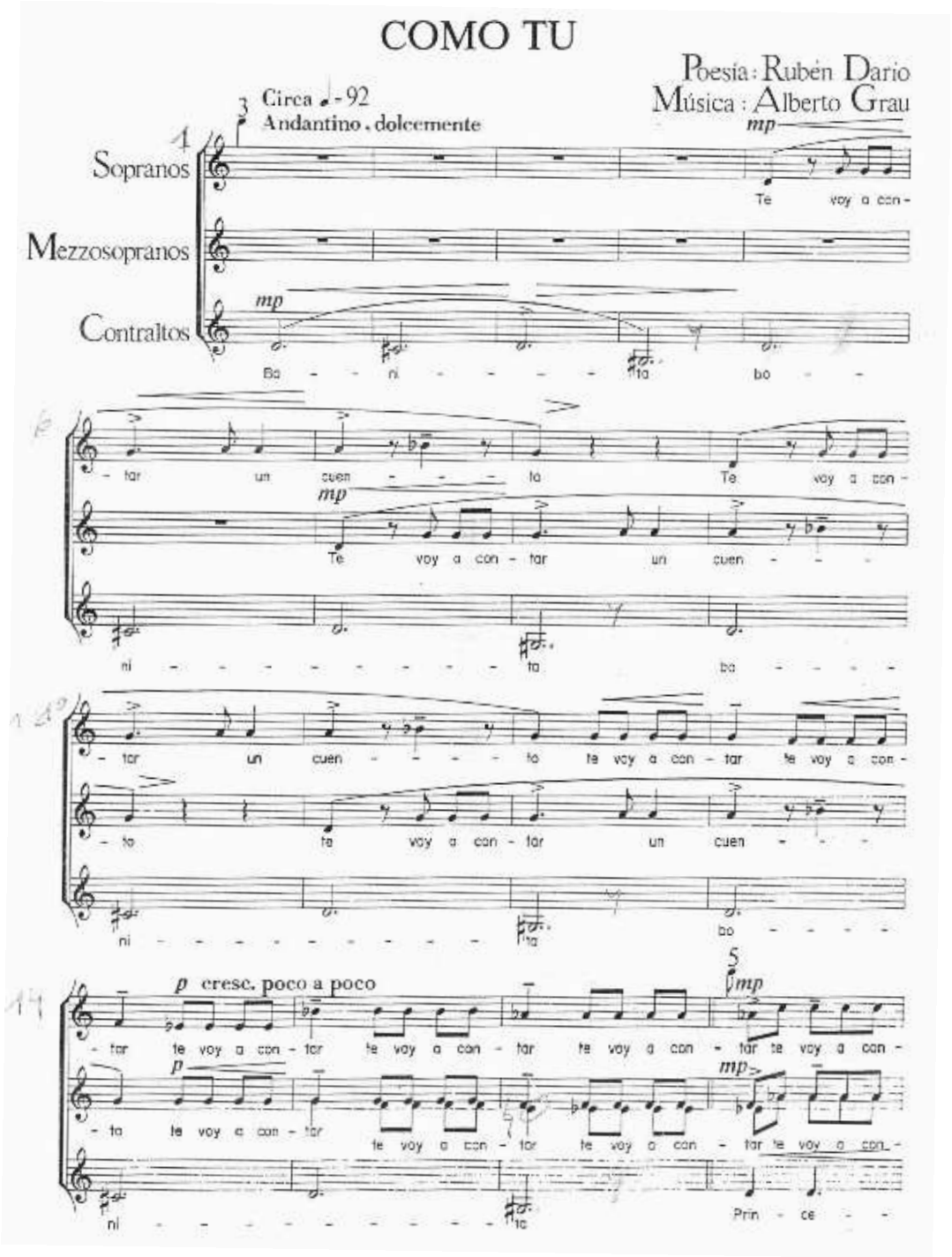

"Bonita, te voy a contar un cuento..."

Como tú

Poesia de Ruben Dario, música de Alberto Grau

Chapter 1

Introduction

In the apparent imperturbability of the starry skies, cataclysmic variables, including classical novae, are among the few privileged astronomical objects that live in a human timescale. If you are lucky enough to be at the right hemisphere by the time a bright nova explodes (in average, one per decade is brighter than $m_v = 3$), for some nights you will see a new star in the sky where there was none before. The magnitude of this *nova stella* will fade in the following days, during a period that can range from a few days to some months. Around 35 novae explode per year in our Galaxy, but only around 5 are discovered, due to high obscuration by the interstellar medium. In spite of their name, classical novae are not new born stars, but old remnants of dead stars that come to life again for some time.

Classical nova outbursts are caused by the explosive hydrogen burning on the white dwarf surface of a cataclysmic variable, a close binary system with transfer of material from the main sequence star (secondary star) to the white dwarf (primary component of the binary system). The first evidence for the binary nature of classical novae was found by Walker (1954), who discovered that Nova Her 1934 (DQ Her) was a short-period eclipsing binary with a $71s$ oscillation in the light curve that could only be due to the presence of a compact object. The transfer of material onto the hot compact object through Roche-lobe overflow was first suggested by Crawford & Kraft (1956) for AE Aqr, and the major advance in the field was provided by Kraft (1964), who confirmed the close binary nature of 10 classical novae.

Hydrodynamic models show that, after $10^{-5}-10^{-4} M_{\odot}$ of H-rich material are transfered from the secondary star to the white dwarf, ignition in degenerate conditions takes place in the accreted envelope and a thermonuclear runaway is initiated (José & Hernanz (1998), Starrfield et al.(1998), Prialnik & Kovetz (1995); see also Starrfield (2002) for a recent review). As a consequence of the thermonuclear runaway, the envelope expands and causes the brightness of the star to increase by ~ 10 magnitudes, reaching maximum luminosities up to $\sim 10^5 L_{\odot}$. A fraction of the envelope is ejected at large velocities (hundreds to thousands of $km\, s^{-1}$), while a part of it returns to hydrostatic equilibrium and remains in steady nuclear burning.

Classical novae are in general discovered during the maximum of optical luminosity or shortly after it. The brightness of the star is observed to decline during the following days, at a rate that can range from a few days to some weeks for a decline of two-three magnitudes. This rate of decline of the optical light-curve defines the speed class of the nova, determined according to its t_2 and t_3, the time spent by the source to decrease in the optical by two and three magnitudes, respectively. Observations in the ultraviolet (UV) with the IUE satellite showed that, by the time of the decline of the optical light-curve, the luminosity in the UV rises, thus keeping the bolometric luminosity at a constant value

of $\sim 10^5 L_\odot$, close to the Eddington limit of the star (the maximum luminosity compatible with hydrostatic equilibrium).

The generally accepted picture for this evolution is that the source is powered by steady hydrogen burning in the envelope left on the white dwarf surface, while the expanding ejected shell causes the spectrum to change with time: as the envelope expands, the photosphere recedes and the emission of inner and hotter layers of the envelope dominates the observed spectrum, shifting the maximum of the emission from optical, through UV and EUV, and finally to soft X-rays. This soft X-ray emission, arising as the ejecta becomes optically thin to X-rays, is thus a direct indicator of the thermonuclear burning of the remaining hydrogen-rich matter on the surface of the white dwarf. It is expected that all novae undergo this phase, showing the spectrum of a hot white dwarf atmosphere (MacDonald & Vennes (1991)), with effective temperatures in the range $10^5 - 10^6 K$ and luminosities close to the Eddington limit. The duration of the soft X-ray emitting phase can be estimated as the nuclear timescale to burn the post-outburst white dwarf envelope. Without any model of the post-outburst nova, the envelope mass was generally assumed to be of the same order of magnitude that the accreted layer needed to trigger the outburst, $\sim 10^{-4} - 10^{-5} M_\odot$, indicating nuclear timescales of tenths or hundreds of years (Starrfield (1989), MacDonald et al.(1985)).

Nevertheless, observations indicate much shorter turn-off times for classical novae. The first detection of soft X-rays from a nova in outburst came from Nova Muscae 1983 (GQ Mus), when observed by EXOSAT in 1984, 460 days after optical maximum. Other novae without soft X-ray emission were also detected some hundred days after optical maximum (PW Vul, QU Vul, Ögelman et al.(1984)). But the *Röntgensatellit* (ROSAT), which represented a major improvement for X-ray astronomy, provided unexpected results regarding classical novae: only 3 novae were found emitting soft X-rays (V1974 Cyg, GQ Mus and Nova LMC 1995), from a sample of 30 galactic and 9 LMC novae which were observed up to 10 years after their explosion (Orio et al.(2001a)). In addition, the longest constant bolometric luminosity phase was observed for GQ Mus, which turned-off nine years after the outburst. From these observations, a puzzling conclusion was extracted: the duration of the soft X-rays emitting phase was too short to be compatible with the evolution of the envelope on a purely nuclear timescale, if the mass of the remaining envelope was to be of the same order of magnitude that the accreted envelope. Some extra mass loss mechanisms were suggested to reduce this envelope mass, related to the interaction with the companion or to an optically thick wind. However, no theoretical model simulated the conditions and evolution of the post-outburst white dwarf envelope with steady hydrogen burning. It was clear as well that a larger sample of novae observed with more sensitive X-ray instruments was necessary.

Since the duration of the soft X-ray emission is related to the envelope and white dwarf masses, its determination has direct consequences for the long term evolution and final fate of the star. Accreting white dwarfs in cataclysmic binaries are good candidates for type Ia supernovae, if accretion causes the white dwarf mass to increase with time. In the case of classical novae, however, the ejection of material in the explosive events makes it difficult to follow the long-term evolution of the white dwarf mass. For some novae there is a disagreement between theory and observations regarding the ejected masses, with observational determinations of the mass in the ejected shell larger than predicted by models. In addition, hydrodynamical models show that the solar-like accreted layer needs to be enhanced with CNO nuclei to produce the nova outburst, indicating the presence of some mixing mechanism between the accreted envelope and the degenerate core. The mixing process itself is still one of the main problems unsolved for classical novae, as well

as the fractions of the envelope that are actually ejected and left on the white dwarf. The independent determination of the post-outburst envelope mass through its X-ray emission would add valuable information to the problem.

Other systems with accreting white dwarfs but without such violent explosive events as classical novae are more likely to grow and reach the Chandrasekhar mass. The so called Supersoft X-ray Sources (SSS) are believed to be powered by the steady hydrogen burning on the surface of a white dwarf in a close binary, with an accretion rate that equals the hydrogen burning rate and thus keeps the source in steady state. For long enough accretion phases, the white dwarf can reach the Chandrasekhar mass.

In addition to the photospheric soft X-ray emission, classical novae have other X-ray emitting mechanisms. During the outburst, and shortly after it, the ejected shell, heated by internal shocks during the expansion, or by external ones with the circumstellar material, can reach high temperatures and emit X-rays as a hot thermal plasma, with a harder spectrum than the white dwarf atmosphere. Finally, when accretion is reestablished onto the white dwarf, the system hosting the nova explosion can emit X-rays as a cataclysmic variable: when material from the secondary is accreted onto the white dwarf surface, there are strong shocks that heat the plasma to X-ray emitting temperatures.

The main aim of this thesis is to shed new light to the turn-off problem of classical novae. A numerical model has been developed for hot, steady hydrogen burning white dwarf envelopes (chapter 2). The conditions for post-outburst classical novae have been simulated, and the evolution has been approximated as a sequence of steady states. The results are compared to archival ROSAT observations of the three classical novae that showed soft X-ray emission when observed by ROSAT (V1974 Cyg, GQ Mus, N LMC 1995, chapter 3). From this comparison, the white dwarf mass, envelope mass, turn-off times and hydrogen abundances of the observed novae are constrained. Keeping the determination of the turn-off time of classical novae as the main goal, monitoring observations of recent novae have been performed with XMM-Newton (chapter 4). Five novae have been observed between two and four years after the outburst, showing surprising results such as the reestablishment of accretion in one of the systems less than 1000 days after the nova event.

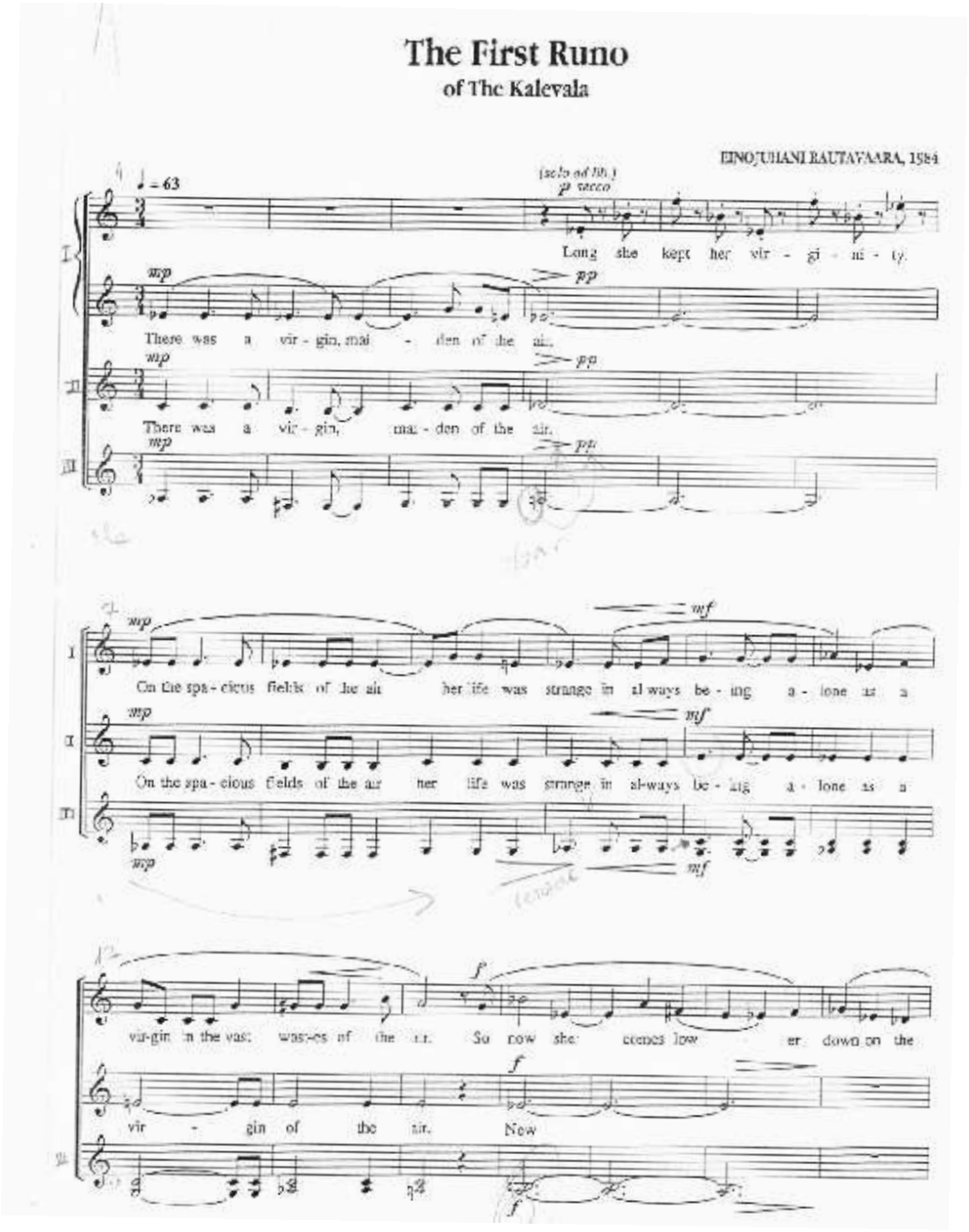

"There was a virgin, maiden of the air
Long she kept her virginity
On the spacious fields of the air her life was strange..."

The First Runo
Einojuhani Rautavara

Chapter 2

Steady H-burning White Dwarf Envelope Model

2.1 Constant bolometric luminosity phase and turn-off of classical novae

The presence of a remaining hydrogen burning envelope on the white dwarf after the nova outburst was already pointed out after the first hydrodynamic simulations (Starrfield et al.(1974)), that indicated that only a fraction of the hydrogen rich accreted material was ejected. The return of the rest of the envelope to hydrostatic equilibrium and its steady hydrogen burning could explain the persistence of the high temperature emission detected in the UV for Nova Serpentis 1970 some months after the decline of the optical light-curve (Gallagher & Code (1973)). Hydrodynamic models also show that the outburst is only possible if the accreted matter (with solar abundances) is enhanced by some mixing mechanism with CNO nuclei from the degenerate core. Analyses of nebular emission lines from classical novae show indeed ejecta enhanced in CNO nuclei compared to cosmic abundances and, in some cases, enhancement in Ne, Mg and other heavier elements. Of the envelope resulting from the mixing, constituted by a part of accreted matter and a part of white dwarf material, only a fraction is ejected during the outburst. The remaining envelope is expected to keep on burning in hydrostatic equilibrium powering a source of constant bolometric luminosity, for a period of time proportional to the mass of the envelope. Hydrodynamic models also indicate that the envelope mass required to trigger the nova outburst is $\sim 10^{-5} M_{\odot}$. Since those models do not simulate the post-outburst envelope, the duration of the constant bolometric luminosity phase could only be estimated as the nuclear timescale of the mass left on the white dwarf surface. Since the outburst ejects a fraction of the accreted envelope, the remaining envelope mass was assumed to be of the same order of magnitude, $\sim 10^{-5} M_{\odot}$. With the expected constant bolometric luminosity, $10^4 - 10^5 L_{\odot}$, the nuclear time-scale, during which the nova is expected to be a bright soft X-ray source, would be between tenths and hundreds of years (MacDonald et al.(1985), Starrfield (1989)).

This long duration predicted by models strongly disagrees with observations. All classical novae are expected to experience this constant bolometric luminosity phase, and shine as soft X-ray sources for decades or centuries. A systematic search for the X-ray emission from classical novae in their post-outburst stages (aged less than 10 years) in the ROSAT archival data was performed by Orio et al.(2001a). Contrary to what was expected, very few novae were discovered as X-ray emitters shortly after their outburst. In fact only 3 novae showed a soft X-ray spectrum: GQ Mus, V1974 Cyg and Nova LMC 1995 (see chap-

ter 3 for more details on these sources). GQ Mus showed the longest constant bolometric luminosity phase so far observed: its soft X-ray emission lasted for 9 years, still much less than predicted.

X-ray observations give direct insights on the hydrogen burning layer on the white dwarf surface after the outburst, but the presence of the soft X-ray source can also be determined by UV observations (Shore (2002)). Shore et al.(1993) showed that the UV is the key spectral regime for studying the dynamics and opacity of the expanding shell, ionized by the central X-ray source: abundances, velocities, spatial structure and mass of the ejecta were then determined for V1974 Cyg, and more recently for V382 Vel 1999 (Shore et al.(2003)). The ultraviolet emission lines are indicators of the ionization and density structure of the ejecta, and their variations reflect the evolution of the expanding shell, but also that of the luminosity and effective temperature of the central ionizing X-ray source. For instance, in the case of Nova Muscae 1983 (GQ Mus), Krautter & Williams (1989) determined that the highly ionization of the nebula observed with IUE was caused by a hot source at $T \geq 4 \times 10^5 K$ $(34.5eV)$ with the temperature increasing with time. Shore et al.(1996) proposed this indirect indicator to determine the turn-off of classical novae and used it for V1974 Cyg. The same technique has been used to determine the turn-off of other novae from IUE observations (González-Riestra et al.(1998), Vanlandingham et al.(2001), Schwarz et al.(2001)). In all cases, turn-off times were smaller than expected, and also smaller than the 9 years of GQ Mus.

The discrepancy between theory and observations pointed out that an extra mass loss mechanism should be present shortly after the nova outburst. Some extra mass loss mechanisms have been suggested, involving the interaction of the ejecta with the secondary and/or thick winds. MacDonald et al.(1985) calculated that a fraction of the envelope could be lost by dynamical friction of the secondary in a common envelope phase following the nova outburst. Regarding the wind theory, Kato & Hachisu (1994) calculated a sequence of thick wind solutions that simulated the decay phase of the light curve of novae.

Nevertheless, the comparison between observations and theory was mainly based on the turn-off times. A model for post-outburst envelopes to which X-ray observations could be compared was lacking. However, a good number of works were devoted to the study of hot white dwarf envelopes, although they did not predict the properties and evolution of the X-ray emission from post-outburst novae. Stellar evolution models following the post AGB phase simulate a similar situation. For population I stars (with $X_H = 0.7$), Paczyński (1970) showed that after exhaustion of He in the core, stars of several initial masses (between 3 and 7 $M_\odot$) follow a common track at constant luminosity. Effective temperature increases along the track, while hydrogen and helium shell burning reduce the envelope mass. Paczyński (1970) was also the first to find that luminosity is directly proportional to the core mass during this phase, that lasts as long as the envelope mass is larger than some critical value. When this critical point is reached, the shell sources die out and the degenerate core starts to cool down.

A number of studies have been devoted to accreting white dwarfs and the development of thermal pulses or flashes on a hydrogen rich envelope. Among them, Iben (1982) and Iben & Tutukov (1989) found a core mass - luminosity relation similar to Paczynski's for accreting white dwarf with steady hydrogen burning, with $X_H = 0.64$. Iben (1982) simulated the evolution of an accreting white dwarf envelope without accretion (or very small values of accretion rate) as a sequence of steady-state models, and found that the constant luminosity phase lasted for decades, in agreement with the nuclear timescales predicted by hydrodynamic models. The steady hydrogen burning solutions were combined with an evolving quasi-static approximation to study the thermal pulses occurring

on accreting white dwarfs. Different points of view of the problem can be found in Fujimoto (1982) and Paczyński (1983), who developed simple approximations for the study of the hydrogen burning envelopes stability, and the evolution of shell flashes for different accretion rates. Taking into account the existing numerical models for degenerate stars with hydrogen-burning shells, Iben & Tutukov (1996) pointed out that the core mass - luminosity relation was not unique, and that it depended on the thermal history of the star. They compared the models with data from symbiotic stars and cataclysmic variables, exploring the effects of mechanisms not present in the models (such as wind mass loss and mixing mechanisms) in the evolution of accreting white dwarfs. Nevertheless, none of those works studied envelopes with abundances typical for classical novae.

Tuchman & Truran (1998) studied the composition influence on the core mass - luminosity relation and its implications for the turn-off times of classical novae. They applied their relation to GQ Mus and V1974 Cyg, and concluded that the envelope masses required to initiate the thermonuclear runaway are larger than the envelope masses below which stable models for steady hydrogen burning exist. They suggested that from this condition, remnant envelope masses in the post-outburst stage could be significantly reduced by dynamical instability.

In this chapter, a numerical model for white dwarf envelopes with steady hydrogen burning is presented. The model does not only provide a composition dependent core mass - luminosity relation, but it is mainly aimed to simulate the conditions of the remaining hydrogen-rich material left on the white dwarf after the nova outburst. Photospheric properties are obtained for comparison with X-ray observations and evolution is approximated as a sequence of steady-states.

After a general presentation of the envelope model in section 2.2, the behaviour of the four stellar equilibrium equations integrated for different conditions at the base of the envelope is discussed in section 2.3. The main results of the numerical white dwarf envelope model are presented in section 2.4. Several series of models have been obtained, for different chemical compositions and white dwarf masses. The accuracy of the stationary approximation is evaluated in section 2.5. Finally, in section 2.6 the evolution of the post-outburst white dwarf envelopes is studied as a sequence of steady states.

In addition, in appendix A, the analytical approximation for envelopes with constant luminosity and mass is presented. Some general aspects of the stellar envelopes are obtained from this analytical model, specially regarding the effect of the outer boundary conditions in the interior structure.

2.2 The white dwarf envelope model

The white dwarf envelope models are constructed integrating the equations of stellar equilibrium for constant chemical composition, in the Eulerian description:

$$\frac{dM}{dr} = 4\pi r^2 \rho \tag{2.1}$$

$$\frac{dP}{dr} = -\frac{GM}{r^2}\rho \tag{2.2}$$

$$\frac{dL}{dr} = 4\pi r^2 \rho \left(\varepsilon + T\frac{ds}{dt}\right) \tag{2.3}$$

$$\frac{dT_r}{dr} = -\frac{3\kappa\rho}{64\pi\sigma}\frac{L}{r^2 T^3}, \tag{2.4}$$

where r is the radius to the center of the star; M is the total mass at radius r; P, ρ and T are pressure, density and temperature, L is the total luminosity crossing the sphere at radius r and s is the entropy per unit mass; G is the gravitational constant, $G = 6.673 \times 10^{-8} dyn\, cm^2\, g^{-2}$; $\sigma = \frac{ac}{4}$, with $a = 7.65 \times 10^{-15} erg\, cm^{-3}\, K^{-4}$, the radiation-density constant, and $c = 2.9979 \times 10^{10} cm\, s^{-1}$, the speed of light; $\varepsilon = \varepsilon_n - \varepsilon_\nu$, with $\varepsilon_n = \varepsilon_n(\rho, T)$ the nuclear energy production rate and ε_ν the neutrino losses; and $\kappa = \kappa(\rho, T)$ is the Rosseland mean opacity for the envelope composition, which is considered homogeneous for the whole envelope. Equation (2.4) is only valid if transport of energy is radiative. In this work, stationary envelopes are considered and neutrino losses are negligible, so (2.3) becomes

$$\frac{dL}{dr} = 4\pi r^2 \rho \varepsilon_n \tag{2.5}$$

In numerical integration, the envelope is tested at each step for convective instability according to the Schwarzschild criterion. When convection appears, (2.4) is no longer valid and the temperature gradient is solved using the standard mixing-length theory of convection (Böhm-Vitense (1958), see Appendix C). Radiative opacities used are those from the OPAL code (Iglesias & Rogers (1996)) and the approximations for the energy generation rates for hydrogen burning are from Reeves (1965) and Paczyński (1983). The equation of state is that of ideal gas with radiation pressure. As will be seen in section 2.4.3 and in appendix B, for the gas conditions in the present models, no significant degeneration (at the base of the envelope) or partial ionization effects (at the outermost layers) need to be taken into account, and the energy production due to helium burning can be neglected. More details on the input physics are given in appendix B.

An analytical approximation can be obtained for outer stellar envelopes assuming constant luminosity and mass. Except for the innermost layers, temperatures are too low for nuclear energy production to be significant and luminosity is constant; density is small, so that the mass varies very slowly with increasing radius and can be taken as constant as well. This analytical approximation and some interesting aspects derived from it are discussed in appendix A.

Integration

Figure 2.1 shows the results of numerical integration of the whole set of stellar structure equations (equations 2.1, 2.2, 2.4 and 2.5) with the OPAL opacity tables (see appendix B), using a Runge-Kutta method (Press et al.(1992)). When convection appears, the temperature gradient is assumed to be adiabatic. Integration starts at the bottom of the envelope, the degenerate core surface, with $M_c = 1.1 M_\odot$ and $R_c = 4.7 \times 10^8 cm$, and is stopped when radiation pressure dominates over the gas pressure, or when very small values of density are reached, if the previous condition is not fulfilled before. The chemical composition is $X = 0.35$, $Z_s = 0.02$, $\Delta X_C = 0.245$ and $\Delta X_O = 0.245$, which corresponds to solar matter accreted onto a CO white dwarf and mixed with the core material at 50% (ΔX_C and ΔX_O are the extra C and O mass fraction beyond that in Z_s, which contains metals in solar fraction). All boundary conditions are fixed at the bottom of the envelope. Luminosity and temperature are fixed in all cases to $L = 1 L_\odot$ and $T_b = 6 \times 10^7 K$, while pressure is indicated for each case in the graphics (indicated as P_{17}, pressure in units of $10^{17}\ dyn\, cm^{-2}$).

Obviously, the results of this integration do not, in general, fulfill the outer boundary conditions for a stellar envelope, which will be specified later. But they show two important features to be noticed and taken into account in the two boundary conditions problem:

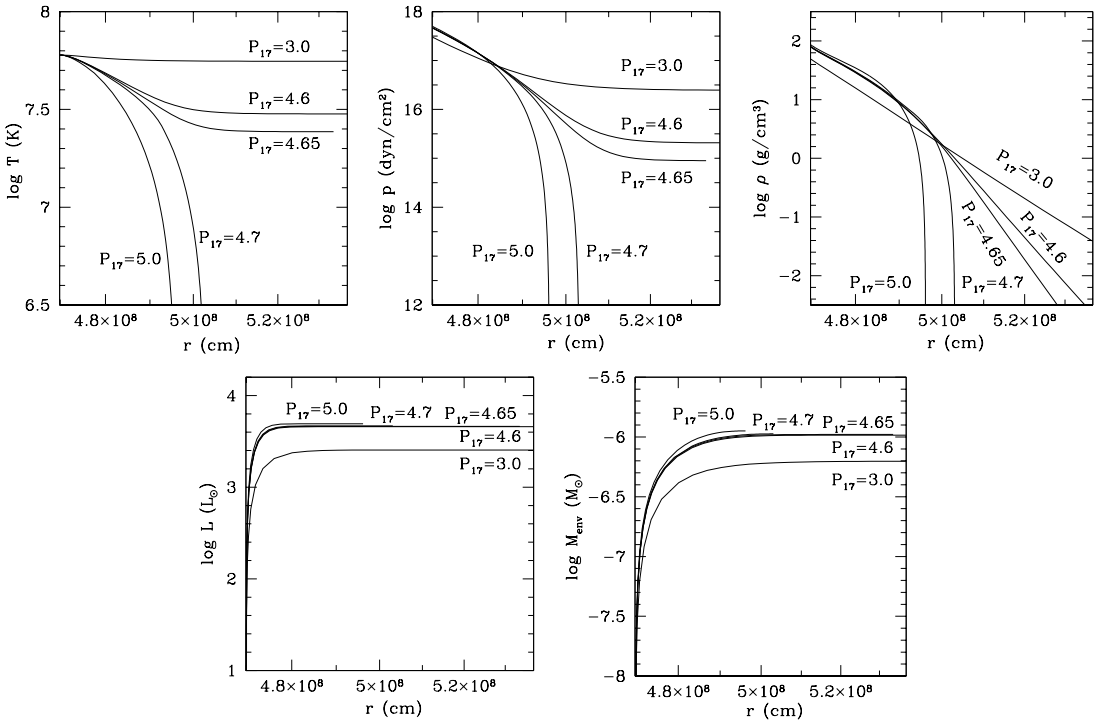

Figure 2.1: Results from integration of the four stellar structure equations with all boundary conditions at the bottom of the envelope. Luminosity and temperature at the bottom of the envelope are fixed in all cases to $L_b = 1L_\odot$ and $T_b = 6 \times 10^7 K$, while pressure is indicated for each case (as P_{17}, pressure in units of $10^{17} dyn\, cm^{-2}$). $M_c = 1.1 M_\odot$, $R_c = 4.7 \times 10^8 cm$.

- For a fixed temperature at the bottom of the envelope, there is a critical value for the pressure that establishes the borderline for the presence of a convective region in the envelope. For a pressure higher than this critical value, convection appears in outer layers. For a pressure smaller than the critical value, no convection appears and the temperature reaches a stable value for the outer layers.

- The total envelope mass and luminosity do not depend strongly on the thermal state of the envelope. Similar values are reached for similar conditions at the bottom of the envelope, no matter whether the envelope has a convective region or not.

2.3 Envelope Properties over the $P_b - T_b$ plane

The results of the integration of the whole set of equations for different conditions at the bottom of the envelope, P_b and T_b, have been studied. The four stellar equilibrium equations are integrated outwards from the core surface or bottom of the envelope, until radiation pressure dominates over the gas pressure, or when very small values of density are reached, if the previous condition is not fulfilled before. The envelopes are classified according to the presence or not of a convective region (which are called for short *convective* -with convective region- or *radiative* -without convection- envelopes).

Figure 2.2 shows the distribution of convective and radiative results on the $P_b - T_b$ plane. Crosses indicate conditions in the borderline between convective and radiative envelopes. The upper limit corresponds to temperatures at the bottom of the envelope such that the radiation pressure equates the gas pressure; for higher temperatures, a static envelope can not exist. A line has been fit to the intermediate and lower limits between structures with convective region and purely radiative ones. The lower limit corresponds to the limit of pressure and temperature for which energy production starts to be efficient. The line corresponding to the analytical model (with no energy production, constant luminosity, and Kramers opacity $T^{8.5} \sim P^2$) is over-plotted for comparison. It does not correspond exactly to the borderline found in the numerical integration, and the difference is caused by the opacities. OPAL opacities are used for the numerical integration, and as shown in appendix A, depending on the density and temperature conditions, OPAL opacity behaviour can be fit either with the Kramers opacity, or with a relation of the kind $\kappa \sim T^{-5}$. With $\kappa \sim T^{-5}$, the radiative analytical model would be $T \sim P^{0.2}$, which corresponds approximately to the best fit line over-plotted on the lower radiation-convection limit in figure 2.2. The main limit between convection and radiation for middle values of P_b and T_b follows the behaviour $T \sim P^{-0.42}$. As will be seen later, envelopes fulfilling the proper outer boundary conditions at the photosphere, have P_b and T_b values over this line.

2.3.1 Photospheric properties of the envelopes in the $P_b - T_b$ plane

Structures resulting from outwards integration of the stellar equilibrium equations do not, in general, fulfill the outer boundary conditions of a stellar envelope and thus are not solutions to our problem. It is however interesting to see the outer boundary values obtained from the previous outwards integration over the $P_b - T_b$ plane. This will provide a hint of what conditions at the base of the envelope cause the outer values to be close to the correct outer boundary conditions. It will also show which of the previously integrated structures are of interest for our study of post-outburst classical novae.

Figures 2.3 and 2.4 show the global properties of the structures obtained for different values of $P_b - T_b$, after integration of the whole set of stellar equilibrium equations. White dwarf degenerate core properties, which are the boundary conditions at the base of the

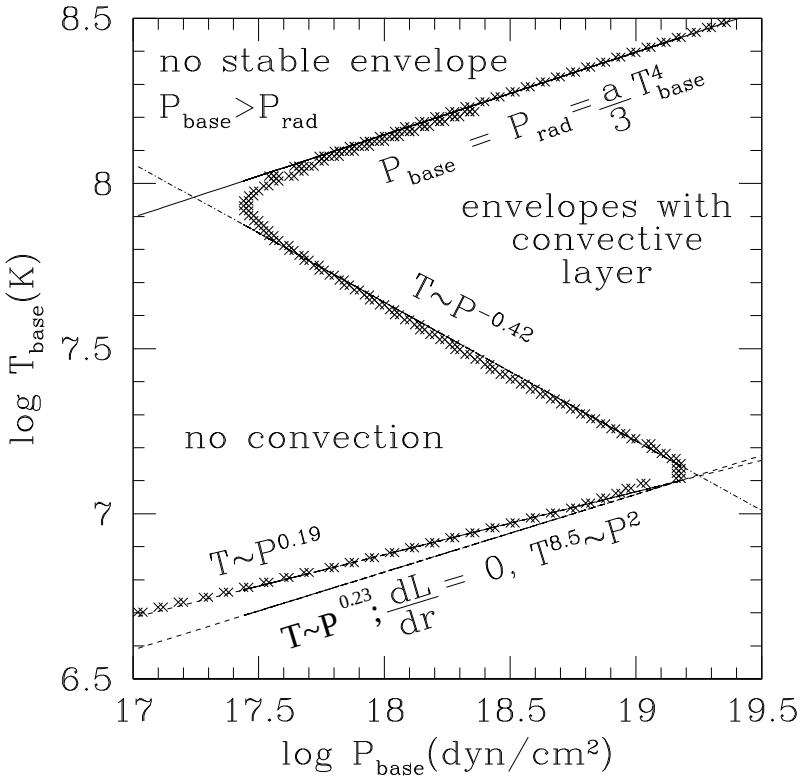

Figure 2.2: Thermal properties of CO $1.1M_\odot$ white dwarf envelopes on the $P_b - T_b$ plane. At the bottom of the envelope, $L_b = 1L_\odot$, $R_c = 4.7 \times 10^8 cm$ (see text for more details).

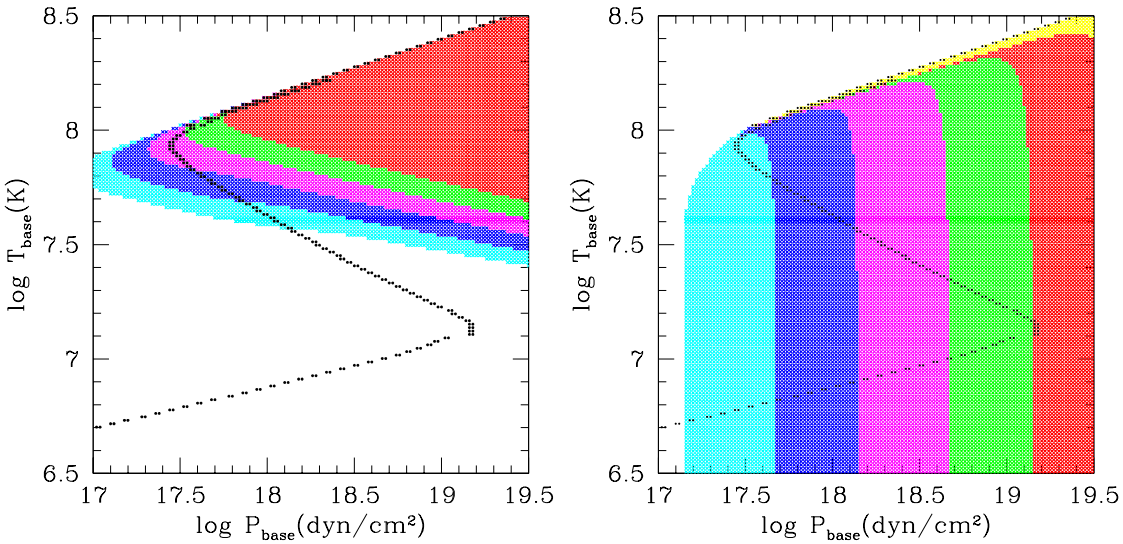

Figure 2.3: Values of total luminosity and envelope mass in the $P_b - T_b$ plane.
Left panel: from bottom to top, $L(L_\odot)$: $10^2 - 10^3$ (cyan), $10^3 - 10^4$ (blue), $10^4 - 10^5$ (magenta), $10^5 - 10^6$ (green) and $L(L_\odot) > 10^6$ (red). **Right panel**: from left to right, $\log M_{env}(M_\odot)$: $3 \times 10^{-7} - 10^{-6}$ (cyan), $10^{-6} - 3 \times 10^{-6}$ (blue), $3 \times 10^{-6} - 10^{-5}$ (magenta), $10^{-5} - 3 \times 10^{-5}$ (green), $3 \times 10^{-5} - 10^{-4}$ (red) , and $M_{env}(M_\odot) > 10^{-4}$ (yellow).

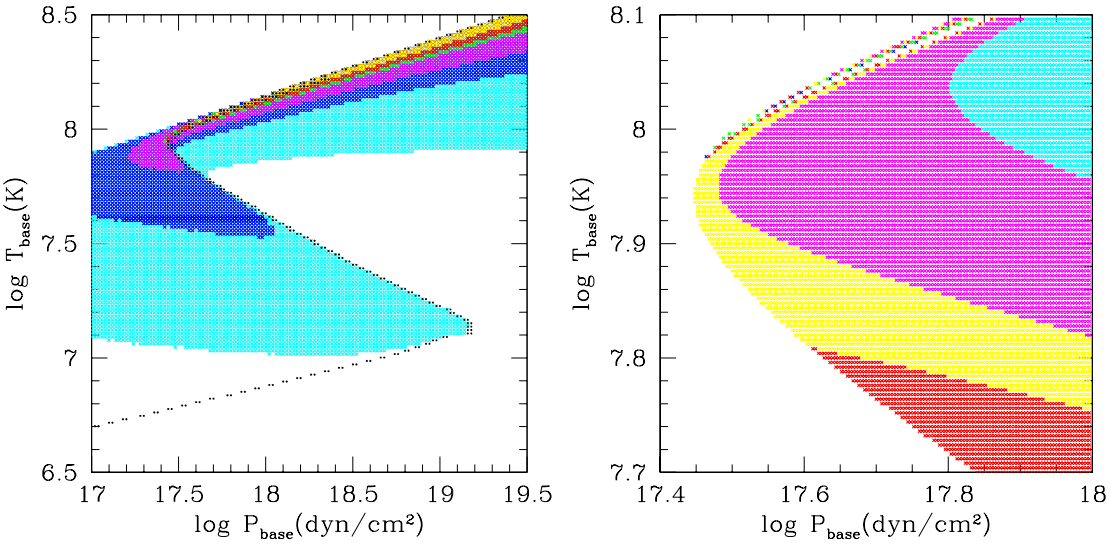

Figure 2.4: Outer radius and photospheric temperature in the $P_b - T_b$ plane.
Left panel: from bottom to left: $R(\times 10^8 cm)$: 5-5.5 (cyan),5.5-6 (blue), 6-8 (magenta), 8-10 (green), 10-50 (red), and $R(cm) > 5 \times 10^9$ (yellow).
Right panel: temperature at the layer where the condition $L = 4\pi R^2 \sigma T^4$ is fulfilled for the cases where this layer is found. From bottom to top, $T(K)$: $5 \times 10^8 - 6 \times 10^5$ (red), $6 \times 10^5 - 9 \times 10^5$ (yellow), $9 \times 10^5 - 2 \times 10^6$ (magenta) and $2 \times 10^6 - 10^7$ (cyan).

envelope, are $M_c = 1.1 M_\odot$, $R_c = 4.7 \times 10^8 cm$ and $L_c = 10^{-3} L_\odot$. Different values for the core luminosity have been tested, and it has been found that they have no effect on the result, as long as core luminosity is smaller than $\sim 10 L_\odot$.

Luminosity increases for increasing temperatures and pressures. Lines of constant luminosity are approximately parallel, except for cases close to the radiation pressure limit. The same is true for lines of constant mass. In the region close to the radiation pressure limit, the equation of state starts to be highly dominated by radiation pressure, unlike for lower temperatures, where ideal gas dominates. For low temperatures, the main source of pressure at the base is the weight of the envelope mass. Pressure is expected to be proportional to envelope mass, which explains the fact that lines of constant mass in figure 2.3 run approximately at constant pressure, with increasing values of pressure at the base for increasing values of envelope mass. For higher temperatures, lines of constant mass bend slightly towards lower pressures, since radiation pressure starts to contribute and helps to sustain the envelope mass, which becomes even more evident for temperatures close to the radiation pressure limit. Both luminosity and mass distributions in the $P_b - T_b$ plane behave unaware of the energy transportation regime. This is not surprising taking into account that, as seen in appendix A, mass and luminosity vary strongly in the deepest layers, but their total values experiment little variation along most of the envelope. As convection appears, when it does, above energy production layers and at small densities, total mass and luminosity values cannot depend on the presence of a convective layer.

The outer boundary of a stellar envelope is set at the photosphere, defined as the layer where stellar material becomes optically thin and temperature equals the effective temperature, T_{eff}, defined as $L = 4\pi R^2 \sigma T_{eff}^4$. Above the photosphere, the assumptions taken in the interior envelope for the energy transport are not valid anymore. In the previously calculated structures over the $P_b - T_b$ plane, it is interesting to see whether this photospheric layer can be defined or not, and which are the photospheric properties in

the cases where it can be found. In cases where no convection appears (purely "radiative" cases), the condition $P = P_{rad}$ is reached before any layer fulfills the condition $L = 4\pi R^2 \sigma T^4$. The assumption of stability is broken before reaching the photosphere, and the present model is no longer valid. The photosphere can only be defined in those cases where a convective region exists, and causes the envelope to cool faster with radius than in cases with only radiative transport. The temperature gradient is in this case steeper than pressure gradient, and the radiation pressure never dominates the equation of state. Figure 2.4 shows the values of outer radius and photospheric temperature. Left panel shows radius values at the last integrated layer. In the purely radiative cases, this corresponds to the point where radiation pressure dominates over gas pressure. For structures with convective regions, since temperature, pressure and density decrease steeply at outer layer (see Figure 2.1), the outermost radius can be taken as the photospheric radius, where the condition $L = 4\pi R^2 \sigma T^4$ is fulfilled. It is worth noticing that radius increases for increasing base temperatures, but depends only weakly on base pressure. Right panel in figure 2.4 indicates values of photospheric temperature in cases where photosphere can be defined.

2.3.2 Photosphere and atmosphere

For the highest bottom temperatures, structures with convective regions have luminosities higher than the Eddington limit, defined as (see, for example, Bowers & Deeming (1984))

$$L_{Edd} = \frac{5.03 \times 10^{37}}{\overline{\kappa}} \left(\frac{M}{M_\odot} \right) erg\, s^{-1} \tag{2.6}$$

In these cases, radiation pressure exceeds the gravitational pressure and no stable layers can stay over the photosphere. A static atmosphere can only exist where radiation pressure at the photosphere is smaller than gravitational pressure. Figure 2.5 shows the regions on the $P_b - T_b$ plane where this condition is fulfilled. The upper borderline for the existence of a stable atmosphere is approximately parallel to the lines of constant luminosity in figure 2.3, and it corresponds to a luminosity in the range $(4.6 - 4.9) \times 10^4 L_\odot$. The exact value decreases for increasing bottom pressures and temperatures. If this luminosity is supposed to be the Eddington luminosity, for the total mass of models in figure 2.3, $1.1 M_\odot$, (2.6) indicates a mean opacity in the atmosphere $\overline{\kappa}$: $0.57 - 0.6$. These are reasonable values, as can be seen in figure B.6 of appendix B, for the temperatures and densities at the photosphere, $T \sim 5 \times 10^5 K$ and $\rho \sim 10^{-7} g\, cm^{-3}$ (see values of the gas at the photosphere for envelopes fulfilling photospheric boundary conditions in section 2.4.3).

After this preliminary study of the results of integration of the equations for different values of the envelope base properties, the main aim of this work is to find a solution for a white dwarf envelope, with the boundary conditions properly fulfilled at the photosphere and at the bottom of the envelope. At the base of the envelope, mass and radius must be those of the degenerate core, while at the photosphere, it is necessary that pressure and temperature of the interior solution, $T_{int,\,phot}$ and $P_{int,\,phot}$, match the bottom values of the atmosphere, $T_{atm,\,phot}$ and $P_{atm,\,phot}$,

$$T_{int,\,phot} = T_{atm,\,phot} \tag{2.7}$$

$$P_{int,\,phot} = P_{atm,\,phot}. \tag{2.8}$$

These outer boundary conditions will be properly used in section 2.4, but it is now interesting to study the regions in the $P_b - T_b$ plane which are candidate to verify these conditions. Let us assume that the photosphere can be found in the interior solution as the layer which verifies $L = 4\pi R^2 \sigma T^4$, and that the effective temperature is the temperature at this layer.

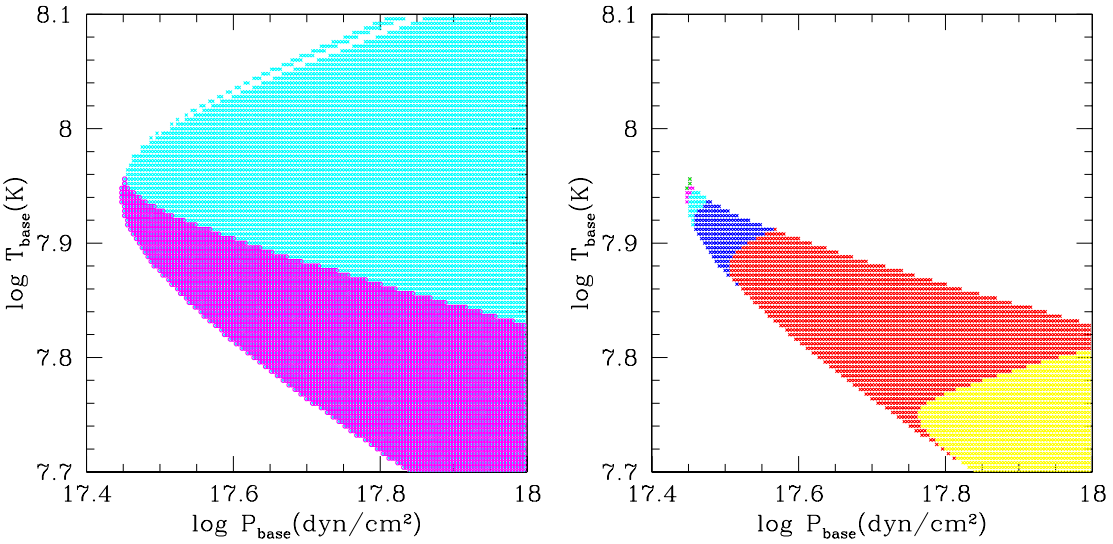

Figure 2.5: Stability of static envelopes and convergence of integration with photospheric boundary conditions.

Left panel: Regions of the $P_b - T_b$ plane with envelopes for which a photosphere can be found before $P_{rad} = P$, but no static atmosphere can exist, i.e., at the photosphere, $L > L_{Eddington}$ (upper region, cyan) and envelopes where both a photosphere and a static atmosphere can exist, i.e., $L < L_{Eddington}$ (lower region, in magenta).

Right panel: differences between interior solution pressure ($P_{int,phot}$) and atmospheric pressure ($P_{atm,phot}$) at the photosphere. The figure shows regions in the $P_b - T_b$ plane with different values of f, where $f = \left|\frac{\log P_{atm,phot} - \log P_{int,phot}}{\log P_{int,phot}}\right|$ must be zero when outer boundary conditions are fulfilled. P_{atm} is calculated integrating the atmosphere with the luminosity L, temperature T, mass M and R obtained at the outermost layers of the interior solution. From left to right, $f < 0.03$ (green), $0.03 < f < 0.05$ (magenta), $0.05 < f < 0.1$ (cyan), $0.1 < f < 0.2$ (blue), $0.2 < f < 0.3$ (red) and $f > 0.3$ (yellow).

A grey atmosphere model for the values of temperature, luminosity and gravity at this layer can be calculated (see section 2.4 for details on the grey atmosphere). By construction, the atmospheric temperature at the photosphere will be the effective temperature, which has been forced to be the photospheric temperature of the interior solution, so that condition (2.7) is automatically fulfilled. The grey atmosphere provides the atmospheric pressure at the photosphere, which must equal the pressure of the solution for the interior envelope at the photosphere (as indicated in (2.8)). The comparison of the interior and atmospheric pressures at the photosphere in the results over the $P_b - T_b$ plane provides an indication of the region in the plane where solutions for the envelopes can be found. Figure 2.5 shows the differences between the $P_{int,phot}$ and $P_{atm,phot}$ in the $P_b - T_b$ plane. The smallest differences are found in the narrow region of limit between convective and radiative envelopes. This result could be expected in view of the analytical approximation results (see appendix A). Although the photospheric boundary conditions are not exactly zero, the temperature and pressure at the photosphere are much smaller that conditions at the base of the envelope, and thus solutions can not differ strongly from the solutions for zero boundary conditions (with $C = 0$) in figure A.1, which correspond to the limit between convective ($C < 0$) and radiative ($C > 0$) solutions.

2.4 White Dwarf Envelope Numerical Model

A grid of white dwarf envelope models with steady hydrogen burning has been computed for six different core masses (from 0.8 to 1.3 $M_{\odot}$). Chemical composition is homogeneous for the whole envelope, and six different cases have been considered. Three of them correspond to realistic envelopes accreted onto ONe white dwarfs in novae from José & Hernanz (1998), who developed hydrodynamic simulations of the nova models with detailed computation of the nucleosynthesis, and obtained results for the composition of the ejecta compatible with observed abundances in many cases. As found already from the first hydrodynamic models of nova outburst, their models showed that the material accreted from the secondary, with solar abundances, needs to be enhanced with CNO nuclei by some mixing mechanism between the envelope and the degenerate core. The three compositions considered here correspond to ONe white dwarf envelopes with 25%, 50% and 75% mixing of the solar accreted matter with the core material. One additional case of CO white dwarf envelopes with 50% mixing, also corresponding to one of the compositions considered in José & Hernanz (1998), has been included to study the differences introduced by the metal abundances. For the calculation of the accreted envelope composition resulting from the mixing, José & Hernanz (1998) took the composition of the degenerate cores from Ritossa et al.(1996) for the ONe white dwarfs, and assumed 50% of oxygen and 50% of carbon in the CO cases.

Finally, two extra series of models have been computed. I82 models are envelopes with abundances similar to those used by Iben (1982), who did not consider realistic envelopes for novae, but white dwarfs accreting hydrogen rich material at the same rate it was burned, keeping a constant envelope mass, and without specific mixing with the degenerate core. Composition can not be exactly the same because he used his own analytical approximations for the opacities, while we use more realistic opacities from OPAL tables, which can only be obtained with two elements enhanced over solar abundance; nevertheless, the resulting composition is very similar to that used by Iben, since his models were poorly enriched by metals. The sixth composition considered (models ONe09) is a poorly ONe enriched envelope, with a mixing degree (9.3%) such that the hydrogen mass fraction is the same as in I82 models, to see the effects of the metals between Iben (1982) and realistic ONe white dwarf envelopes in novae. Table 2.1 shows the details of the chemical compositions.

2.4.1 Numerical Method and Boundary Conditions

In the numerical code, the four stellar equilibrium equations (2.1-2.4) are integrated inwards using an embedded (adaptative stepsize controlled) Runge-Kutta method with Cash-Karp parameters (Cash & Karp (1990), Press et al.(1992)). The two point boundary problem is solved using a shooting method (Press et al.(1992), see Appendix C for details on the numerical procedure).

For numerical integration, the variable M is substituted by q, defined as

$$q \equiv \frac{M}{M_c} - 1 = \frac{M^{env}}{M_c} \tag{2.9}$$

$$M = M_c\,(q+1)\,,\ M^{env} = qM_c$$

where $M^{env} = M - M_c$ is the envelope mass at radius r. Since integration progresses from the photosphere ($r = R_{fotos}$) inwards down to the surface of the degenerate core ($r = R_c$),

Table 2.1: Chemical compositions of the white-dwarf envelope models, in mass fractions. $X = X_H$, $Y = X_{He}$. Z_s contains metals (all elements except H and He) in solar fraction. δX_i indicates extra mass fraction of element i beyond that included in Z. The total abundance of metals is indicated by Z_{total}. In the case of the I82 models, only N and O overabundances are taken into account for the opacities (because the OPAL opacity tables can only have two metals in excess over solar abundance).

WD	Mixing	Name	X	Y	Z_s			Z_{total}
						δX_O	δX_{Ne}	
ONe	75%	ONe75	0.18	0.08	0.12	0.38	0.24	0.74
ONe	50%	ONe50	0.35	0.15	0.09	0.25	0.16	0.5
ONe	25%	ONe25	0.53	0.2	0.06	0.13	0.08	0.27
						δX_C	δX_O	
CO	50%	CO50	0.35	0.14	0.02	0.245	0.245	0.51
						δX_N	δX_O	
-	-	I82	0.6378	0.35		0.0033	0.0073	0.01
						δX_O	δX_{Ne}	
ONe	9.3%	ONe09	0.6378	0.25	0.03	0.05	0.03	0.11

the independent variable r is substituted by the geometrical depth, D, defined as

$$D = \frac{R_{fotos} - r}{R_{fotos} - R_c} \tag{2.10}$$

which runs from $D = 0$ at the photosphere to $D = 1$ at the base of the envelope.

The integration starts at the photosphere, with a fixed value for the total luminosity, L, and trial values for the total mass of the envelope, M_{env}, and for the photospheric radius, R_{fotos}, and proceeds inwards to the base of the hydrogen burning layer. As will be seen later, for all white dwarf masses and compositions there is a plateau of constant luminosity where models experiment little change in the total luminosity for a wide range of effective temperatures. In this plateau, the total luminosity does not determine a unique solution anymore and the photospheric radius is fixed instead.

The boundary conditions at the photosphere are obtained from a grey atmosphere model of the same composition as the envelope. The external layers above the photosphere contain a small fraction of the total envelope mass, and densities are much smaller than in interior layers (little change in the total mass); in addition, the atmosphere thickness is very small compared to the total distance to the center of the star, and thus the gravity can be considered to be constant thorough the atmosphere integration $\left(g = \frac{G(M_c+M_{env})}{R^2_{fotos}}\right)$. There is no significant energy production, so that the luminosity L remains constant. In these conditions, the temperature and pressure stratifications are given by the theory of stellar atmospheres, that use the optical depth τ as independent variable, defined as

$$d\tau = -\kappa\rho dr \tag{2.11}$$

where $\kappa = \kappa(T, \rho)$ is the mean opacity for the composition of the atmosphere. As a first approximation, the temperature stratification can be described by the Eddington approximation for the grey case of radiative transport in stellar atmospheres:

$$T^4(\tau) = \frac{3}{4}\left(\tau + \frac{2}{3}\right) T^4_{eff} \tag{2.12}$$

Table 2.2: Masses, radii (from Hamada & Salpeter (1961)) and gravity of the white dwarf degenerate cores.

$M_c(M_\odot)$	0.8	0.9	1.0	1.1	1.2	1.3
$R_c(\times 10^8 cm)$	6.9	6.1	5.4	4.7	3.8	3.0
$log\ g$	8.35	8.51	8.66	8.82	9.04	9.28

where T_{eff} is the effective temperature, defined as $T_{eff}^4 = \frac{L}{4\pi\sigma R_{fotos}^2}$. The mass distribution can be written as a function of the optical depth combining (2.1) and (2.11),

$$\frac{dM_r}{d\tau} = \frac{dM_r}{dr}\frac{dr}{d\tau} = -\frac{4\pi R^2}{\kappa}$$

which together with the hydrostatic equilibrium equation (2.2) give the pressure distribution for the atmosphere,

$$\frac{dP}{d\tau} = \frac{GM_c}{\kappa R^2} \tag{2.13}$$

Equation (2.13) is integrated from the outer boundary of the atmosphere, where $\tau = 0$, $P = P_{rad}$ and $T = T(\tau = 0) = \left(\frac{1}{2}\right)^{\frac{1}{4}} T_{eff}$, to the photosphere, defined as the layer where $T = T_{eff}$, that with the Eddington approximation (2.12) corresponds to $\tau = \frac{2}{3}$.

The integration of (2.13) provides the value of the atmosphere pressure at the photosphere, $P_{atm,fotos}$, for the fixed value of the luminosity L and the trial values of M_{env} and R_{fotos}. The integration of the envelope starts at the photosphere with $P_{atm,fotos}$ and T_{eff} as the outer boundary conditions.

The atmosphere is tested for convective instability during integration, which has never appeared before reaching the photosphere in this work. In previous works on convective white dwarf envelopes (Fontaine & Van Horn (1976)) atmosphere was integrated down to $\tau = 10$ when no convection appeared in upper layers. Nevertheless, in the present work, if the atmosphere was integrated for $\tau > \frac{2}{3}$, the assumption of constant gravity was found to fail, indicating that the atmosphere model is not valid for deeper layers.

From the photosphere, the stellar structure equations are integrated inwards until the luminosity reaches a value sufficiently small ($L = 1L_\odot$, see section A.3 in appendix A), which is considered as an indicator of the base of the burning shell. At this point, the boundary conditions at the base of the envelope are tested. The envelope mass, M_{base}^{env}, is required to be smaller than $10^{-13}M_\odot$, while the radius, R_{base}, is compared to the core radius, R_c (taken from the $M_c - R_c$ relation by Hamada & Salpeter (1961), see table 2.2), requiring the factor $\left|\frac{R_{base}-R_c}{R_c}\right|$ to be smaller than 10^{-5}. If these conditions are not fullfiled, the integration restarts from the photosphere with new trial values of R_{fotos} and M_{env}.

It must be noticed that, although the integration method sees the values of pressure and temperature at the photosphere as outer boundary conditions, the true fixed conditions for each model are the luminosity L and the relationship between the luminosity, the photospheric radius and the effective temperature, $T_{eff}^4 = \frac{L}{4\pi\sigma R_{fotos}^2}$. When the luminosity is the fixed parameter at the photosphere, it is also a peculiarity of the integration method the fact that, although integration is performed by the Runge-Kutta method with the geometrical depth D_r (proportional to the radius) as the independent variable, the limits of the integration interval are defined by the luminosity, which acts as an "effective independent variable", while the geometrical depth is only fixed at the photosphere.

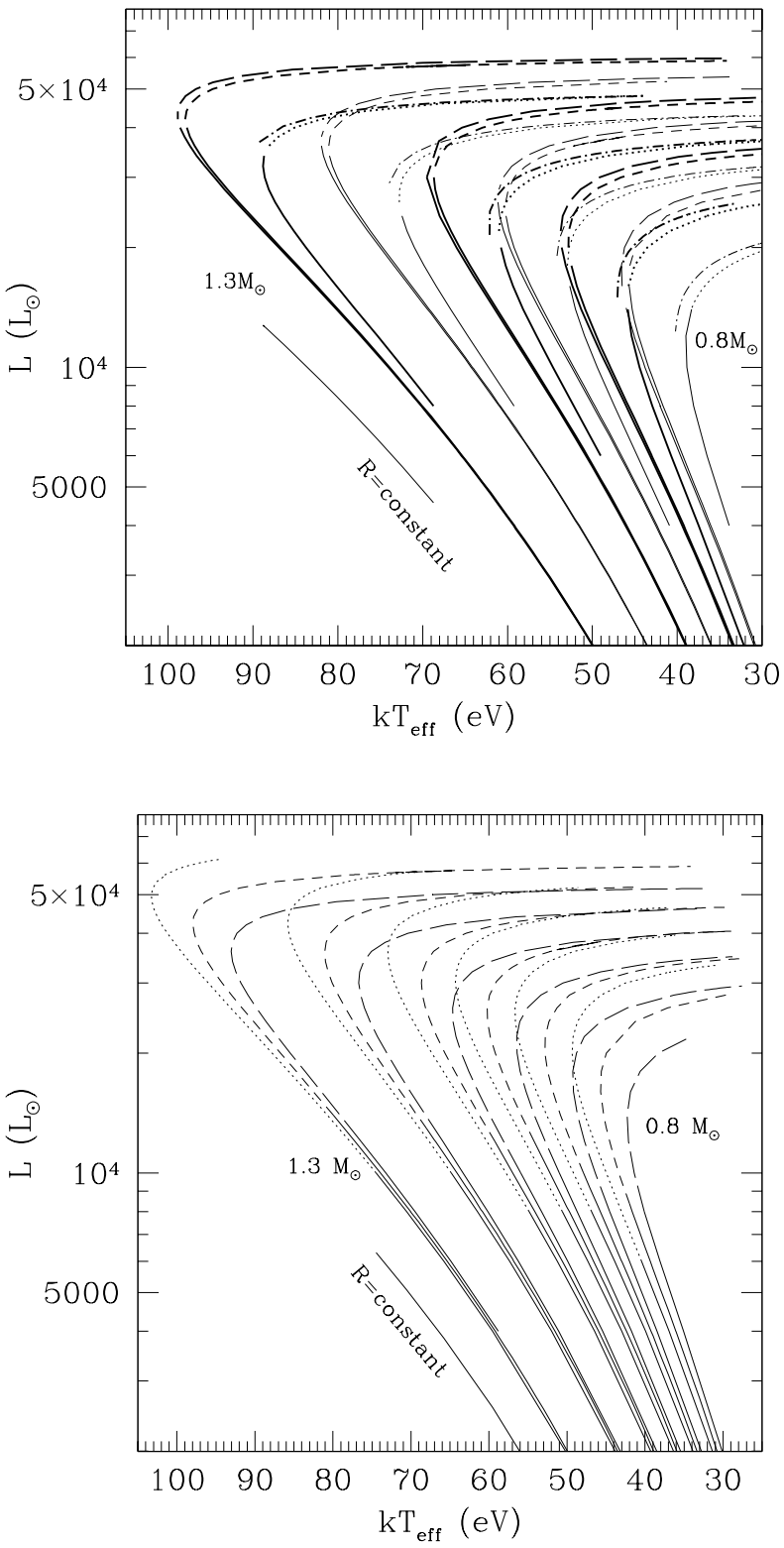

Figure 2.6: Total luminosity versus effective temperature for all stationary white dwarf envelope models. **Upper panel:** CO50 (long-dash), ONe50 (short-dash), ONe09 (dash-dot) and I82 (dotted line). Solid lines indicate envelopes without convective regions (for the ONe09 models, this purely radiative branch is not plotted). Six series of models are plotted for each chemical composition, corresponding to total masses 0.8, 1.0 and 1.2 $M_{\odot}$ (thin lines) and 0.9, 1.1 and 1.3 $M_{\odot}$ (thick lines).
Lower panel: ONe25 (long-dash), ONe50 (short-dash) and ONe75 (dotted line). Solid lines indicate purely radiative solutions.
A line indicating the luminosity-effective temperature relation for constant photospheric radius ($R = 2 \times 10^7 cm$) is over-plotted in both panels.

2.4.2 General properties of the envelopes

Figures 2.6 and 2.7 show the luminosity and the photospheric radius versus the effective temperature for all models. For all compositions considered here, the results follow a behaviour similar to that found for hot accreting white dwarfs with steady hydrogen burning by Iben (1982), whose models had X=0.64 and metal abundances quite different from envelopes on post-nova white dwarfs. For each composition and white dwarf mass, there exists a maximum luminosity and a maximum effective temperature. The maximum effective temperature divides the series of models into two branches: a branch of high, quasi-constant luminosity, where the maximum value for the luminosity is reached; and a branch of low luminosity, at constant photospheric radius. The models of the high luminosity branch have in all cases a convective region below the photosphere, while the energy transportation in most of the envelopes of the low luminosity branch is radiative in the whole structure. Figure 2.8 shows the envelope mass as a function of effective temperature. For every white dwarf mass there exists a minimum value for the envelope mass, which occurs in the vicinity of the maximum effective temperature. The mass of the high luminosity branch envelopes is almost constant, increasing only slowly for decreasing effective temperatures, while the mass in the low luminosity branch grows for cooling models.

2.4.2.1 Stable and unstable branches

Evolution of an envelope can be approximated as a succession of stationary hydrogen burning models with decreasing envelope masses. Along the high luminosity branch, an envelope evolves at quasi-constant luminosity. As the envelope mass is reduced due to hydrogen burning, the photospheric radius shrinks, increasing its effective temperature as the photosphere sinks deeper into the envelope. Nevertheless, the envelope as a whole is slowly cooling down and the energy production decreases with time, with the luminosity and the temperature at the base of the envelope slowly decreasing (figures 2.6 and 2.9). Hydrogen burning continues until the minimum envelope mass is reached; evolution can not proceed further with stationary hydrogen burning, since no equilibrium configuration for a smaller envelope mass exists.

If evolution along the low luminosity branch is considered, the photospheric radius would be kept constant, while effective temperature and luminosity would increase for decreasing envelope masses. In this case, the effective temperature would increase as a result of the heating of the whole envelope, also reflected in the increase of the luminosity and of the temperature at the bottom of the burning layer (figure 2.9). Steady state evolution can not proceed along this low luminosity branch, since for decreasing envelope masses, the temperature at the bottom would increase. This immediately indicates that quasi-static evolution along this branch is not possible, since it would require an extra source of energy to heat the envelope. Along the high luminosity branch, as the envelope mass is consumed, the temperature at the base decreases and the whole envelope cools down (although effective temperature increases as a consequence of the shrinking of the photosphere).

Stability analysis of the shell source indicates indeed that stationary solutions along the low luminosity branch are unstable. Following the stability analysis from Kippenhahn & Weigert (1990), we assume that the burning shell of the envelope, at a distance r of the center of the star and with a thickness D, expands as a result of the addition of a small amount of heat. Suppose that the expansion is homologous, so that (see for instance Kippenhahn & Weigert (1990)),

$$\frac{d\rho}{\rho} = -\frac{r}{D}\frac{dr}{r}$$

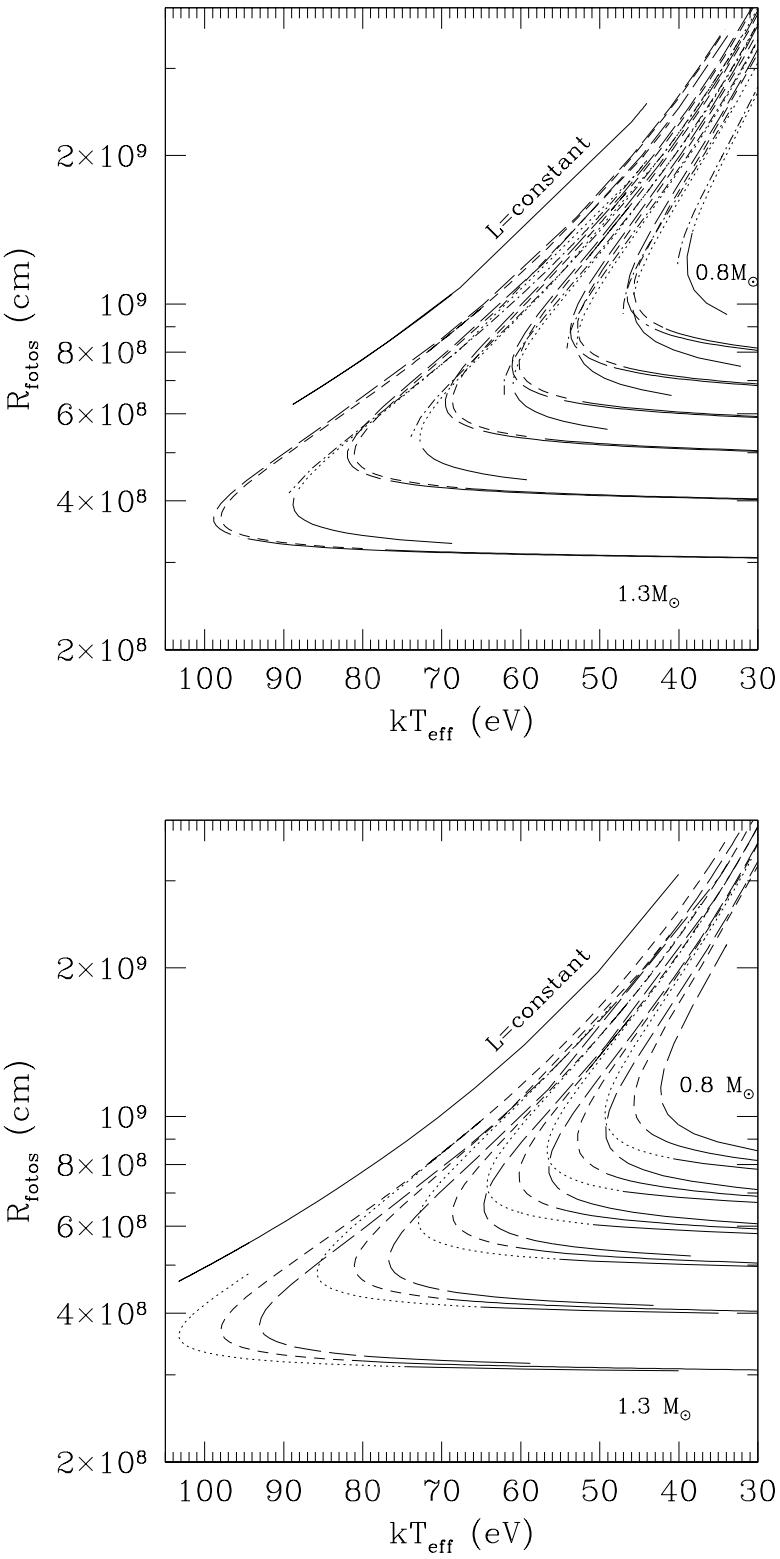

Figure 2.7: Photospheric radius versus effective temperature for same models as in figure 2.6. A line indicating the radius-effective temperature relation for constant luminosity ($L = 6.3 \times 10^4 L_\odot$) is over-plotted.

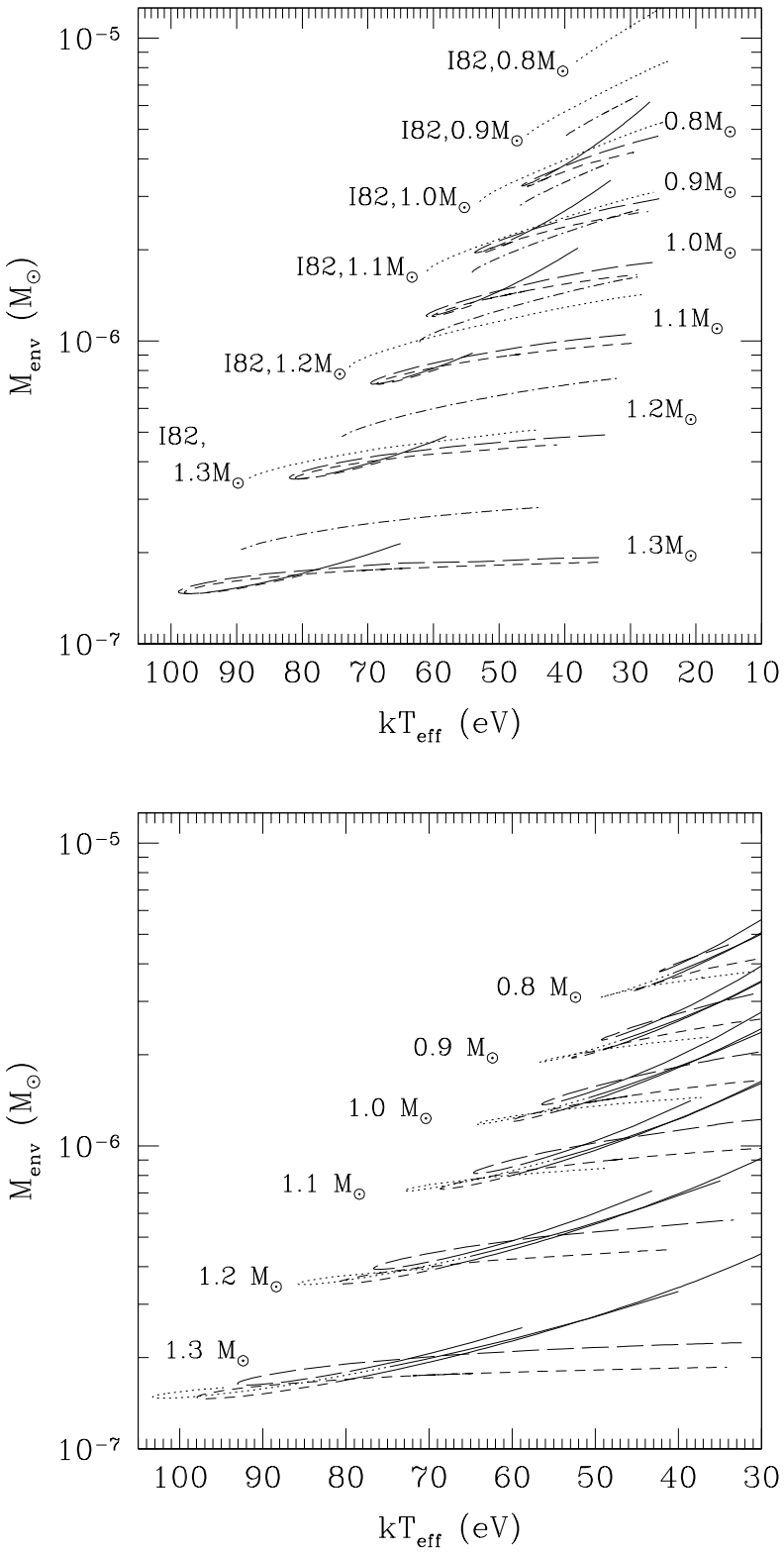

Figure 2.8: Envelope mass versus effective temperature for same models as in figure 2.6. In left panel, non convective envelopes are plotted only for the CO50 models for simplicity. The behaviour is similar in all models.

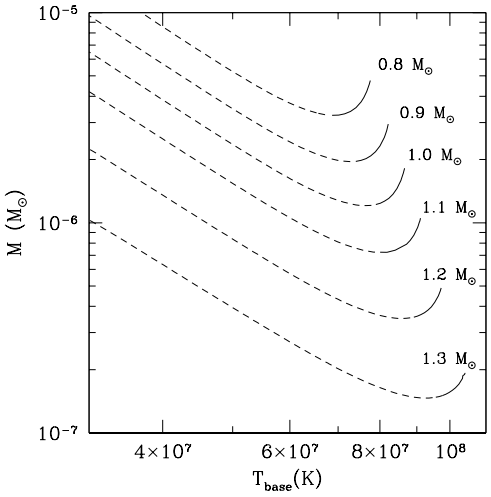

Figure 2.9: Envelope mass versus base temperature for CO50 models.
Solid lines indicate envelopes with convective region. Steady state evolution can not proceed along the low luminosity branch (with low bottom temperatures), since for decreasing envelope masses, the temperature at the base would increase, which would require an extra source of energy. Along the high luminosity branch (with high bottom temperatures), as the envelope mass is consumed, the temperature at the base decreases and the whole envelope cools down (although effective temperature increases as a consequence of the shrinking of the photosphere).

$$\frac{dP}{P} = -4\frac{dr}{r} \tag{2.14}$$

With the equation of state in differential form

$$\frac{d\rho}{\rho} = \alpha\frac{dP}{P} - \delta\frac{dT}{T}$$

where $\alpha = \left.\frac{\partial \ln \rho}{\partial \ln P}\right|_T = \frac{1}{\beta}$ and $\delta = \left.\frac{\partial \ln \rho}{\partial \ln T}\right|_P = \frac{4-3\beta}{\beta}$, it is possible to write

$$\frac{dP}{P} = \frac{4\delta}{4\alpha - \frac{r}{D}}\frac{dT}{T} \tag{2.15}$$

The first law of thermodynamics can be written as

$$dq = du + Pdv = c_p T\left(\frac{dT}{T} - \nabla_{ad}\frac{dP}{P}\right)$$

Using 2.15,

$$dq = c_{grav}dT$$

where the *gravothermal specific heat*, c_{grav}, is defined as

$$c_{grav} = c_p\left(1 - \nabla_{ad}\frac{4\delta}{4\alpha - \frac{r}{D}}\right) \tag{2.16}$$

This quantity is a specific heat per unit mass under the condition that the gas pressure is kept in equilibrium with the weight of all the layers above the burning shell. $dT = dq/c_{grav}$ indicates the variation of temperature of the shell if the heat dq is added. With a negative c_{grav} , if the energy production is slightly enhanced and heat is added to the shell, $dT < 0$ and the temperature decreases, thus reducing the overproduction of energy. This is only

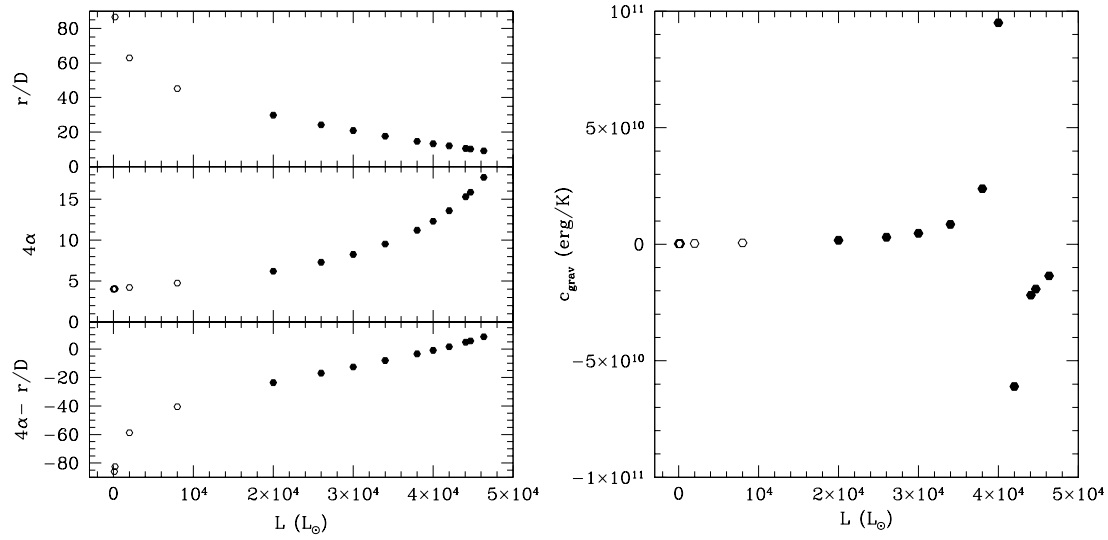

Figure 2.10: Gravothermal specific heat of the burning shell for ONe50 1.1$M_\odot$ envelope models. Open symbols indicate absence of convection in the envelope, while filled hexagons correspond to envelopes with convective regions. **Left panel:** Elements of the denominator in the gravothermal specific heat (2.16). **Right panel:** Gravothermal specific heat.

possible if, as a consequence of the input of energy, the shell expands enough. But for given properties of the gas (fixed α), the possibility of expansion depends on the shell thickness: if the shell is very thin, it can not lift the upper layers and the expansion is not possible. In the definition of c_{grav} (2.16), if the thickness D is small enough, $\frac{r}{D}$ can be larger than 4α which would give a positive gravothermal specific heat and an unstable burning shell: for an accidental excess of energy production, the burning layers heat up, enhancing the energy production and leading to a thermal runaway.

This is the case of the envelope models along the low luminosity branch of the preceding section. In figure 2.10, the gravothermal specific heat and the terms in the denominator of (2.16) are plotted against the luminosity for some ONe50 1.1 $M_\odot$ models. The burning shell, whose thickness is of interest for this analysis, has been defined as the layers of the envelope where 99.9% of the total outcoming energy is produced. Figure 2.10 shows that the shell thickness increases for increasing luminosities, causing the factor r/D to decrease. For increasing luminosities (which is equivalent to increasing core masses), β decreases as well, as seen in figure 2.11, causing the factor $4\alpha = 4/\beta$ to increase. As a consequence, the denominator in (2.16) vanishes at a critical point in the neighborhood of the maximum effective temperature and the minimum envelope mass, which divides the solutions into a stable (high luminosity) branch and an unstable (low luminosity) branch. The resulting stability line that separates stable and unstable models is indicated in the luminosity-effective temperature plane in figure 2.12 for ONe50 models.

2.4.2.2 Core mass - luminosity relation

From figure 2.6 it is clear that luminosity is almost constant along the stable, high-luminosity branch, and that its value increases with the core mass. In the left panel of figure 2.13, plateau luminosities are plotted against core mass for all models. The resulting core mass - luminosity relation can be roughly approximated by

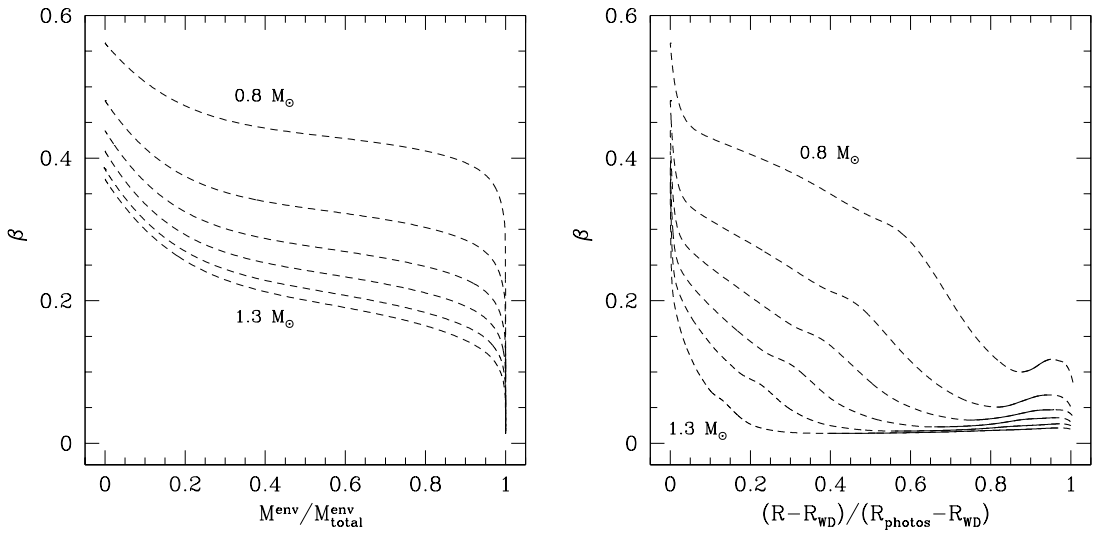

Figure 2.11: Distribution in envelope mass fraction (left panel) and radius fraction (right panel) of gas pressure over total pressure ($\beta = P_g/P$) for some stable envelope models.
β decreases strongly at outer layers (radiation pressure becomes important), and its value is smaller for increasing masses. Solid lines indicate convective zones. ONe50 models with core masses of 0.8, 0.9, 1.0, 1.1, 1.2 and 1.3 $M_\odot$, all of them with the same effective temperature, $kT_{eff} = 40eV$, are represented.
(Note that the interior structure of these cases will be plotted and commented in section 2.4.3)

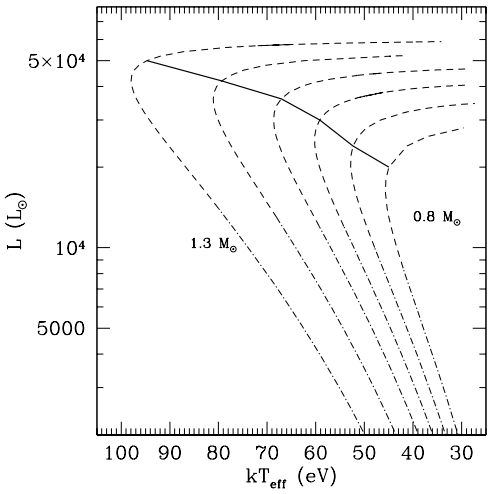

Figure 2.12: Stability line (thick line) of the ONe50 models on the L-kT plane.

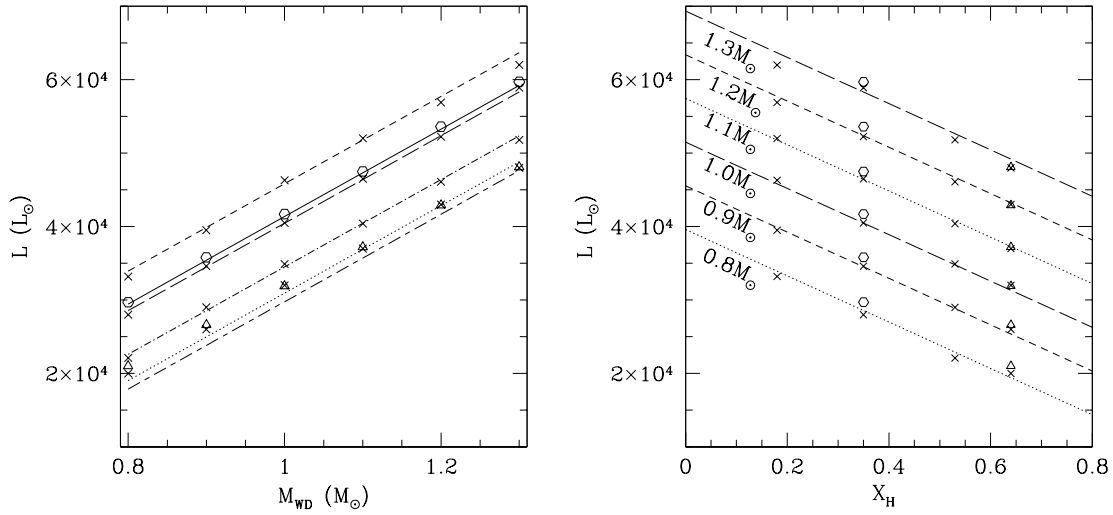

Figure 2.13: Plateau luminosity as a function of core mass and hydrogen mass fraction.
Left panel: Plateau luminosity versus core mass, for all models: I82 (with X=0.64, triangles), CO50 (X=0.35, circles), ONe75 (X=0.18, with the largest luminosities for each mass), ONe50 (X=0.35), ONe25 (X=0.53) and ONe09 (X=0.64, crosses, with the lowest luminosities, similar to I82 models). The relationship between luminosity and white dwarf mass found by Iben (1982) is shown in short-long dashed line (the line indicating lowest luminosities for each mass), while relation (2.17) is shown in solid line for CO50, short-dashed for ONe75, long-dashed for ONe50, dot-dashed for ONe25 and dotted for ONe09 and I82 models (both with the same X).
Right panel: Plateau luminosity versus hydrogen mass fraction. Points indicate model results, while lines correspond to relation 2.18 for ONe models.

$$L_{plateau}(L_\odot) \simeq 5.95 \times 10^4 \left(\frac{M_c}{M_\odot} - m_0 \right) \tag{2.17}$$

where, for CO50 envelopes $m_0^{CO50} = 0.3$, for ONe75 envelopes $m_0^{ONe75} = 0.24$, for ONe50 envelopes $m_0^{ONe50} = 0.32$, for ONe25 envelopes $m_0^{ONe25} = 0.42$, and for ONe09 and I82 models $m_0^{ONe09} = m_0^{I82} = 0.48$.

Relation (2.17) and the values for m_0 show that the plateau luminosity increases with the white dwarf mass and with increasing mixing factors of the accreted solar matter with the core material (that is, with decreasing hydrogen abundances). Envelopes with a lower hydrogen fraction, which need higher temperatures to reach an equilibrium configuration, have larger luminosities. For ONe models, taking into account the values found for m_0 for each hydrogen fraction, a general expression relating plateau luminosity, hydrogen fraction and core mass can be found:

$$L_{plateau}(L_\odot) \simeq 5.95 \times 10^4 \left(\frac{M_c}{M_\odot} - 0.536 X_H - 0.14 \right) \tag{2.18}$$

The effect of the exact metal abundances is small, since for the hydrogen mass fraction used by Iben (1982) ($X_H = 0.64$), who did not consider ONe enhanced envelopes but much metal poorer compositions (with Z_{total} =0.01 instead of Z_{total}=0.11) the $0.536 X_H + 0.14$ factor in equation (2.18), 0.48, is very similar to the value found in that work, 0.5. Nevertheless, it can not be neglected. The plateau luminosity versus the hydrogen fraction is shown in the right panel in figure 2.13 for all models. Relation (2.18) is over-plotted for each core mass. While ONe models follow (2.18) (except for the most massive white dwarf), CO models are slightly more luminous than ONe, which can also be seen in figure 2.6. These

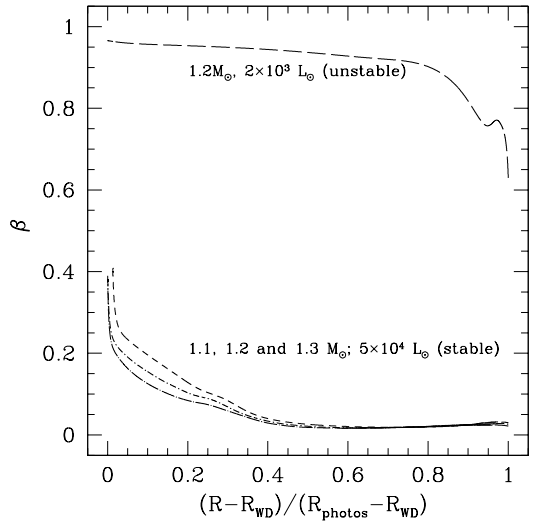

Figure 2.14: Distribution of gas pressure over total pressure ($\beta = P_g/P$) for some envelope models. Three models belong to the stable, high luminosity branch, all with the same total luminosity and effective temperature ($L = 5 \times 10^4 L_\odot$ and $kT_{eff} \simeq 45eV$): ONe25 with $M_c = 1.3 M_\odot$(long dash-dotted line), ONe50 with $M_c = 1.2 M_\odot$(short dash-dotted line) and ONe75 with $M_c = 1.1 M_\odot$(short dashed line). Radiation pressure dominates the equation of state at outer layers ($\beta \ll 1$). For comparison, a model from the unstable, low luminosity branch but with the same effective temperature is also plotted (ONe50 with $M_c = 1.2 M_\odot$, $L = 2 \times 10^3 L_\odot$, $kT_{eff} \simeq 45eV$, long-dashed line). Solid lines indicate convective zones.

and other differences caused by the different metal abundances will be discussed in section 2.4.3.

It is since long known that the luminosity of a shell-burning star with a degenerate core is essentially determined by its core mass. An analytical justification for the linear dependence of the luminosity with the core mass was obtained by Kippenhahn (1981) (see also Kippenhahn & Weigert (1990)). He started from the homology approximations (A.2.19-A.2.22) developed by Refsdal & Weigert (1970) commented in appendix A,

$$\rho(r/R_c) \sim M_c^{\varphi_1} R_c^{\varphi_2}$$

$$T(r/R_c) \sim M_c^{\psi_1} R_c^{\psi_2}$$

$$P(r/R_c) \sim M_c^{\tau_1} R_c^{\tau_2}$$

$$L(r/R_c) \sim M_c^{\sigma_1} R_c^{\sigma_2}$$

Using the equation of state of ideal gas plus radiation pressure in the form obtained in appendix B (equation B.1.8),

$$P \sim \rho^\beta T^{4-3\beta}$$

homology approximations for the pressure, the density and the temperature indicate that

$$\tau_1 = \beta\varphi_1 + (4-3\beta)\psi_1, \quad \tau_2 = \beta\varphi_2 + (4-3\beta)\psi_2$$

Requiring the homology relations to be a solution of the stellar equilibrium equations (2.2), (2.4) and (2.5), using a power law approximation for the energy generation rate, $\varepsilon = \varepsilon_0 \rho^{n-1} T^\nu$, and assuming the opacity to be constant (which would be the case for innermost layers of our envelopes, where opacity is dominated by Thomson scattering),

Kippenhahn (1981) determined the other exponents of the homology approximations for shell sources to be

$$\varphi_1 = \frac{4-\nu}{N}, \quad \varphi_2 = \frac{\nu - 12 + 6\beta}{N}$$
$$\psi_1 = \frac{1+n}{N}, \quad \psi_2 = \frac{2\beta - n - 3}{N}$$
$$\sigma_1 = \frac{4n+\nu}{N}, \quad \sigma_2 = \frac{3-\nu-3n}{N}\beta \tag{2.19}$$

with

$$N = (4-3\beta)(1+n) + (1-\beta)(\nu-4)$$

He also showed that β strongly decreases for increasing core masses. In the present models, this can be seen in figure 2.11, where the profile of the parameter β is plotted for ONe50 stable envelope models with different total masses. The contribution of the radiation pressure increases with the mass, decreasing β to values close to zero and affecting deeper layers of the envelope. With $\beta \ll 1$, (2.19) indicates $\sigma_1 \approx 1$ and $\sigma_2 \approx 0$, so that the luminosity depends linearly on the core mass, $L \sim M_c$. Figure 2.14 shows the β profile for three stable models of different compositions and white dwarf masses. In all of them, radiation pressure dominates in most part of the envelope. For comparison, an envelope from unstable, low luminosity branch is also plotted. It is clear that the contribution of the radiation pressure is much smaller in this case and that the core mass-luminosity relation would not be linear in this case.

With this linear relation, Kippenhahn (1981) confirmed the results found with numerical evolutionary calculations by Paczyński (1970), who showed that the luminosity of post-AGB stars with a double burning shell (H, He) on top of a mostly degenerate CO core could be expressed as

$$L(L_\odot) = a\left(\frac{M_c}{M_\odot} - b\right)$$

with a = 59,250 and b = 0.522. Later works found similar results, with small changes in the parameters. Among them, Iben (1982), who studied hot accreting white dwarfs with hydrogen burning, found that in the case of steady state, a = 59,500 and b = 0.5. This is over-plotted in figure 2.13, as well as (2.17) for every composition. The models in the present work with composition similar to that in Iben (1982) do not follow exactly the relation found in that work, which can be caused by differences in the input physics involved in models (opacities, reaction rates, treatment of convection).

The increase of luminosity with decreasing hydrogen mass fraction was also found in analytical studies by Tuchman et al. (1983) and with numerical calculations of steady hydrogen burning on white dwarfs by Tuchman & Truran (1998). Tuchman & Truran (1998) found that, for a fixed metalicity (Z=0.25), the luminosity decreased with the hydrogen mass fraction with a factor similar to ours. They also found that luminosity increased with metalicity (for constant He/H ratio, assumed to be solar, ≈ 0.1) and summarized their dependences in the relation $L(L_\odot) = 5.2 \times 10^4 (M_C/M_\odot - 0.205 - 0.5(X-Z))$. According to the authors, this relation holds also for other metalicities. For the metalicities of our models, Tuchman & Truran (1998) is in agreement with the corresponding factor m_0 in (2.17). More recently, Marigo (2000) used an homology formalism similar to that used above to justify the linear core mass - luminosity relation to study the dependence of the luminosity with the chemical composition through μ , but her studies were concerned with RGB stars (for which she found $L \propto \mu^7$) and AGB stars with M_c between 0.5 and $0.7 M_\odot$ (with $L \propto \mu^3$) .

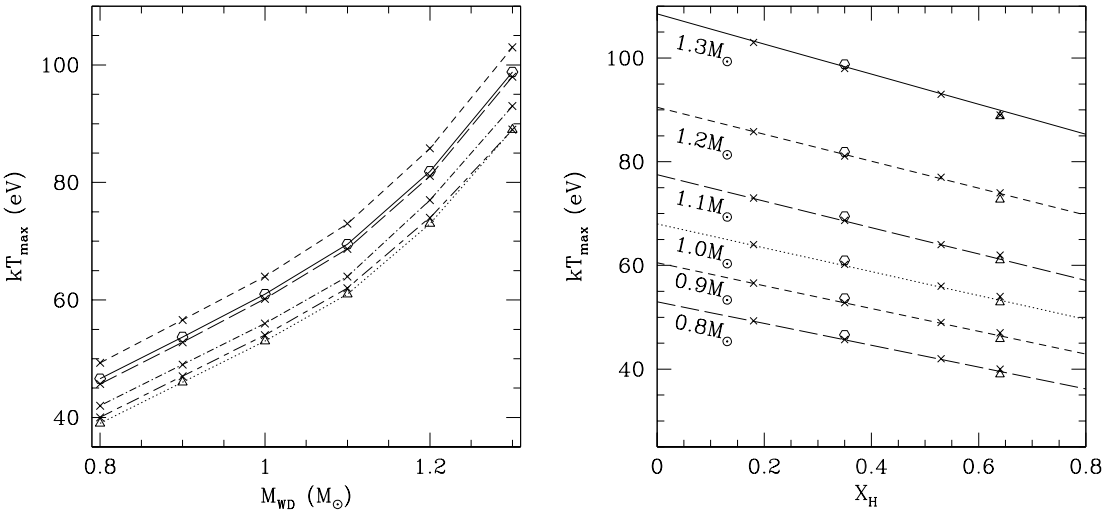

Figure 2.15: Maximum effective temperature as a function of core mass and hydrogen mass fraction.
Left panel: Maximum effective temperature versus core mass for all models: I82 (X=0.64, triangles, with the lowest temperatures), CO50 (X=0.35, circles), ONe75 (X=0.18, with the highest temperatures), ONe50 (X=0.35) , ONe25 (X=0.53) and ONe09 (X=0.64, crosses). Lines joining points are for orientation purposes.
Right panel: Maximum effective temperature versus hydrogen mass fraction for ONe models (crosses), CO50 (circles) and I82 (triangles), for all white dwarfs from $0.8M_\odot$to $1.3M_\odot$. Lines are for orientation purposes.

2.4.2.3 Core mass - maximum effective temperature

Maximum effective temperature also increases with decreasing hydrogen mass fraction and with increasing core mass (see figure 2.15), but in this case, no clear relation has been found. As shown in the figure, maximum effective temperature does not follow any unique linear relation or power law with the core mass. Its behaviour can be only approximated by a power law, with an exponent between 9/10 (for core mass smaller than $1.1M_\odot$) and 5/9 (for most massive white dwarfs). Nevertheless, it behaves linearly with hydrogen mass fraction, decreasing with a slope (between -22 and -28) that steepens for higher core masses.

2.4.2.4 Core mass - envelope mass relation

As in the case of the luminosity, figure 2.8 shows that the envelope mass in the luminosity plateau depends on the core mass and on the hydrogen mass fraction. Iben (1982) found that the relationship between the envelope mass and the white dwarf mass in the luminosity plateau was $log\, M^{Iben82}_{plateau}(M_\odot) \simeq -4.38 - 4.96\left(\frac{M_c}{M_\odot} - 1\right)$. As shown in figure 2.16, results of the present work differ from any similar linear relation of $log\, M_{plateau}$ with the core mass. A general relation between the envelope mass, the core mass and the hydrogen mass fraction can be found for the ONe25, ONe50 and ONe75 envelopes:

$$\log M^{ONe}_{plateau}(M_\odot) \simeq 0.42X_H - \left(\frac{M_c}{M_\odot} - 0.13\right)^3 - 5.26 \qquad (2.20)$$

which is indicated in figure 2.16.

The minimum envelope mass does not have a strong dependence on the hydrogen mass fraction (see figure 2.17). For the ONe25, ONe50 and ONe75 models, it can be represented

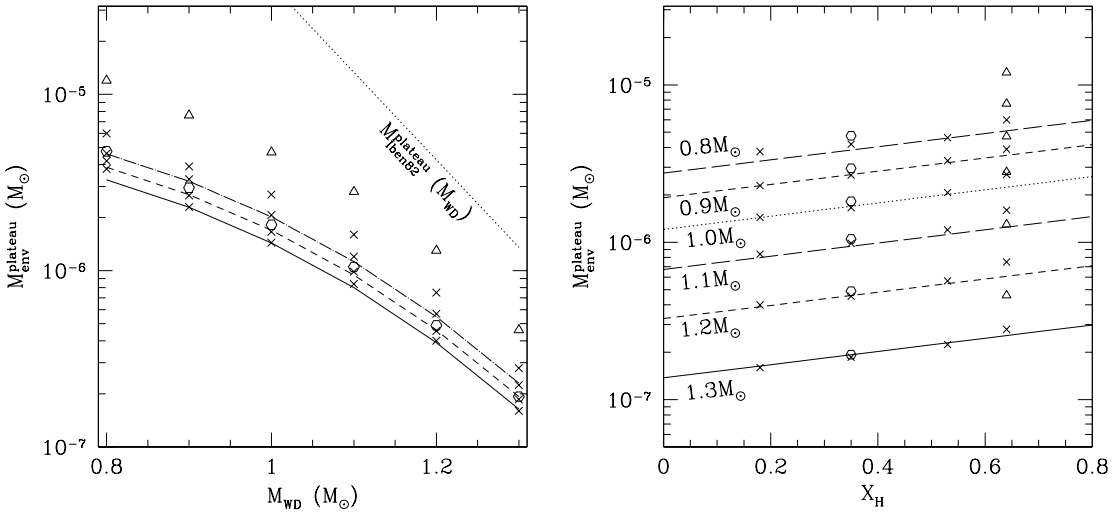

Figure 2.16: Plateau envelope mass as a function of core mass and hydrogen mass fraction.
Left panel: Envelope mass in the plateau versus core mass, for all models: I82 (X=0.64, triangles, with the highest envelope masses), CO50 (X=0.35, circles), ONe75 (X=0.18), ONe50 (X=0.35), ONe25 (X=0.53) and ONe09 (X=0.64, crosses). Envelope mass - total mass relation found by Iben (1982) is shown in dotted line; relation (2.20) is shown in solid line for ONe75, short-dashed for ONe50 and dot-long-dashed for ONe25.
Right panel: Envelope mass in the plateau versus hydrogen fraction. Dots indicate model results, while lines correspond to relation (2.20).

by the relation

$$\log M_{min}^{ONe}(M_\odot) \simeq 0.13 X_H - \left(\frac{M_c}{M_\odot} - 0.13\right)^3 - 5.26 \qquad (2.21)$$

It is worth noticing that I82 models have larger envelope masses than other models (Figures 2.16 and 2.17). Although relations (2.20) and (2.21) apply only to ONe25, ONe50 and ONe75 models, CO50 envelopes follow approximately the same behaviour as ONe50. In the case I82 models, the differences in composition cause the envelope mass for a stable configuration to be larger than 2.20 and 2.21 would indicate. This fact will have important consequences on the typical nuclear timescales, as will be seen later.

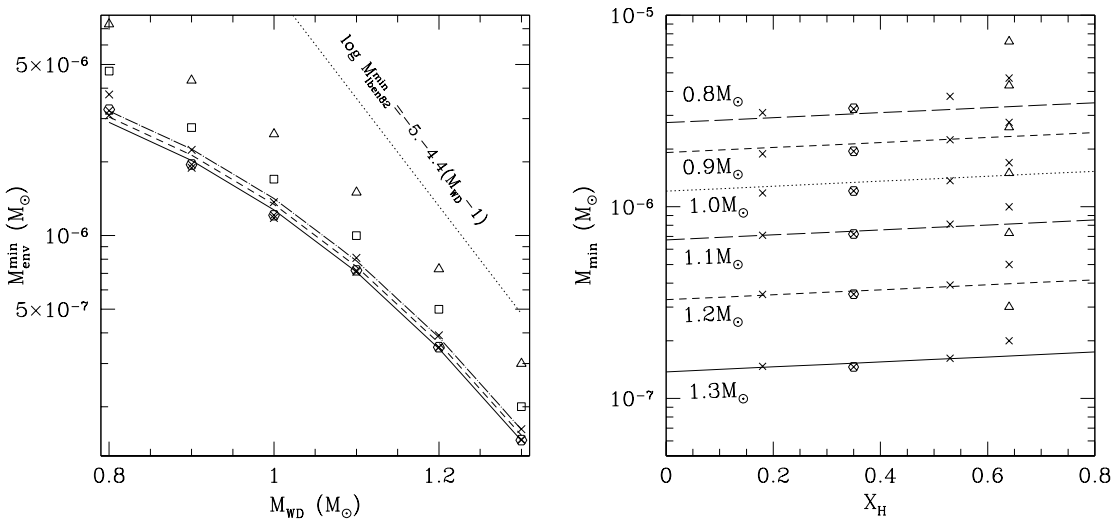

Figure 2.17: Minimum envelope mass as a function of core mass and hydrogen mass fraction.
Left panel: Minimum envelope mass versus total mass, for all models: I82 (X=0.64, triangles, with larger masses), CO50 (X=0.35, dots), ONe75 (X=0.18), ONe50 (X=0.35), ONe25 (X=0.53) and ONe09 (X=0.64, crosses). ONe75, One50 and CO50 have very similar minimum masses. Minimum envelope mass - total mass relation found by Iben (1982) is shown in dotted line; relation (2.21) is shown in solid line for ONe75, short-dashed for ONe50 and dot-long-dashed for ONe25.
Right panel: Minimum envelope mass versus hydrogen fraction. Points indicate model results, while lines correspond to relation (2.21).

2.4.3 Interior structure

Figure 2.18 shows the interior structure of some of the CO50 and ONe50 envelope models of the high luminosity branch, for $1.1M_{\odot}$ white dwarfs. The first general trend that can be observed is the convergence of all models to similar conditions at the innermost layers, as found with the analytical approximation (appendix A). The temperature and luminosity profiles show that only the deepest layers have temperatures high enough to contribute to the energy production. Luminosity stays constant in most of the envelope. Highest temperatures at the base are needed for the most luminous envelopes, and in a similar way, most massive envelopes produce higher pressures at the bottom. Surprisingly enough, base density decreases for increasing envelope masses. This is a consequence of the higher base temperatures in the most massive envelopes. Density profiles are steeper for smaller envelopes, causing the mass to increase slowly in massive envelopes, which can explain that the total envelope mass is larger in spite of having a smaller density at the base. The effect of the different metal abundances is evident for temperatures lower than some $10^7 K$ and will be discussed later; for hotter layers, opacity is dominated by scattering (see appendix B), which only depends on the hydrogen fraction, X=0.35 both for One50 and CO50 models. As mentioned above, envelopes on the high luminosity branch have a convective region (indicated with solid line in figure 2.18) just below the photosphere, where opacity reaches its highest values. As convection transports energy outwards more efficiently than radiation, temperature gradient is flatter in the convective regions, as well as pressure and density gradients, contributing to a larger photospheric radius and luminosity.

Convective layers in stellar envelopes are most commonly related to partial ionization regions, where mainly hydrogen or helium recombinations cause the opacity to increase and rend the radiative energy transportation inefficient. At the conditions of the present models, hydrogen and helium are fully ionized. Only at the photospheric temperatures

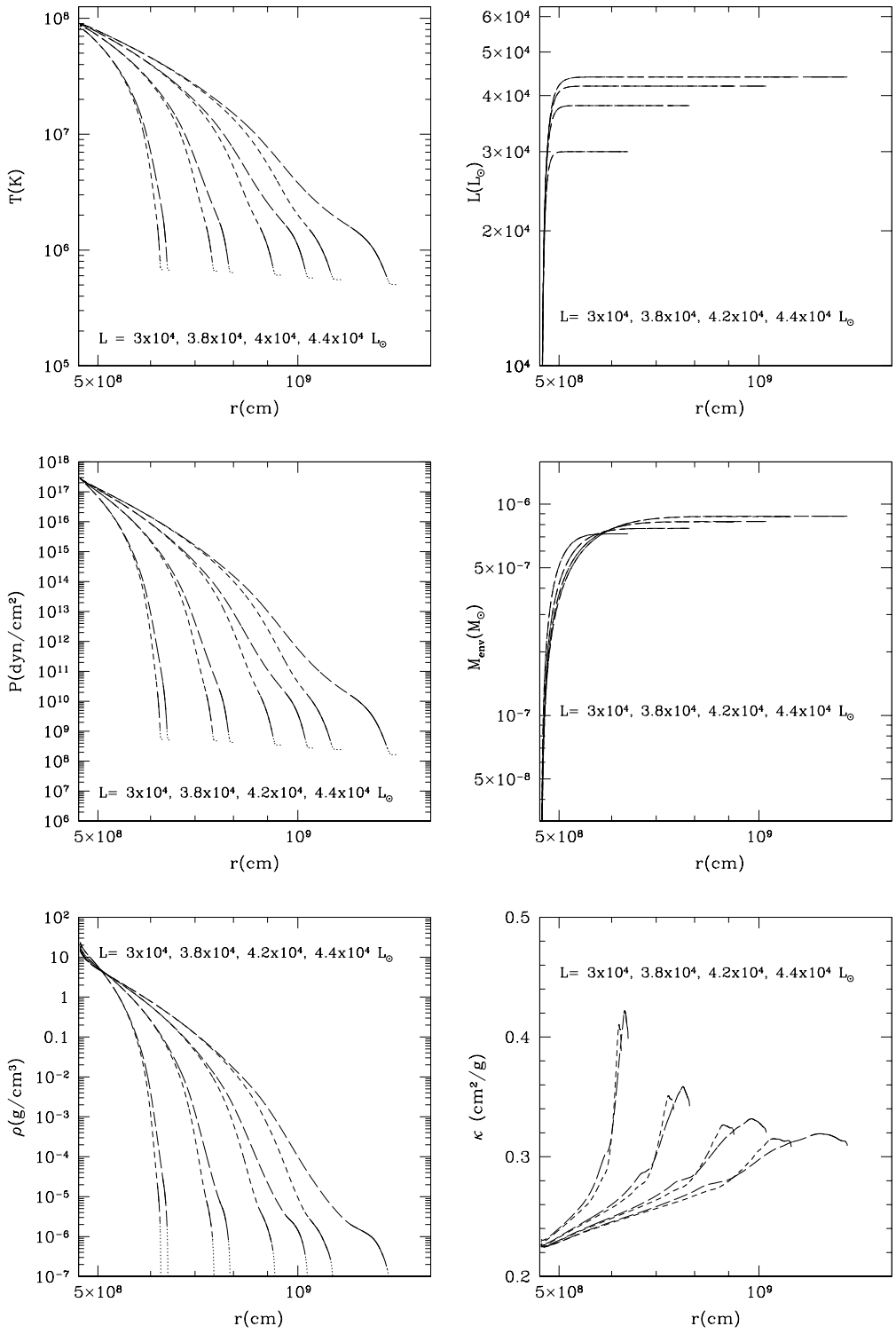

Figure 2.18: Interior structure of some envelopes with different total luminosities. All models belong to the high luminosity branch. CO50 models are plotted with short-dashed line and ONe50 models with long-dashed line. White dwarfs masses are $1.1M_{\odot}$ and the mixing degree with accreted solar matter is 50%. Solid lines indicate convective zones, and the atmospheres are plotted with dotted lines.

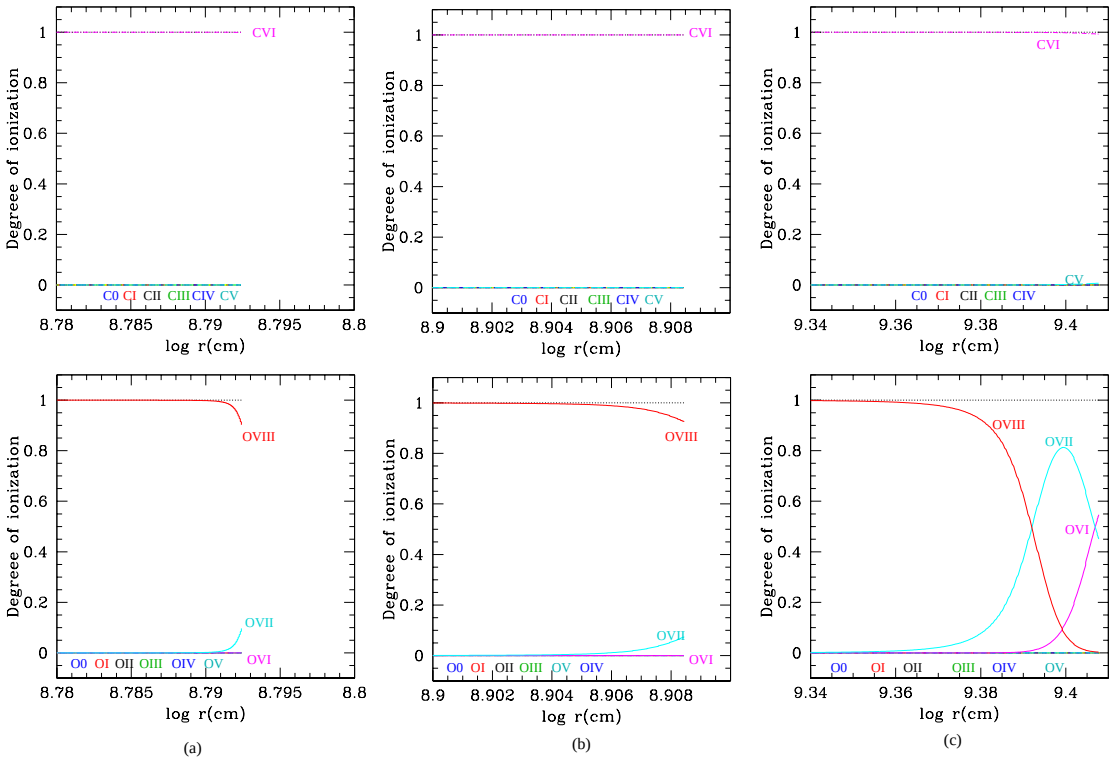

Figure 2.19: C and O ionization fractions for the gas conditions of three sample CO50 white dwarf envelope models. Models have $M_c = 1.1 M_\odot$ and luminosities $L = 3.0 \times 10^4 L_\odot$ (a), $L = 4.0 \times 10^4 L_\odot$ (b) and $L = 4.7 \times 10^4 L_\odot$ (c). Gas composition is $X_C = 0.5$ and $X_O = 0.5$.

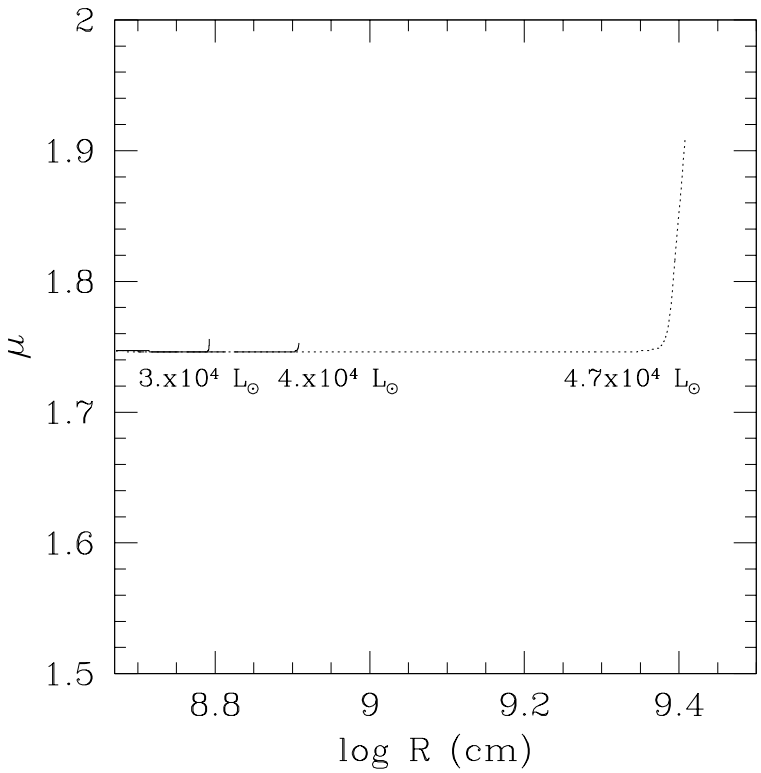

Figure 2.20: Change of molecular weight due to recombinations of C and O for gas conditions in CO50 white dwarf envelope models. Gas composition is $X_C = 0.5$ and $X_O = 0.5$.

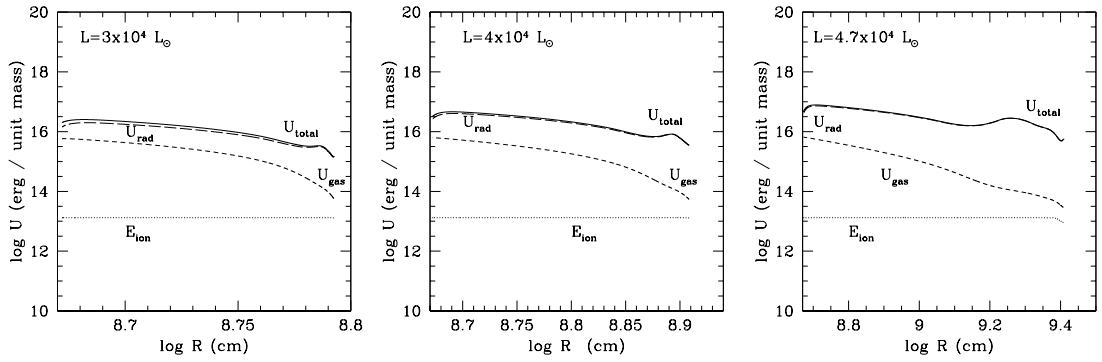

Figure 2.21: Contribution to total internal energy, U_{total}, due to recombinations of C and O, E_{ion}, for gas conditions in CO50 white dwarf envelope models. Energy contribution from gas, U_{gas}, and radiation, U_{rad}, are also shown. Gas composition is $X_C = 0.5$ and $X_O = 0.5$.

could carbon and oxygen be partially ionized and have effects on the equation of state of the gas. Ionization fractions of C and O in a gas with $X_C = 0.5$ and $X_O = 0.5$ have been computed for the gas conditions obtained in three sample CO50 $1.1M_\odot$ white dwarf envelope models, with luminosities of $3 \times 10^4 L_\odot$, $4 \times 10^4 L_\odot$ and $4.7 \times 10^4 L_\odot$ (see Appendix B for details on the ionization calculation). As shown in figure 2.19, C and O are completely ionized in most of the envelope layers. Only some recombinations appear in the external layers of the highest luminosity model. The contribution of these recombinations to the internal energy in the three envelope models is shown in figure 2.20, and the change of the mean molecular weight in figure 2.21. The contribution to internal energy, as seen in these figures, is negligible compared to radiation and gas contribution. Only the mean molecular weight reflects the presence of partial ionization in the most external layers. But taking into account that the envelope mass and luminosity are almost constant in these layers, it is not expected that carbon and oxygen partial ionization effects can have any significant contribution to the global structure and properties of the envelopes, and thus are not taken into account in this work.

ONe50 and CO50 models with the same effective temperature ($kT_{eff} = 40eV$) but different core masses are shown in figure 2.22. The convective region is more extended for increasing white dwarf masses. As a consequence, temperature, pressure and density gradients in the inner radiative layers are steeper for massive white dwarfs, causing the energy production layer to be thinner in these cases, which is clearly visible in the luminosity profiles. In a similar way, the envelope mass increases only in the deepest layers in massive white dwarfs, since most of the envelope has small density values.

It can be observed that for the highest luminosity models and most massive white dwarfs, the density gradient in the convection region is close to zero. As found by Latour (1970), the density gradient steepens for higher effective temperatures (corresponding to lower luminosities in figures 2.18) or for decreasing gravities, being very flat for the most massive and luminous white dwarfs. For high luminosities and gravities, inversions of the density gradient are frequently found in convective layers when using the mixing length theory (Fontaine & Van Horn (1976), Henyey et al.(1965), Latour (1970), Mihalas (1965)). However, although the density gradient is very flat in some of the present models, such inversions do never appear.

The effects of the chemical composition in the interior structure are shown in figure 2.23, where profiles for five models with different abundances but the same core mass and total luminosity are plotted. The strongest difference in behaviour corresponds to the hydrogen poorest model, ONe75. In this case, the larger metalicity cause the opacities to be larger than in hydrogen richer envelopes, causing the convective region to be much more extended. As a consequence, profiles in the radiative regions are steeper, specially in the deepest layers.

Different chemical compositions and white dwarf masses combinations give envelopes with the same observable properties (luminosity and effective temperature), as can be seen in figure 2.6. Figure 2.24 plots the interior structure of three ONe envelopes with the same effective temperature and luminosity ($kT_{eff} = 45eV$, $L = 5.2 \times 10^4 L_\odot$), and thus the same photospheric radius ($R_{fotos} \simeq 2 \times 10^9 cm$), but different masses and compositions (ONe25 with $1.3M_\odot$, ONe50 with $1.2M_\odot$ and ONe75 with $1.1M_\odot$). In spite of the differences in abundances, the profiles are very similar, resulting in equal photospheric properties. The convection region is more extended for the hydrogen richest model, ONe25, which is in general cooler (except for the innermost layers). It has also the smallest densities, and thus the smallest envelope mass. An ONe50 model of the unstable, low luminosity branch and with the same effective temperature is also plotted. Its temperature, pressure and

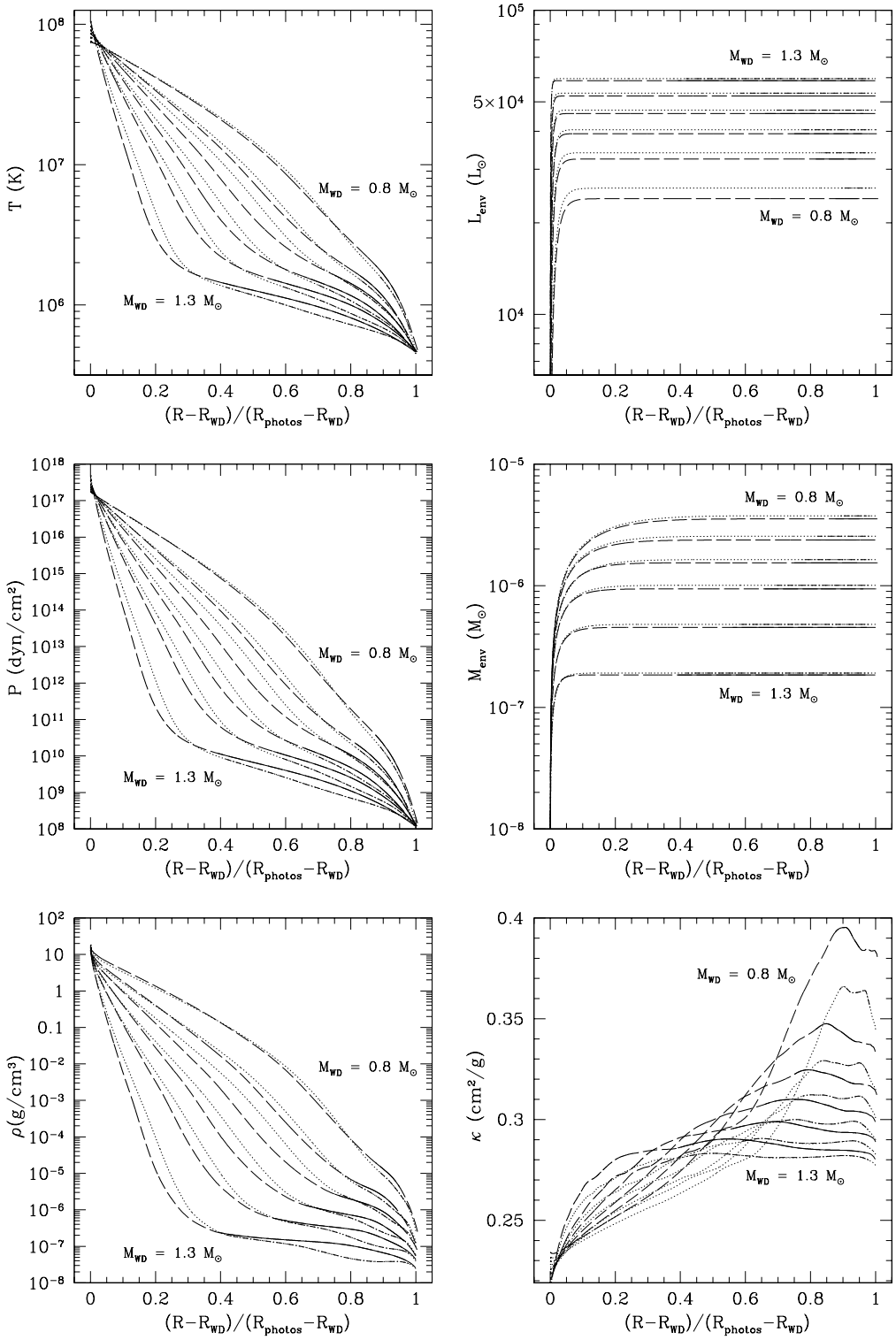

Figure 2.22: Interior structure of ONe50 (dashed line) and CO50 (dotted line) envelopes with core masses of 0.8, 0.9, 1.0, 1.1, 1.2 and 1.3 $M_\odot$, all of them with a similar effective temperature, $kT_{eff} \simeq 40eV$. Photospheric radii are, for ONe50 models, between $1.6 \times 10^9 cm$ for 0.8 $M_\odot$ and $2.6 \times 10^9 cm$ for 1.3 $M_\odot$; and for CO50 models, between $1.7 \times 10^9 cm$ for 0.8 $M_\odot$ and $2.5 \times 10^9 cm$ 1.3 $M_\odot$. Solid (ONe50) and dash-dotted (CO50) lines indicate convective zones.

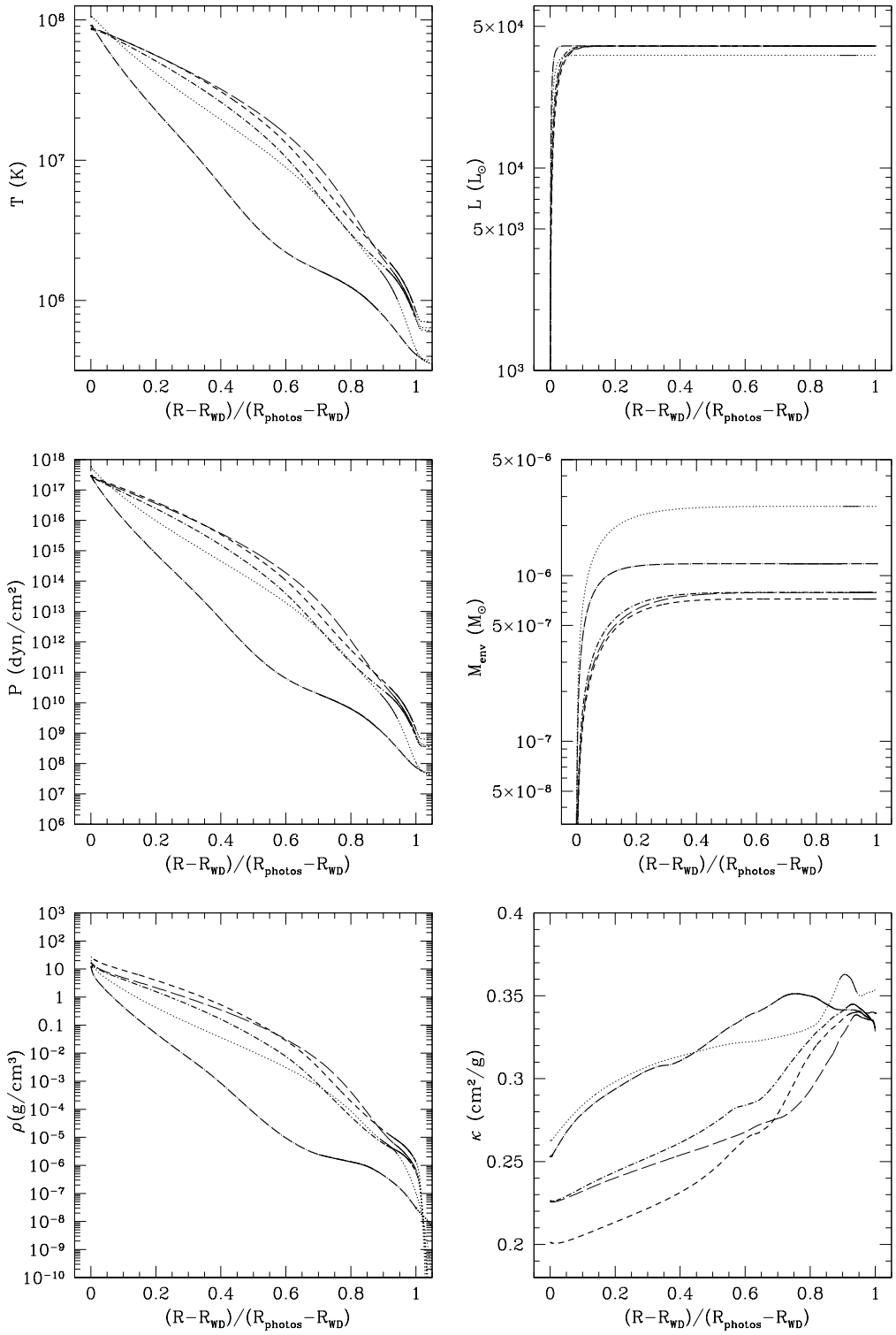

Figure 2.23: Interior structure of five envelope models with the same core mass ($M_c = 1.1M_\odot$) and similar luminosity ($L = 4 \times 10^4 L_\odot$for CO and ONe models, and $3.6 \times 10^4 L_\odot$ for I82), but with different compositions. CO50, with $R_{fotos} = 8.1 \times 10^8 cm$ (thin, long-dashed line), ONe25, with $R_{fotos} = 2.7 \times 10^9 cm$ (thick, long dash-dotted line), ONe50, with $R_{fotos} = 8.7 \times 10^8 cm$ (thick, short dash-dotted line), ONe75 , with $R_{fotos} = 6.6 \times 10^8 cm$ (thick, short-dash dotted line) and I82, with $R_{fotos} = 2.2 \times 10^9 cm$ (thin, dotted line). Solid line indicates convection regions, and the atmosphere is plotted with dotted line for all cases.

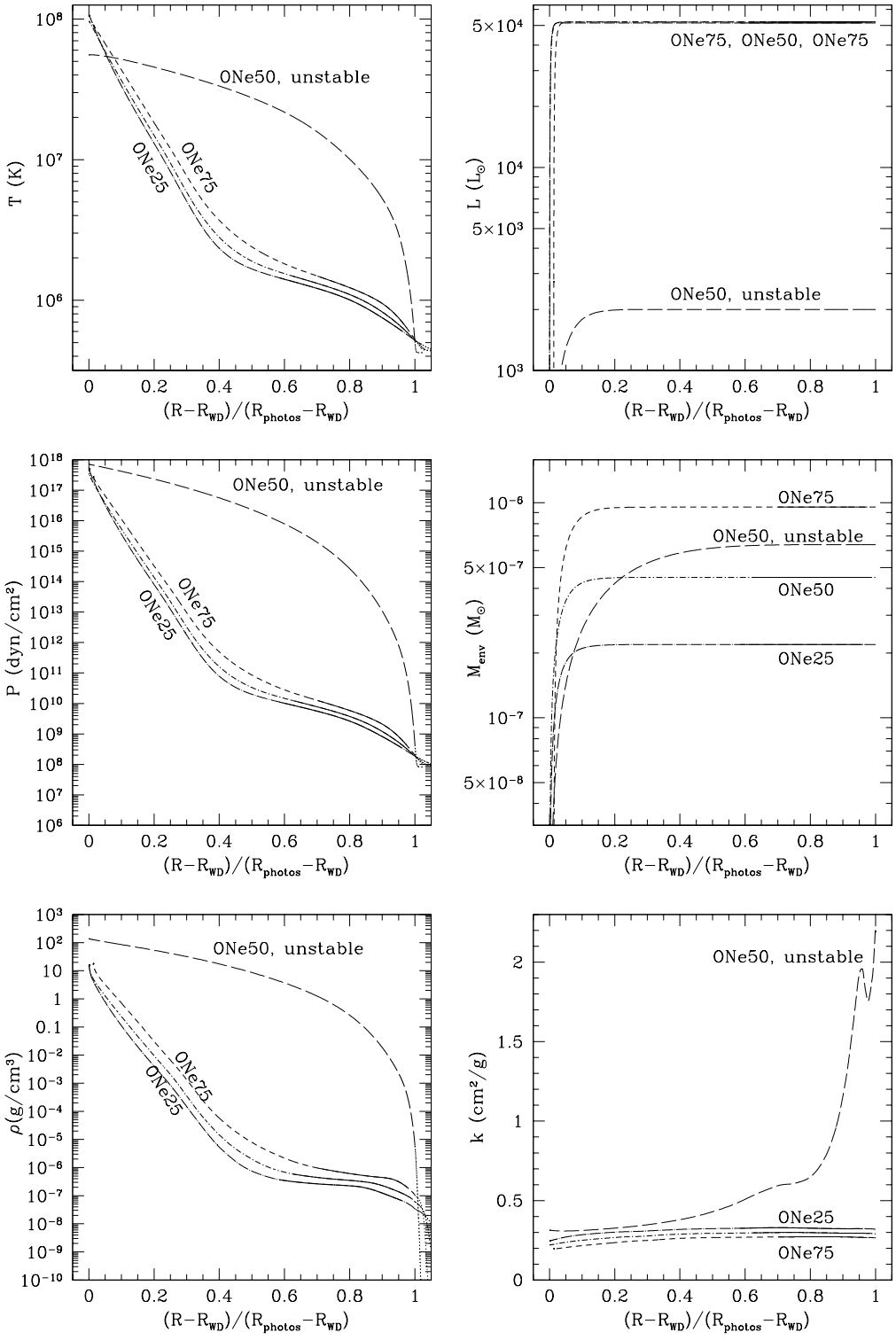

Figure 2.24: Interior structure of some ONe white dwarf envelope models with different white dwarf masses and composition, with the same luminosity, $\sim 5.2 \times 10^4 L_\odot$, and effective temperature, $kT_{eff} \simeq 45eV$. Three models belong to the high luminosity branch, all three with the same total luminosity: ONe25 with $M_c = 1.3M_\odot$ (long dash-dotted line), ONe50 with $M_c = 1.2M_\odot$ (short dash-dotted line) and ONe75 with $M_c = 1.1M_\odot$ (short dashed line). All of them have $R_{fotos} = 2 \times 10^9 cm$. A fourth model from the low luminosity branch but with the same effective temperature is also plotted (ONe50 with $M_c = 1.2M_\odot$, $L = 2 \times 10^3 L_\odot$ and $R_{fotos} = 4 \times 10^8 cm$, long-dashed line). Solid lines indicate convective zones, and atmospheres are plotted with dotted lines.

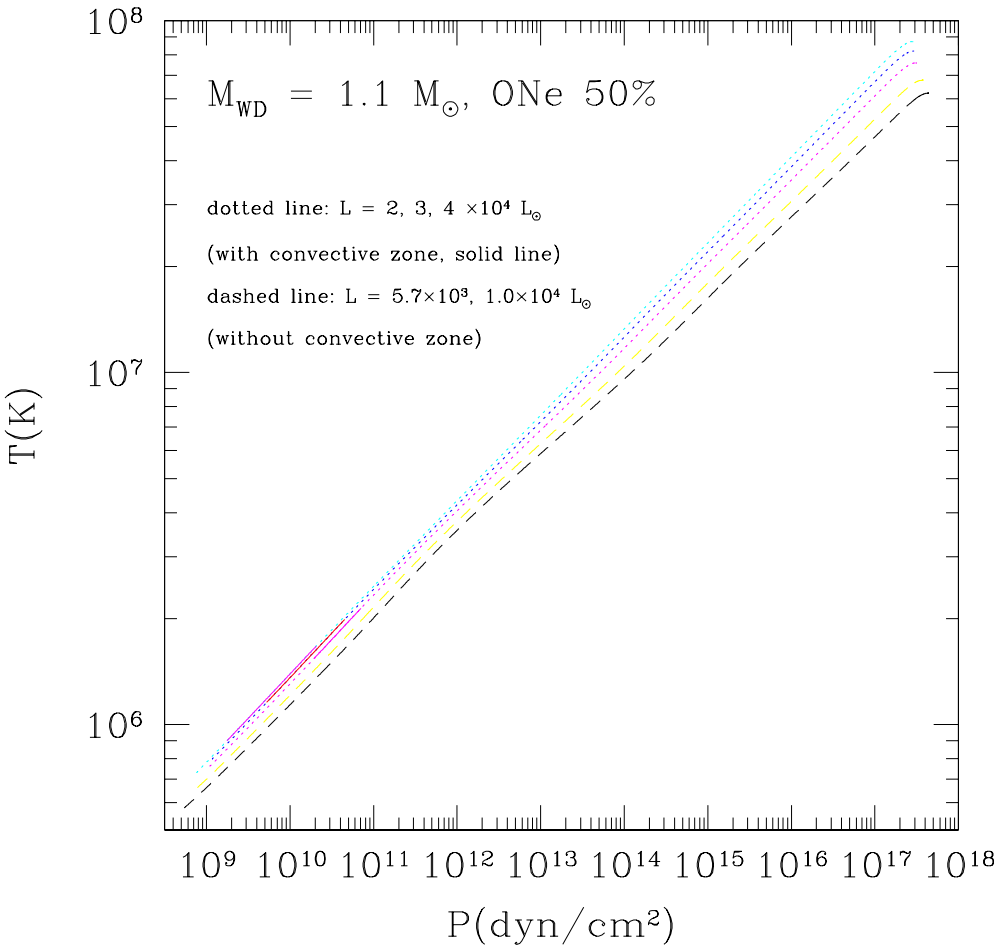

Figure 2.25: $logP - logT$ diagram for ONe50 envelopes with $M_{WD} = 1.1 M_\odot$.

density profiles are completely different from the models of the high luminosity branch. It has no convection region, although opacities below the photosphere are much larger than in convective models. As the temperature gradient in these outer regions is much steeper in this case, radiative transport is efficient enough to transfer all the energy despite the large opacities. This steep temperature gradient in the outer regions is compensated by a flat profile in most part of the envelope. Temperature at the base is much lower than in convective envelopes, generating a smaller total luminosity, but energy generation is more extended thorough the envelope, since there is a larger fraction of the total envelope mass at high temperatures. In a similar way, the density profile is also flat at most part of the envelope, causing the mass to increase slowly with radius.

In appendix A it is shown that in case of constant mass and luminosity, the envelope model has an analytical solution, which in the case of zero outer boundary conditions, establishes a power law relation between temperature and pressure. The behaviour of our envelope models can now be compared to the analytical solution, plotting temperature versus pressure in figure 2.25. The envelope models calculated with the full set of equations and photospheric boundary conditions do not deviate strongly from the analytical approximation with zero outer boundary conditions, even when convection appears. Since the outer boundary conditions are much smaller pressures and temperatures than inner

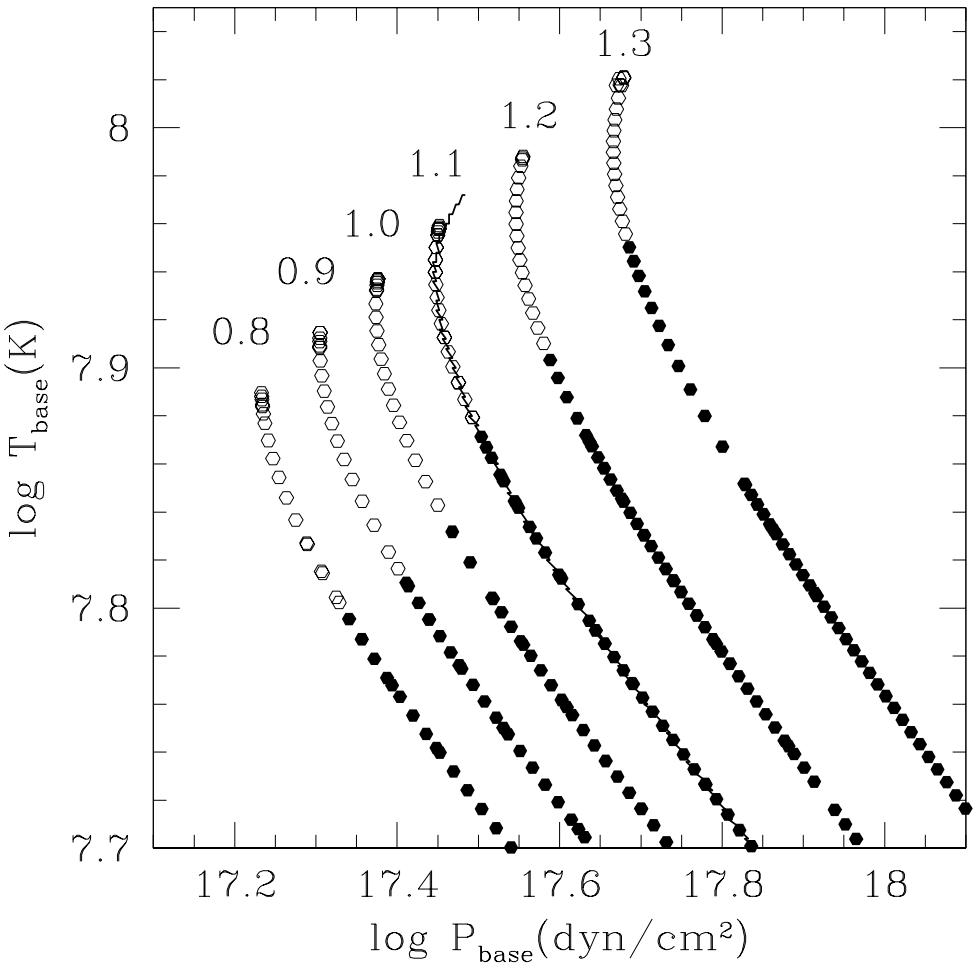

Figure 2.26: Pressure and temperature at the base of the CO50 white dwarf envelope models. White dwarf mass is indicated for each series of models. Empty circles indicate convective envelopes, full circles correspond to radiative envelopes, and the solid line under the $1.1M_{\odot}$ series is the borderline between convective and radiative structures from figure 2.2.

values, the solution does not differ largely from the zero outer boundary conditions one. But the numerical integration of the full set of equations with improved input physics (opacities, treatment of convection...) allows us to obtain more accurate details of the envelopes, specially for the photospheric properties and the envelope masses.

It is interesting to situate the present models in the $P_b - T_b$ plane studied in section 2.3 for a CO50 $1.1M_{\odot}$ white dwarf. Figure 2.26 shows the pressure and temperature values at the base of the numerical CO50 white dwarf envelope models. The borderline between convective and radiative envelopes found in section 2.3 is also shown for comparison. The CO50 $1.1M_{\odot}$ white dwarf envelope models with photospheric boundary conditions lay just along the radiative-convective borderline in the plane $P_b - T_b$.

2.4.3.1 ONe50 versus CO50 models. I82 versus ONe09

In section 2.4.2 it has been seen that there are small differences in the general properties of the CO50 and the ONe50 envelope models, despite having the same hydrogen mass fraction. From figures 2.6, 2.7 and 2.8 it is clear that, for the same effective temperature, the CO50

models have slightly higher luminosities (as a consequence of a larger photospheric radius) and larger envelope masses. Equivalently, for the same luminosity, CO50 envelope models have higher effective temperatures and smaller photospheric radii. This is evident in figure 2.18, where profiles for pairs of CO50 and ONe50 models with the same luminosity are plotted, and in figure 2.22, where CO50 and ONe50 models are plotted for several masses, all of them with the same effective temperature. As can be seen in figure 2.22, for the same effective temperature, distributions of temperature, pressure and density (in fraction of total envelope radius) are steeper for ONe50 models. This is directly related to larger opacities for ONe50 that for CO50 compositions in the temperature range of the radiative region of the envelopes, with $T > 10^6 K$ (see opacity profiles in figure 2.22 and appendix B, figure B.6), that cause the temperature distribution 2.3 to change more rapidly with radius. Since temperature decreases more rapidly in the inner regions of ONe50 models than for CO50, the energy production layer is thinner and the total luminosity of the envelope is smaller. Analogously, the density profile in the inner regions is also steeper for ONe50 models, causing the envelope mass to increase only in a region thinner than in CO50 models and the total envelope mass to be smaller.

To check that the differences between CO50 and ONe50 models are due to the differences in the opacities, some envelope models have been reintegrated with opacities artificially altered by a certain factor. We have found that, as in the case of the CO50-ONe50 comparison, envelopes with higher opacities have smaller luminosities and envelope masses. A global increase (decrease) of the opacity in the envelope by a 10% causes a decrease (increase) in the envelope mass of 4% and a decrease (increase) in the luminosity of 10%.

Differences in the opacities are probably one of the causes of the differences in the envelope masses found between our I82 models and the results obtained by Iben (1982). In our I82 models with $M_c = 1.1 M_\odot$, the minimum envelope mass (mass at the critical point between stable and unstable solutions) is $1.5 \times 10^{-6} M_\odot$, while Iben (1982), with the same chemical composition, obtained $\sim 3.6 \times 10^{-6} M_\odot$, which is a factor 2.4 larger. For the range of temperatures in the radiative regions of the envelopes ($T > 10^6 K$), opacities used by Iben (1982) can be up to a factor 10 smaller than OPAL opacities for the same composition, as can be seen in figure B.6 in appendix B. In view of the exercise mentioned above and the CO50-ONe50 comparison, it is possible that these large differences in the opacities can explain the differences in the envelope masses. In addition to the opacities, there are other differences in the input physics that could be the cause of the larger envelope mass. In section 2.5 it is shown that uncertainties in the energy generation rate only affect the luminosity by a maximum of a 7%, but can alter the envelope mass by a factor ~ 1.7. It is therefore possible that differences in opacities and in the energy generation rates between our I82 models and Iben (1982) can explain the differences in envelope masses.

Differences in the energy generation rate also affect the comparison between ONe09 and I82 models, where the difference in chemical composition does not only affect the opacities. While in the ONe50 and CO50 models the total metal fraction was similar, the ONe09 models have a total metal fraction a factor $\sim$10 larger than the I82. This causes differences, not only in the opacities, but also in the energy generation rate, which is directly proportional to Z in the approximation taken in this work. As a result, for the same effective temperature, I82 have slightly smaller luminosities (due to a smaller energy generation rate), but larger envelope masses than the equivalent ONe09 model. With a less efficient energy generation, temperature and pressure at the base of the envelope need to be higher to provide a similar luminosity, and the total envelope mass needs to be larger for the envelopes with stationary hydrogen burning to be in equilibrium.

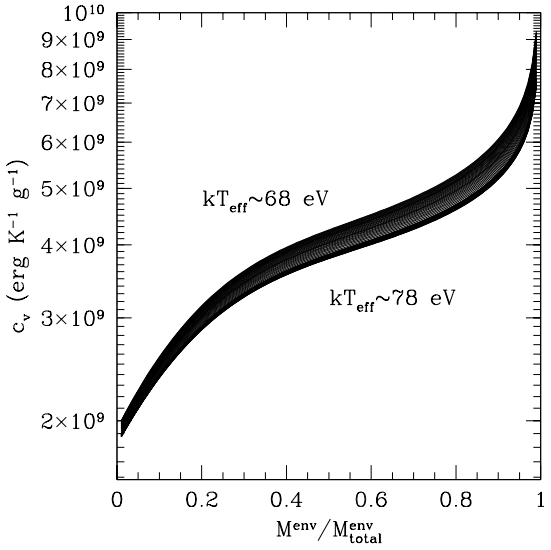

Figure 2.27: Specific heat per unit mass, c_v, for some ONe50 1.3 $M_\odot$ models.

2.5 Estimation of uncertainties

2.5.1 Accuracy of the stationary approximation

At this point, it is necessary to check the accuracy of the stationary approximation, that is, whether the $T\frac{ds}{dt}$ term in equation 2.3 can indeed be neglected. First of all, let us consider the timescales dominating the evolution of the envelope. Expression (2.26) indicates that the nuclear timescale is of the order of years, that is , $\tau_{nuc} \approx 10^7 s$. For the stationary approximation to be accurate, it is necessary that any thermal deviation out of equilibrium is balanced in a timescale shorter than τ_{nuc}. The *thermal adjustment time* can be evaluated as the time needed for the envelope to release its thermal energy,

$$\tau_{adj} = \frac{\overline{c_v}\,\overline{T} M_{env}}{L} \tag{2.22}$$

where $\overline{T}$ and $\overline{c_v}$ are average values in the envelope, and c_v is the specific heat at constant volume per unit mass (B.1.12). As seen in section 2.4.3, temperature in the inner envelope (where most of the mass is found, and thus most of the thermal energy is stored) is around $10^7 - 10^8 K$. Since radiation pressure contributes substantially to the equation of state, c_v has large values in the present envelopes, of the order $10^9 erg\, K^{-1}\, g^{-1}$, as can be seen in figure 2.27, where c_v is plotted for some ONe50 1.3 $M_\odot$ models. With this and the typical values for the envelope mass ($\sim 10^{-6} M_\odot$) and luminosity ($\sim 10^{38} erg\, s^{-1}$) of the envelope models, the thermal timescale is $\tau_{adj} \approx 10^5 - 10^6 s$. Although this indicates that in general τ_{adj} will be smaller than τ_{nuc}, the difference is not large enough to be sure that the time dependent terms in (2.3) can be safely neglected.

To test in more detail the accuracy of the stationary approximation, the $T\frac{ds}{dt}$ term has been estimated from the solutions to the stationary problem. This term can be expressed as

$$T\frac{ds}{dt} = c_p \frac{dT}{dt} + \frac{\delta}{\rho}\frac{d\rho}{dt} \tag{2.23}$$

where $c_P = \left(\frac{dq}{dT}\right)_P = \left(\frac{du}{dT}\right)_P + P\left(\frac{dv}{dT}\right)_P$ and $\delta = \left(\frac{\partial \ln \rho}{\partial \ln T}\right)_P$. (2.23) can be evaluated from

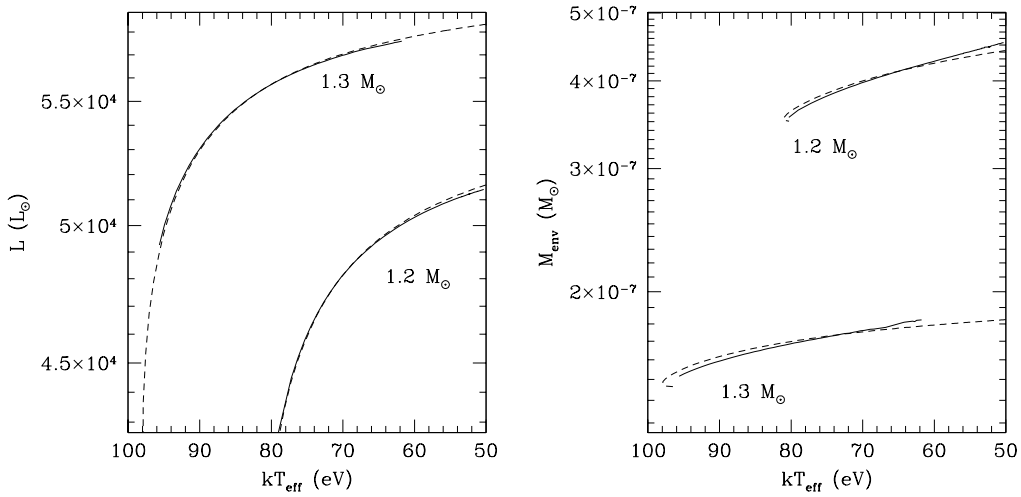

Figure 2.28: Luminosity and envelope mass versus effective temperature for ONe50 1.2 and 1.3 $M_\odot$ models with the $T\frac{dS}{dt}$ term included (solid lines). Purely stationary models are shown in dashed line for comparison.

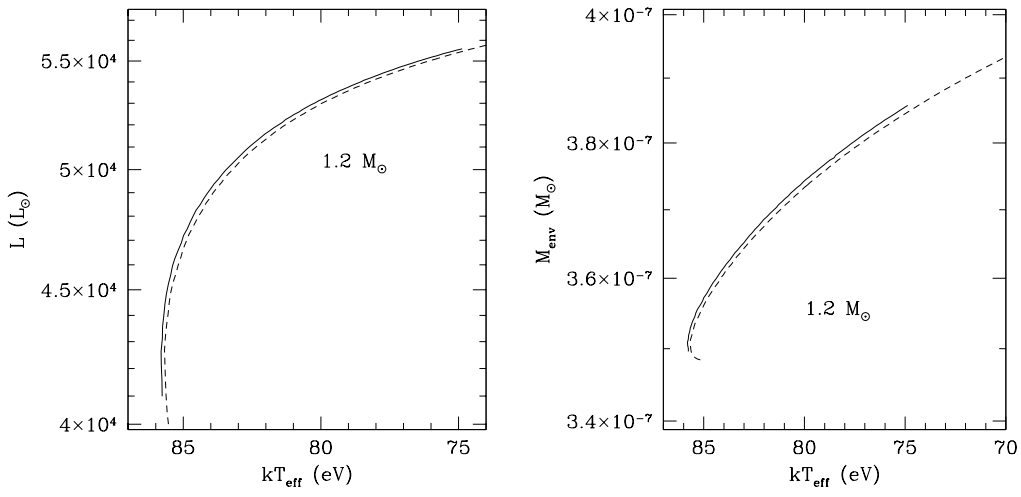

Figure 2.29: Luminosity and envelope mass versus effective temperature for ONe75 1.2 $M_\odot$ models with the $T\frac{dS}{dt}$ term included (solid lines). Purely stationary models are shown in dashed line for comparison.

the differences of T and ρ between successive stationary solutions. Since the envelope mass is changing for each stationary solution, it is necessary to assume where this change of mass is occurring to evaluate the differences of temperature and density at equivalent layers. If successive stationary solutions are considered and there is no external mass loss, the layers included in the hydrogen burning zone in one solution are assimilated to the core in the next solution and do not take part in the envelope integration anymore. This change of mass will occur at the base of the envelope and it has been assumed to be so for this estimation. The time elapsed between two successive models is assumed to be (2.24), the time necessary for the burning layer to consume the difference of envelope masses between the two solutions.

This exercise has been performed with the ONe50 and ONe75 models. Once the $T_r \frac{\partial s_r}{\partial t}$ term has been calculated for each layer, it has been integrated for the whole envelope and its total contribution to the luminosity has been evaluated. The change in the luminosity has been found to be smaller than 2% (for ONe50) and 5% (for ONe75) in most of the cases. For a given white dwarf mass and composition, only the envelopes with the highest effective temperatures (the last 2-3 eV before the maximum) have a larger thermal contribution to the luminosity, which never reaches the 10% in the ONe50 models and can be as much as 14% in the ONe75 envelopes. For this last composition, the $1.3 M_{\odot}$ models are the most affected by the thermal contribution, which is in all the computed cases larger than 5%, while the 1.1 and $1.2 M_{\odot}$ envelopes have changes larger than 2% in most cases.

Since the evaluation of this thermal contribution has been performed from the stationary problem results, it must be taken with care. The change introduced by the time-dependent term in (2.3) will not only change the luminosity, but it will also affect the whole structure of the envelope, changing its global properties. The global effect has been calculated for some of the most critical cases, that is, for the ONe50 1.2 and 1.3 $M_{\odot}$ envelopes, and for the ONe75 1.2 $M_{\odot}$ case. The values for the $T \frac{ds}{dt}$ evaluated from the stationary solutions have been introduced in the integration of the envelopes, to estimate the global change in its properties. The results are shown in figures 2.28 and 2.29, where the resulting luminosity and envelope mass are plotted versus the effective temperature, together with the purely stationary solution. The changes are never larger than previously mentioned. In addition, as shown in appendix B, it must be taken into account that the uncertainties in the energy generation rates translate into an uncertainty in the determination of the envelope mass larger than the error introduced by the stationary approximation.

This study indicates that the stationary approximation is accurate enough for most of the results of this chapter, and only some extreme cases must be taken with care: the highest effective temperature end of each series and the most massive models of the ONe75 composition.

2.5.2 Uncertainty introduced by the analytical approximations for the energy generation rates

For simplicity of the numerical calculation, the energy generation rate is calculated using an analytical approximation, instead of computing the whole nuclear network. Several analytical approximations can be found in the literature for the CNO cycle energy generation rate. As commented in appendix B, the various approximations differ in the numerical factors and in the evaluation of the X_{CNO} mass fraction, which in some cases includes oxygen (Kippenhahn & Weigert (1990), Allen (1973)) and in some other does not (Reeves (1965), Clayton (1968), Cox & Giuli (1968), Paczyński (1983)). Since C, N and O are elements strongly enhanced in our envelopes, the X_{CNO} can vary in a factor $\sim$10 for the same composition, depending on the inclusion of oxygen or not. To avoid strong differences due

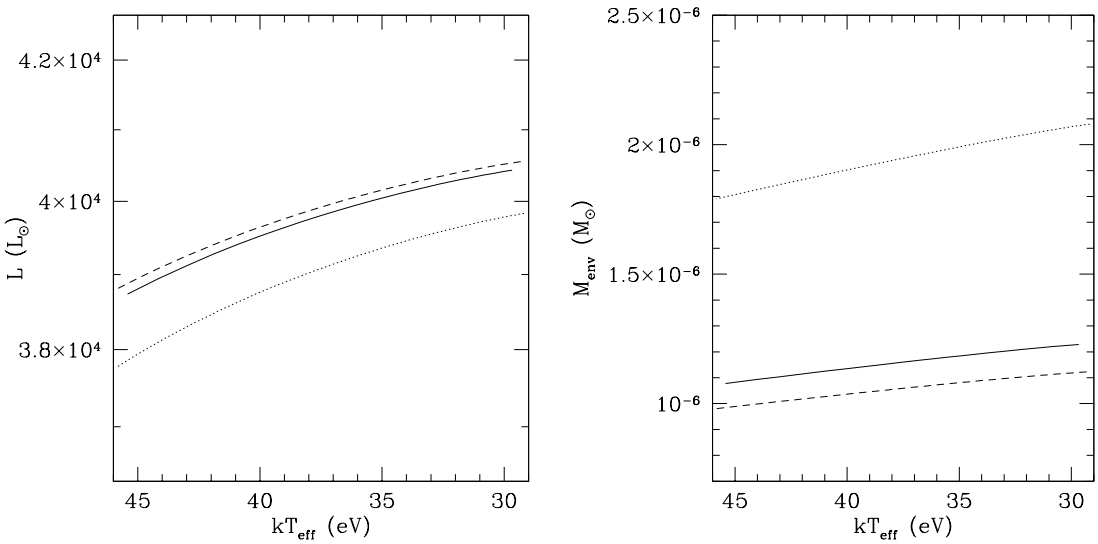

Figure 2.30: Luminosity and envelope mass versus effective temperature for some ONe25 $1.1M_{\odot}$ white dwarf envelopes, with $X_{CNO} = 0.13$ (dotted line), with $X_{CN} = 0.01$ (dotted line) and with $Z/3$ (as all models in 2.4, solid line).

to the inclusion or not of oxygen and for simplicity, the approximation used in Paczyński (1983), $X_{CNO} = \frac{Z}{3}$ has been adopted as a unified criterium. The uncertainty introduced by this approximation has been evaluated for some ONe25 envelopes with $M_c = 1.1M_{\odot}$, which have been reintegrated with $X_{CNO} = 0.01$ and with $X_{CN} = 0.13$ (values corresponding to the detailed composition resulting from the 25% mixing of the solar accreted material with the ONe core). The results obtained are shown in figure 2.30, compared to the results from section 2.4. The change in the luminosity is smaller than 2% in all tested cases, but the change in the energy generation rate causes the envelope mass to be ~8% smaller with $X_{CNO} = 0.13$ and a factor ~ 1.7 larger if only C and N are considered, with $X_{CN} = 0.01$. Since the uncertainty introduced by the evaluation of X_{CNO} or X_{CN} is similar for all ONe models (see table B.1 in appendix B), the error in the luminosity and envelope mass caused by the approximation for this factor is also expected to be similar.

2.6 Quasi-static evolution

An estimation of the evolution of a steady hydrogen burning white dwarf envelope in the plateau of quasi-constant luminosity can be approximated by a series of stationary envelope models with decreasing envelope masses. The layers of the envelopes whose hydrogen has been processed are assimilated to the core and do not take part in the integration of the next envelope model (the increment in the core mass is negligible). In this way, as hydrogen is consumed, the envelope is losing mass. The time Δt needed for the envelope to change its mass ΔM_{env} only due to hydrogen burning can be estimated as

$$\Delta t = \epsilon \frac{\Delta M_{env} X_H}{L} \tag{2.24}$$

where X_H is the hydrogen mass fraction, L is the mean luminosity in this period (which varies little in the constant bolometric luminosity phase) and ϵ is the energy released per gram of hydrogen processed ($\epsilon = 5.98 \times 10^{18} erg\, g^{-1}$). In figures 2.31-2.35, time intervals needed for the envelope to evolve between two adjacent marked points are indicated in days

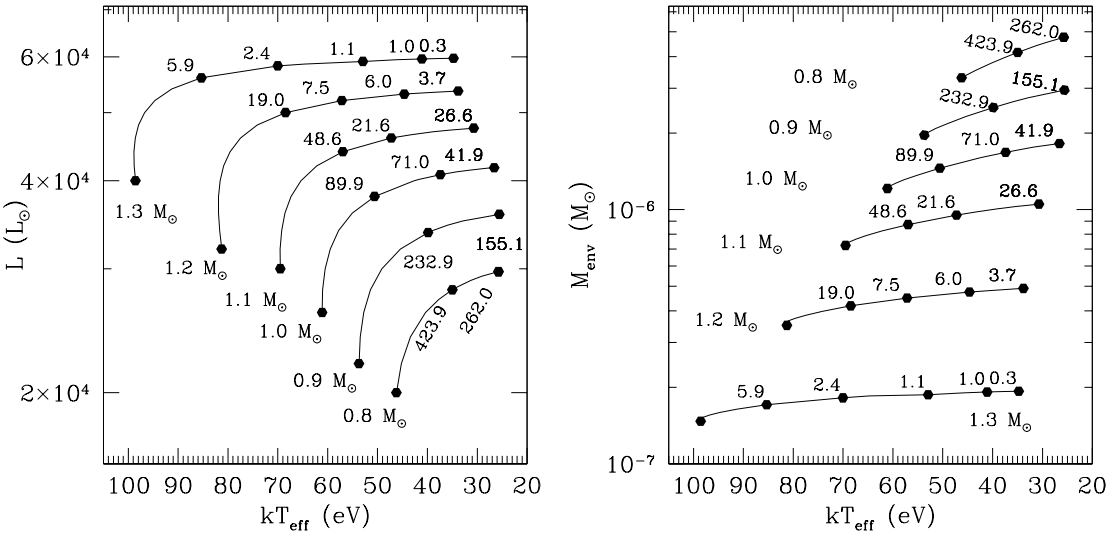

Figure 2.31: Luminosity and envelope mass versus effective temperature for the high luminosity branch of CO50 envelopes. Time in days needed for the envelope to evolve from one tick to another is indicated.

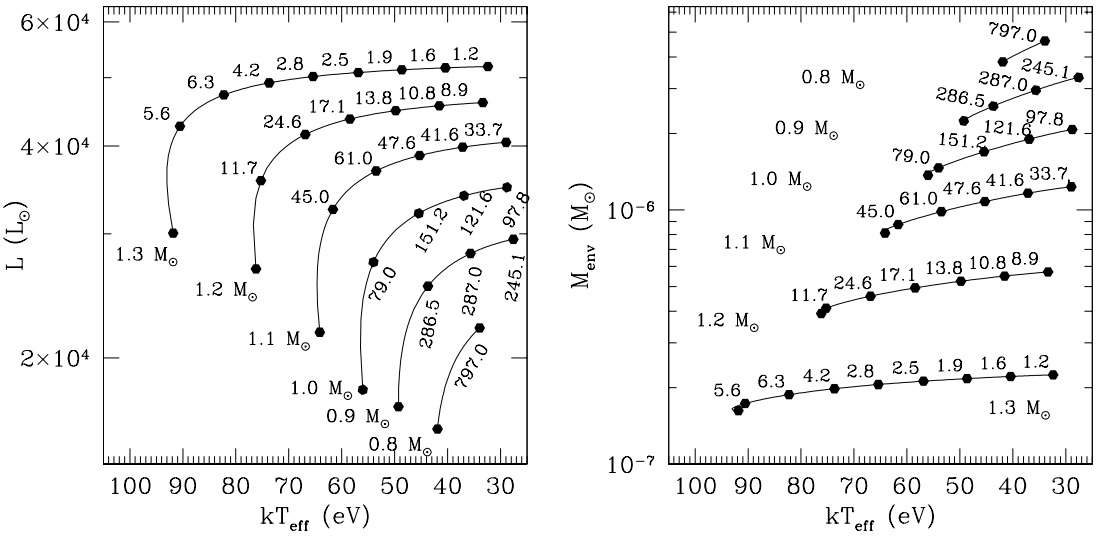

Figure 2.32: Same as figure 2.31 for ONe25 (25% mixing) envelope models.

(for ONe and CO models) or years (for the I82 models). Evolution proceeds slower for smaller white dwarfs, with lower luminosities. Time intervals are also longer for envelopes with increasing hydrogen abundance, which have smaller luminosities.

The times found in this work are much shorter than the evolution times usually found in the literature for stationary hydrogen burning on white dwarfs, including for instance the times found by Iben (1982). The difference can be explained by the smaller hydrogen fraction in the envelope: the equilibrium configuration is hotter and brighter for hydrogen poorer envelopes, and envelopes masses are smaller. To keep this higher luminosity, hydrogen is consumed faster and, in addition, for the same amount of hydrogen consumed, a larger fraction of the envelope mass is reduced. As envelope masses are smaller and are reduced at a faster rate, the total timescale to consume the envelope is shorter.

These timescales can be compared with the nuclear-burning lifetime for classical novae

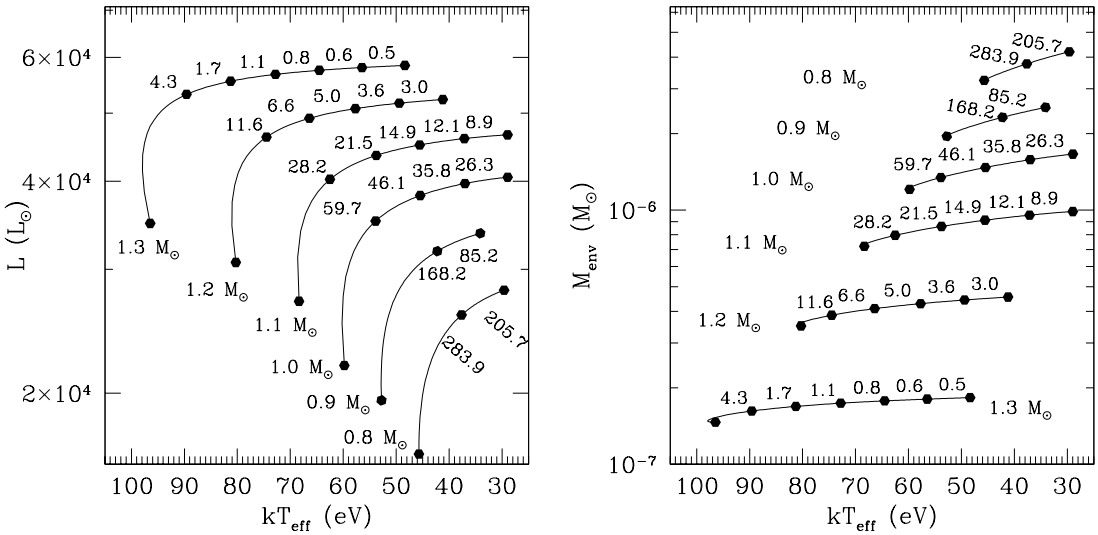

Figure 2.33: Same as figure 2.31 for ONe50 (50% mixing) envelope models.

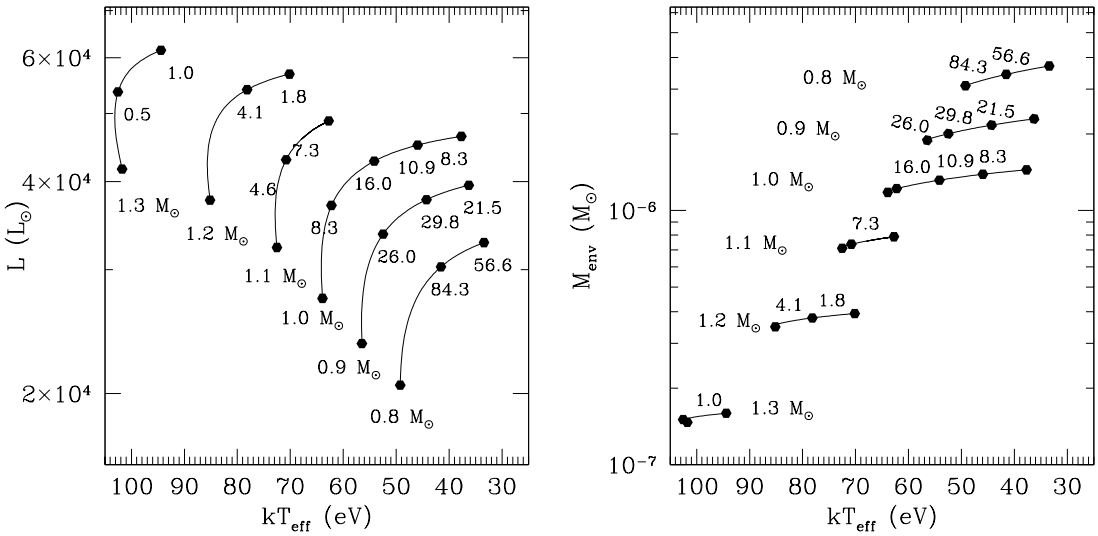

Figure 2.34: Same as figure 2.31 for ONe75 (75% mixing) envelope models.

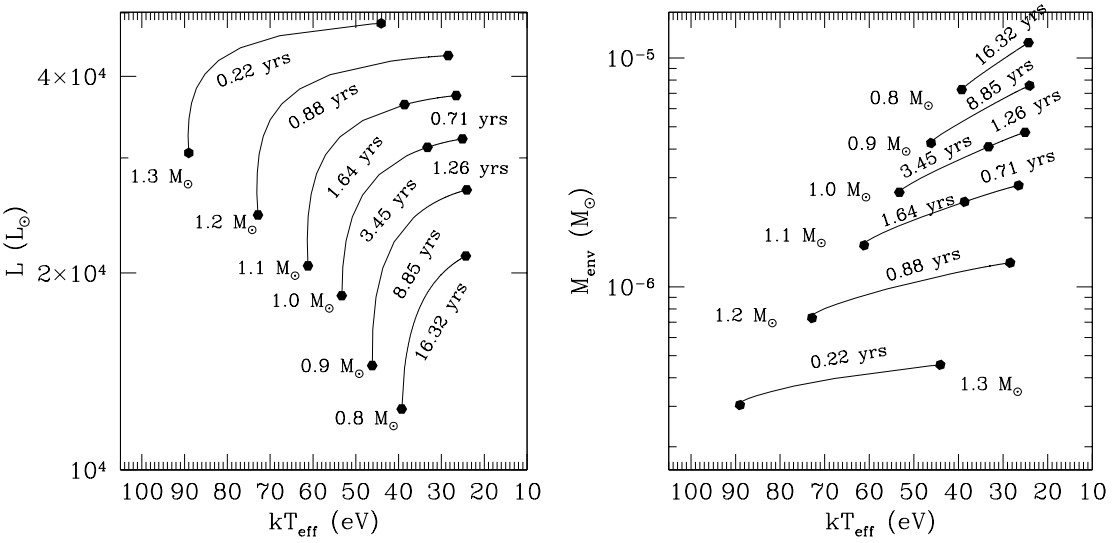

Figure 2.35: Same as figure 2.31 for I82 envelope models.
Note that time elapsed between to tick marks is indicated in years, instead of days as in previous figures.

hydrostatic remnants from previous works. In Starrfield (1989), this lifetime is estimated as

$$\tau_{nuc} = 400 \left(\frac{M_H}{10^{-4} M_\odot} \right) \left(\frac{L}{2 \times 10^4 L_\odot} \right)^{-1} yr \tag{2.25}$$

where M_H is the hydrogen mass and L the total luminosity. A similar expression, only a factor $\frac{5}{4}$ larger, was found by MacDonald et al.(1985). In both cases, the nuclear lifetime for an envelope of $10^{-5} - 10^{-4} M_\odot$ is of decades or even centuries. According to hydrodynamical simulations, $10^{-5} - 10^{-4} M_\odot$ is the mass required for the thermonuclear runaway to be triggered (José & Hernanz (1998),Starrfield et al.(1998),Prialnik & Kovetz (1995)), and the fraction of the accreted mass that is expected to be ejected is not large enough as to reduce the mass of the remnant by two orders of magnitude. But in the present work, envelope masses in a stationary configuration have been found to be $\sim 10^{-6} M_\odot$, which requires an extra mass loss mechanism after the nova outburst for the envelope to reach the equilibrium configuration. Once the envelope has reached the steady hydrogen burning phase, the nuclear lifetime (2.25) can be rewritten with our typical values ($M_{env} = 10^{-6} M_\odot$, $L = 4 \times 10^4 L_\odot$) as

$$\tau_{nuc} = 2 X_H \left(\frac{M_{env}}{10^{-6} M_\odot} \right) \left(\frac{L}{4 \times 10^4 L_\odot} \right)^{-1} yr \tag{2.26}$$

For X=0.35 (as in ONe50 and CO50 models), $\tau_{nuc} = 0.7yr \simeq 255days$, which agrees with the times in figures 2.31 and 2.33. For I82 models, with X=0.64, $\tau_{nuc} \simeq 9yr$.

2.7 Summary

A numerical model has been developed to simulate the physical conditions in the steady hydrogen burning envelope of a white dwarf after a nova outburst. A grid of envelope models has been computed for six different white dwarf masses, from 0.8 to 1.3 $M_\odot$, and six chemical compositions, corresponding to realistic CO and ONe white dwarf envelopes, with several degrees of mixing between the core material and the solar-like accreted matter. The results show that there exists a maximum luminosity and a maximum effective temperature

for every white dwarf mass and composition. The maximum effective temperature divides the series of models into two branches: a stable branch of high, quasi-constant luminosity, and a low luminosity unstable branch, with constant photospheric radius. For every white dwarf mass and composition there is also a minimum envelope mass, which occurs in the vicinity of the maximum effective temperature. The mass of the stable branch envelopes is almost constant, decreasing only slowly for increasing effective temperatures. The plateau luminosity, maximum effective temperature, and plateau and minimum envelope mass for each model are summarized in table 2.3.

Each of the overall properties of the envelopes are related to the total white dwarf mass and its chemical composition. The core mass -luminosity relation derived from our models is

$$L_{plateau}(L_\odot) \simeq 5.95 \times 10^4 \left(\frac{M_c}{M_\odot} - m_0 \right)$$

with, for CO50 envelopes $m_0^{CO50} = 0.3$, for ONe75 envelopes $m_0^{ONe75} = 0.24$, for ONe50 envelopes $m_0^{ONe50} = 0.32$, for ONe25 envelopes $m_0^{ONe25} = 0.42$, and for ONe09 and I82 models $m_0^{ONe09} = m_0^{I82} = 0.48$. We find that this relation is fully compatible with core mass - luminosity relations derived from other works on white dwarf envelopes with different chemical compositions (Iben (1982), Tuchman & Truran (1998)). For the ONe models,

$$L_{plateau}(L_\odot) \simeq 5.95 \times 10^4 \left(\frac{M_c}{M_\odot} - 0.536 X_H - 0.14 \right)$$

$$\log M^{ONe}_{plateau}(M_\odot) \simeq 0.42 X_H - \left(\frac{M_c}{M_\odot} - 0.13 \right)^3 - 5.26$$

$$\log M^{ONe}_{min}(M_\odot) \simeq 0.13 X_H - \left(\frac{M_c}{M_\odot} - 0.13 \right)^3 - 5.26$$

Our results show that masses of stable envelopes with steady hydrogen burning ($\sim 10^{-6} M_\odot$) are in general smaller by at least one order of magnitude than envelope masses needed to trigger the outburst ($\sim 10^{-5} M_\odot$), according to hydrodynamical models. Since those models predict that only a fraction of the accreted envelope is ejected, it is clear that some mass loss mechanism must act after the outburst, before the steady hydrogen burning can be established in the envelope. An interesting possibility for the mass loss is, as pointed out by Tuchman & Truran (1998), the dynamical instabilities of the envelope itself when it is left after the outburst with a mass much larger than that of stable configurations.

An estimation of the evolutionary sequence of a steady hydrogen burning white dwarf envelope in the plateau of quasi-constant luminosity can be obtained as a series of stationary envelope models with decreasing envelope masses. The envelope evolves at quasi-constant luminosity along the stable branch, shrinking its photospheric radius as the envelope mass is reduced due to hydrogen burning, and increasing its effective temperature as the photosphere sinks deeper into the envelope. Hydrogen burning continues until the minimum envelope mass and maximum effective temperature are reached; since no equilibrium configuration for smaller envelope mass exists, hydrogen burning can not proceed further in stationary conditions and the white dwarf starts to cool down. The time intervals needed for the envelope to evolve between stationary solutions are estimated as the time needed to burn the difference of envelope mass at the mean luminosity of the interval. As a summary of the evolution "speed" of each envelope on the HR diagram, the last column in table 2.3 lists the time needed for the envelope to change its effective temperature the last

Table 2.3: Main properties of the envelope models.

Model	M_{WD} ($M_\odot$)	$L_{plateau}$ ($10^4 L_\odot$)	kT_{eff}^{max} (eV)	T_{eff}^{max} ($10^5 K$)	$M_{env}^{plateau}$ ($10^{-6} M_\odot$)	M_{env}^{min} ($10^{-6} M_\odot$)	$\Delta t_{10\,eV}^{(1)}$ (days)
ONe75 (X=0.18)	0.8	3.3	49	5.7	3.8	3.1	97
	0.9	3.9	57	6.6	2.3	1.9	47
	1.0	4.4	64	7.4	1.4	1.2	24
	1.1	5.2	73	8.5	0.84	0.71	12
	1.2	5.7	86	9.9	0.40	0.35	4.6
	1.3	6.2	103	11.9	0.16	0.15	1.1
ONe50 (X=0.35)	0.8	1.8	46	5.3	4.2	3.2	340
	0.9	3.5	53	6.1	2.7	1.5	160
	1.0	4.1	60	7.0	1.7	1.2	78
	1.1	4.7	69	8.0	9.9	0.72	37
	1.2	5.2	81	9.4	0.45	0.35	14
	1.3	5.6	98	11.4	0.19	0.15	4.9
ONe25 (X=0.53)	0.8	2.2	42	4.9	4.6	3.8	800
	0.9	2.9	49	5.7	3.0	2.2	430
	1.0	3.5	56	6.5	2.1	1.4	210
	1.1	4.0	64	7.5	1.20	0.81	98
	1.2	4.6	77	8.9	0.60	0.39	36
	1.3	5.2	93	10.8	0.22	0.16	12
CO50 (X=0.35)	0.8	3.0	47	5.4	4.7	3.3	420
	0.9	3.6	54	6.2	2.9	1.9	230
	1.0	4.2	61	7.1	1.8	1.2	90
	1.1	4.7	70	8.1	1.0	0.72	48
	1.2	5.4	82	9.5	0.49	0.35	19
	1.3	6.0	99	14.7	0.19	0.15	6
I82 (X=0.64)	0.8	2.1	39	4.6	1.2	7.3	3700
	0.9	2.7	46	5.4	7.6	4.3	1600
	1.0	3.2	53	6.2	4.7	2.6	980
	1.1	3.7	61	7.1	2.8	1.5	600
	1.2	4.3	73	8.4	1.3	0.73	250
	1.3	4.6	89	10.3	0.46	0.30	52
ONe09 (X=0.64)	0.8	2.0	40	4.7	6.0	4.7	2000
	0.9	2.6	47	5.5	3.9	2.8	860
	1.0	3.2	54	6.3	2.7	1.7	390
	1.1	3.7	62	7.2	1.6	1.0	190
	1.2	4.3	74	8.6	0.75	0.50	59
	1.3	4.8	89	10.3	0.28	0.20	18

(1) Time needed for the envelope to evolve from $kT_{eff} \simeq kT_{eff}^{max} - 10eV$ to kT_{eff}^{max}.

$\sim$10 eV before reaching the maximum effective temperature. Evolution times are longer for less massive white dwarfs, since luminosity is lower in these cases. The evolution also proceeds slower for envelopes with increasing hydrogen abundance.

The times-scales found from our models with realistic abundances for a post-nova white dwarf envelope are shorter than those obtained in previous estimations, even from those works that computed stable solutions for the hydrogen burning envelope and obtained similar luminosities (Iben (1982)). Differences are mainly due to the smaller hydrogen mass fraction in our post-nova envelopes: the equilibrium configuration is hotter and brighter for hydrogen-poor envelopes, and envelopes masses are smaller. For envelopes of a $\sim 1 M_{\odot}$ white dwarf and with X=0.35 (corresponding to 50% mixing between solar-like accreted material and the degenerate core), typical time-scales from our models are $\sim$200-300 days, similar to the turn-off times observed in classical novae.

The photospheric properties obtained with the envelope models and their temporal evolution can be directly compared with the results derived from X-ray observations for post-outburst classical novae. In next chapter, observations of the three classical novae with soft X-ray emission observed by ROSAT are compared with our envelope models.

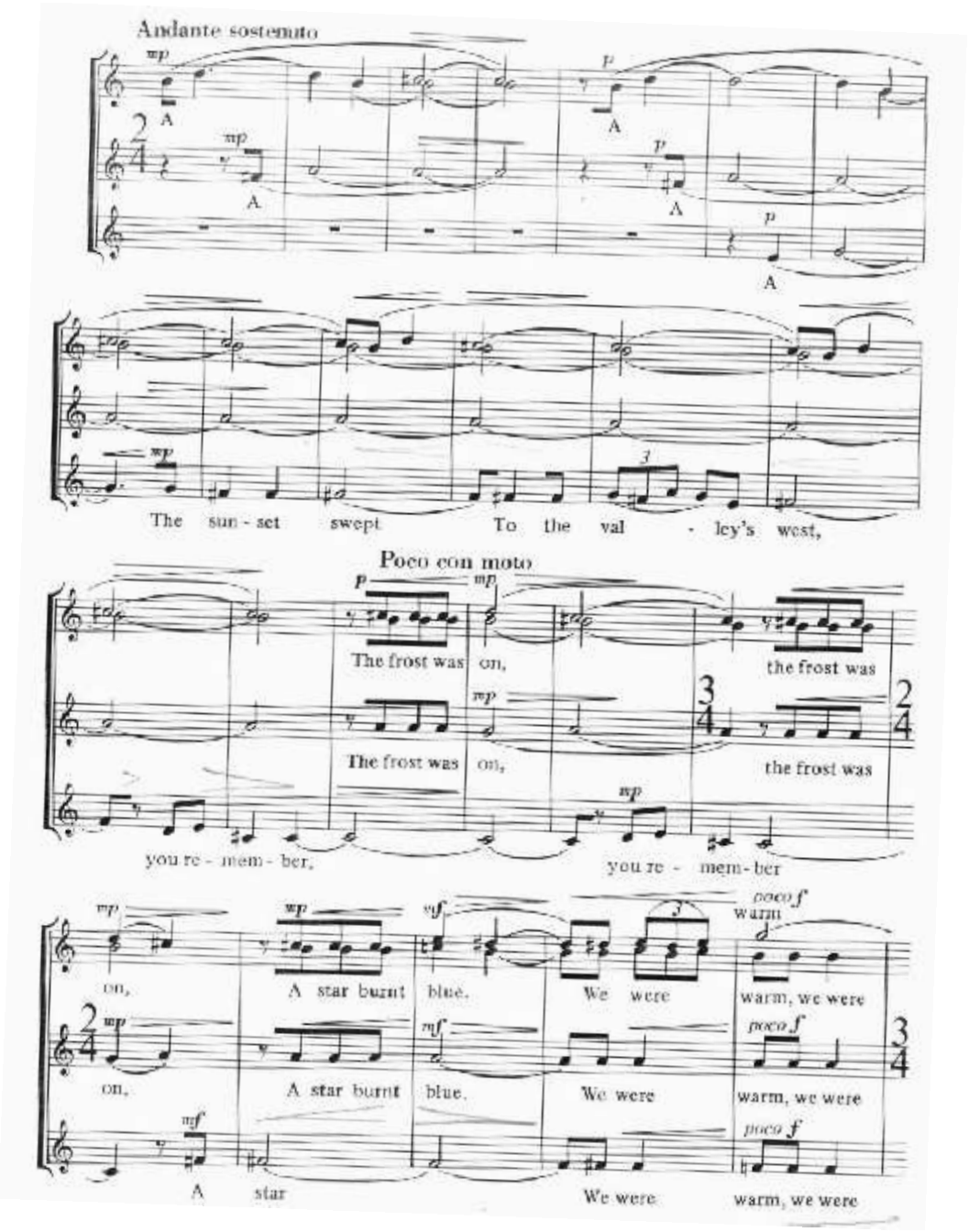

"The sunset swept to the valley's west
You remember, the frost was on
A star burnt blue..."

Valley's Song
Micklós Coksár

Chapter 3

ROSAT observations of classical novae

3.1 Introduction

The ROSAT satellite (*Röntgensatellit*, Briel et al.(1997)), launched on 1990, opened a new era for X-ray astronomy. It obtained better results than previous missions thanks to its much larger effective area, better angular and energy resolution, and a program including an all-sky survey and pointed observations. Remarkable results on classical novae and other stellar objects were obtained with the PSPCs (*Position Sensitive Proportional Counter*s), with an energy range of 0.1 to 2.4 keV and an improved energy resolution with respect to previous missions ($\frac{\Delta E}{E}$ $\sim$50%).

ROSAT observations of classical novae gave new insight on the physics of the outburst and post-outburst phases. Observations of Nova Cygni 1992 (V1974 Cyg) followed the whole X-ray light curve, with an initial rise due to a decrease in the absorption of the ejecta, the expected plateau of constant luminosity and a final decline. The short duration of the soft X-ray emission of this nova (only 18 months) and the fact that only three novae were detected with soft X-ray emission out of the 39 post-outburst novae observed, contrasted with the duration expected for the constant bolometric luminosity phase and was one of the main motivations for the present thesis.

For the three classical novae with soft X-ray emission, a simple blackbody model resulted inadequate to fit the observed spectra with reasonable parameters, yielding unreasonably large values for the luminosity (as will be further commented in section 3.4 for V1974 Cyg). As has been commented before, it is known from theoretical models that some mixing between the solar-like accreted matter and the degenerate core is needed for the thermonuclear runaway to produce the ejection of the shell and the nova outburst. These overabundances have been indeed observed in nova ejecta, and found to agree with hydrodynamic models including nucleosynthesis (José & Hernanz (1998)). The opacities of the envelope enhanced with these heavy elements deviate the hydrogen burning shell emission from the blackbody model and makes necessary the use of white dwarf atmosphere models to fit the soft X-ray spectra (MacDonald & Vennes (1991)).

In this chapter, the results obtained from ROSAT are compared to the white dwarf envelope models developed in the previous chapter. In section 3.2, the ROSAT observatory is presented and the results obtained for classical novae are summarized. ROSAT observations of V1974 Cyg are revisited in section 3.4 and compared to the envelope models. In addition, the contribution of the photoionization of the ejecta is studied. The white dwarf envelope models are also used to interpret the results obtained for the other two supersoft

novae detected by ROSAT, GQ Mus and Nova LMC 19965 (section 3.5).

3.2 The ROSAT observatory

The ROSAT mission was the result of a proposal made by the Max-Planck-Institut für extraterrestrische Physik (MPE) in 1975 and approved in 1983 by the Bundesministerium für Forschung und Technologie (BMFT). Cooperational agreements were reached between MPE, NASA (American National Aeronautics & Space Administration) and the British Science & Engineering Research Council (SERC). MPE was the responsible for the scientific management, the focal plane instrumentation and the Science Data Center (where the analysis an interpretation of all scientific data were developed). NASA provided the Delta-II rocket for the launch and the High Resolution Imager (HRI), while the Wide Field Camera (WFC) was built by a consortium of English institutes. In return, 50% of pointing observing time was made available for US Principal Investigators (PI's) and 12% for UK PI's.

ROSAT had two main scientific objectives: first, an all-sky survey in the X-ray and EUV (Extreme Ultraviolet) ranges; and second, a detailed study of selected sources through pointed observations. During the first 6 months, the satellite operated in a "scan mode" to complete the all-sky survey in the bands 0.1-2.4 keV (X-rays) and 0.04-0.2 keV (EUV). More than 60.000 sources were found, discovering objects 100 times weaker than previous missions (previous all-sky survey by HEAO-1 had 840 sources). Once the survey was completed in February 1991, ROSAT operated in the "pointing mode", obtaining detailed information on selected sources (spectra, spatial structure and time variability). The ROSAT mission finished in February 1999,

3.2.1 Orbit, operations and mission phases

ROSAT satellite was originally planned to be launched on board the Space Shuttle, but the Challenger accident in January 1986 brought changes in the spacecraft design and a delay in the launch. In December 1987 it was decided to use a McDonald Douglas Delta-II rocket to situate ROSAT into a low Earth orbit, and it was finally launched from Cape Canaveral on 1990 June 1. Details of the orbit are given in table 3.1.

The only responsible of any communication with the spacecraft was the German Space Operation Center (GSOC, in Oberpfaffenhofen, Germany), where the Mission Control Center was located. The GSOC conducted all mission operations related functions such as data processing, spacecraft instruments performance analysis, orbit and attitude determination and control and command generation. All scientific data was sent to the Science Data Center at Max-Planck-Institut für extraterrestrische Physik (MPE, in Garching, Germany) for analysis.

During the first 6 months of the mission, ROSAT monitored systematically the celestial sphere to obtain an all-sky survey in X-rays. As posterior missions have not planned any similar survey, this work is of great importance for present X-ray satellites, such as XMM-Newton and Chandra.

In the 'scan mode', the satellite had a rotation synchronous with the orbit: the spacecraft completed a revolution around the sun vector (thus keeping a constant solar angle) per orbit around the Earth. As a result of the movement of the Earth in its orbit, the direction of the strip of sky scanned by the telescope in each orbit of the satellite changed by about 1^o per day, and the all-sky survey was completed in 180 days. As the FOV of the instrument was 2 degree wide and it was shifted 4 arcmin per orbit, each source was

Table 3.1: ROSAT Orbit parameters.

Launch	1990 June 1
Altitude	580km
Inclination	53°
Eccentricity	<0.1%
Orbit Period	96.2 minutes
Precession	66 days
Ground Station Contacts	6 per day
Duration of Contacts	8 minutes

observed for a period of 2 days. X-ray object coordinates were determined within 30 arcsec of accuracy.

Once the all-sky survey was completed, the second phase of the ROSAT mission started. Pointed observations with coordinate determination accuracy of less than 10 arcsec were scheduled with a maximum duration of 3h. The spacecraft needed to keep a sun aspect angle of 90°±15°, making possible observations in a 30° band at each moment. This phase lasted until the end of the mission in 1999 February 12.

3.2.2 Scientific payload

Figure 3.1 shows a general scheme of the ROSAT spacecraft and a cross section of the telescopes and focal plane instruments. The scientific payload consisted of two imaging telescopes: the X-ray Telescope (XRT), with 2 Position Sensitive Proportional Counters (PSPC's) and a High Resolution Imager (HRI) on the focal plane; and the Wide Field Camera (WFC), with a curved microchannel plate on the focal plane. Externally attached to the body of the X-ray telescope, two star trackers coaligned with the telescopes and the gyro package provided the main attitude control.

The X-Ray Telescope

Working in the range 0.1-2.4 keV, the X-ray Telescope (XRT) had a maximum effective area of about 1000 cm^2 at ~0.15 keV. The X-ray Mirror Assembly (XMA) consisted of 4 nested grazing incidence Wolter-I mirrors (see figure 3.1). Each Wolter-I mirror was constructed with a pair of mirror shells, a paraboloid and a hyperboloid made of Zerodur, a glass ceramic with almost negligible thermal coefficient, and coated with a thin layer of gold to improve the X-ray reflectivity. The maximum aperture of the mirrors was of 83.5 cm and their focal length 240 cm. The focal plane instrumentation consisted of two Position Sensitive Proportional Counters (PSPCs), each with a filter wheel carrying a boron filter, and a High Resolution Imager (HRI). All of them were mounted on a turret for alternate positioning in the focus.

The Position Sensitive Proportional Counters The PSPCs provide X-ray (0.11-2.4 keV) images over a 2 degree diameter field-of-view, with modest energy resolution ($\Delta E/E=0.43\left[\frac{E}{0.93}\right]^{-0.5}$), high spatial resolution (~25 arcsec at 1 keV) and relative time resolution (down to ~130 microseconds).

Four Position Sensitive Proportional Counters were developed and constructed by MPE. Two of them (PSPC-A and PSPC-D) were used for ground calibration measurements, while the other two were mounted on a carrousel in the focal plane turret of the X-ray telescope. Of the two redundant PSPCs in orbit, PSPC-C was planned to be the

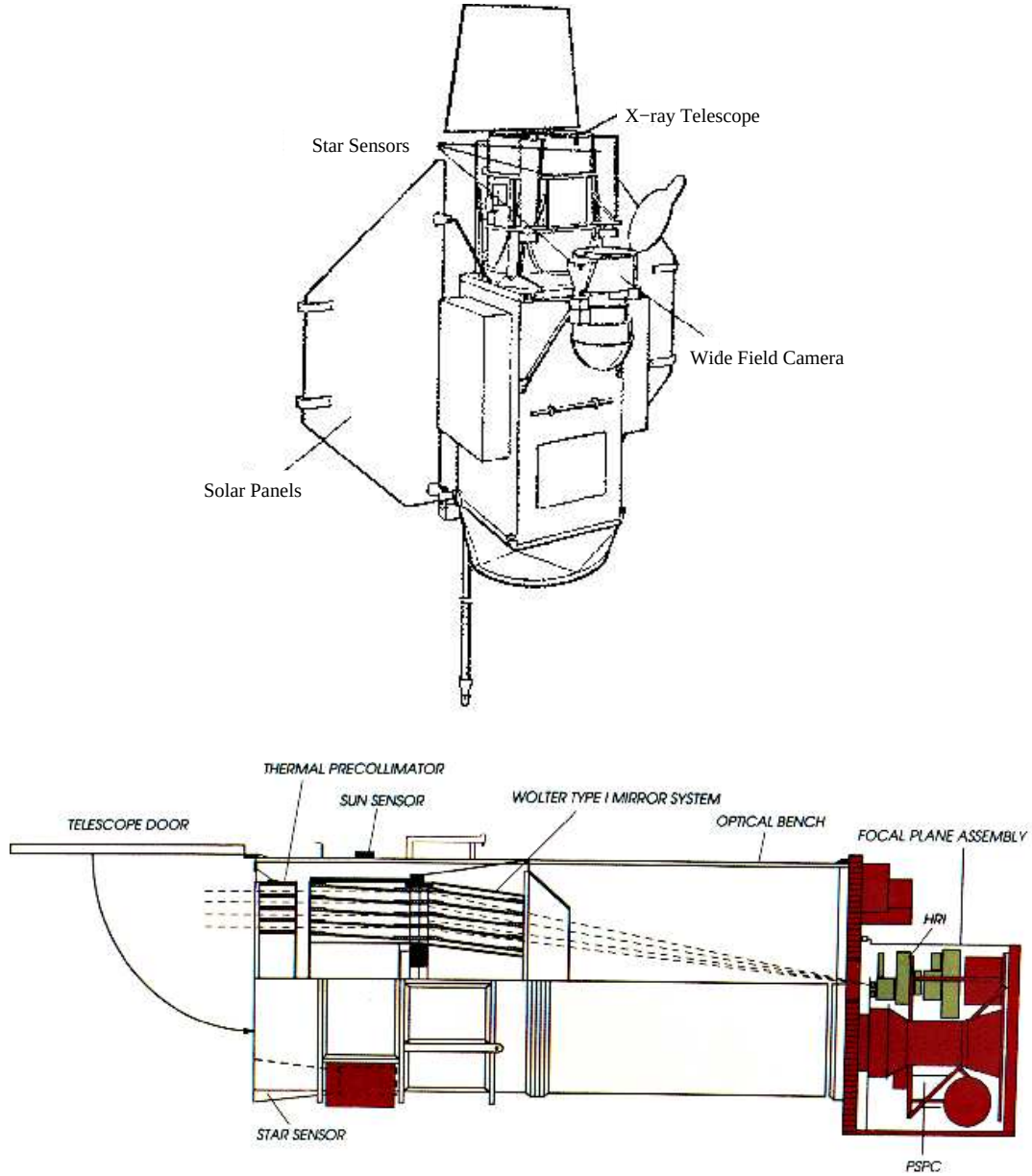

Figure 3.1: Sketch of the ROSAT spacecraft (upper figure) and cross section of the X-ray telescope (lower figure). *Sources:* ROSAT User's Handbook (Briel et al.(1997)) and Max Planck Insitut für extraterrestrische Physik web pages (http://wave.xray.mpe.mpg.de/rosat/mission/rosat).

primary detector for the mission. It was used during the Performance Verification and Calibration (PVC) phase and for the main part of the all-sky survey. But on 1991 January 25, it was destroyed during a solar slew. The spare PSPC-B detector was used from that moment for all AO pointed observations until 1994 September 11. It was shut down after four years in order to conserve the remaining gas to complete the all-sky survey in 1997.

Each PSPC consisted essentially of two multi-wire proportional counters. A multi-wire proportional counter is formed by two wire grids bonded onto a ceramic support structure: the wires of one of the grids act as anodes while those of the second grid are the cathodes. Of the four grids of the two counters in each PSPC, one of the anodes grid and the two cathodes grid acted as position sensitive counters and the second anodes grid as anti-coincidence counter for background rejection. All electrodes were contained in a gas-filled counter housing containing a mixture of 65% argon, 20% xenon and 15% methane.

The X-ray photons were focused onto the PSPC by the XRT. They passed through a thin plastic entrance window and were photo-electrically absorbed by the counter gas producing a photo-electron. This electron was accelerated by the electric field generated by the electrodes and created new electron-ion pairs on its way to one of the anodes, amplifying the final registered signal.

The gas container was closed by a thin plastic entrance window that required a support to withstand the pressure of the gas against vacuum. The support structure consisted mainly of a rigid circle with eight radial struts. On a smaller scale, the plastic layer was supported by two mesh systems (a coarse mesh with 2 mm spacing and a fine one with 0.4 mm spacing). All these elements were opaque to X-rays in the ROSAT energy band, being the average energy transmition through the meshes 79%. The shadow of the main structure is visible in many PSPC images (see figure 3.2 as an example). To prevent that the structure occulted X-ray sources in pointed observations, a slow spacecraft "wobble" was performed in a direction diagonal to the mesh structure.

The High Resolution Imager The ROSAT High Resolution Imager (HRI), developed in the US, was very similar to the Einstein Observatory HRI, and consisted basically of two cascade micro-channel plates (MCPs). It was designed to obtain good X-ray images with low spectral resolution. Spatial resolution of $\sim$2 arcsec FWHM was provided by a crossed grid position readout system over a square field-of-view of 38 arcminutes on a side. HRI observations had relative time resolution (down to 61 microseconds).

The High Resolution Imager had a limited (2-band) spectral response. This spectral capability could give X-ray hardness ratios on spatial scales of 5 arcseconds. But the variations of gain with time and position on the detector and the wobbling of the satellite difficulted the scientific use of HRI spectral response.

The Wide Field Camera

The Wide Field Camera, built by the United Kingdom, obtained images in the EUV (0.04-0.2 keV). It had its own mirror system and star tracker. Three Wolter-Schwarzschild Type I nested mirrors focused the EUV photons to the focal plane situated at 0.525 m. Two identical micro-channel plates (MCP) were mounted on a turret for selection and positioning on the focus, with a carrousel containing eight filters. The instrument had a 5 degree field-of-view (FOV) and a spatial resolution of 2.3 arcmin. Spectral information could be obtained by the use of different filters.

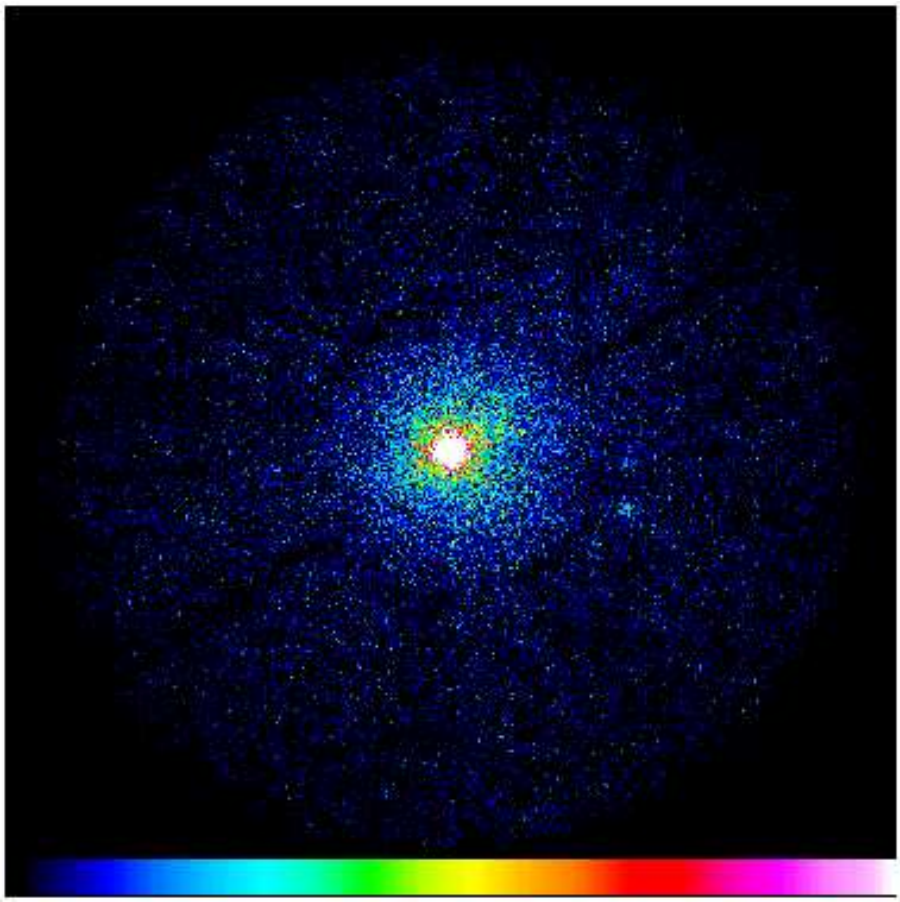

Figure 3.2: ROSAT/PSPC image of V1974 Cyg area on day 434 after outburst.
The field of view (FOV) is 2 degrees across. The central source is V1974 Cyg, but other X-ray sources are present in the image. The pattern of the detector structure is also visible.

3.3 Classical Novae observed by ROSAT

During the first phase of the mission, the ROSAT All-Sky Survey (RASS), about 283 positions of known nova or nova-like objects were observed in X-rays (Ögelman & Orio (1995), Orio (1999), Orio et al.(2001a), Orio (2004)). Only seven classical novae were detected during the all-sky survey, six of them being old novae with reestablished accretion. Out of the 283 explored positions, 26 corresponded to novae that had their outburst in the ten years before the ROSAT survey, but only one of them, GQ Mus (Nova Mus 1983, already discovered by EXOSAT in 1983, Ögelman et al.(1984)), was detected in the survey. During the second phase of the mission, ROSAT observed some classical novae in pointed observations (Table 3.2).

A systematic search of X-ray emission from classical novae was done by Orio et al.(2001a) in the ROSAT archival data, which contains the results from the survey and from the pointed observations. In total, ROSAT observed 39 classical novae aged less than ten years, thus expected to be bright soft X-ray sources. But very few of them detected as X-ray emitters shortly after their outburst. Among them, only three novae showed the expected soft X-ray spectrum: GQ Mus, V1974 Cyg (Nova Cyg 1992, Krautter et al.(1996), Balman et al.(1998)), and Nova LMC 1995 (Orio & Greiner (1999)). GQ Mus was the one with the longest observed soft X-ray emission phase (around nine years, Ögelman et al.(1993), Shanley et al.(1995), Balman et al.(2001)). V1974 Cyg turned off only 18 months after the outburst. In the case of Nova LMC 1995, it was detected by ROSAT as a soft X-ray source three years after outburst, and in a second observation with XMM-Newton in the year 2000, five years after outburst. These results indicated that in most cases, either thermonuclear burning of the remaining material on the white dwarf lasted less than 10 years or that absorption was unusually high and the soft X-rays could not reach the Earth.

Other novae were detected in X-rays with ROSAT, but without any soft component, i.e., V351 Pup (Nova Pup 1991, Orio et al.(1996)) and V838 Her (Nova Her 1991, Lloyd et al.(1992), O'Brien et al.(1994)). V838 Her was observed by ROSAT only five days after outburst, and again one year and 19 months after optical maximum. In the first observation it showed a hard spectrum with a count-rate of 0.16 $cts\ s^{-1}$. Lloyd et al.(1992) fitted the spectrum with a Raymond-Smith thermal spectrum and found two possible fits, for $kT \geq 10$ keV and for $kT = 0.74$ keV. They concluded that the observed emission was too hard to come from the thermonuclear burning layer. In addition, the column density at this early stages of the outburst is expected to be large enough to absorb all soft photons coming form the surface of the white dwarf. The emission of V838 Her was supposed to be caused by shocks of the ejected material with circumstellar material or within the ejecta itself. A year after outburst, V838 Her appeared in ROSAT observations only as a very faint source ($L_X \leq 10^{31} erg\, s^{-1}$, Ögelman & Orio (1995)).

Nova Puppis 1991 (V351 Pup) was observed 16 months after the outburst, with 0.2-0.3 $cts\ s^{-1}$ (Orio et al.(1996)). As in the case of V838 Her, the best-fit of a blackbody spectrum yielded a too high effective temperatures for a thermonuclear burning layer on the surface of the white dwarf. In addition, the determination of the distance from optical observations made it possible to determine the unabsorbed bolometric flux ($L_{bol} \simeq 4.5 \times 10^{33} erg\, s^{-1}$), and it resulted too low for a hydrogen-burning white dwarf. The best model was again the Raymond-Smith spectrum of a thermal plasma, with $kT \simeq 1.1$ keV and a source luminosity of $7.5 \times 10^{33} erg\, s^{-1}$. Orio et al.(1996) studied the upper limits for a possible supersoft component not detected. They fitted a two component model to the data, a blackbody plus the thermal plasma component. The 3σ upper limit to the blackbody temperature was found to be 20 eV, with a bolometric luminosity of $L \leq 10^{36} erg\, s^{-1}$. Both values

were lower than expected. From optical lines in the nebular spectrum, they determined the photospheric temperature to be (2-3)$\times 10^5 K$, consistent with the upper limit for the blackbody temperature (20 $eV = 2.3\times 10^5 K$). To determine whether the soft X-ray source had not still emerged or the burning layer was already cooling down, they studied the evolution of the ratio of the line He II $\lambda 4686$ to Hβ. This ratio was decreasing at the time of the ROSAT observation (while for GQ Mus it kept on increasing as long as soft X-ray emission was detected), indicating that probably the remnant on the white dwarf was already cooling down. Regarding the thermal plasma component, they could not conclude whether it was originated in the ejected shell or in a reestablished accretion stream.

Finally, 11 out of the 81 galactic quiescent novae observed by ROSAT were detected in hard X-rays (Orio (1999)). DQ Her (Nova Her 1934), CP Pup (Nova Puppis 1942) and V603 Aql (Nova Aql 1918) were already known to be bright X-ray sources from observations with the Einstein satellite. DQ Her had been considered a prototype polar, although in ROSAT observations it appeared as a faint X-ray source, with $L_x \simeq 10^{31} erg\, s^{-1}$. ROSAT observations of CP Pup indicate that it is probably a polar system, with a high luminosity ($L_x \geq 10^{32} erg\, s^{-1}$) and plasma temperature ($kT > 2.2\ keV$), and X-ray modulations with the orbital cycles (Balman et al. (1995)). The most luminous quiescent nova in X-rays is V603 Aql, which changed dramatically its X-ray properties since the previous Einstein observation (Orio (1999)). The time variations were quite different, the luminosity had changed and the plasma temperature was much lower in the ROSAT detection. For the other galactic novae not detected, Orio (1999) established an upper limit for the luminosity of $L_x \leq 10^{32} erg\, s^{-1}$, assuming a distance of 3 *kpc* and a plasma temperature of $\sim$1 *keV*. As intermediate polar systems have a higher luminosity and harder spectra (less affected by interstellar absorption), the previous limit indicates that the fraction of novae in intermediate polar systems can not be very high. Finally, Balman & Ögelman (1999) obtained the first resolved X-ray images of the GK Per nova shell with ROSAT HRI. In this case, they found that 20% of the X-ray flux was not coming from the central source but from the circumstellar shell. GK Per shell has been further studied with Chandra (Balman (2002)).

3.4 Nova Cygni 1992 (V1974 Cyg)

Nova Cygni 1992 (V1974Cyg) was discovered on 1992 February 19.07 UT (Collins (1992)). It was the brightest nova since Nova Cyg 1975 (V1500 Cyg), reaching a maximum brightness of V = 4.4 on 1992 February 21.17, and was classified as an ONe nova (Austin et al.(1996), Shore et al.(1993), Shore et al.(1994)). V1974 Cyg was the first classical nova to be observed in all wavelengths, from radio to γ-rays. It was observed in X-rays by the ROSAT observatory between April 1992 and December 1993 (Krautter et al.(1996)).

Several determinations of the distance to V1974 Cyg can be found. Quirrenbach et al.(1993) determined the distance to be $\sim$2.5 *kpc* using optical interferometry to measure the diameter of the expanding shell. Adopting an expansion velocity of $\sim 1100\, km\, s^{-1}$, Shore et al.(1994) obtained a distance of $\sim$3 *kpc* from optical and ultraviolet observations of the early stages of the nova, assuming the bolometric luminosity to be $5 \times 10^4 L_\odot$ (the same as the two ONe novae observed in the LMC at that time, LMC 1988 No.2 and LMC 1990 No.1). Paresce et al.(1995) assumed an expanding velocity $\sim$830-1500 $km\, s^{-1}$ to determine the distance to be 1.8-3.2 *kpc* from HST observations of the expanding shell. Chochol et al.(1997) used available optical and UV spectroscopic, HST and radio observations to develop a kinematic model for the expanding shell and determined a distance of 1.77$\pm$0.11 *kpc*. Using ROSAT observations and their white dwarf atmosphere fits, Balman

Table 3.2: ROSAT pointed observations of classical novae.

	Discovery Date	PI	Total Time	Begin	End
Nova Per 1901 (GK Per)	1901	Reinsch - Balman	75 155 s	Aug 92	Feb 96
Nova Aql 1918 (V603 Aql)	1918	Pietsch- Schwarzenber	52806 s	Apr 91	Oct 92
Nova Her 1934 (DQ Her)	1934	Patterson	13191 s	Mar 92	Mar 92
Nova Cyg 1975 (V1500 Cyg)	1975 August 29 Honda (1975)	Orio	7 189 s	May 91	Nov 92
Nova Mus 1983 (GQ Mus)	1983 January 18 Liller (1983)	Ögelman	23 738 s	Feb 92	Jul 94
Nova Vul 1984 no.1 (PW Vul)	1984 July 27 Kosai (1984)	Ögelman	4 624 s	Mar 91	Mar 92
Nova Vul 1984 no.2 (QU Vul)	1984 December 22 Collins (1984)	Ögelman	8 531 s	Apr 91	Apr 91
Nova And 1986 (OS And)	1986 December 4 Kosai (1986)	Krautter	5 249 s	Dec 91	Dec 91
Nova Her 1987 (V827 Her)	1987 January 25 Kosai (1987)	Krautter	4 614 s	Mar 91	Mar 92
Nova LMC 1987	1987 September 17 McNaught (1987)	Ögelman	7 802 s	Mar 92	Mar 92
Nova Vul 1987 (QV Vul)	1987 November 15 Beckmann et al.(1987)	Krautter	4 905 s	Mar 91	Mar 92
Nova LMC 1988 a	1988 March 21 Garradd (1988)	Ögelman	13 150 s	May 92	Jun 93
Nova LMC 1988 b	1988 October 13 McNaught (1988)	Krautter	4 030 s	Apr 92	Apr 92
Nova Sct 1989 (V443 Sct)	1989 September 20 Wild (1989)	Ögelman	5 789 s	Mar 92	Mar 92
Nova Mus 1991 (GU Mus)	1991 January 8 Lund et al. (1991)	Greiner	16 393 s	Mar 92	Mar 92
Nova Her 1991 (V838 Her)	1991 March 24 Matsuo et al.(1991)	O'Brien - Szkody	30 989 s	Mar 91	Oct 92
Nova Pup 1991 (V351 Pup)	1991 December 27 Camilleri (1991)	Ögelman	9 878 s	May 93	May 93
Nova Cyg 1992 (V1974 Cyg)	1992 February 19 Collins (1992)	Krautter	72 058 s	Apr 92	May 94
Nova LMC 1995	1995 March 2 Liller (1995)	Greiner	2 531 s	Dec 98	Dec 98

et al.(1998) found 2.4-2.8 *kpc* from the relation between photospheric radius and effective temperature of MacDonald & Vennes (1991) atmosphere models. More recently, Cassatella et al.(2004) have found a distance of 2.9±0.2 *kpc* from IUE high resolution spectroscopy. In this work, taking into account all these determinations, a distance of 2.45±0.75 *kpc* (corresponding to the range 1.7-3.2 *kpc*) has been assumed.

In this section, the analysis of the data with simple analytic models performed by Krautter et al.(1996) is revisited, and the more realistic analysis performed by Balman et al.(1998) is compared to the envelope models of chapter 2. In addition, the possible contribution of the photoionization to the X-ray spectrum is studied.

3.4.1 ROSAT/PSPC V1974 Cyg observations

V1974 Cyg was observed by ROSAT for a period of two years, from April 1992 to May 1994 (Krautter et al.(1996)). The output data from the 16 observations are available in the ROSAT Results Archive (RRA), a public archive that contains the source detections in all the released High Resolution Imager (HRI) and Position Sensitive Proportional Counter (PSPC) pointed observations. The PI of each pointed observation received the output of the observation and the results of the Standard Analysis Software System, including a list of the sources in the field of view and derived results such as light-curves and spectra; after one year the data (without derived results) were put into the ROSAT Data Archive (RDA) where they can be publicly accessed (http://www.xray.mpe.mpg.de/ rosat/ archive/ index.html). Since 2001 February 5 all ROSAT data are public.

The first 12 observations of V1974 were performed with the PSPC instrument and contain useful spectral information. Some of the observation files contain more than one exposure, separated in time up to more than a month. For this reason, some observations need to be splited and reagrupated in exposures taken during a period shorter than a day or two (depending on the flux) (Table 3.3).

Data reduction has been performed using EXSAS/MIDAS (Extended Analysis Software, Zimmerman et al.(1998)); and the XSPEC package (Arnaud et al.(1996)) has been used for spectral analysis (see appendix F for details on X-ray data reduction and analysis).

3.4.2 X-ray light curve

Figure 3.3 shows the X-ray light curve of V1974 Cyg in different bands (see also table 3.3). Points in black in figure 3.3 correspond to the total ROSAT/PSPC band (0.1-2.4 keV). The time evolution of the flux follows three clearly distinct phases: a first rise phase during which the count rate increases from an initial value of 0.02 $cts\ s^{-1}$ on day 63 after outburst up to 13 $cts\ s^{-1}$ on day 255; a plateau phase without great variations on the count rate follows from day 255 to 511, with a maximum of 83 $cts\ s^{-1}$ on day 434; and a final and fast decline from 79 $cts\ s^{-1}$ on day 511 down to 0.22 $cts\ s^{-1}$ on the last observation on day 653.

Points in red in figure 3.3 show the X-ray light curve in the soft band C_s (0.1-0.4 keV), while points in blue plot the count rate in the hard band C_h (0.5-2.0 keV). During the rise phase, the soft component is almost null (in the first two days it is compatible with zero) and all the emission is received in the hard band. But from day 255 to the end (plateau and decline phases) the light curve in the soft and in the hard band follow parallel evolution and have similar count rates, being the flux in the soft band always higher than in the hard one.

Table 3.3: Date, Julian day, day after outburst, exposure time, total count rate (0.1-2.4 keV) and hardness ratio HR1 of the ROSAT/PSPC observations of V1974 Cyg.

Date	Julian Day 2,400,000	Day	Exposure (s)	Count rate ($cts\,s^{-1}$)	HR1 ($\times 10^{-2}$)
1992 Apr 22	48734	63	2590	0.02±0.003	72 ±33
1992 May 20	48762	91	1226	0.14±0.01	95±17
1992 May 26	48769	97	3734	0.18±0.01	87±10
1992 Jul 14	48818	147	2474	0.35±0.01	95±1.0
1992 Oct 31	48927	255	1769	12.53±0.09	-34±1.0
1992 Nov 4	48930	259	4217	14.64±0.06	-30±0.6
1992 Nov 6	48932	261	2843	17.72±0.08	-28±1.0
1992 Dec 6	48963	291	2240	34.0±0.1	-21±0.6
1992 Dec 7	48964	292	683	30.6±0.2	-23±0.8
1993 Apr 28	49106	434	2884	82.5±0.2	-0.2±0.5
1993 Jul 14	49183	511	2294	79.1±0.2	5.4±0.5
1993 Oct 23	49283	612	6980	4.43±0.03	-40±1.0
1993 Nov 4	49295	624	3830	1.61±0.02	-49± 0.02
1993 Nov 15	49307	635	4724	0.64±0.01	-51±0.02
1993 Nov 27	49318	647	3915	0.32±0.01	-54±0.03
1993 Nov 28	49319	648	1784	0.31±0.02	-54±0.06
1993 Nov 29	49321	649	789	0.28±0.01	-48±0.1
1993 Dec 2	49323	652	3863	0.23±0.01	-49±0.04
1993 Dec 3	49324	653	6642	0.22±0.01	-47±0.05

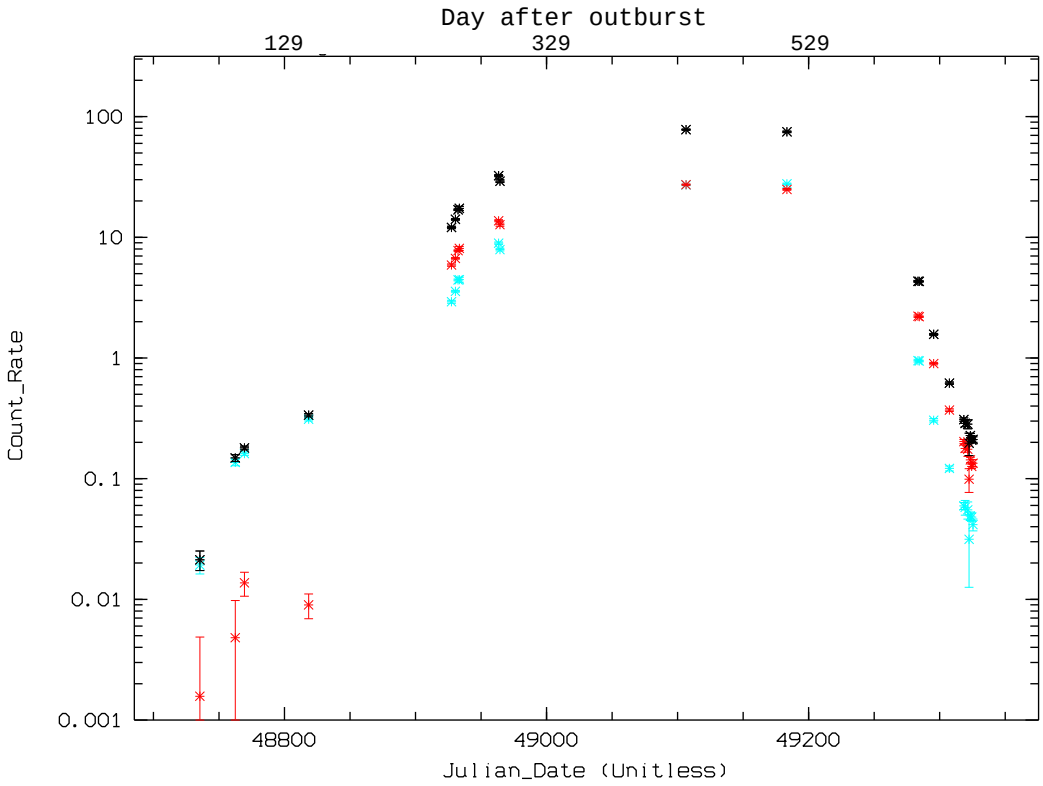

Figure 3.3: X-ray light curve of V1974 Cyg. Black points are the observed *counts* s^{-1} in the total ROSAT/PSPC band (0.1-2.4 keV). Red points plot the soft X-ray light curve (0.1-0.4 keV) while the blue ones show the count rate in the hard band (0.5-2.4 keV).

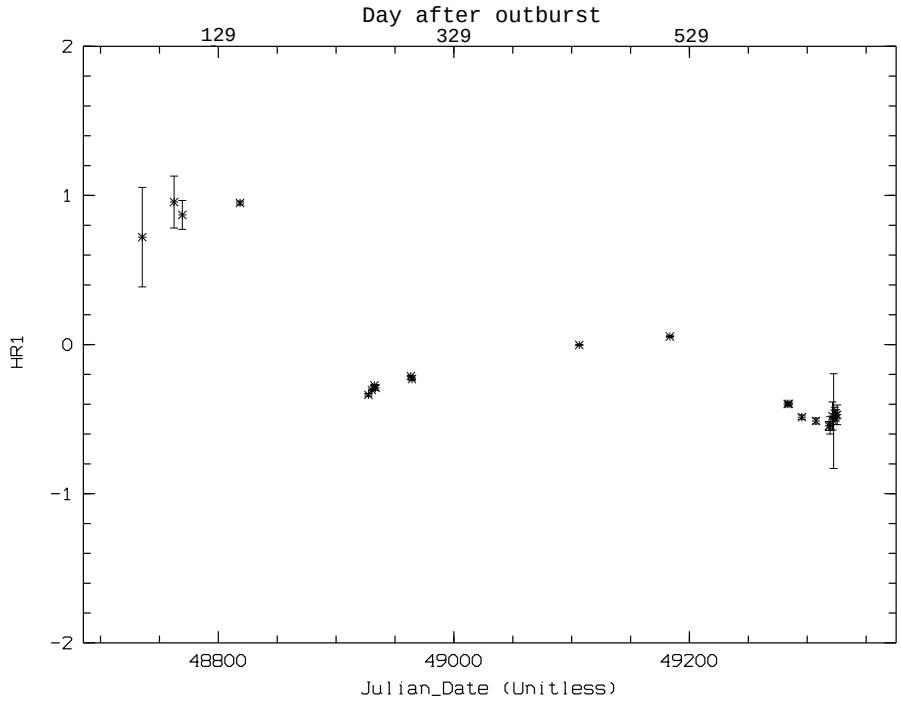

Figure 3.4: Time evolution of hardness ratio HR1.

To further examine the evolution, figure 3.4 shows the hardness ratio HR1, defined as

$$HR1 = \frac{C_h - C_s}{C_h + C_s}$$

Once again, it is clear that the spectral distribution of the X-ray flux is different in the rise phase than during the plateau and decline phases. For the first observations, HR1 has a value close to one, indicating that the spectrum is hard and there is little emission in the soft band. But for the remaining observations, the hardness ratio falls down to negative values similar to those found for Supersoft X-ray Sources (Greiner et al.(1996), Hasinger (1994), Kahabka et al. (1994)).

3.4.3 Spectral evolution

The differences in the soft and hard light curves, and the behaviour of the hardness ratio HR1 indicate that the spectral energy distribution is changing with time. The observational data are thus expected to be fitted with different spectral models in the different phases.

3.4.3.1 Rise phase

During the rise phase, the count rate is very low and any model can fit the data. Krautter et al.(1996) fitted the spectra with an absorbed thermal bremsstrahlung, corresponding to the emission generated in the expanding shell. We have reproduced that analysis, attempting to fit the spectra with blackbody models and with a thermal bremsstrahlung (see figure 3.5 and tables 3.4 and 3.5). The spectra for several days during the rise phase show an increase of the soft band, while small changes are detected in the shape of the hard end of the thermal emission. This evolution suggests that the change in the count rate is due to a decreasing column density rather than an increasing soft X-ray flux. To study this

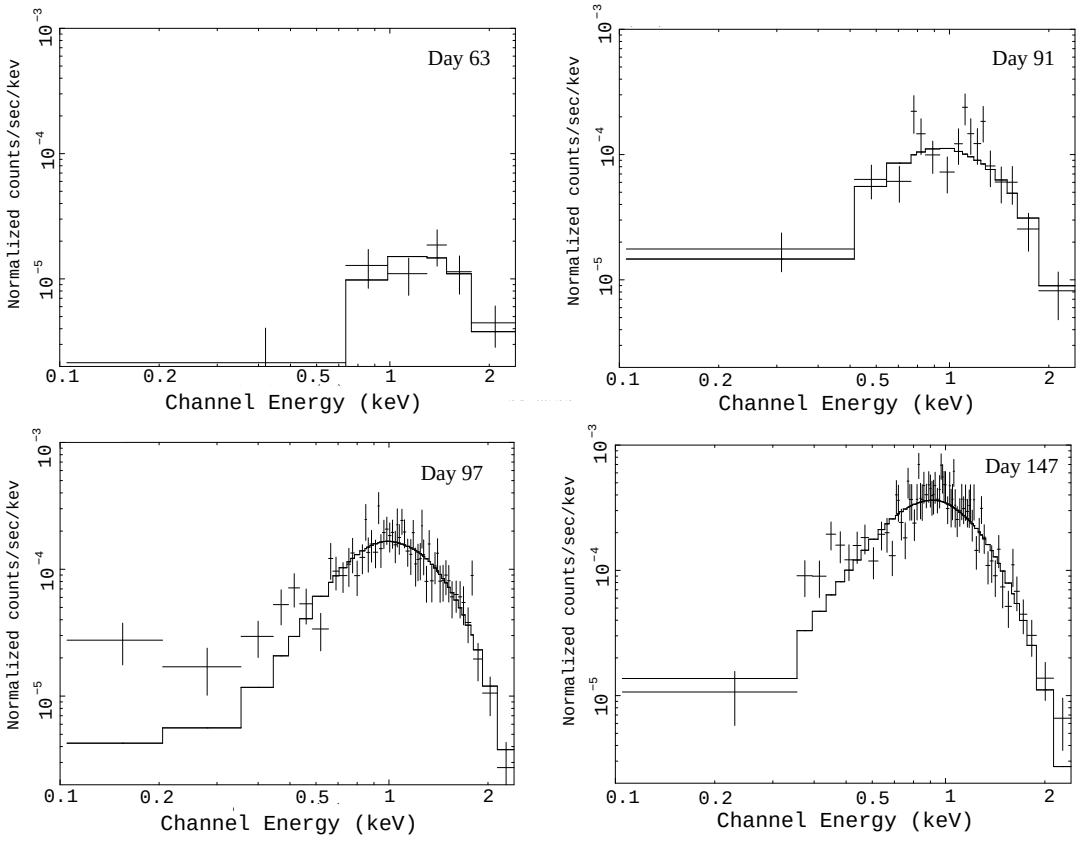

Figure 3.5: Spectra on days 63, 91, 97 and 147 fitted with a thermal bremsstrahlung model.

Table 3.4: Parameters of a blackbody model fitted during the rise phase.

Day	N_h $(\times 10^{21} cm^{-2})$	$K_{bbdy}^{(1)}$ $(\times 10^{-5})$	kT_{eff} (eV)	Flux$^{(2)}$ $(\times 10^{-12} erg\ cm^{-2} s^{-1})$	χ^2_ν
91	0.30(±0.4)	2.2 (±0.5)	355(±75)	1.6	1.26
97	2.35(±1.6)	4.5 (±2)	270(±60)	1.8	1.11
147	2.15(±1.4)	10 (±7)	200(±40)	3.2	1.38

(1) Normalization constant of the model in XSPEC, $K_{bbdy} = \frac{L_{39}}{D_{10}^2}$, with L_{39} being the source luminosity in units of $10^{39} erg\, s^{-1}$ and D_{10} the distance to the source in units of 10 kpc.

(2) Absorbed X-ray flux in the range 0.1-2.4 keV.

Table 3.5: Parameters of a thermal bremsstrahlung model for the rise phase.

Day	N_h $(\times 10^{21} cm^{-2})$	$K_{br}^{(1)}$ $(\times 10^{-2})$	kT_{br} (keV)	Flux$^{(2)}$ $(\times 10^{-12} erg\ cm^{-2} s^{-1})$	χ^2_ν
91	1.0 (±0.7)	0.17 (±0.08)	2.3 (±5)	1.7	1.33
97	4.6 (±0.5)	1.2 (±0.8)	0.5 (±0.2)	1.8	1.12
147	4.1(±0.4)	5.8 (±4.6)	0.3 (±0.1)	3.2	1.08

(1) Normalization constant, $K_{br} = 3.01 \times 10^{-15} \frac{EM}{4\pi D^2}$, where D is the distance to the source in cm and $EM = \int n_e n_i dV$ is the emission measure (n_e, n_i are the electron and ion densities in cm^{-3} and the integration is over the emitting volume).

(2) Absorbed X-ray flux in the range 0.1-2.4 keV.

possibility, data were fitted with a thermal bremsstrahlung with constant temperature and luminosity, and photoelectric absorption with variable hydrogen column density N_H. Table 3.6 and figure 3.6 show the time evolution of N_H. As found by Krautter et al.(1996), the column density decreases with time during the rise phase and reaches a stable value after day 200. This picture of the rise phase was confirmed by Shore et al.(1996), who developed a model consisting of a white dwarf atmosphere continuum plus a uniform-density isothermal slab to simulate the turn-on of the soft X-ray component.

3.4.3.2 Plateau and decline phases

The spectra of the observations from day 255 to the end is softer than during the rise phase, as indicated by the hardness ratio HR1 (see figure 3.4). No single analytic model is able to fit the observed spectra. When fitted with a blackbody or a thermal bremsstrahlung, the data show always an excess in the hard tail of the spectrum (for energies above ~1 keV). Krautter et al.(1996) attempted to fit the spectra of the plateau phase with a two component model: a soft blackbody, with effective temperatures between 19 and 26 eV, and

Table 3.6: Evolution of the column density during the rise phase, for variable absorption with a constant thermal bremsstrahlung model.

Day	N_h $(10^{21}$ cm$^{-2})$	χ^2_ν
63	14.6 - 29.0	1.46
91	6.1 - 8.8	1.71
97	6.4 - 7.5	1.17
147	3.7 - 4.3	1.34

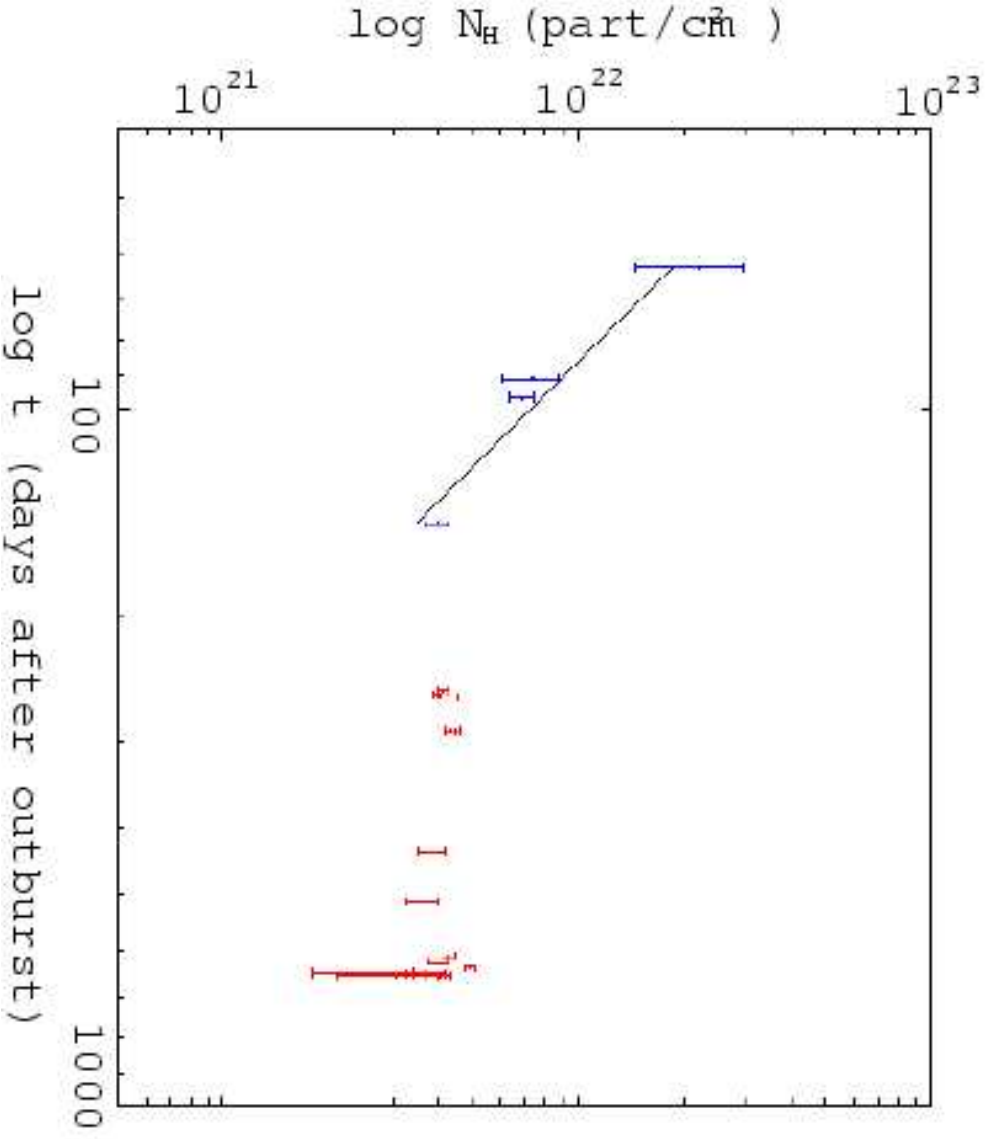

Figure 3.6: Evolution of the column density. The straight line plots the t^{-2} evolution.

Table 3.7: Spectral fit parameters for a blackbody+thermal bremsstrahlung model during the plateau and decline phases. Ranges correspond to 1-σ error.

Day	N_h $\times 10^{21}$ cm^{-2}	$K_{bbdy}^{(1)}$ $\times 10^4$	kT_{eff} eV	$K_{br}^{(2)}$ $\times 10^{-3}$	kT_{br} keV	Flux$^{(3)}$ $\times 10^{-10}$ $erg\ cm^{-2}s^{-1}$	χ^2_ν
255	4.0-4.3	6-8	19.4-20.8	30-260	0.20-0.45	6.07	1.78
259	3.9-4.1	6-9	20.5-21.5	30-100	0.30-0.40	7.44	2.70
261	4.0-4.1	8-20	20.7-21.5	3000-20000	0.50-0.35	9.01	2.67
291	4.2-4.6	19-31	20.0-21.4	100-400	0.40-1.30	16.9	5.36
292	4.2-4.5	11-23	20.1-21.6	$<2\times10^5$	0.20-1.50	15.3	2.81
434	3.5-4.2	0.4-3.4	24.8-29.5	< 10	$< 10^4$	32.0	12.43
511	3.3-4.0	0.1-0.7	27.1-31.8	<10	$<10^4$	30.7	10.03
612	4.1-4.5	5-9	18.4-20.8	<10	$<10^4$	2.27	3.01
624	3.8-4.3	0.7-1.3	18.2-20.6	100-300	0.30-0.80	0.79	1.39
635	3.8-4.1	1-7	17.2-21.0	$<2\times10^4$	0.20-0.40	0.29	1.71
647	1.8-3.4	10-70	17.5-23.4	1.1-2.5	0.15-0.25	0.13	1.61
648	3.3-4.2	20-45	17.5-29.4	<1	0.20-0.60	0.12	1.65
649	3.4-3.7	18-38	16.0-30.0	<1	0.25-0.70	0.13	1.27
652	2.1-4.0	0.01-0.08	18.0-27.5	0.1-1.5	0.15-0.30	0.10	1.33
653	3.7-4.4	0.15-0.23	15.5-20.5	0.1-1.2	0.15-0.25	0.08	1.55

(1) Normalization constant of the model in XSPEC, $K_{bbdy} = \frac{L_{39}}{D_{10}^2}$, with L_{39} being the source luminosity in units of $10^{39} erg\ s^{-1}$ and D_{10} the distance to the source in units of 10 kpc.

(2) Normalization constant for the thermal bremsstrahlung, $K_{br} = 3.01 \times 10^{-15} \frac{EM}{4\pi D^2}$, where D is the distance to the source in cm and $EM = \int n_e n_i dV$ is the emission measure (n_e, n_i are the electron and ion densities in cm^{-3} and the integration is over the emitting volume).

(3) Absorbed X-ray flux in the range 0.1-2.4 keV.

a thermal bremsstrahlung for the hard tail. We have revisited this analysis of the plateau phase (figure 3.7). As found by Krautter et al.(1996) and listed in table 3.7, the best fits with this model give reasonable column densities and effective temperatures. Nevertheless, the normalization constant for the blackbody implies completely unrealistic bolometric luminosities. Assuming a distance of 2.45 kpc, a normalization constant for the blackbody of $10^3 - 10^5$ implies a luminosity in the range $10^{40} - 10^{43} erg\ s^{-1}$, several hundreds or even thousand times the Eddington limit for a $1 M_\odot$ white dwarf. In addition, for the days with the highest flux, this model results inadequate and no acceptable fits can be obtained. The need for more detailed models for this phase is evident. Nevertheless, some conclusions regarding the spectral evolution can be extracted. The effective temperature is found to increase from day 255 to maximum values on days 434 and 511. Because of the lack of observations from day 292 to day 434 (due to observational constrains of the satellite) it is not possible to follow in detail the rise evolution. For the same reason, it was not possible to obtain observations during the whole decrease of flux and effective temperature, from the maximum on days 434-511 to the final of the decline phase (days 612-653), when the effective temperatures dropped to values of $\sim 20\ eV$ again.

Since the white dwarf envelope is strongly enhanced in heavy elements due to mixing of the accreted material with the degenerate core, the opacities of the white dwarf envelope deviate the outcoming soft X-ray emission from the blackbody model. The need of hot

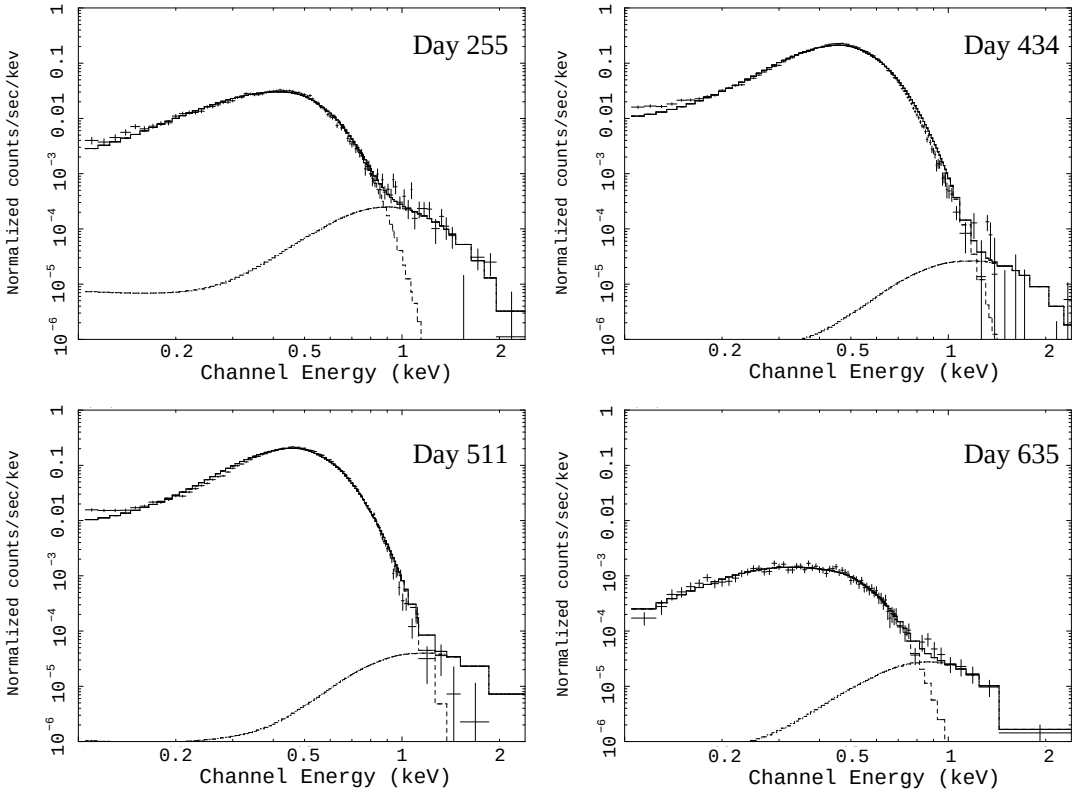

Figure 3.7: ROSAT/PSPC spectra for days 255, 434, 511 and 635. The fitted model is the addition of a blackbody and a thermal bremsstrahlung.

Table 3.8: Spectral fit parameters for ONe enhanced white dwarf atmosphere models during the plateau and decline phases (results from Balman et al.(1998)). Ranges correspond to 3-σ error.

Day	N_H $10^{21} cm^{-2}$	K_{atmos} (1) 10^{-25}	$R_{photos}^{2.45kpc}$ (2) $10^9 cm$	kT_{eff} eV	Flux (3) $10^{-7} erg\, cm^{-2} s^{-1}$	χ^2_ν
255	2.0-2.2	0.6-2.4	1.8-3.7	34.3-38.3	1.2-3.4	1.9
261	1.9-2.1	0.3-0.9	1.3-2.3	38.4-41.8	1.0-1.9	3.4
291	2.0-2.2	0.4-0.8	1.5-2.1	41.2-44.3	1.5-2.3	6.7
434	2.0-2.2	0.32-0.36	1.3-1.4	49.4-49.7	2.0-2.2	20.0
511	2.0-2.2	0.22-0.26	1.1-1.2	50.6-51.0	1.6-1.7	12.0
612	2.1-2.5	>0.18	>1.0	<38.4	>0.4	2.5
624	2.1-2.5	>0.18	>1.0	<34.4	>0.3	1.0
635	1.9-2.3	>0.18	>1.0	<33.5	>0.2	1.0
653	2.0-2.4	>0.18	>1.0	<32.9	>0.1	1.0

(1) Normalization constant of the white dwarf atmosphere model; $K_{at} = (R/D)^2$, where R and D are the photospheric radius and the distance to the source in cm.

(2) Photospheric radius assuming a distance of 2.45 kpc.

(3) Unabsorbed soft X-ray flux between 0.1 and 2.4 keV.

white dwarf atmosphere models for the interpretation of ROSAT observations of classical novae was already pointed out by MacDonald & Vennes (1991), who developed hydrostatic LTE atmosphere models for the X-ray emission of hot white dwarfs (see Appendix E). Balman et al.(1998) used those models to fit V1974 Cyg X-ray spectra during the plateau phase. Two series of models were used, with representative compositions of CO and ONe white dwarf atmospheres. As a result of the absorption edges at hard energies, white dwarf atmosphere models radiate a larger fraction of the total energy in a softer band than the blackbody models at the same effective temperature. This causes the fits with blackbody models to underestimate the effective temperature of the remnant. Table 3.8 summarizes Balman et al.(1998) results of the fit of the soft component of V1974 Cyg with ONe enhanced white dwarf atmosphere models, which fitted the observations better than CO enhanced models. These results will be used in next section for comparison with the white dwarf envelope models of chapter 2.

The soft component of the ROSAT V1974 Cyg spectra can be interpreted as the emission of the hydrogen burning layer on top of the white dwarf. After the nova event, the left H-rich matter remained on thermonuclear combustion. The expansion of the ejected material caused the column density to decrease (as found during the rise phase) and the photosphere to shrink to smaller radii. As the envelope became optically thinner, the observed emission came from deeper and hotter layers. The resulting spectrum became harder and evolved to higher effective temperatures. Once the envelope had become thin to X-rays, the nova reached the plateau phase.

ROSAT observations alone indicate that for V1974 Cyg, this plateau phase lasted between 8 and 15 months, starting between day 147 and day 255, and finishing between the last X-ray observation during the plateau (day 511 after outburst) or shortly before the next ROSAT pointing on day 612. Nevertheless, the cessation of the X-ray emission was confirmed by the UV observations performed by the International Ultraviolet Explorer (IUE) and the Hubble Space Telescope. Shore et al.(1996) found that, ~500 days after discovery, the ejecta reached a maximum ionization and started to recombine, indicating

that the central X-ray ionizing source was turning off and starting to cool down.

During the decline phase, the column density remains constant while the effective temperature decreases. The decreasing flux is then consistent with a cooling of the shell source rather than a change in the absorption.

3.4.4 V1974 Cyg soft component and white dwarf envelope models

The fits of the ROSAT data with white dwarf atmosphere models performed by Balman et al.(1998) give as a result a best-fit effective temperature and a normalization constant, $K_{at} = (R/D)^2$ (where R is the photospheric radius in km and D is the distance in units of 10 kpc), for each observation, as listed in table 3.8. For the determination of the luminosity (or what is equivalent, the photospheric radius) to be compared with our envelope models, a distance of 2.45±0.75 kpc (corresponding to the range 1.7-3.2 kpc) has been assumed.

Balman et al.(1998) results on the soft component of V1974 Cyg have been compared to our steady hydrogen burning white dwarf envelope models. In figures 3.8-3.11, the 3σ contours of the spectral parameters found by Balman et al.(1998) are over-plotted to the photospheric radius - effective temperature results from our ONe envelope models. For each model, the lower panels show the corresponding envelope mass with the time intervals (in days) for the quasi-static evolution. The comparison has been performed with the ONe models alone, since V1974 Cyg is known to have exploded on an ONe white dwarf. Evolution of CO50 models is very similar to that of ONe50 models (see section 2.6) and thus we do not expect that the results obtained from the comparison with observations are sensitive to the CO or ONe enhancements of the envelope models.

The contours of the plateau phase lay in the region of the stable branch, and are compatible with the soft X-ray emission of V1974 Cyg evolving along the high quasi-constant luminosity branch of our steady hydrogen burning envelope models. The large uncertainty in the distance makes an analysis based on the photospheric radius rather unreliable. But the evolution of the effective temperature alone restricts the possible models that can explain the observational results to very few.

Maximum effective temperature

The first distance independent parameter to compare observations and envelope models is the maximum effective temperature. According to Balman et al.(1998), the maximum effective temperature observed by ROSAT was ∼50 eV, on day 511 after outburst (see table 3.8). Nevertheless, the actual maximum of temperature could have been missed by ROSAT. Envelope models on previous chapter show that the maximum effective temperature is reached just before the turn-off. In the case of V1974 Cyg, the X-ray light curve in figure 3.3 indicates that the end of the plateau phase (and therefore the maximum effective temperature) occurred between days 511 and 612 after outburst. In addition, as mentioned before, UV observations indicated that the hot central source had ceased to photoionize the ejecta about day ∼ 530 after outburst, in July 1993 (Shore et al.(1996)). In this case, the actual maximum effective temperature could not have occurred much later than day 511 and thus should be close to the value obtained for that day, ∼50 eV.

Taking into account this limit, some models of figures 3.8-3.11 can be rejected (see also table 2.3 for the maximum effective temperature of each model). For the ONe75 models, any white dwarf more massive than 0.9 $M_\odot$ has an effective temperature higher than observed; only the $0.8 M_\odot$ model has a maximum effective temperature similar to observations, but evolutionary models show that this mass is too small for an ONe white dwarf. For the ONe50 models, only the 0.9 $M_\odot$ white dwarf envelopes have a good maximum

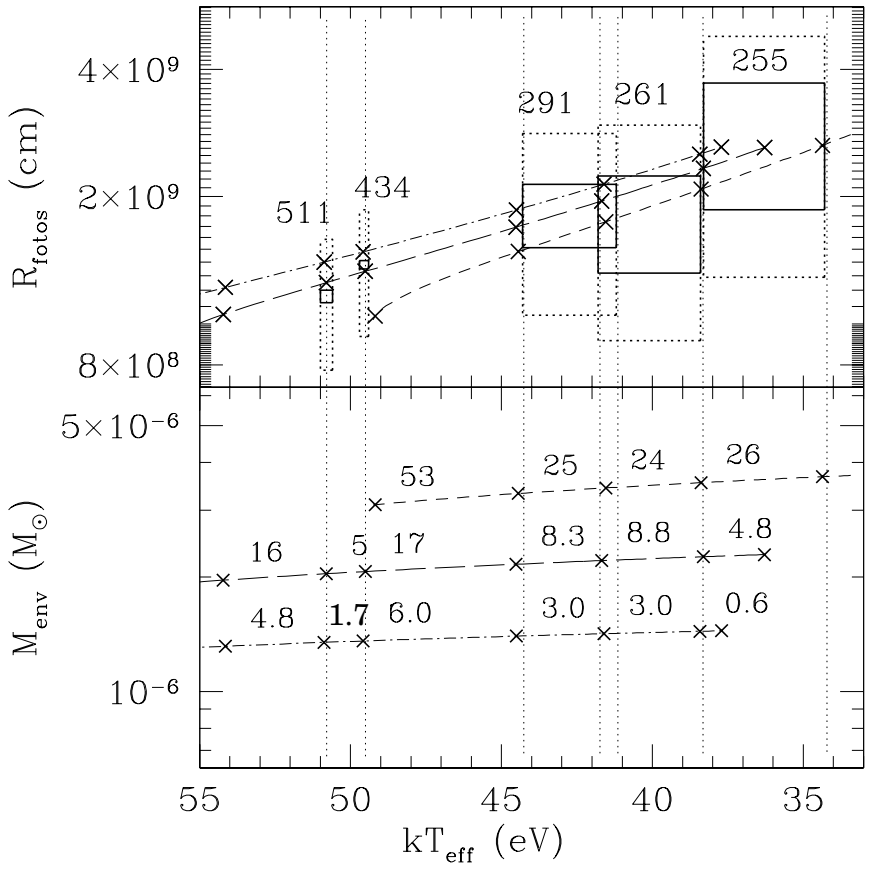

Figure 3.8: Results for V1974 Cyg obtained by Balman et al.(1998) in the $R_{photos}-kT_{eff}$ plane compared to ONe75 white dwarf envelope models.

Upper panel: 3σ confidence contours obtained by Balman et al.(1998) for white dwarf atmosphere models fitting ROSAT/PSPC observations of V1974 Cyg during the X-ray luminosity plateau phase on the photospheric radius - effective temperature plane. Contours in solid line indicate results for a distance of 2.45 *kpc*, while contours in dotted line correspond to results with all the uncertainty in the distance, 1.7-3.2 *kpc*. Numbers indicate the day of ROSAT observation after outburst. Envelope models are plotted for $0.8M_{\odot}$ (short-dashed line), $0.9M_{\odot}$ (long-dashed) and $1.0M_{\odot}$ (short dash - dot). Thin vertical dotted lines are orientative for comparison with the envelope mass in the lower panel.

Lower panel: Envelope masses for the models plotted in the upper panel. Numbers between ticks indicate the time in days needed for the envelope to evolve due to pure hydrogen burning (as in figures 2.31-2.35).

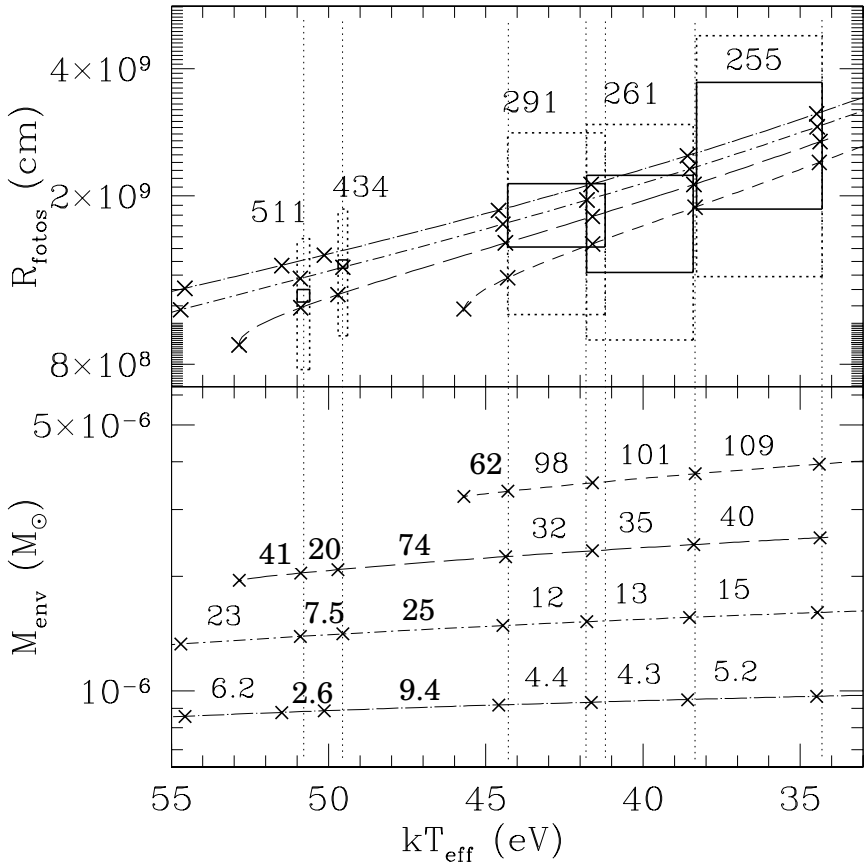

Figure 3.9: Results for V1974 Cyg obtained by Balman et al.(1998) in the $R_{photos} - kT_{eff}$ plane compared to ONe50 white dwarf envelope models, with $0.8 M_{\odot}$ (short-dashed line), $0.9 M_{\odot}$ (long-dashed), $1.0 M_{\odot}$ (short dash - dot) and $1.1 M_{\odot}$ (long dash - dot).

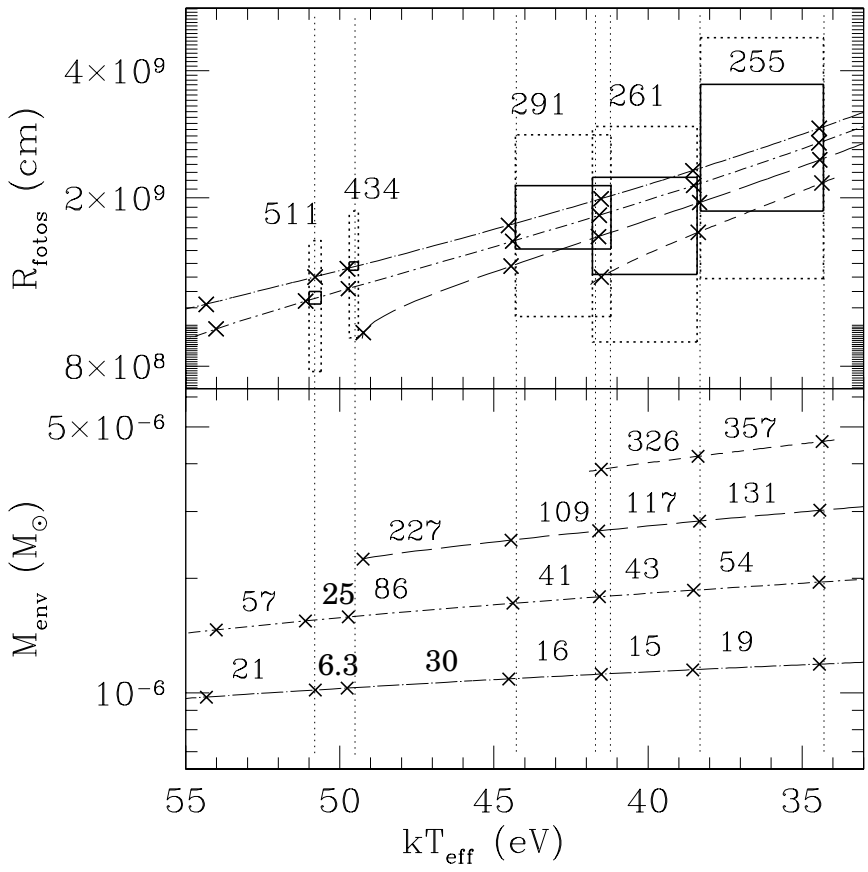

Figure 3.10: Results for V1974 Cyg obtained by Balman et al.(1998) in the $R_{photos} - kT_{eff}$ plane compared to ONe25 white dwarf envelope models, with $0.8M_{\odot}$ (short-dashed line), $0.9M_{\odot}$ (long-dashed), $1.0M_{\odot}$ (short dash - dot) and $1.1M_{\odot}$ (long dash - dot).

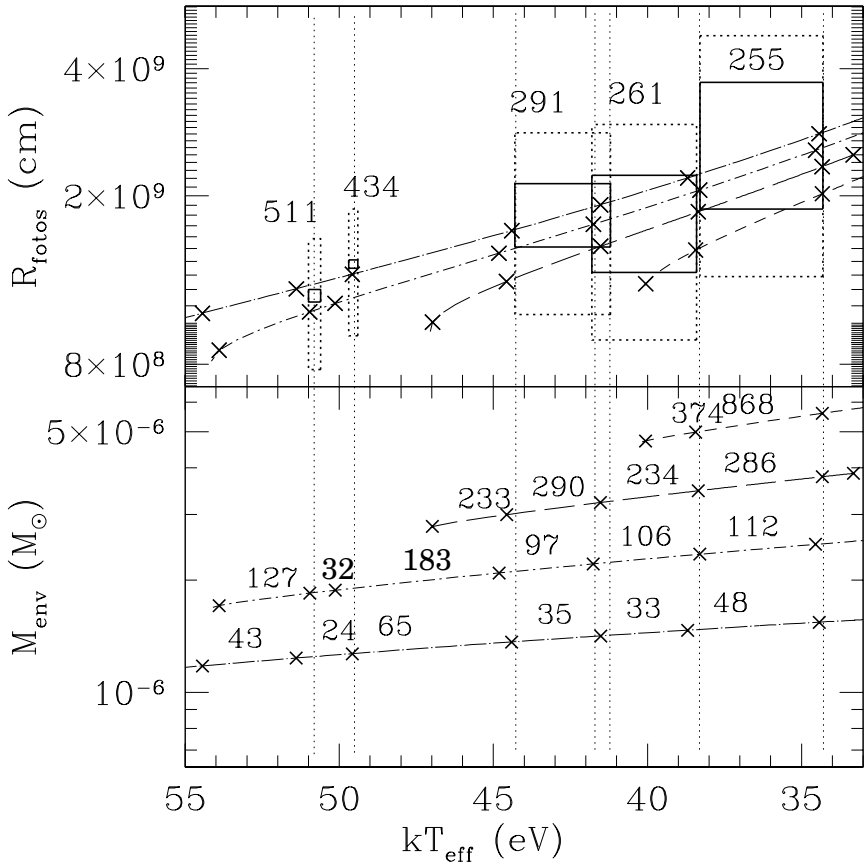

Figure 3.11: Results for V1974 Cyg obtained by Balman et al.(1998) in the $R_{photos} - kT_{eff}$ plane compared to ONe09 white dwarf envelope models, with $0.8M_{\odot}$ (short-dashed line), $0.9M_{\odot}$ (long-dashed), $1.0M_{\odot}$ (short dash - dot) and $1.1M_{\odot}$ (long dash - dot).

Table 3.9: Time in days elapsed between ROSAT observations and simulated by the envelope models.

Observation dates (days after outburst)	Days between observations	ONe75 $0.8M_\odot$	ONe50 $0.9M_\odot$	ONe25 $1.0M_\odot$	ONe09 $1.1M_\odot$
255-511	256	-	161-201	195-249	157-205
255-434	179	102-128	141-181	170-224	133-181
255-261	6	<50	<75	<97	<81
261-291	30	<49	<67	<84	<68
291-434	143	53-78	74-106	86-127	65-100
434-511	77	-	20	25	24
255-291	36	24-75	35-107	43-138	33-116
261-434	173	78-102	106-141	127-170	100-133

effective temperature (53 eV). In the case of the ONe25 composition, this requirement is fullfiled by a white dwarf of mass between 0.9 $M_\odot$ (kT_{max} =49 eV) and 1.0 $M_\odot$ (kT_{max} =56 eV). Finally, the ONe09 models have the observed maximum effective temperature also for white dwarf masses 0.9-1.0 $M_\odot$ (with kT_{max} 47 and 54 eV respectively). Nevertheless, this last model is too hydrogen-rich and metal-poor compared to abundances determinations for V1974 Cyg ejecta (Austin et al.(1996)) and for novae envelopes in general.

Evolution of the effective temperature

The comparison of the observed and simulated evolution establishes some more constrains on the possible models for V1974 Cyg. For each composition, only one of the white dwarf masses considered has an evolution of the envelope with time-scales comparable to observations. Interestingly enough, the cases with evolution times compatible with observations are among the ones with maximum effective temperature similar to the maximum effective temperature derived from observations, except for the ONe09 models: $0.8M_\odot$ for ONe75, $0.9M_\odot$ for ONe50, $1.0M_\odot$ for ONe25 and $1.1M_\odot$ for ONe09. The days elapsed between ROSAT observations during the plateau phase and the corresponding time intervals from selected envelope models are listed in table 3.9 for an easier comparison. The time elapsed until day 511 should be taken with care: if the maximum effective temperature and the following turn-off occurred close to that day, several factors can affect the evolution. It is possible that the X-ray observation took place shortly after reaching the maximum effective temperature, and not before. In this case, if the envelope was already starting to cool down, with still a high effective temperature, the luminosity and effective radius would have been slightly smaller than the corresponding values for the source still being on, which is fully compatible with contours in figures 3.8-3.11. The time estimated from the envelope models for the evolution along the high luminosity branch would then be smaller than observed, and this is indeed the case for the envelope models with time-scales more similar to observations, as can be seen in figures 3.8-3.11 and in table 3.9. In addition, as mentioned in section 2.5, the stationary approximation is not accurate in the vicinity of the maximum effective temperature. Therefore, in our comparison mainly the evolution until day 434 is taken into account.

The ONe75 envelope models (with $X_H = 0.18$) can not, in any case, simulate the observed evolution. Even for the smallest white dwarf ($0.8M_\odot$, which is too small for an ONe white dwarf), the total time elapsed between effective temperatures corresponding to days 255 and 434 is 102-128 days, smaller than the 179 days elapsed between observations. For the ONe50 $0.9M_\odot$ white dwarf envelope models, the time-scale for the same interval of

effective temperatures (141-181 days) is much closer to the observed one. ONe25 $1.0M_{\odot}$ models simulate the most similar evolution, even for the total time interval (from day 255 to 511). Finally, the ONe09 $1.1M_{\odot}$ models is compatible with the observed time evolution, but the maximum effective temperature in this model is higher than observed. An ONe09 models with a smaller white dwarf has a lower maximum effective temperature, but then the simulated evolution is slower, as can be seen in figure 3.11. In summary, the best candidates for a white dwarf envelope model for V1974 Cyg are the ONe50 0.9 $M_{\odot}$ and the ONe25 $1.0M_{\odot}$ models.

3.4.5 Discussion

Ejected mass

If the evolution during the rise phase is assumed to be entirely due to a change in the absorption, it is possible to obtain an estimation for the mass in the expanding shell. Assuming the material ejected by the nova explosion to form a spherical shell expanding at constant velocity v and with radius $R = vt$, it is possible to have a simple model for the evolution of the column density during the rise phase. The column density N_H is defined as the number of hydrogen atoms per volume, n, integrated along the path from the source to the observer, R. Assuming a constant hydrogen volume density, $N_H = nR$. The hydrogen mass density of the shell will evolve in time like

$$\rho = \frac{M_H}{\frac{4}{3}\pi v^3 t^3}$$

where M_H is the ejected hydrogen mass. Assuming a constant density, the column density of hydrogen is $N_H = \frac{\rho R}{m_H} = \frac{\rho v t}{m_H}$, where m_H is the mass of the hydrogen atom. Then, column density at time t will be

$$N_H = \frac{M_H}{\frac{4}{3}\pi m_H v^2 t^2} \tag{3.1}$$

Krautter et al.(1996) performed this exercise for V1974 Cyg and, taking the column density on day 100 ($6 \times 10^{21} cm^{-2}$) and an expansion velocity of 1500 km/s (Shore et al.(1994)), obtained an hydrogen ejected mass of $3 \times 10^{-5} M_{\odot}$.

In figure 3.6 we have fitted the time evolution of the column density during the rise phase with a power law $\left(N_H = At^B\right)$. The best fit (with a correlation coefficient of 0.97) corresponds to a power law of exponent $B = -2.0(\pm 0.3)$ and $A = 7.04 \times 10^{25} day^2 cm^{-2}$, where $A = \frac{M_H}{\frac{4}{3}\pi m_H v^2}$. The value obtained for the exponent confirms the model of evolution for the column density as $N_H \sim t^{-2}$. From the value of A and the expansion velocity of the ejecta, it is possible to obtain an estimation of the ejected mass using (3.1).

Chochol et al.(1997) used optical and UV spectroscopy, as well as HST and radio imaging observations of V1974 Cyg, to derive a kinematic model of the nova shell. They found two components of the envelope: a fast outer low-mass envelope (spherical except for the polar regions) and a slow inner massive envelope (consisting of an equatorial ring and polar blobs). Both components of the envelope were found to be accelerated by the nova wind (also consisting of spherical and polar components), but the velocities experimented little change during the X-ray rise phase. Chochol et al.(1997) determined that any expanding component of the main inner envelope should have a true velocity in the range between 800 and 1100 $km\,s^{-1}$ before day 200. With this range of velocities, equation 3.1 indicates that the ejected mass of hydrogen in the main envelope would be

$1.2 \times 10^{-5} M_\odot < M_H < 2.2 \times 10^{-5} M_\odot$. From optical and UV observations, the hydrogen mass fraction on the ejecta was found to be 0.1-0.4 (90% confidence range, Austin et al.(1996)), leading to a total ejected mass of $3 \times 10^{-5} M_\odot < M_{ej} < 2.2 \times 10^{-4} M_\odot$. This is a rough estimation. Since the velocity taken is that of the main slow envelope, the determined range of masses is only representative for the inner envelope. In addition, this mass can not be taken with confidence as a lower limit because the inner envelope has been assumed to be spherical and with constant density, while Chochol et al.(1997) found it to be shaped as a slow ring and faster polar blobs.

If the envelope as a whole is considered to expand with the velocity of the outer envelope, an upper limit for the ejected mass can be established. Chochol et al.(1997) found that the expansion velocity of the spherical component of the outer envelope increased from 800 $km\,s^{-1}$shortly after outburst to 1700 $km\,s^{-1}$ on day 45, and remained constant at this value for the next 10 days. Assuming this velocity to be constant during the X-ray rise phase, the ejected mass of hydrogen would be $M_H = 5.3 \times 10^{-5} M_\odot$; taking the minimum hydrogen mass fraction in the confidence range found by Austin et al.(1996), the upper limit for the ejected mass would be $M_{ej} < 5.3 \times 10^{-4} M_\odot$.

It is worth noticing that the range of masses found here is not far from other independent determinations. Shore et al.(1993) derived from UV observations that the ejected mass exceeded $10^{-4} Y^{-1/2} M_\odot$, where Y is the helium abundance enhancement factor. From their abundances determinations (Y=4.4), Austin et al.(1996) used this expression to find an ejected mass of $\sim 5 \times 10^{-5} M_\odot$. More precisely, Austin et al.(1996) abundances translate into an ejected mass in the range (4.8-19.1)$\times 10^{-5} M_\odot$ (a similar result was found by Hayward et al.(1996) from mid-infrared observations).

White dwarf mass

The comparison of ROSAT observations with the envelope models indicates that V1974 Cyg probably occurred on a 0.9-1.1$M_\odot$ white dwarf, on which accreted solar matter mixed by less than 50% with the ONe core. Comparison with independent determinations of the composition and white dwarf mass of V1974 Cyg will help to decide between these possibilities.

The ONe50 envelope models, with X=0.35, are favored by independent determinations of the hydrogen mass fraction in the V1974 Cyg ejecta. Austin et al.(1996) determined the hydrogen mass fraction to be 0.1-0.4 (90% confidence range) from optical and ultraviolet observations. And independently, using mid-infrared spectroscopy, Hayward et al.(1996) determined X=0.30. The problem with the ONe50 models is that the corresponding white dwarf mass lays at the lower end of the range derived in previous works and is rather small for an ONe white dwarf.

Balman et al.(1998) used the mass-luminosity relation by Iben & Tutukov (1996) to find a white dwarf mass in the range 0.9-1.4$M_\odot$. Krautter et al.(1996) estimated the star mass to be 1.25$M_\odot$ using the mass-luminosity relation by Iben (1982) (which is equal to our core-mass luminosity relation for ONe09 models, equation 2.17). He took the nova luminosity early in the outburst, $5 \times 10^4 L_\odot$, determined by Shore et al.(1993, 1994), who assumed a distance of 3 *kpc*. Nevertheless, later distance determinations situated the nova closer and thus the luminosity would be smaller, indicating a less massive white dwarf. In addition, core mass determinations from Krautter et al.(1996) and Balman et al.(1998) are not independent from ours, since they relied on a core-mass luminosity relation derived from white dwarf envelope models with abundances unrealistic for a nova envelope. The relations they were using were obtained for envelopes with X_H=0.64, equivalent to our ONe09 models, which can simulate the observed evolution with a 1.1$M_\odot$ core.

The white dwarf mass derived from comparison with our envelope models (0.9-1.1 $M_{\odot}$) is therefore compatible with previous determinations. But the smallest white dwarf masses of our envelope models would be in contradiction with the minimum mass for ONe degenerate cores. Recent evolutionary calculations by Gil-Pons et al.(2003) have shown that final ONe white dwarfs in cataclysmic variables have typical masses between 1.0 and $1.1 M_{\odot}$.

A small value of the white dwarf mass alleviates the general disagreement regarding the observed ejected mass and the predictions from hydrodynamic nova models. As mentioned above, the evolution of the hydrogen column during the rise phase of the X-ray emission indicates that the ejected mass from V1974 Cyg is $3 \times 10^{-5} M_{\odot} < M_{ej} < 2.2 \times 10^{-4} M_{\odot}$, in agreement with other independent determinations. Hydrodynamic nova models by José & Hernanz (1998) predict smaller ejected masses for novae on massive ONe white dwarfs (as small as $3.4 \times 10^{-6} M_{\odot}$ for a $1.35 M_{\odot}$ white dwarf with a 75% degree of mixing). But for a nova with $1.0 M_{\odot}$ and 50% mixing, as indicated by our envelope models, the predicted ejected mass is $4.7 \times 10^{-5} M_{\odot}$ (model ONe1 of José & Hernanz (1998)), which lays in the lower end of the range derived from observations. Similar or even smaller ejected mass are predicted by other hydrodynamic models (Prialnik & Kovetz (1995),Starrfield et al.(1998)).

José & Hernanz (1998) models also indicate that the ejected matter represents between 60% and 80% of the accreted envelope. Taking into account the accreted envelope needed to trigger the outburst and the ejected mass for each model in José & Hernanz (1998), a post-outburst white dwarf envelope of $1.7 \times 10^{-5} M_{\odot}$ is derived for a $1.0 M_{\odot}$ white dwarf with 50% mixing (model ONe1), and as small as $10^{-6} M_{\odot}$ for a $1.35 M_{\odot}$ white dwarf with the same mixing (model ONe6). For our ONe25 and ONe50 models on $0.9 M_{\odot}$ or $1.0 M_{\odot}$ white dwarfs, envelopes masses are $\sim (2-3) \times 10^{-6} M_{\odot}$, an order of magnitude smaller than predicted by the hydrodynamic models for these white dwarf masses.

Taking into account the accreted envelope needed to trigger the outburst, the fact that only a fraction of it is ejected and the masses for stable envelopes with steady hydrogen burning, it is clear that some mass loss mechanism must have been present after the outburst and ejected an extra $\sim 10^{-5} \mathrm{M}_{\odot}$. Since the evolution of V1974 Cyg from day 255 after outburst to the end of the constant bolometric luminosity phase can be explained as a result of pure hydrogen burning, without an extra mass loss, the mechanism responsible for the reduction of the post-outburst envelope mass probably acted during the first eight months after the outburst.

3.4.6 A Photoionization Model for Nova Cyg 1992

Krautter et al.(1996) suggested that X-ray emission corresponding to the thermal bremsstrahlung component of their model arose within the expanding shell, from the interaction of the nova wind with some density condensations. Images of old nova shells and high-resolution HST images of V1974 Cyg show bright knots that can be interpreted as these density inhomogeneities (Paresce et al.(1995)). A similar mechanism is responsible for the X-ray emission from hot OB stars, but despite the similarities, Krautter et al.(1996) found some important differences, as the ratio L_x/L_{bol}, which in V1974 Cyg is at least 2 orders of magnitude higher than for OB stars. Balman et al.(1998) used a two component model to analyze ROSAT observations: a white dwarf atmosphere for the soft range of spectrum, and a Raymond-Smith model (which simulated the thermal plasma spectrum from a hot, diffuse gas including line emissions from several elements, Raymond & Smith (1977)) to explain the hard component associated to the shock-heated ejecta.

Another possible contribution to the X-ray spectrum of V1974 Cyg is the photoionization of the ejected nebula. Optical and UV observations show that the ejected shell is

Table 3.10: Abundances of V1974 Cyg taken for the XSTAR models.

Element	Mass fraction	$\frac{(N_i)_{Nova}}{(N_i)_{\odot}}$
H	0.17	0.671
He	0.29	3.378
C	0.051	47.24
N	0.073	220.5
O	0.248	82.61
Ne	0.103	168.0
Mg	0.0198	84.66
Si	0.024	95.05
S	0.011	63.30
Ar	0.0014	41.81
Ca	0.00071	30.55
Fe	0.0069	15.44
Ni	0.000616	23.30

indeed photoionized by a central hot source, and photoionization models have been successfully used to interpret the observed optical and UV spectra (see Austin et al.(1996) for V1974 Cyg).

The photoionization code XSTAR (Kallman (2002)) calculates the spectrum generated by a spherical nebula photoionized by a central X-ray source. To analyze ROSAT observations of V1974 Cyg and see the possible contribution of the photoionization to its X-ray spectrum, a grid of 144 spectral models for reasonable conditions has been generated using XSTAR2XSPEC (see appendix G). For this task, it has been necessary to previously find which are these reasonable conditions and which is the chemical composition of the photoionized material from optical observations (Austin et al.(1996)).

3.4.6.1 Properties of V1974 Cyg from optical spectrophotometry

Optical spectrophotometry of V1974 Cygni was obtained by Austin et al.(1996) from day 4 to 450 after visual maximum. They used CLOUDY photoionization code to model the emission-line fluxes relative to Hβ. CLOUDY was used to generate $\approx 10^4$ trial models, which where fitted to spectra for different days. We have used the results of their best fit to derive the input parameters for XSTAR.

Chemical composition and physical conditions of the gas shell

Table 24 in Austin et al.(1996) gives their best fit for V1974 Cyg mass fractions. Table 3.10 shows the abundances used in all XSTAR models in this work, both in mass fraction (from Austin et al.(1996)) and in number abundance relative to solar, as required for XSTAR input.

The gas temperature is computed by XSTAR in each iteration. Only a first guess is needed for calculating the thermal equilibrium value. Density or pressure are kept constant along the different shells. If density is kept constant, the given value for pressure is taken as an initial guess (and vice versa).

Austin et al.(1996) obtained T_e and n_e from some line ratios. By applying the full equations of statistical equilibrium to two [O III] emission-line ratios, they obtained solutions ranging from high-density low-temperature regime ($T_e \approx 8000K, n_e \approx 10^8 cm^{-3}$)

Table 3.11: Parameters of grid of spectra generated with XSTAR2XSPEC.
The minimum density is the lowest value allowed in the program input.

	Minimum	Maximum	Type of interpolation
Effective temperature kT_{eff} (eV)	20	50	linear
Density n (cm^{-3})	1	10^{12}	logarithmic
Column density N_H (cm^{-2})	10^{14}	10^{24}	logarithmic
Thickness ΔR(cm)*	10^{14}	10^{12}	-
Ionization parameter $log\,\xi$	-4	7	linear
Inner radius R_{in} (cm)*	3.16×10^{9}	10^{21}	-

* The thickness and the inner radius are not parameters of the model but values derived from the other parameters, and are not interpolated in XSTAR2XSPEC.

to low-density high-temperature regime ($T_e \approx 20000K, n_e \approx 3 \times 10^6 cm^{-3}$). Other line diagnostics showed values around 10^4K for electron temperature for days 300, 400 and 500, and $n_e \approx 10^7 cm^{-3}$.

An approximate value for pressure can be derived assuming the gas to be ideal. For the ranges of temperature and density found by Austin et al.(1996), $3 \times 10^{-6} < P_{id} < 3 \times 10^{-4} (dyn/cm^2)$.

Central continuum source and shell geometry

In this case, the central continuum ionizing source is the layer of nuclear burning material on top of the white dwarf. The spectrum is of the blackbody type, with its effective temperature being one of the fitting parameters of the model. The range of temperatures considered by Austin et al.(1996) was 21-43 eV.

During the first 40 days of the outburst, the light curve resulting from the integration of ultraviolet and optical observations of V1974 Cygni was approximately constant at $\approx 10^{-7} erg\,s^{-1}\,cm^{-2}$ (Shore et al.(1994)). Austin et al.(1996), taking into account that the X-ray light curve indicated that the nuclear burning on the white dwarf was still active (Krautter et al.(1996)), assumed this bolometric flux to be constant through the first 500 days. For the distance derived in the same work (2.8 ± 0.7 kpc), the luminosity is $5 \times 10^{37} erg\,s^{-1} < L < 1.4 \times 10^{38} erg\,s^{-1}$. This luminosity is near the Eddington limit for a $1M_\odot$ star ($1.5\times10^{38} erg\ s^{-1}$) and is the expected luminosity resulting of the thermonuclear burning on the surface of the white dwarf.

The nebular region of ionized gas is assumed to be a spherical shell in all cases. The covering factor for the best fit of Austin et al.(1996) on day 450 was 0.43. This value has been fixed in the XSTAR models.

Taking into account the observed expansion velocities, Austin et al.(1996) estimated the inner radius of the shell to be between $1.9 \times 10^{15}$and $5.6 \times 10^{15} cm$, and Paresce et al.(1995) estimated the shell thickness for day 467 to be about $6 \times 10^{13} cm$. These will be the fitting (therefore the studied) parameters in XSTAR, as well as effective temperature of the ionizing blackbody and the gas density.

3.4.6.2 XSTAR table models

To compare ROSAT/PSPC spectra of classical novae with photoionization models, a grid of 135 XSTAR spectral models has been generated. In all cases, the spectrum of the central source has been assumed to be a blackbody and the density is kept constant along

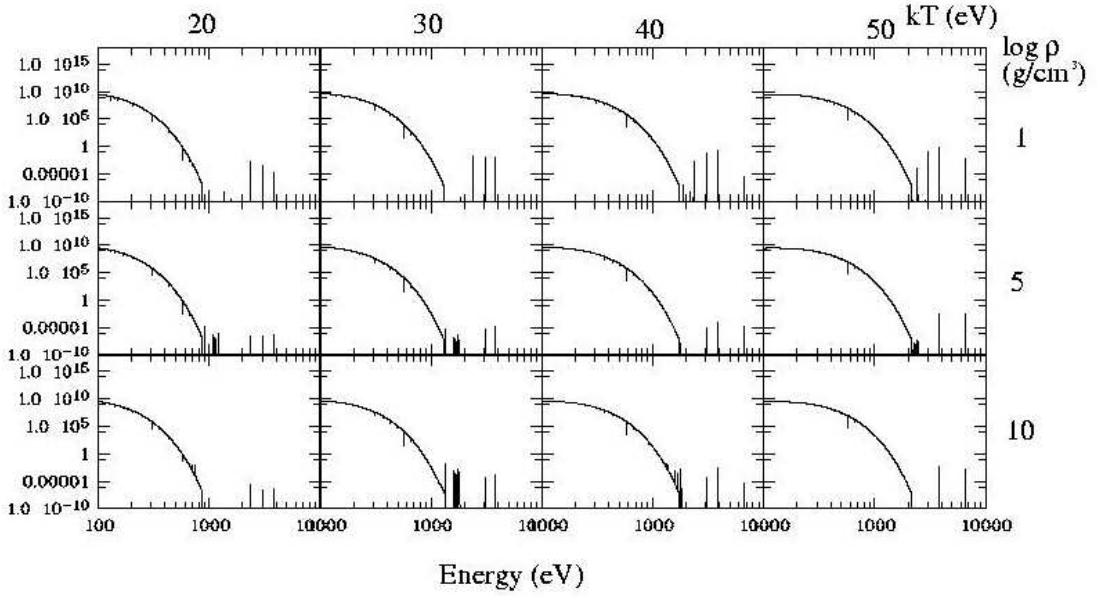

Figure 3.12: Spectrum of the photoionized gas shell for different gas densities and effective temperatures of the incident blackbody.
These spectra result from the addition of the transmitted plus the emitted spectra. All spectra have been calculated to see the effects of different density and effective temperature, keeping constant values of column density ($N_H = 10^{18} cm^{-2}$) and ionization parameter ($log\,\xi = 3$), which implies a same geometry thorough the rows, but changing from row to row (shell thickness and inner radius decrease for increasing values of density, since $N_H = n\,\Delta R$ and $\xi = L/nR^2$); with abundances from table 3.10 (XSTAR 2.1h).

the integration of the gas shell, with an initial guess for the gas temperature of 10^4K. The blackbody luminosity is 10^{38}erg s^{-1}for all models, since it is not expected to change much except during the decline phase, and every free parameter increases the time of computation and fitting. The chemical composition of the gas in the shell has been fixed to best-fit values obtained in Austin et al.(1996) (see table 3.10).

Four parameters are allowed to vary within the grid (and will also be the fitting parameters for spectral analysis): the hydrogen number density of the gas $n\,(cm^{-3})$, the effective temperature of the ionizing blackbody spectrum $kT_{eff}\,(eV)$, the inner radius $R_{in}\,(cm)$ and the thickness of the shell $\Delta R\,(cm)$ (both controlled in XSTAR2XSPEC by the column density $N_H = n\,\Delta R$ and the ionization parameter ξ at the innermost radius, $\xi = L/nR^2$). The ranges considered for each parameter are listed in table 3.11.

The output of the program consists of the transmitted and the emitted spectrum. The actual spectrum an observer would see is the addition of the two components. Figure 3.12 shows some spectra of the model grid generated with XSTAR 2.1h (see appendix D for more details on the XSTAR code).

3.4.6.3 Fitting ROSAT/PSPC V1974 Cyg spectra with XSTAR photoionization models

In our first analyses of V1974 Cyg ROSAT spectra with photoionization models, where the XSTAR versions available at that moment were used (XSTAR 2.0 and XSTAR 2.1d), we showed that photoionization was able to explain the whole ROSAT/PSPC X-ray spectra of classical novae. In those models, some recombination emission features appeared at energies higher than 1 keV, which could account for the hard X-ray emission detected by ROSAT in the spectra of V1974 Cyg, V838 Her and V351 Pup. But some of those recombination

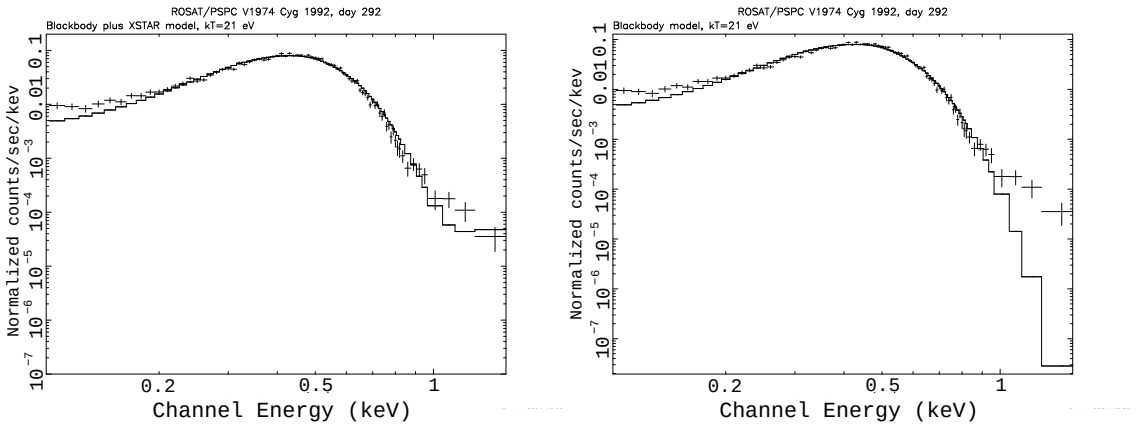

Figure 3.13: ROSAT/PSPC spectrum of V1974 Cyg on day 292 after outburst. **Left**: The solid line shows the XSTAR model fitted to the data, with galactic $N_H = 4.2 \times 10^{21} cm^{-2}$, *kT=21 eV*, $n = 10^8 cm^{-3}$, column density $10^{16} cm^{-2}$, $log\xi = -1$, $\chi^2_\nu = 3$. **Right**: ROSAT/PSPC spectrum for the same observation fitted with a single absorbed blackbody model ($N_H = 4.2 \times 10^{21} cm^{-2}$, *kT=21 eV).*

features were due to an error on the XSTAR code (Tim Kallman, private communication- see appendix D). This was corrected in the June 2002 version of the program, XSTAR 2.1h.

In this chapter, XSTAR version 2.1h has been used to simulate the photoionization of a gas shell with the typical conditions for a classical nova. After the correction of the errors in the code, some emission features still contribute to the hard end of the main soft X-ray component of the spectrum (assumed to be a blackbody), but the contribution to the hard band is not so significant as shown in our previous analyses based on older XSTAR versions.

The XSPEC package (Arnaud et al.(1996)) has been used to fit ROSAT/PSPC spectra with the XSTAR photoionization table models. We have compared the photoionization spectra simulated with the present XSTAR version to ROSAT/PSPC spectra of V1974 Cyg, V838 Her and V351 Pup. The new photoionization models can fit the hard X-ray excess observed in the case of V1974 Cyg (see figures 3.13), but cannot explain the hard X-ray emission from V838 Her and V351 Pup.

The photoionization of the ejected gas shell modulates and changes the spectrum of the soft X-ray emission from the central white dwarf, but does not contribute significantly to the hard X-ray band. Although this emission can not account for the hard X-ray emission observed by ROSAT in some cases, it adds some emission features at the hard end of the soft X-ray band that can explain the hard X-ray excess detected from V1974 Cyg. With the spectral resolution of ROSAT/PSPC it is not possible to distinguish the contribution of the photoionized shell from other models, but further studies with photoionization codes and using white dwarf atmosphere models as central ionizing source spectrum may be crucial to understand the high-resolution data.

3.5 Other classical novae with supersoft X-ray emission

3.5.1 Nova Muscae 1983 (GQ Mus)

Nova Mus 1983 (GQ Mus) was discovered in outburst on 1983 January 18.14 UT (Liller (1983)) and was classified as a CO nova (Livio & Truran (1994), Starrfield et al.(1998)). It was the only nova detected during the ROSAT All-Sky Survey (RASS) out of the 26 classical novae observed less than 10 years after outburst. It was also the first classical nova to be detected in X-rays by EXOSAT close to the outburst, 463 days after the optical discovery (Ögelman et al.(1984), Ögelman et al.(1987)). Given the poor spectral resolution of those early EXOSAT observations, the physical origin of the X-ray emission could not be determined. Assuming a fixed interstellar column density of $(2-4)\times10^{21}cm^{-2}$ (corresponding to $E_{B-V}=0.45\pm0.15$, Krautter et al.(1984)), the observed X-ray flux was compatible either with a thermal bremsstrahlung associated to the shocked expanding shell (with 10^7K and $10^{35}erg\,s^{-1}$), or with a $\sim 3.5\times10^5K$ ($\sim 30eV$) blackbody at $10^{37}erg\,s^{-1}$ (Ögelman et al.(1984)). The second possibility was confirmed by optical and ultraviolet (with IUE) observations during the nebular phase in the period 1984-1988 (Krautter & Williams (1989)). Spectroscopic observations showed a steady increase of the ionization of the ejected envelope over a period of four years after the outburst. The high ionization was found to be caused by the photoionization from a hot source at $T\geq 4\times10^5K\,(34.5eV)$ with the temperature increasing with time. Moreover, assuming a distance of 4.8 *kpc* and $E_{B-V}=0.4$ (Krautter et al.(1984)), the UV flux at 1500A in 1988 January was compatible with the emission of a 5×10^5K blackbody with a radius of 2.8×10^9cm (which implies $L=3.5\times10^{38}erg\,s^{-1}$), in good agreement with a hot white dwarf properties. The picture of the shell photoionized by a hot central source was also confirmed by Morisset & Péquignot (1996a), who used a detailed photoionization model to study the nova shell between 1984 and 1990. They determined uniquely the central source to have $L=(1.75\pm0.2)\left(\frac{v_{exp}}{630km\,s^{-1}}\right)^2\times10^{38}\,erg\,s^{-1}$ (where v_{exp} is the mean expansion velocity of the shell) and $T_{eff}=(2.65\pm0.2)\times10^5K$ ($kT=22.8\pm1.7eV$) for day 441, regardless of the precise values of the distance or the reddening correction.

Pointed observations with PSPC in February 1992 showed a very soft spectrum similar to those of the supersoft X-ray sources of the Large Magellanic Cloud (Ögelman et al.(1993)). In the first spectral analysis with an absorbed blackbody model, Ögelman et al.(1993) found that the best fit (with $\chi^2=18.5$ for 16 degrees of freedom) was obtained for a column density $3.7\times10^{21}cm^{-2}$ and an effective temperature of $2.7\times10^5K\,(23\,eV)$. These properties agreed with a burning layer of H-rich material on the surface of the white dwarf after the outburst, but the bolometric luminosity of the best-fit model was a factor 100 too large for the Eddington limit of a $1M_\odot$ white dwarf at 4.7 ± 1.5 *kpc* (Ögelman et al.(1993)). The 2σ and 3σ confidence contours included lower fluxes and higher temperatures. Fixing the bolometric luminosity to the Eddington value and taking into account the whole range in the distance determination, the effective temperature was limited to $3.3-3.6\times10^5K\,(28.8-30.9\,eV)$. But a reanalysis of the ROSAT observations using white dwarf atmosphere models showed once more the inappropriateness of simple blackbody models for the X-ray spectra of hot white dwarfs. Balman et al.(2001) fitted the observed spectra with atmosphere models of MacDonald & Vennes (1991) for CO white dwarfs, since the nova was known to be enriched in CNO and the $Ne/Ne_\odot$ was low (Livio & Truran (1994), Morisset & Péquignot (1996a)). Balman et al.(2001) determined that in February 1992 the H-burning at the surface of the white dwarf had already ceased. Eleven months after this first pointed observation, ROSAT confirmed that the soft X-ray source of GQ Mus had indeed turned off: in January 1993 the count rate had decreased by a factor

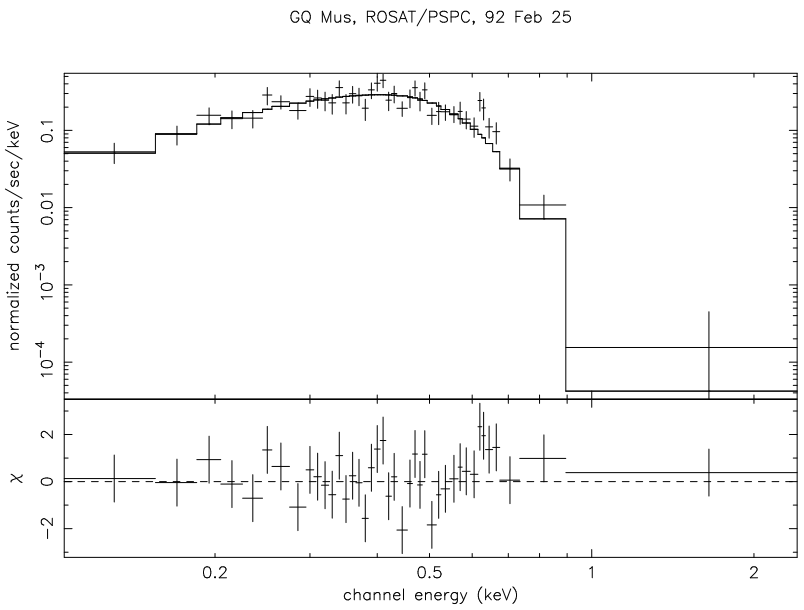

Figure 3.14: ROSAT/PSPC spectrum of GQ Mus on February 1992 and best-fit CO white dwarf atmosphere model ($\chi^2_\nu = 1.06$), obtained with $N_H = 2 \times 10^{21} cm^{-2}$, $T_{eff} = 4.6 \times 10^5 K$ and normalization constant $K_{at} = 4.1 \times 10^7 (K_{at} = (R/D)^2$, where R and D are the photospheric radius -in km- and the distance to the source -in units of 10 kpc-).

17, and it was below the ROSAT/PSPC threshold limit in September 1993, implying a decrease of the count-rate by a factor ≥ 30 (Shanley et al.(1995)). According to Balman et al.(2001), only the RASS observation in August 1991 showed evidence for hydrogen burning, implying an actual duration of ~8 years.

3.5.1.1 Spectral analysis

The observational results obtained for GQ Mus have been compared to our envelope models, as in the case of V1974 Cyg. However, for this nova the atmosphere parameters are only constrained for the first pointed observation (performed in February 1992, day 3320 after outburst). To obtain the true confidence contour for this observation, we have revisited the analysis with white dwarf atmosphere models performed by Balman et al.(2001). The spectrum and best-fit model are shown in figure 3.14. The best-fit model is obtained for $N_H = 2 \times 10^{21} cm^{-2}$ and $T_{eff} = 4.6 \times 10^5 K$, with $\chi^2_\nu = 1.06$ and an absorbed flux (0.1-2.4 keV) of $4.4 \times 10^{-12} erg\, cm^{-2}\, s^{-1}$. The best-fit value for the column density is compatible with the determination by Krautter et al.(1984) ($(2-4) \times 10^{21} cm^{-2}$), but smaller than the average value in the direction of the source, $\sim 4 \times 10^{21} cm^{-2}$ (Dickey & Lockman (1990)). Nevertheless, no acceptable fit is obtained with hydrogen columns larger than $\sim 2 \times 10^{21} cm^{-2}$. We have obtained confidence contours for the absorption versus effective temperature (figure 3.15), and they indicate that only values smaller than $\sim 2.5 \times 10^{21} cm^{-2}$ are compatible with data at 1σ and smaller than $3 \times 10^{21} cm^{-2}$ at 3σ level, always smaller than the average interstellar value. The best possible fit with these upper limits is worse than with $2 \times 10^{21} cm^{-2}$, with $\chi^2_\nu = 1.12$ for $2.5 \times 10^{21} cm^{-2}$, and $\chi^2_\nu = 1.3$ for $3 \times 10^{-2} cm^{-2}$. Confidence contours for the white dwarf atmosphere parameters have been obtained and are shown in figure 3.16; they have also been included in the comparison with models that follows.

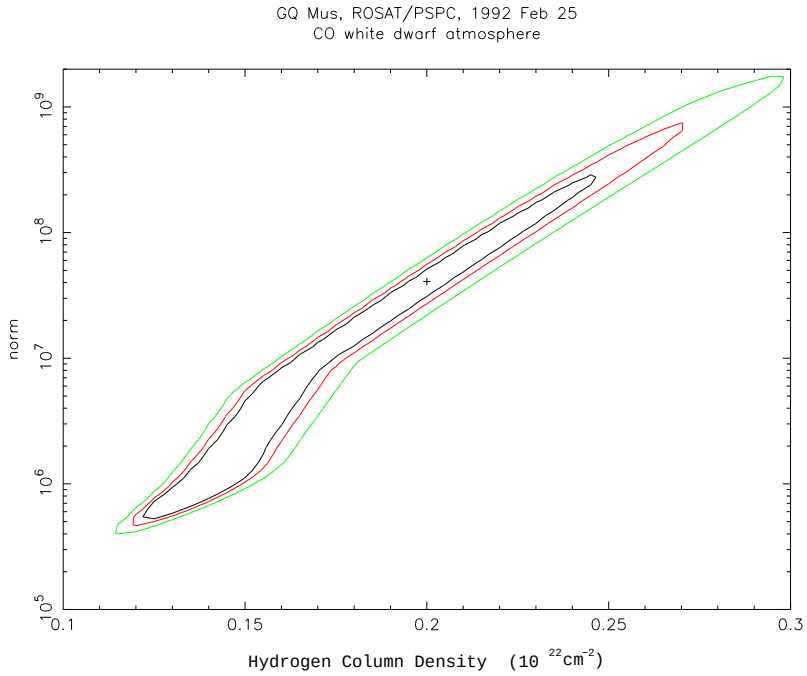

Figure 3.15: Normalization versus hydrogen column density 1σ, 2σ and 3σ confidence contours for ROSAT observation of GQ Mus on February 1992.

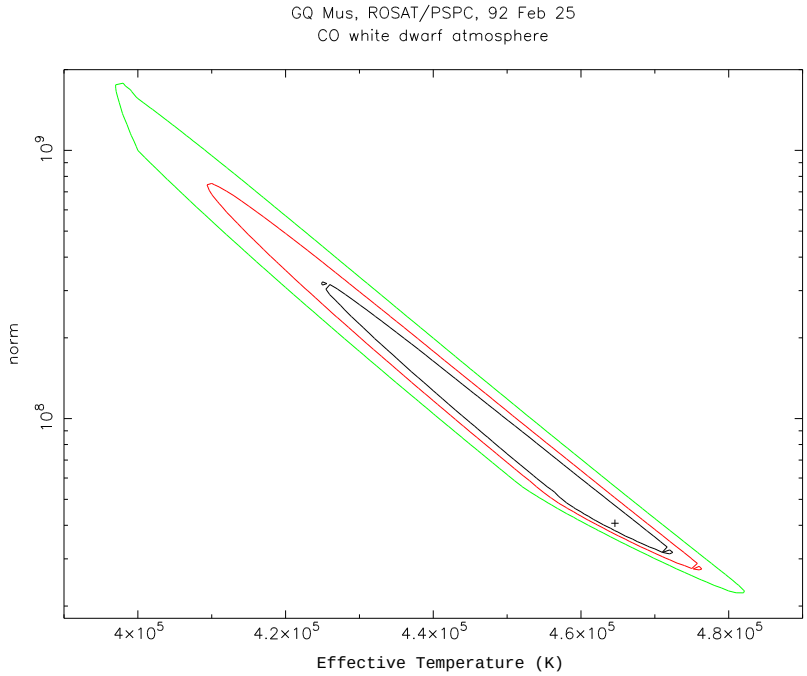

Figure 3.16: Effective temperature and normalization 1σ, 2σ and 3σ confidence contours for ROSAT observation of GQ Mus on February 1992. The normalization constant is $\left(\frac{R_{km}}{D_{10}}\right)^2$, where R_{km} is the source radius in km, and D_{10} is the distance in units of 10 kpc. N_H is fixed to $2 \times 10^{21} cm^{-2}$.

Table 3.12: Summary of optical and X-ray observations of GQ Mus included in the comparison with our envelope models in figure 3.17.

Day after outburst	Observatory	kT_{eff} (eV)	L $(erg\,s^{-1})$	R_{photos} $(10^9 cm)$	References
441	ESO, IUE	23	3×10^{38} (1)	7.1 (2)	Morisset & Péquignot (1996a)
~1800	ESO, IUE	43	3.5×10^{38}	2.8 (2)	Krautter & Williams (1989)
3118	ROSAT	<54		>1.3	Balman et al.(2001)
3322	ROSAT	38-43		1.8-6.3	
3641	ROSAT	<35		>1.8	
3871	ROSAT	<27		>1.8	
4161	ROSAT	<18		>1.8	

(1) Assuming an expansion velocity of 800 km/s (Péquignot et al. (1993)).

(2) Derived from the temperature and luminosity.

3.5.1.2 Comparison with envelope models

In order to compare the observed properties for GQ Mus with our envelope models, figure 3.17 shows the GQ Mus photospheric properties derived from observations over-plotted to the CO50 and I82 models. Both the results obtained by Balman et al.(2001) (see table 3.12) and the contour derived from our reanalysis are shown. Only including the whole distance indetermination in the 3σ confidence contour are the results of February 1992 observation compatible with the smallest white dwarf envelope models. But the only possible compatibility occurs at large photospheric radius and low effective temperature, a configuration unlikely for a nova 3320 days after outburst. As indicated by Balman et al.(2001), by the time of the first ROSAT pointed observation, the hydrogen burning on the white dwarf surface had most probably already ceased. The RASS detection (in August 1991) is compatible with the source still being 'on', with a higher effective temperature. The properties derived for the central source of the ionized nebula by Krautter & Williams (1989) from optical spectroscopic observations 5 years after outburst are also shown in figure 3.17, as well as the results obtained by Morisset & Péquignot (1996a) using a detailed photoionization model for optical observations 441 days after outburst (see also table 3.12). The photospheric properties derived by those works are compatible with the evolution at quasi-constant luminosity, but given the uncertainties in those determinations, no further conclusions can be extracted form the direct comparison with models.

3.5.1.3 Discussion

The relations found in chapter 2 for the luminosity and envelope mass as a function of the white dwarf mass and hydrogen mass fraction can be applied to GQ Mus. Morisset & Péquignot (1996a,b) determined the mass fraction of elements beyond helium in the ejected envelope to be Z=0.23, and for helium Y=0.4. Assuming X=0.37 (=1-Y-Z), and with the luminosity during the hydrogen burning phase $L = (1.75 \pm 0.2) \times 10^{38} erg\,s^{-1} (4.53 \times 10^4 L_\odot$, Morisset & Péquignot (1996a)), the core mass-luminosity relation 2.18 in section 2.6 can be used to derive a white dwarf mass of $1.1 \pm 0.1 M_\odot$, in agreement with previous estimations that indicated a mass of $1.1 - 1.2 M_\odot$ for GQ Mus (Starrfield et al.(1996), Morisset & Péquignot (1996b), Balman et al.(2001)). With $M_{WD} = 1.1 \pm 0.1 M_\odot$, relation 2.20 can now be used to derive an average envelope mass during the hydrogen burning phase $M_{env} \sim 10^{-6} M_\odot$.

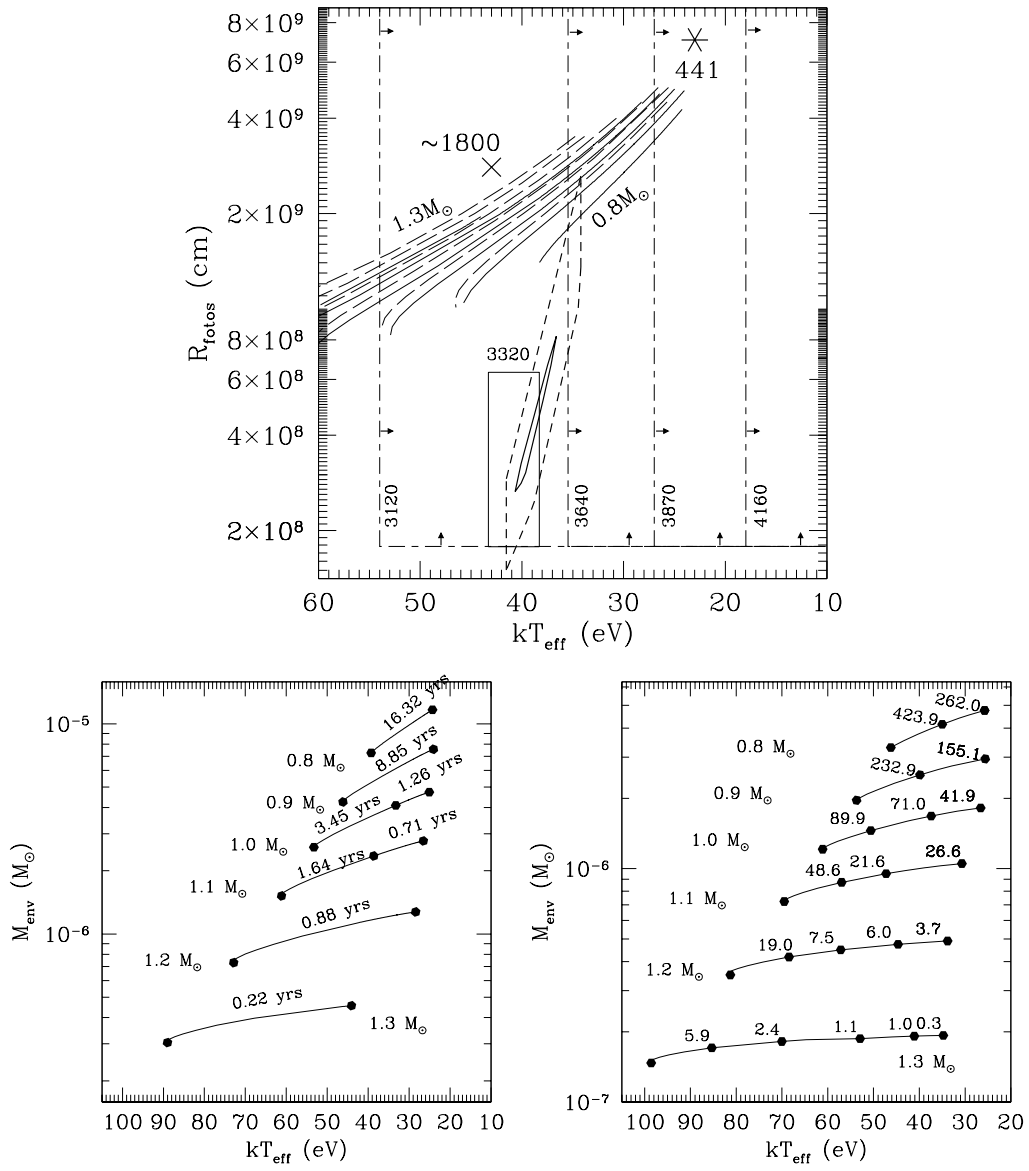

Figure 3.17: Observational results for GQ Mus in the $R_{photos} - kT_{eff}$ plane compared to envelope models.

Upper panel: The 1σ confidence contour obtained in the present work for ROSAT observation on fay 3320 after outburst is shown in thick solid line, assuming a distance of 4.7 *kpc*. The thick dashed line indicates the 3σ confidence contour including the whole distance indetermination 4.7 ± 1.5 *kpc*. The squared contour in solid line corresponds to the 1σ confidence contour for the same observation (day 3320 after outburst) obtained by Balman et al.(2001), for a distance of 4.7 *kpc*; vertical and horizontal long-short dashed lines indicate upper limits for the effective temperature and lower limits for the photospheric radius, respectively, obtained by the same authors for days 3120 (RASS observation), 3640, 3870 and 4160 after outburst. The cross and the star indicate the results obtained by Krautter & Williams (1989) and by Morisset & Péquignot (1996a), respectively. Numbers indicate day of observation after outburst. Stable branches of CO50 (long-dash) and I82 (solid line) white dwarf envelope models are plotted, with core mass increasing from right to left, from $0.8 M_{\odot}$ to $1.3 M_{\odot}$.

Lower panels: envelope masses and time-scales for quasi-static evolution for the envelope models in upper panel (I82 in left panel, with time-scales in years; and CO50 in right panel, with time-scales indicated in days; the same as figures 2.31 and 2.35).

This envelope mass can be compared to the mass consumed to power the X-ray source during the constant bolometric luminosity phase. Accepting that the turn-off occurred between August 1991 and February 1992, GQ Mus had burned hydrogen on the white dwarf surface during ~9 years. With $X_H = 0.37$ and $L = (1.75 \pm 0.2) \times 10^{38} erg\, s^{-1}$(Morisset & Péquignot (1996a)), expression 2.26 for the nuclear time-scale in section 2.6 can be used to determine the envelope mass consumed during the total 9 years to be $(1.4 \pm 0.2) \times 10^{-5} M_\odot$, an order of magnitude larger than the envelope mass estimated above using relations 2.18 and 2.20 from chapter 2. In addition, according to results found in section 2.4, the burnt mass and the average envelope mass are expected to be of the same order of magnitude, and there is no stable white dwarf envelope with this high mass ($\sim 10^{-5} M_\odot$) and small hydrogen fraction.

A possible way out is that the actual mass fraction in the envelope was larger than observed in the ejecta. But as shown by nucleosynthesis models in José & Hernanz (1998), the hydrogen mass fraction in the ejecta is not expected to be much smaller than in the accreted material, and the same applies for the left hydrogen rich envelope. In addition, according to the envelope models in section 2.4, a larger hydrogen fraction would be incompatible with the high observed luminosity. For example, with $X_H = 0.64$ as in I82 models, the envelope mass burnt in 9 years with the observed luminosity ($1.75 \times 10^{38} erg\, s^{-1}$,Morisset & Péquignot (1996a)) would be $8 \times 10^{-6} M_\odot$, which would agree with the envelope masses of the smallest white dwarfs (0.8 and 0.9 $M_\odot$) in section 2.4. The contradiction here is that I82 models with these masses have smaller luminosity than observed for GQ Mus.

Another possibility is that the turn-off time for GQ Mus was shorter than 9 years. The low statistics in the RASS observation (in August 1991) do not allow to determine well enough its spectral parameters. According to Balman et al.(2001), the flux of that first ROSAT observation in 1991 was not well constrained. Assuming that the flux in August 1991 was the same as in February 1992, the spectral analysis showed evidence that the white dwarf temperature was higher than in February 1992. But no further conclusions could be extracted. The RASS data are compatible both with the hydrogen burning still going on, or alternatively, with a white dwarf hotter than in February 1992 but already cooling down. In this case, the last evidence for hydrogen burning would come from the March 1988 optical observation of the ionized nebula (Krautter & Williams (1989)) and the turn-off time of GQ Mus could be as short as 5 years. Assuming this lower limit for the duration of hydrogen burning, the minimum consumed mass would be $(7.6 \pm 0.8) \times 10^{-6} M_\odot$. This is still too large for $1.1 M_\odot$ envelope models with the observed hydrogen mass fraction.

Nevertheless, this envelope mass derived for a 5 years turn-off time is similar to the difference between the accreted and the ejected masses from hydrodynamical models of nova outbursts in José & Hernanz (1998), for $1.0 - 1.15 M_\odot$ CO white dwarfs with degrees of mixing between accreted matter and the degenerate core of 50% and 25% (models CO3 and CO4, respectively). For these models, the predicted hydrogen mass fraction in the ejecta is 0.32 and 0.47, similar to the observed abundances in the shell of GQ Mus. The CO3 and CO4 models predict an ejected mass of $3.9 \times 10^{-5} M_\odot$ and $2.1 \times 10^{-5} M_\odot$ ($1.6 \times 10^{-5} M_\odot$ and $6 \times 10^{-6} M_\odot$ smaller than the accreted envelope). This can also be compared to the estimation of the mass in the ejected shell obtained in Morisset & Péquignot (1996a), $M_{shell} = (12.5 \pm 1.5) \left(\frac{D}{4kpc}\right)^2 \times 10^{3.1(E_{B-V}-0.5)} \times 10^{-5} M_\odot$, which for $E_{B-V} = 0.45$ (Krautter et al.(1984)) and a distance of 4.7 *kpc* would indicate $M_{shell} = (8.5 \pm 1.0) \times 10^{-5} M_\odot$, a factor ~ 2 larger than predicted.

To summarize, the comparison of observations and white dwarf envelope models in this work indicate that GQ Mus probably occurred on a $1.1 \pm 0.1 M_\odot$ white dwarf. Relations obtained in section 2.4 indicate an average envelope mass during the hydrogen burning

phase $M_{env} \sim 10^{-6} M_{\odot}$. X-ray data and optical observations of the ionization nebula in GQ Mus indicate that the turn-off time could be between 5 and 9 years. Given the observed luminosity and hydrogen mass fraction, the envelope mass consumed during the post-outburst ($7.6 \times 10^{-6} M_{\odot}$) is too large compared to the mass of stable envelope models from previous chapter. Hydrodynamical simulations in José & Hernanz (1998) for $1.0 - 1.15 M_{\odot}$ CO white dwarfs with 50% and 25% of mixing, respectively, give hydrogen mass fractions similar to the observed in GQ Mus nebula and predict an ejected mass only a factor 2 smaller than observed.

3.5.2 Nova LMC 1995

Nova LMC 1995, discovered in 1995 March 2 (Liller (1995)), was first observed with the HRI on board ROSAT in September and October 1995, with a count rate of 0.006 $cts\ s^{-1}$, and remained stable until the next observation in September 1996 (with 0.004 $cts\ s^{-1}$). In February 1998, the PSPC instrument was used again during only a week with residual gas, and N LMC 1995 was serendipitously observed during pointed observations of other important LMC sources close to the nova, with a count rate of 0.061 cts s^{-1} (equivalent to 0.008 cts s^{-1}in HRI). Orio & Greiner (1999) fitted successfully this PSPC observation with an LTE atmosphere model by MacDonald & Vennes (1991), for a CO $1.2 M_{\odot}$ white dwarf with luminosity fixed to $4.2 \times 10^4 L_{\odot}$. They obtained a best-fit model with effective temperature around 31 eV ($\sim 3.6 \times 10^5 K$). The spectrum was similar to the other two supersoft novae, but the slow evolution resembled more that of GQ Mus.

The nova was observed again as a luminous supersoft X-ray source with XMM-Newton in 2000 December by Orio et al.(2003). No hard component was present, with no counts above background for energies higher than 0.6 keV. The spectra obtained with EPIC and with RGS were fitted with NLTE atmosphere models. Five sets of different composition were used: cosmic abundances, LMC-like abundances, CNO enhanced by 10, ONeMg enhanced by 10, and enhanced He and C/N ratio.. The best-fit models yielded unreasonable large values for the normalization constant K ($K = \left(\frac{R}{D}\right)^2$, with R being the photospheric radius and D the distance). The best fit with reasonable values for the normalization constant was obtained with the "LMC-like" abundances, and indicated a white dwarf mass of $0.9 M_{\odot}$ and a bolometric luminosity of $2.3 \times 10^{37} erg\ s^{-1}$ for a distance of 51 kpc. According to the authors, a distance of 55 kpc (used by other authors) does not change the main conclusions. With this NLTE atmosphere models, the white dwarf mass is obtained from the surface gravity (which is one of the fitting parameters) and the radius derived from the normalization constant.

3.5.2.1 Comparison with envelope models

In figures 3.18 and 3.19, the results obtained by Orio & Greiner (1999) and Orio et al.(2003) are over-plotted to our ONe09 and I82 envelope models. Other envelope models poorer in hydrogen do not need to be compared with the data, since their time-scales are different enough to reject them. No CO enhanced model has been computed with a hydrogen mass fraction similar to ONe09 and I82 models, but it seems not to be necessary, since ONe50 and CO50 models gave results similar enough as to neglect the differences for the comparison with the present observations. In the X-ray observational results shown in figures 3.18 and 3.19, the whole uncertainty range in effective temperature derived from the fits is taken into account. For day 1100 after outburst, the best fit obtained by Orio & Greiner (1999) from the ROSAT/PSPC observation fitted with LTE atmosphere models is indicated by a square, while the thick line shows the 3σ confidence range for

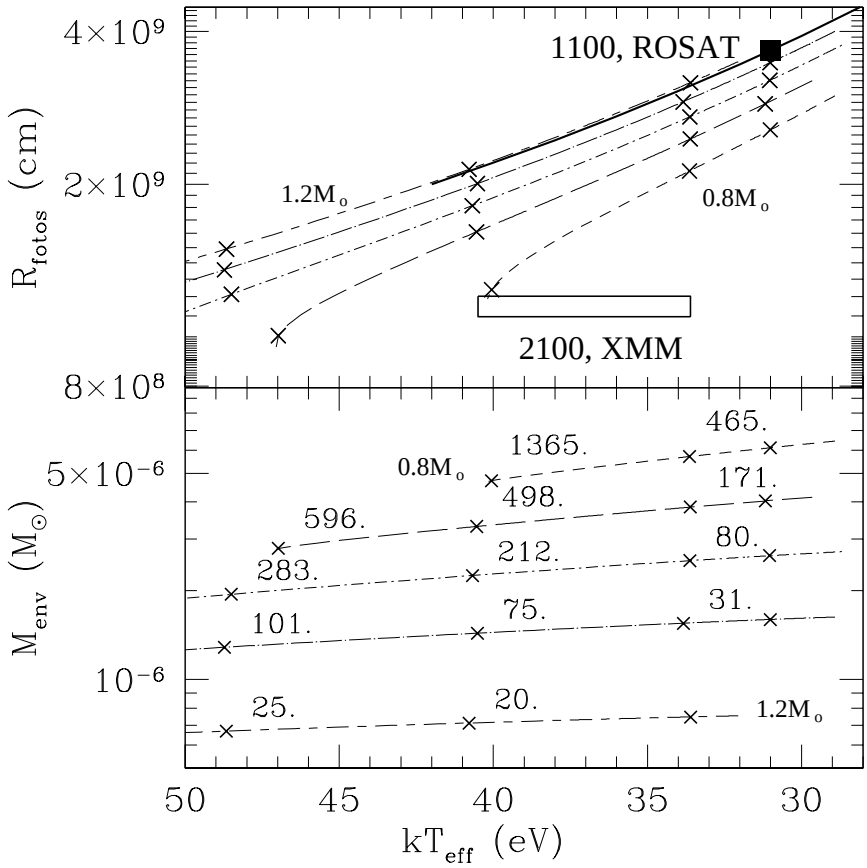

Figure 3.18: Results from X-ray observations of Nova LMC 1995 obtained by Orio & Greiner (1999) and Orio et al.(2003) in the $R_{photos} - kT_{eff}$ plane compared to ONe09 white dwarf envelope models.
Upper panel: Photospheric radius versus effective temperature. Numbers indicate the day of observation after outburst: for day 1100 after outburst, the best fit obtained by Orio & Greiner (1999) from the ROSAT/PSPC observation fitted with LTE atmosphere models is indicated by a square, while the thick line shows the 3σ confidence range for effective temperature. Since luminosity and white dwarf mass is fixed in these models to $4.2{\times}10^{-4}L_{\odot}$ and $1.2M_{\odot}$, the thick line indicates the corresponding photospheric radius. Contour for day 2100 corresponds to the whole range of effective temperatures found by Orio et al.(2003) from XMM-Newton observations fitted with NLTE atmosphere models; the range of photospheric radius is obtained from the normalization constant for the best fit with the distance varying between 51 and 55 *kpc*.
Lower panel: Envelope mass for models plotted in upper panel. Numbers between ticks indicate the time in days needed for the envelope to evolve due to pure hydrogen burning. Envelope models are plotted for $0.8M_{\odot}$ (short-dashed line), $0.9M_{\odot}$ (long-dashed), $1.0M_{\odot}$ (short dash - dot), $1.1M_{\odot}$ (long dash - dot) and $1.2M_{\odot}$ (short dash - long dash).

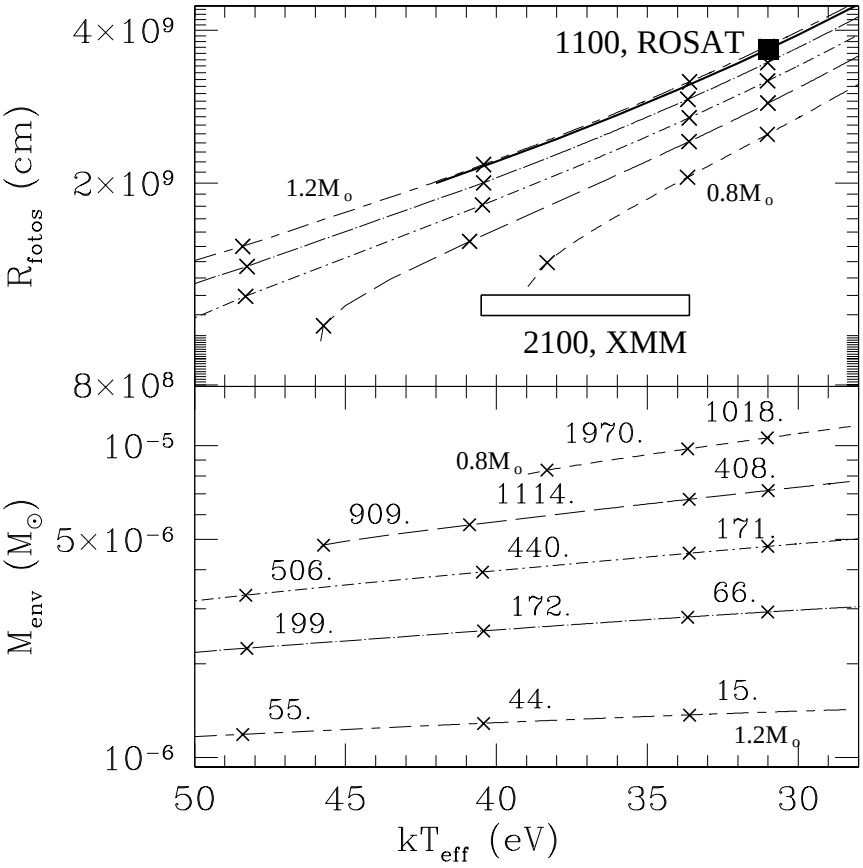

Figure 3.19: Results from X-ray observations of Nova LMC 1995 obtained by Orio & Greiner (1999) and Orio et al.(2003) in the $R_{photos} - kT_{eff}$ plane compared to I82 white dwarf envelope models.

effective temperature. Since luminosity and white dwarf mass are fixed in these models to $4.2\times10^{-4}L_{\odot}$ and $1.2M_{\odot}$, the thick line indicates the corresponding photospheric radius. Contour for day 2100 corresponds to the whole range of effective temperatures found by Orio et al.(2003) from XMM-Newton observations fitted with NLTE atmosphere models; the range of photospheric radius is obtained from the normalization constant for the best fit with the distance varying between 51 and 55 *kpc*. The whole uncertainty in the photospheric radius derived from the white dwarf atmosphere models in this second observation is not included, since it is even larger than the scale of the plot. For this reason the comparison with models must rely mainly on the effective temperature evolution, as in the case of V1974 Cyg.

The ROSAT observation results (day 1100 after outburst) are coherent with a $1.2M_{\odot}$, as was assumed for the white dwarf atmosphere models used by Orio & Greiner (1999). But the results obtained with XMM-Newton by Orio et al.(2003) on day 2100 after outburst indicated a much smaller mass. In addition, the time-scales from our envelope models with $1.2M_{\odot}$ cores are always far too short for Nova LMC 1995. Concerning the effective temperature derived from the ROSAT observation, the fact that the source was still "on" 1000 days after, when observed by XMM-Newton, indicates that it should be close to the best-fit value for the effective temperature from Orio & Greiner (1999), or even cooler, because according to envelope models, the temperature should increase during those 1000 days elapsed between observations. Therefore, the highest effective temperatures included in the uncertainty range for day 1100 are unlikely to represent the actual temperature of the source. According to the models, no envelope could have been that hot at the time of ROSAT observations and still be "on" 1000 days after.

Assuming the best-fit effective temperature for the ROSAT observation to be the actual temperature of the source, the time elapsed until the XMM-Newton observation and its effective temperature indicate that, among the ONe09 models, only the smallest white dwarf, with $0.8M_{\odot}$, could simulate the evolution. Accepting the white dwarf mass determination from the best-fit atmosphere model obtained by Orio et al.(2003), $0.9M_{\odot}$, the I82 models with this mass would also successfully simulate the evolution of the temperature of Nova LMC 1995. In any of these cases, it is possible that the maximum effective temperature was still not reached by the time of the XMM-Newton observation (in December 2000). If the time of the ROSAT observation and its best-fit effective temperature are taken as starting point, the maximum effective temperature could be reached as late as ~2400 days after the ROSAT/PSPC observation (with the I82 $0.9M_{\odot}$ model), i.e, by August 2004.

XMM-Newton pointed once again Nova LMC 1995 in April 2003 (observation 0148870101, PI: Marina Orio) and data are public since 19 May 2004. No results have been published at the moment, but according to the satellite observation log, the observation was affected by high radiation and the exposure time was shorter than in the first XMM-Newton observation. A first look at the archival data shows that the source is not so clearly visible in the EPIC cameras as was in the 2000 observation. Nevertheless, the source detection algorithms of the automatic pipeline performed on all XMM-Newton observations detected a source in the MOS1 image at ~9 arcsec from the nominal position of Nova LMC 1995 (2000 detection was at ~5 arcsec, less than the XMM-Newton resolution, which is 6 arcsec), with a count-rate $\sim 10^{-3} cts\, s^{-1}$ (for the MOS1 camera, the count-rate in the 2000 observation was $0.1 cts\, s^{-1}$). This would indicate that the source had already turned-off by April 2003, but given the contamination of the observation by high radiation, this must be taken with care and a detailed analysis needs to be performed.

3.6 Summary and conclusions

X-ray observations of the three novae detected by ROSAT with a supersoft component have been compared to our white dwarf envelope models from chapter 2. In all cases, the photospheric properties (radius and effective temperature) obtained with white dwarf atmosphere models fitted to the X-ray spectra have been used for comparison with the envelope models.

ROSAT/PSPC observations of V1974 Cyg have been reanalyzed with simple spectral models, as the analysis performed by Krautter et al.(1996). The X-ray light curve has three clear phases: an initial rise, due to the decrease of the absorption in the ejected shell, a plateau of constant luminosity and a final decline, due to the extinction of the hydrogen burning in the envelope. The evolution of the hydrogen column density responsible for the rise of the X-ray flux is compatible with the decrease in density of the ejected shell, assuming that it is spherical and its outer radius expands at constant velocity. When compared to our envelope models, the evolution of V1974 Cyg during the plateau of constant luminosity, between days 255 and 511 after outburst, is found to be compatible with the evolution of an envelope with steady hydrogen burning, on either a ONe 0.9 $M_{\odot}$ white dwarf with 50% mixing, or on a ONe 1.0$M_{\odot}$ with 25% mixing, with a turn-off time between 8 and 15 months. In both cases, the luminosity of the envelope models is compatible with independent determinations of the luminosity, given the distance uncertainty. The hydrogen mass fraction observed in the ejecta is between 0.1 and 0.4 (Austin et al.(1996), Hayward et al.(1996)), thus compatible with the envelope models with 50% mixing. In any of the possible cases, the envelope mass for stable hydrogen burning ($\sim 10^{-6}M_{\odot}$) is much smaller than the mass needed to trigger the nova outburst ($\sim 10^{-5}M_{\odot}$). Taking into account that the fraction ejected, according to hydrodynamical models, is not enough to reduce the envelope mass to the values for stable hydrogen burning, it is clear that some extra mass loss mechanism must be present after the outburst.

In the case of ROSAT observations of GQ Mus, the comparison with white dwarf envelope models indicate that the mass of the white dwarf can be $1.1 \pm 0.1M_{\odot}$, with an average envelope mass $M_{env} \sim 10^{-6}M_{\odot}$. Both X-ray data and optical observations of the ionized nebula indicate a turn-off time of 5-9 years. In this case, not only is the mass of stable envelope models smaller than expected from hydrodynamical simulations, but it is also smaller than the envelope mass burned during the constant bolometric luminosity phase of GQ Mus taking into account the observed luminosity and hydrogen mass fraction, even assuming the shortest turn-off time of 5 years ($7.6 \times 10^{-6}M_{\odot}$). Hydrodynamical simulations in José & Hernanz (1998) for $1.0 - 1.15M_{\odot}$ CO white dwarfs with 50% and 25% of mixing, respectively, give hydrogen mass fractions similar to observed in GQ Mus ejecta and predict an ejected mass only a factor 2 smaller than observed.

For Nova LMC 1995, only two observations are available, one with ROSAT and one with XMM-Newton. The source was still on in December 2000, when observed with XMM-Newton. This long evolution as a soft X-ray source is only compatible with models for hydrogen rich envelopes (i.e., I82 models) on a small white dwarf, with 0.8-0.9$M_{\odot}$. This mass is compatible with the best-fit atmosphere model found by Orio et al.(2003) (0.9$M_{\odot}$) for the XMM-Newton observation. In this case, the envelope models indicate that the source should turn-off by August 2004.

In all previous cases, the uncertainty in the distance determination (a common problem for classical novae) makes a direct comparison between observations and models based on the photospheric radius or the luminosity rather unreliable, but the comparison of the effective temperature alone has proved to be a powerful tool. First of all, the envelope models in chapter 2 show that, as evolution of the hydrogen burning envelope proceeds,

the effective temperature increases, reaching its maximum value just before the turn-off of the source. This maximum effective temperature depends on the white dwarf mass and on the envelope composition. Therefore, the maximum effective temperature observed in a post-outburst nova constrains the star mass and/or the hydrogen mass fraction of the envelope, related to the mixing degree of the solar accreted envelope with the degenerate core. Second, the time spend by the envelope to change its effective temperature by a certain amount also depends on the white dwarf mass and envelope composition. If the X-ray emission is followed by monitoring observations of the post-outburst nova (as was the case of V1974 Cyg), the observed evolution of the effective temperature, when compared to the envelope models, constrains the parameters of the post-outburst envelope still more than the maximum effective temperature. In the case of V1974 Cyg, only two combinations of white dwarf mass and hydrogen mass fraction could explain the observed evolution of the effective temperature. When combined to independent determinations of the composition in the ejecta, the star mass is deduced by a completely distance-independent method. It must be stressed that previous determinations of the white dwarf mass in classical novae relied on core mass-luminosity relations, and obviously the luminosity is highly affected by the distance uncertainty.

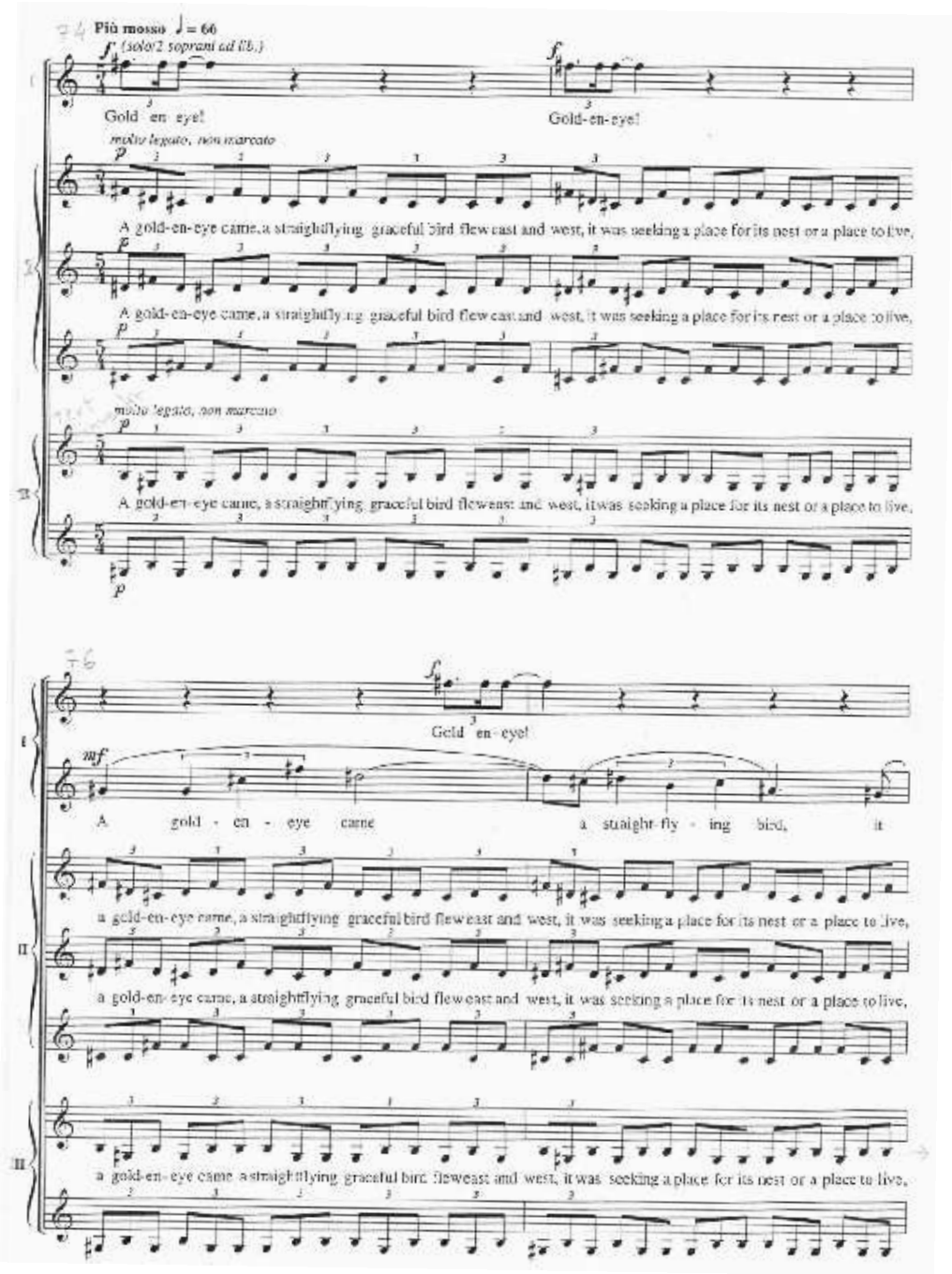

" A Golden Eye came,
a straightflying gracefuld bird..."

The First Runo
Einojuhani Rautavara

Chapter 4

XMM-Newton observations of post-outburst classical novae

4.1 Classical novae in the XMM-Newton and Chandra era

At the time the ROSAT mission was finishing, a new generation of X-ray observatories was starting a new era in X-ray astronomy. The Japanese ASCA and the Italian Beppo SAX obtained interesting results by the last times of the ROSAT mission, but a major step forward in X-ray astronomy was given in 1999, with the launch of Chandra and XMM-Newton. This new generation of X-ray observatories, with much more sensitive detectors and a high spectral resolution, provides an excellent opportunity for the study of classical novae. To start with, XMM-Newton followed ROSAT in the observations of Nova LMC 1995, showing the ongoing hydrogen burning on the white dwarf surface almost six years after outburst (Orio et al.(2003)). In this case, non-LTE atmosphere models were used to fit the soft X-ray spectrum, although spectral features of the emission line crowded atmosphere could not be resolved. In other cases, however, the complex emission spectrum could not be fitted by atmosphere models. The supersoft component of Nova Velorum 1999 (V382 Vel), when first observed six months after outburst with BeppoSAX, could only be fitted superimposing some emission lines to a white dwarf atmosphere model (Orio et al.(2002b)). Later Chandra observations, performed between December 1999 and August 2000, showed a fast decrease of the soft component and a wealth of emission lines on the hard component, never seen before in novae observed in this energy range (Burwitz et al. (2002)). Chandra LETG+HRC-S observations of Nova Aquila 1999 (V1494 Aql) performed ten months after the outburst showed a supersoft component that was not present four months before, and a surprising variability in the X-ray light curve never seen before in any classical nova: a double-peaked, short time-scale "burst" and periodic pulsations (Drake et al. (2003)). While the authors do not find any explanation for the "burst", they suggest that the pulsations could be driven either by the κ/γ mechanism (responsible for pulsations in planetary nebula nuclei) or by the ϵ mechanism, i.e, the vibrational destabilization induced by nuclear burning near the surface. Pulsations of the white dwarf have also been suggested as a possible explanation for the large amplitude oscillations recently found in the 25 *ks* Chandra LETG+HRC-S observation of Nova Sgr 2002 no.3 (V4743 Sgr) (Ness et al. (2003)). According to the authors, in a preliminary analysis, its soft X-ray spectrum seems compatible with a hot white dwarf atmosphere with absorption features (from which only some lines are identified).

In addition to classical novae, hydrogen burning on white dwarf envelopes is the source of soft X-ray emission from other systems, such as supersoft X-ray sources (SSS), where

Table 4.1: XMM Orbit parameters

Launch	1999 December 10
Apogee/Perigee	114,000 km/7,000 km
Inclination	40^o
Orbit Period	48 hours

hydrogen is processed on the white dwarf surface at the same rate it is accreted from the companion. High resolution X-ray spectra are providing new visions of these sources as well. Observations of the famous SSS in LMC CAL 87 performed with the SISs instruments on-board ASCA, with superior energy resolution than previous instruments, were fitted with white dwarf atmosphere models, obtaining an estimation of the white dwarf mass (0.8-1.2 $M_{\odot}$, a wide range) and the intrinsic luminosity (Ebisawa et al. (2001)). In the same work, a very high surface gravity and temperature was required to explain the observed spectrum of RX J0925.7-4758. The Reflection Grating Spectrometers (RGSs) on-board XMM-Newton provided the first high resolution spectra of CAL 83, considered the prototype of SSS, showing a spectrum that resembled a white dwarf atmosphere with the superposition of numerous, unresolved absorption features (Paerels et al. (2001)). The authors state that a reliable determination of the stellar parameters will be only possible with a detailed analysis using improved and specially conceived atmosphere models. In addition to galactic, LMC, SMC and M31 sources (see for instance SSS catalogue, mainly from ROSAT observations, Greiner (2000)), numerous Supersoft X-ray Sources have been also found by Chandra in M31 and other external galaxies (Swartz et al. (2002),Di Stefano (2003)). As in the case of the Magellanic Clouds observations, the low absorption and easy determination of distance to the sources are advantages with respect to galactic sources in the analysis of soft spectra and the determination of luminosities.

In this chapter, our XMM-Newton observations of two post-outburst novae, Nova Sgr 1998 (V4633 Sgr) and Nova Oph 1998 (V2487 Oph), are presented. They are two of the five novae included in our XMM-Newton observational program, aimed to monitor the X-ray emission of classical novae between two and four years after the outburst.

4.2 The XMM-Newton satellite

The X-Ray Multi-Mirror Mission, XMM-Newton (Jansen et al.(2001)), is one of the four ESA cornerstones defined in the Horizon 2000 Programme. Three golden coated X-ray telescopes, its "golden eyes", effective for energies between 0.1 and 10 keV, make XMM-Newton the most sensitive X-ray telescope in space, with a mirror effective area at 1 keV more than 5 times larger than Chandra and 11 times larger than ROSAT. The X-ray telescopes are complemented with an optical/UV monitor that offer simultaneous access to images and spectra on these wavelengths.

4.2.1 Orbit and operations

The XMM-Newton satellite was launched on 10th December 1999 by an Ariane 5 launcher into a highly elliptical orbit (see table 4.1), with an apogee of 114,000 km and an orbital period of 48h. As XMM-Newton is operated with three ground stations, located at Perth, Kourou and Santiago, this orbit provides long visibility periods (145 ks per orbit), only interrupted during some hours close to the apogee due to the high background generated by the radiation belts.

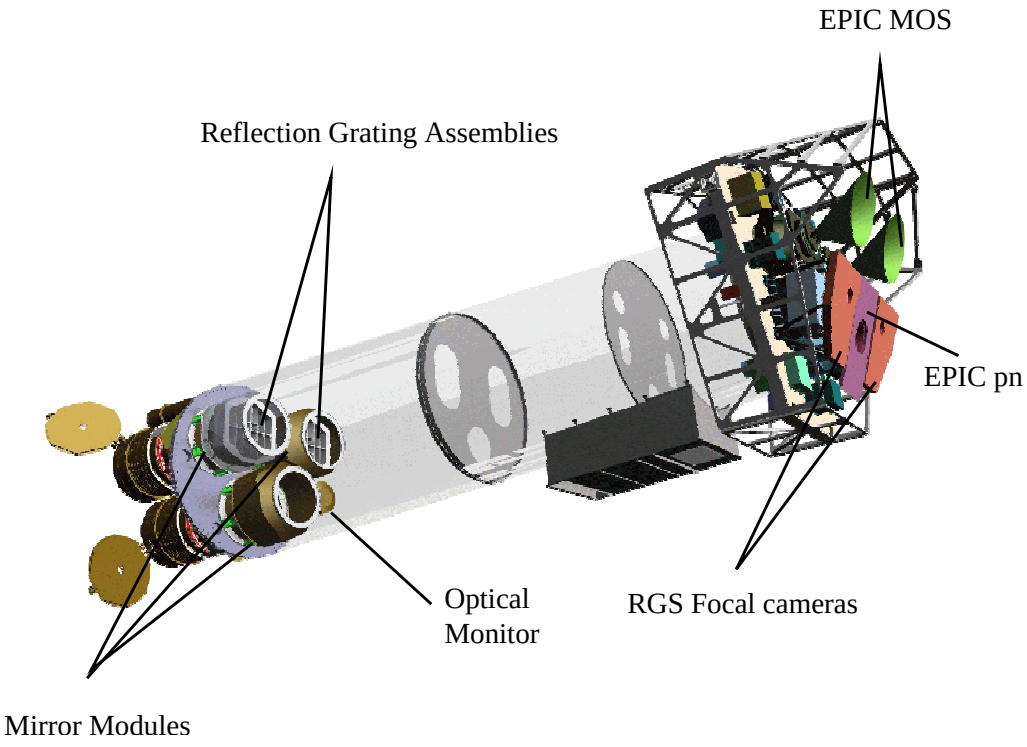

Figure 4.1: Sketch of the XMM-Newton satellite payload (*source:* XMM User's Handbook, Ehe et al. (2003)).

After an initial phase of commissioning, calibration and performance verification, XMM-Newton started its scientific task three months after the launch, with only guaranteed time observations for another three months. Afterwards, during the first year, a 50% of the total observing time was open to guest observers, while still the other 50% was used for guaranteed time observations. The proportion changed gradually, increasing the open time up to a 75%. Guest observers can apply to perform open time observations during the "Announcements of Opportunity" issued by the XMM-Newton Project Scientist once a year.

4.2.2 Scientific payload

The XMM-Newton carries on board three X-ray telescopes, each with an European Photon Imaging Camera (EPIC) at its focal plane, and an optical/UV telescope (OM, Mason et al.(2001)). The detectors of two of the EPIC cameras use MOS CCDs (Turner et al.(2001)), whereas the third one uses pn CCDs (Strüder et al.(2001)). In addition, two Reflection Grating Spectrometers (den Herder et al.(2001)) for high resolution X-ray spectroscopy are mounted in the light path of the two EPIC MOS cameras (see figure 4.1 for a sketch of the satellite payload). All instruments work simultaneously, obtaining high sensitivity X-ray images (with EPIC cameras), high resolution X-ray spectra (with the RGS) and optical/UV images or spectra of the same objects.

The X-Ray Telescopes

Each of the three Wolter tpye-I X-ray telescopes on board XMM-Newton is formed by 58 thin nested mirrors shells, that provide a total effective are of $\sim$4650 cm^2 at 1 keV ($\sim$ $1550cm^{-2}$ each telescope). This high sensitivity is achieved with a good angular resolution,

with full width at half maximum (FWHM) of ~ 6". For comparison, Chandra four nested mirrors are designed for a better angular resolution (0.2" of FWHM), but with a smaller effective area (800 cm^{-2} at 1 keV).

One of the X-ray telescopes focuses the incoming X-rays to the EPIC pn camera, while the other two have Reflection Grating Assemblies (RGA) in their light paths. The grating arrays diffract $\sim 40\%$ of the incoming light to a linear strip of CCDs, the cameras of the Reflection Grating Spectrometers, while a $\sim 42\%$ is directed to the EPIC MOS cameras in the main focus. The remaining light is absorbed by the support structures of the RGAs.

The EPIC cameras

The EPIC cameras provide extremely sensitive imaging observations over a filed of view of 30' in the energy range from 0.2 to 10 keV, with moderate spectral resolution ($E/\Delta E \sim 20 - 50$) and angular resolution (6" FWHM). Two of the XMM-Newton X-ray telescopes are equipped with EPIC MOS (Metal Oxide Semiconductor) CCD cameras, while the third telescope, without grating array in its light-path, focuses its image on a EPIC pn camera. EPIC MOS chip arrays are constituted by 7 identical, front-illuminated CCD chips. They are not mounted on the same plane, but the central chip is slightly behind the outer ring formed by the other 6 chips, following closely the curvature of the telescope focal plane. In the case of the pn camera, it is formed by 12 CCD's, covering a field of view similar to that of the MOS cameras. The EPIC pn camera, with a higher quantum efficiency than the MOS cameras and mounted on focus of the X-ray telescope free of grating spectrometer, is the most sensitive X-ray instrument on board XMM-Newton.

Since CCD cameras are not only sensitive to X-rays, but also to IR, optical and UV, blocking filters are needed to obtain X-ray images free from contamination of other wavelengths. Depending on the optical to X-ray flux ratio of the source, one of the three available filters (thin, medium or thick) is needed. The blocking filters, however, affect the EPIC effective area, specially in the low part of the spectrum. The effect of the filter used needs to be taken into account in the analysis of the spectra.

All CCD cameras on-board XMM-Newton operate in photon counting mode, producing event lists, where all photons are listed with time of arrival, position on the camera and energy. From the event lists, images, light curves and spectra (thanks to the intrinsic energy resolution of the pixels) of every source in the field of view can be extracted.

The Reflection Grating Spectrometers

The Reflection Grating Spectrometers (RGS) mounted on two of the X-ray telescopes provide high spectral resolution ($E/\Delta E$ from 200 to 800) X-ray spectroscopy between 0.35 and 2.5 keV, an energy range particularly rich in X-ray emission lines (including the L shell transitions of heavy elements like Fe and Ni, and the K shell transitions of N, O, Ne, Mg and Si). Each RGS consists of a Reflection Grating Assembly (RGA) mounted behind the mirror module (see figure 4.1), that diffracts $\sim 40\%$ of the X-ray photons onto the corresponding RGS Focal Camera (RFC). RFCs consist of linear arrays of 9 MOS CCD chips (similar to those in the EPIC MOS cameras) located along the dispersion direction of the RGAs. MOS chips in RFCs are back-illuminated, to maximize their soft energy response, and aluminum-coated to suppress optical/UV light.

The Optical Monitor

Co-aligned with its X-ray telescopes, XMM-Newton has a 30 cm optical/UV telescope, providing for the first time simultaneous X-ray and optical/UV observations from a single

platform. In the absence of atmospheric extinction, diffraction and background, the small telescope is a powerful instrument, sensitive to optical and UV, from 160 to 600 *nm,* and with a sensitivity limit of 24 magnitudes for a 1000 *s* exposure (for a B0 star). A filter wheel with 6 optical and UV filters, a magnifier and two grisms (optical and UV) permit to perform photometry and spectroscopy in these wavelengths as well.

4.3 Observational program: recent galactic novae

To shed new light to the problem of novae turn-off times, we proposed the observation of five recent classical novae (aged less than three years) during the first XMM-Newton observing cycle. The targets selected were classical novae that had experienced their outburst during the two years before the deadline for AO1 proposal submission (April 1999), with the exception of Nova Sco 1997 (which was selected because of its Beppo SAX detection reported in Orio et al.(1997)). Each target was monitored during one year, with three observations at intervals of six months (see table 4.2). In the case of V2487 Oph a fourth observation was performed, because the third one was affected by a flare. Exposure times of $\sim$ 6000 seconds were selected, since it was enough to detect the sources in case they were still emitting. Without any information about the X-ray emission from the selected targets at that time, longer exposure times could have been a waste of XMM-Newton observing time. A pilot/follow-up observation would have been preferred to choose the optimal observation time, but this type of observation was discouraged in the first cycle of XMM-Newton.

Nova Sco 1997 (V1141 Sco) was not detected in any of the three exposures, but this is not a surprising case. Although it was included in our observational program because of its detection reported in Orio et al.(1997), the identification of the source was not confirmed later on (Orio (1999)). Nova Sco 1998 (V1142 Sco) and Nova Mus 1998 (LZ Mus) were detected in the last observations performed by XMM-Newton, but the pipeline source detection algorithm did not identify them in the first observations. Detailed spectral analysis has been performed for the two brightest sources of our observational program: Nova Sgr 1998 (V4633 Sgr) and Nova Oph 1998 (V2487 Oph).

4.4 Data analysis

Data reduction has been performed with the Science Analysis System, SAS, software package for XMM-Newton data reduction (versions 5.3.3 and 5.4.1; see appendix F). The calibrated and concatenated event lists (i.e., pipeline products) delivered by the XMM-Newton Science Survey Center (SSC) have been taken as starting point. In some cases, the pipeline data reduction has been reproduced from the original observation data files (ODFs) to check that the final results were the same as the products from SSC. Standard procedures for analysis of EPIC MOS and pn point-like sources described in the SAS documentation (Loiseau (2003), Snowden et al. (2002)) have been applied. As a general rule, source photons have been extracted from a circle of $\sim 30''$, whereas the background has been extracted from an annulus around the source of inner and outer radius 30" and 60". Other extraction regions were tried with similar results. Except for the third observation of V2487 Oph, no flaring background intervals are present in the other observations. The short exposures and the poor statistics of the data prevent a timing analysis, which would have been crucial to determine if there was some periodicity in the systems, as observed by Lipkin et al.(1998) in the optical for V4633 Sgr.

Table 4.2: XMM-Newton observations of recent galactic classical novae

Target	Discovery date	XMM-Newton observation date	Time after outburst	EPIC detection
N Sco 1997 (V1141 Sco)	5 Jun. 1997	Oct. 11, 2000	1224 d, 3.4 y	NO
		Mar. 24, 2001	1388 d, 3.8 y	NO
		Sep. 7, 2001	1555 d, 4.3 y	NO
N Sgr 1998 (V4633 Sgr)	22 Mar. 1998	Oct 11, 2000	934 d, 2.6 y	YES
		Mar. 9, 2001	1083 d, 3.0 y	YES
		Sep. 7, 2001	1265 d, 3.5 y	YES
N Oph 1998 (V2487 Oph)	15 Jun.1998	Feb. 25, 2001	986 d, 2.7 y	YES
		Sep. 5, 2001	1178 d, 3.2 y	YES
		Feb. 26, 2002	1352 d, 3.7 y	YES
		Sep. 24,2002	1562 d, 4.3 y	YES
N Sco 1998 (V1142 Sco)	21 Oct. 1998	Oct. 11, 2000	721 d, 2.0 y	NO?
		Mar. 24, 2001	885 d, 2.4 y	NO?
		Sep. 7, 2001	1052 d, 2.9 y	NO?
N Mus 1998 (LZ Mus)	29 Dec. 1998	Dec. 18, 2000	730 d, 2.0 y	YES?
		Jun. 26, 2001	910 d, 2.5 y	YES?
		Dec. 26, 2001	1093 d, 3.0 y	YES?

The signal to noise ratio on the RGS data of our observations is not enough to obtain grating spectra. The optical monitor was used with ultraviolet grisms, but unfortunately it has been not possible yet to reduce the data because this type of observation is not supported for A01 observations by current SAS versions.

4.5 Nova Sgr 1998 (V4633 Sgr)

Nova Sgr 1998 (V4633 Sgr) was discovered on 1998 March 22.3 UT, with magnitude 7.8 (Liller (1998)). Spectroscopic observations obtained two days later confirmed the nova (Della Valle et al.(1998)), and found relatively low expansion velocities and the presence of iron, thus indicating that the nova belonged to the Fe II class (Williams (1992)). It was a moderately fast nova (Liller & Jones (1999)), with $t_2 \sim 28$ days and $t_3 \sim 55$ days. No optical polarization was detected (Ikeda et al.(2000)). Lynch et al.(2001) obtained near-infrared spectroscopy, in the range 0.8 to 2.5 μm, 525 and 850 days after peak brightness. Their observations revealed some symmetric lines with widths (FWHM) 1800 $km\,s^{-1}$. No evidence for dust formation was found and the shell was hydrogen-deficient. Optical observations during the period 1998-2000 revealed two photometric periodicities, which could be interpreted as the orbital period (3.014h, constant) and the spin of the white dwarf (3.08h, and slightly variable) in a nearly synchronous magnetic system (Lipkin et al.(1998)). According to the authors, this results suggested that a process of mass transfer had occurred in the system no later than two months and a half after the nova eruption. They also obtained a reddening of $E_{B-V} = 0.21 \pm 0.03$, which is unusually low, but in agreement with other independent determinations of the reddening towards the direction of the nova. Using this reddening and an intrinsic magnitude at maximum of $M_V^{max} \approx -7.7$, Lipkin et al.(1998) estimated the distance to V4633 Sgr to be 8.9 ± 2.5 kpc.

V4633 Sgr was observed by XMM-Newton three times, with a time interval of 6 months between the three epochs, 2.6, 3.0 and 3.5 years after outburst (see table 4.3). During the second observation, the EPIC pn exposure was rescheduled and its data were not processed

Table 4.3: EPIC exposure details of XMM-Newton observations of V4633 Sgr.

Observation date	Camera	Exposure time (s)	Total counts (0.2-8.0 keV) (cts)	Count rate (0.2-8.0 keV) ($\times 10^{-2}$cts s^{-1})
Oct 11, 2000	pn	6782	723	9.7 ± 0.4
	MOS1	8862	267	2.6 ± 0.2
	MOS2	9000	261	2.4 ± 0.2
Mar. 9, 2001	pn	...	...	...
	MOS1	6463	136	1.5 ± 0.2
	MOS2	6382	144	1.4 ± 0.2
Sep. 7, 2001	pn	5684	561	8.1 ± 0.4
	MOS1	8962	219	2.0 ± 0.2
	MOS2	...	...	...

in the pipeline. The most detailed spectral analysis has been performed with the first and the third observation, with larger exposure times than the second one.

4.5.1 Spectral analysis

As can be seen for instance in figure 4.2, the EPIC spectra show that X-ray emission spans up to the upper bound of the cameras energy range ($\sim 8\ keV$) and that there is an important soft component. Spectral analysis has been performed using XSPEC (Arnaud et al.(1996), see appendix F). White dwarf atmosphere emission models gently provided to us by Jim MacDonald (MacDonald & Vennes (1991), see appendix E) have been included for analysis of the soft component. Spectral models have been fitted to the data from all available cameras at each observation simultaneously (the three EPIC cameras in the first observation, EPIC MOS1 and MOS2 in the second one and EPIC MOS2 and pn in the last observation). It must be noticed that only the EPIC pn camera has good calibrated response in the range 0.2-0.3 keV. For EPIC MOS cameras, channels below 0.35 keV have been ignored due to its bad calibration (see appendix F for more details).

The fits to the data do not constrain well the value of the hydrogen column density, N_H, probably due to the poor statistics at the lower energy band. Only an upper limit of $7 \times 10^{21} cm^{-2}$ is obtained from confidence contours, which is larger than the mean value of interstellar N_H towards the direction of V4633 Sgr, $1.6 \times 10^{21} cm^{-2}$ (Dickey & Lockman (1990)). Nevertheless, fits tend to give absorptions smaller than the interstellar value, which is not possible. The interstellar value is also consistent with the N_H derived from the Gorenstein (1975) empirical relationship between interstellar X-ray absorption and optical extinction, $A_V = 4.5 \times 10^{-22} N_H$, and the extinction measured by Lynch et al.(2001) for V4633 Sgr, $A_V = 0.9 \pm 0.6$, that is, $N_H = (2 \pm 1) \times 10^{21} cm^{-2}$. In the following, this column density, $1.6 \times 10^{21} cm^{-2}$, has been fixed for all fits.

The X-ray spectrum is dominated by thermal plasma emission, simulated by a Raymond-Smith model (Raymond & Smith (1977), distributed with XSPEC, see appendix F). More detailed models such as MEKAL do not make much sense for V4633 Sgr data, since these models increase largely the number of parameters while the EPIC number of counts is low. Nevertheless, it has been checked for some cases that the best-fit parameters obtained with MEKAL were similar to the results using the Raymond-Smith model. In all observations, the rather flat spectrum can not be fitted with a single Raymond-Smith model, and at least two- (or even three-) temperature components are required, regardless of the inclusion of a white dwarf atmosphere model to simulate the soft part of the spectrum.

A two-temperature thermal plasma?

Keeping the presence of the white dwarf atmosphere, we have first attempted to fit the data with a two-temperature thermal plasma model. Since it is not known whether Nova Sgr 1998 is a CO or an ONe nova, several chemical compositions have been tried: CO and ONe white dwarf atmosphere with solar abundances for the thermal plasma model, and CO/ONe atmosphere with CO/ONe abundances for the thermal plasma. The model with solar abundances would correspond to emission from fresh, H-rich material in a reestablished accretion flow, while the CO/ONe enriched plasma would simulate the emission from the nova ejected shell. For the white dwarf atmospheres, two representative compositions (one for CO and one for ONe) are available in MacDonald & Vennes (1991) models. For the CO and ONe enriched plasma models, fits have been attempted with 14 different compositions, corresponding to the seven different models for each type of white dwarf from José & Hernanz (1998). Enhancements have been specified in the plasma model by number relative to H relative to solar for He, C, N, O, Ne, Mg, Si and S, keeping the other elements at solar abundances relative to H.

Tables 4.4 and 4.5 summarize the spectral parameters and the quality of the best-fit (the χ^2_ν) obtained for each composition using a two-temperature plasma model, for the first and the third observation of V4633 Sgr respectively. In general, CO enhanced models give worse fits than ONe abundances. None of the models tried fits the data with a χ^2_ν better than 1.1 in any of the observations, and most of them have $\chi^2_\nu > 1.2$. For the models with a best χ^2_ν, the same composition does not fit at the same level of accuracy the first observation and the third. Only ONe5 and ONe7 models have χ^2_ν smaller than 1.2 in the third observation, but it is worse than 1.2 in the first observation. In any case, the results are always worse than with a three-temperature plasma (see tables 4.6 and 4.7 for comparison).

The main reason for the need of a third component is the broad energy band of emission detected in V4633 Sgr, combined with the maximum at $\sim 0.5 - 1\ keV$. As can be seen in figures 4.2 and 4.3, a low temperature ($\sim 0.1\ keV$) component is needed to fit the soft part of the spectrum, which is not soft enough to be accounted for by the white dwarf atmosphere; and only a high temperature ($> 3\ keV$) component can explain the flux at hard energies (see the behaviour of the Raymond-Smith model for several temperatures in figure 4.4). With only two components, the observed spectra have always an excess at $\sim 1\ keV$, which can be related to the emission of a plasma at this temperature, although the inclusion of a third component adds two more parameters to the fit. But both in the two and in the three component models, the temperatures of the models are probably representative of a continuum, a gradient of temperatures in the plasma, which in the case of V4366 Sgr cannot be represented only by two extreme temperatures.

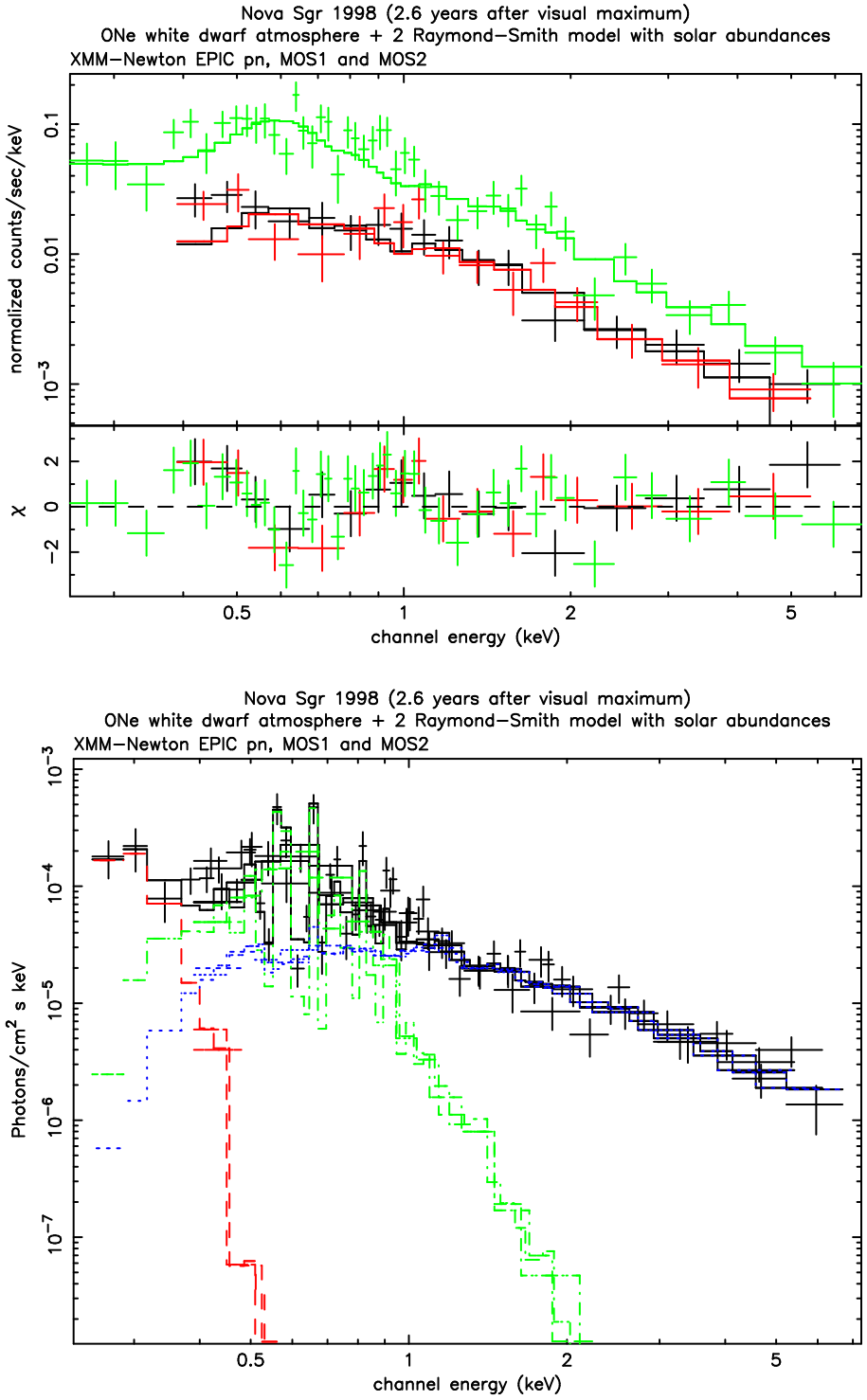

Figure 4.2: **Upper panel:** EPIC pn (green, with higher count rate), MOS1 (black) and MOS2 (red) spectra of V4633 Sgr on the first observation, 2.6 years after outburst, with a two-temperature Raymond-Smith model with solar abundances, and ONe white dwarf atmosphere.
Lower panel: Unfolded spectrum, showing the contribution of each of the model components. From left to right, ONe white dwarf atmosphere (red dashed line) and Raymond-Smith models with $kT_1 = 0.18$ keV (green dash-dotted line) and $kT_2 = 5.07$ keV (blue dotted line). Total model and unfolded data are plotted with black line and crosses, respectively.

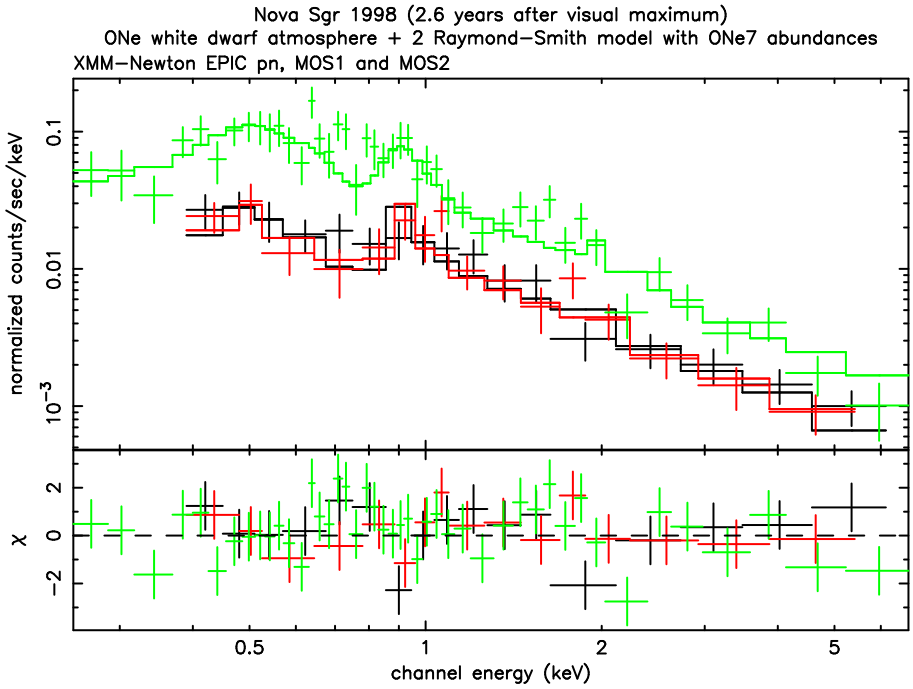

Figure 4.3: EPIC pn, MOS1 and MOS2 spectra of V4633 Sgr on the first observation, 2.6 years after outburst, fitted with a two-temperature (with 0.19 keV and 23 keV) Raymond-Smith model with abundances from ONe7 model in José & Hernanz (1998), and ONe white dwarf atmosphere.

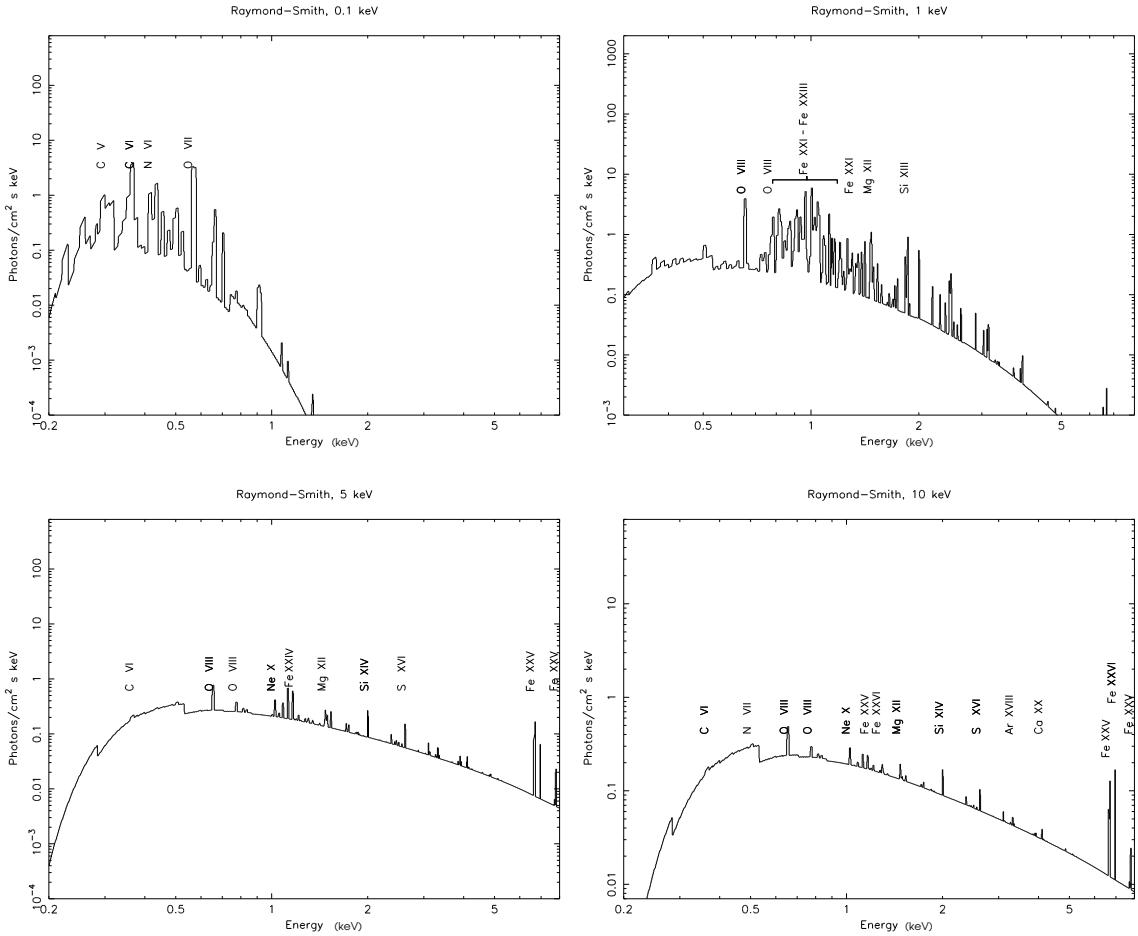

Figure 4.4: Raymond-Smith models with solar abundances, for kT: 0.1, 1, 5 and 10 keV.

Table 4.4: Spectral-parameters for two-temperature Raymond-Smith model fits, to V4633 Sgr first XMM-Newton observation. A white dwarf atmosphere model is also included in all cases, with the indicated composition. CO and ONe compositions for the plasma correspond to models in José & Hernanz (1998). Column density is always fixed to $1.6 \times 10^{21} cm^{-2}$.

Model	T_{atm} $10^5 K$	K_{atm}	kT_1 keV	kT_2 keV	K_1 10^{-6}	K_2 10^{-6}	χ^2_ν
CO wd+sol	1.9	0.14	0.18	5.05	107	136	1.50
CO1	2.1	0.01	0.18	3.80	3.75	57.3	1.53
CO2	1.0	10^{-8}	20.3	4.60	1.48	22.2	1.50
CO3	1.0	10^{-14}	19.4	4.60	1.45	21.5	1.50
CO4	2.0	0.01	0.19	4.02	4.11	54.8	1.49
CO5	2.4	0.001	0.14	3.33	1.54	23.4	1.53
CO6	2.4	0.0004	0.14	3.33	0.45	67.9	1.56
CO7	2.4	0.001	0.14	3.33	1.53	23.2	1.53
ONewd+sol	2.3	0.16	0.18	5.07	104	136	1.48
ONe1	3.0	0.004	0.18	12.6	2.40	18.7	1.40
ONe2	1.0	0.02	0.17	19.6	10.6	46.9	1.27
ONe3	3.0	0.006	0.18	21.6	2.76	20.2	1.38
ONe4	3.0	0.008	0.17	20.1	0.69	6.0	1.45
ONe5	4.7	10^{-5}	0.18	24.8	2.86	19.4	1.26
ONe6	1.0	10^{-6}	0.20	22.8	2.03	15.7	1.42
ONe7	1.0	10^{-7}	0.19	23.5	0.45	3.64	1.22

Table 4.5: Spectral-parameters for two-temperature models for the third XMM-Newton observation.

Model	T_{atm} $10^5 K$	K_{atm}	kT_1 keV	kT_2 keV	K_1 10^{-6}	K_2 10^{-6}	χ^2_ν
CO wd+sol	3.5	1.68	0.16	4.21	101	103	1.35
CO1	2.3	0.09	0.14	3.17	4.11	42.0	1.31
CO2	2.3	0.08	0.14	3.17	1.72	17.5	1.40
CO3	2.3	0.09	0.14	3.17	1.65	16.9	1.39
CO4	2.3	0.08	0.17	3.34	4.08	35.9	1.39
CO5	2.4	0.03	0.12	3.05	1.81	16.8	1.34
CO6	2.4	0.03	0.12	3.05	0.52	4.85	1.39
CO7	2.4	0.04	0.13	3.15	1.31	17.5	1.35
ONewd+sol	3.8	10^{-4}	0.18	4.30	68.4	101	1.27
ONe1	2.3	0.88	0.14	6.74	3.47	11.3	1.26
ONe2	2.3	0.55	0.17	9.98	10.1	24.7	1.22
ONe3	2.3	0.88	0.16	7.88	2.68	9.88	1.30
ONe4	2.3	0.98	0.17	12.1	0.58	3.63	1.37
ONe5	2.3	0.61	0.17	12.0	2.69	11.1	1.16
ONe6	2.3	0.50	0.19	20.9	1.66	11.3	1.31
ONe7	2.7	0.08	0.18	12.9	0.36	2.16	1.14

Table 4.6: Spectral-parameters for three-temperature Raymond-Smith model fits, to V4633 Sgr first XMM-Newton observation. A white dwarf atmosphere model is also included in all cases, with the indicated composition. CO and ONe compositions for the plasma correspond to models in José & Hernanz (1998). Column density is always fixed to $1.6 \times 10^{21} cm^{-2}$.

Model	T_{atm} $10^5 K$	K_{atm} 10^{-3}	kT_1 keV	kT_2 keV	kT_3 keV	K_1 10^{-6}	K_2 10^{-6}	K_3 10^{-6}	χ^2_ν
CO wd+sol	1.9	100	0.12	0.82	13	289	22	114	1.11
CO1	1.0	4.3	0.11	0.80	37	6.1	13	45	1.04
CO2	1.0	1.9	0.10	0.77	19	3.1	5.6	22	1.27
CO3	1.0	1.8	0.10	0.76	19	2.9	5.5	21	1.27
CO4	1.0	4.1	0.13	0.80	36	4.8	14	36	1.01
CO5	1.0	1.6	0.10	0.72	15	2.6	5.1	19	1.23
CO6	1.0	4.8	0.10	0.73	14	0.77	1.4	5.7	1.42
CO7	1.0	1.6	0.10	0.72	15	2.6	4.9	19	1.24
ONe wd+sol	1.9	100	0.12	0.82	13	288	22	114	1.11
ONe1	2.8	2.6	0.11	0.31	20	7.2	0.58	21	1.29
ONe2	1.0	9.3	0.16	0.57	38	11	1.1	50	1.22
ONe3	2.5	11	0.14	0.53	41	4.1	0.42	22	1.27
ONe4	3.1	0.94	0.12	0.37	31	1.4	1.3	6.4	1.34
ONe5	1.00	3.0	0.16	0.57	46	3.3	0.57	21	1.21
ONe6	1.00	1.6	0.19	0.62	32	1.9	0.35	15	1.38
ONe7	1.00	0.4	0.18	0.65	40	0.43	0.07	3.8	1.18

Table 4.7: Spectral-parameters for three-temperature models for the third XMM-Newton observation.

Model	T_{atm} $10^5 K$	K_{atm}	kT_1 keV	kT_2 keV	kT_3 keV	K_1 10^{-6}	K_2 10^{-6}	K_3 10^{-6}	χ^2_ν
CO wd+sol	1.7	12	0.09	0.85	10	820	18	81	1.05
CO1	1.9	0.40	0.13	0.89	30	5	12	30	1.10
CO2	1.7	1.1	0.09	0.90	22	5.9	5.2	15	1.27
CO3	2.0	0.16	0.09	0.90	22	6.5	5.2	14	1.25
CO4	2.0	0.36	0.10	0.87	52	8.8	13	34	1.04
CO5	2.0	0.14	0.09	0.89	24	4.4	5.2	13	1.23
CO6	2.1	0.04	0.09	0.89	18	1.7	1.4	4.1	1.38
CO7	2.1	0.49	0.09	0.88	22	3.9	5.0	13	1.19
ONe wd+sol	1.7	13	0.09	0.85	10	890	18	81	1.06
ONe1	2.3	0.4	0.09	0.39	19	19	0.39	15	1.15
ONe2	2.1	0.79	0.14	0.56	15	11	0.85	29	1.15
ONe3	2.4	0.37	0.11	0.44	21	6.7	0.31	14	1.12
ONe4	2.7	0.09	0.13	0.45	21	1.1	0.08	4.2	1.17
ONe5	2.4	0.40	0.14	0.54	24	3.4	0.29	13	1.10
ONe6	2.6	0.10	0.19	60	20	1.6	0.03	11	1.38
ONe7	2.7	0.05	0.14	0.18	13	0.11	0.29	2.1	1.20

Table 4.8: Abundances by number relative to H relative to solar and main parameters for the CO1 and CO4 nova models from José & Hernanz (1998).

Model	M_{WD}	Mixing	He	C	N	O	Ne	Mg	Si	S
CO1	$0.8 M_\odot$	25%	1.08	21.7	119	18.2	3.13	1.06	1.07	1.04
CO4	$1.15 M_\odot$	25%	1.36	35.1	124	15.5	3.26	36.4	2.09	1.11

Best-fit model: a three-temperature thermal plasma

The best fit is obtained with a three-temperature Raymond-Smith and a white dwarf atmosphere (see figures 4.5-4.10). The second observation, with a final exposure time shorter than in the other two observations and problems in the EPIC pn camera, has a smaller count-rate and significant flux is only detected up to 5 keV by the MOS cameras (see figures 4.6 and 4.9). For this observation, a two-temperature Raymond-Smith with an added white dwarf atmosphere are enough to fit the data, since the contribution of the third component for the not very steep spectrum at energies $\sim 3-7$ keV is not necessary in this case.

Once again, a total of sixteen compositions have been considered (see tables 4.6 and 4.7 for a summary of the fit parameters). The compositions which give the best fit, both in the first and in the third observation, are the solar (plus CO or ONe white dwarf atmosphere), with $\chi^2_\nu = 1.11$ in the first observation and 1.05-1.06 in the third one; and the CO1 and the CO4 models, with a χ^2_ν of 1.04 and 1.01 in the first observation and 1.10 and 1.04 in the third one. Models with other abundances for the Raymond-Smith components have χ^2_ν larger than 1.1 for the third observation, and larger than 1.2 in the first one. Only the ONe5 give a fit as good as CO1 model in the third observation, but the result is worse in the first observation ($\chi^2_\nu = 1.2$).

The abundances of the two CO models which give the best fits, CO1 and CO4, result from José & Hernanz (1998) hydrodynamic models of the outburst on white dwarfs with different mass (see table 4.8), but have very similar abundances of the elements with emission lines at the energies of interest (C, N and O lines around 1 keV, see figure 4.11). It is therefore not surprising that the results of the fit give similar parameters and fit the data with a similar accuracy; CO1 is taken as representative of both in the following.

Parameters for the best-fit three-temperature thermal plasma models with solar and with CO1 abundances are summarized in tables 4.9 and 4.10, respectively. The error bars for each parameter have been obtained computing 1σ, 2σ and 3σ confidence contours (see figures 4.12-4.17), corresponding to an increase in $\Delta\chi^2$ of 2.3, 4.61 and 9.21 respect to the best-fit model, for the following pairs of parameters: $T_{atm} - K_{atm}$, $kT_{RS1} - K_{RS1}$, $kT_{RS2} - K_{RS2}$, $kT_{RS3} - K_{RS3}$, $kT_{RS1} - kT_{RS2}$ and $kT_{RS2} - kT_{RS3}$, where K_{atm} is the normalization constant for the atmosphere, proportional to its luminosity, and $K_{RS\#}$ are the normalization constants for each Raymond-Smith component, proportional to the emission measure (EM) of the plasma (see appendixes E and F).

The best-fit values for the plasma temperatures are very similar for the solar and the CO1 models, as well as the emission measure from the second and third components. The main difference between the two models is the emission measure of the first and coolest plasma component, at $\sim 0.1\,keV$. As can be seen in figure 4.11, at this temperature, the model with CO1 abundances has enhanced C, N and O emission lines that can account for the observed count-rate at $\sim 0.5 - 0.6\,keV$ with a global emission measure for the whole low-temperature plasma component smaller than in the solar abundances model.

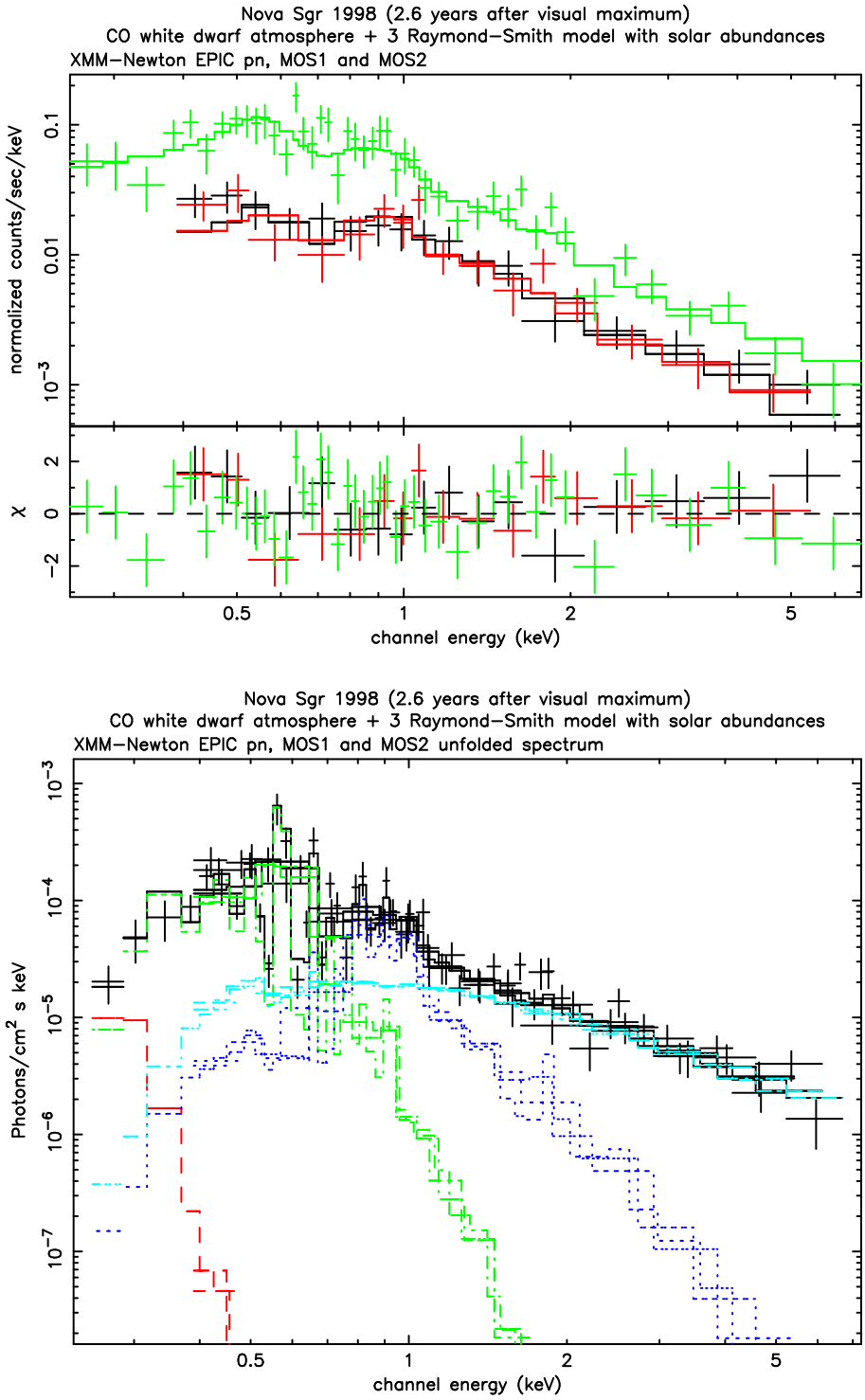

Figure 4.5: V4633 Sgr observed spectrum 2.6 years after outburst and best-fit model with solar abundances.

Upper panel: Observed spectrum and residuals (data minus folded model) plotted in terms of sigmas, with error bars of size one. Data from the three EPIC cameras are indicated: pn (green, with higher count-rate), MOS1 (black) and MOS2 (red). The solid lines indicate the best-fit model with CO white dwarf atmosphere and a 3-temperature Raymond-Smith with solar abundances.

Lower panel: Unfolded spectrum, showing the contribution of each component lines. From left to right, CO white dwarf atmosphere (red dotted line) and Raymond-Smith models with $kT_1 = 0.11\ keV$ (green dash-dotted), $kT_2 = 0.82\ keV$ (dark blue dotted) and $kT_3 = 37\ keV$ (light blue dash-dotted). The upper black solid line plots the total resulting model.

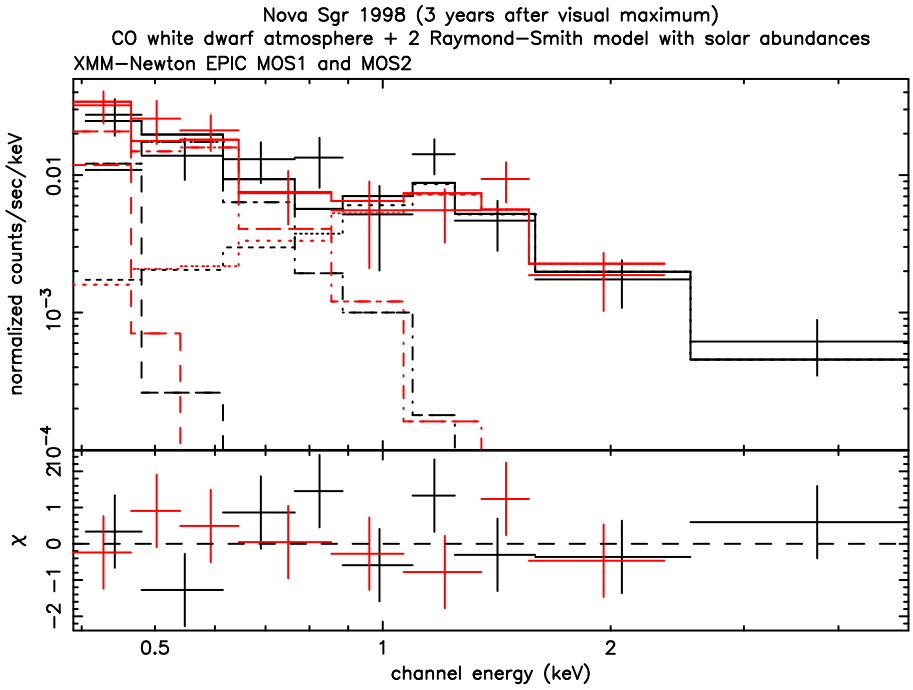

Figure 4.6: V4633 Sgr observed spectra in the second XMM-Newton observation, 3.0 years after outburst. EPIC MOS1 (black) and EPIC MOS2 (red) spectra are shown. Contribution of the various components of the model are displayed; from left to right, CO white dwarf atmosphere (dashed line), and Raymond-Smith model with solar abundances, at low temperature (dash-dotted line) and high temperature (dotted line).

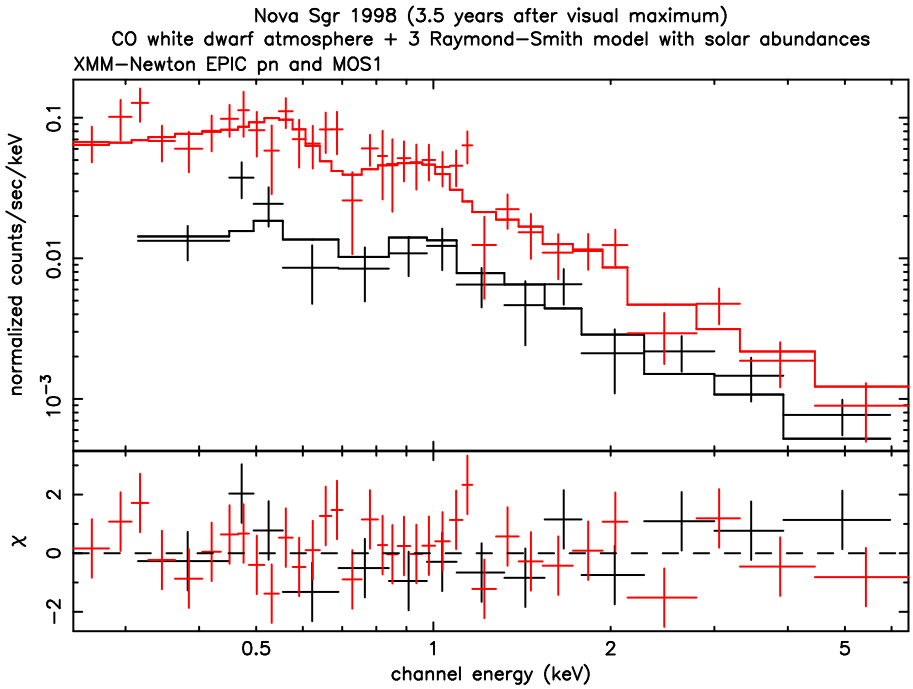

Figure 4.7: V4633 Sgr observed spectra with EPIC pn (red) and MOS1 (black) in the third observation, 3.5 years after outburst, with best fit CO white dwarf plus three-temperature Raymond-Smith model with solar abundances, and residuals.

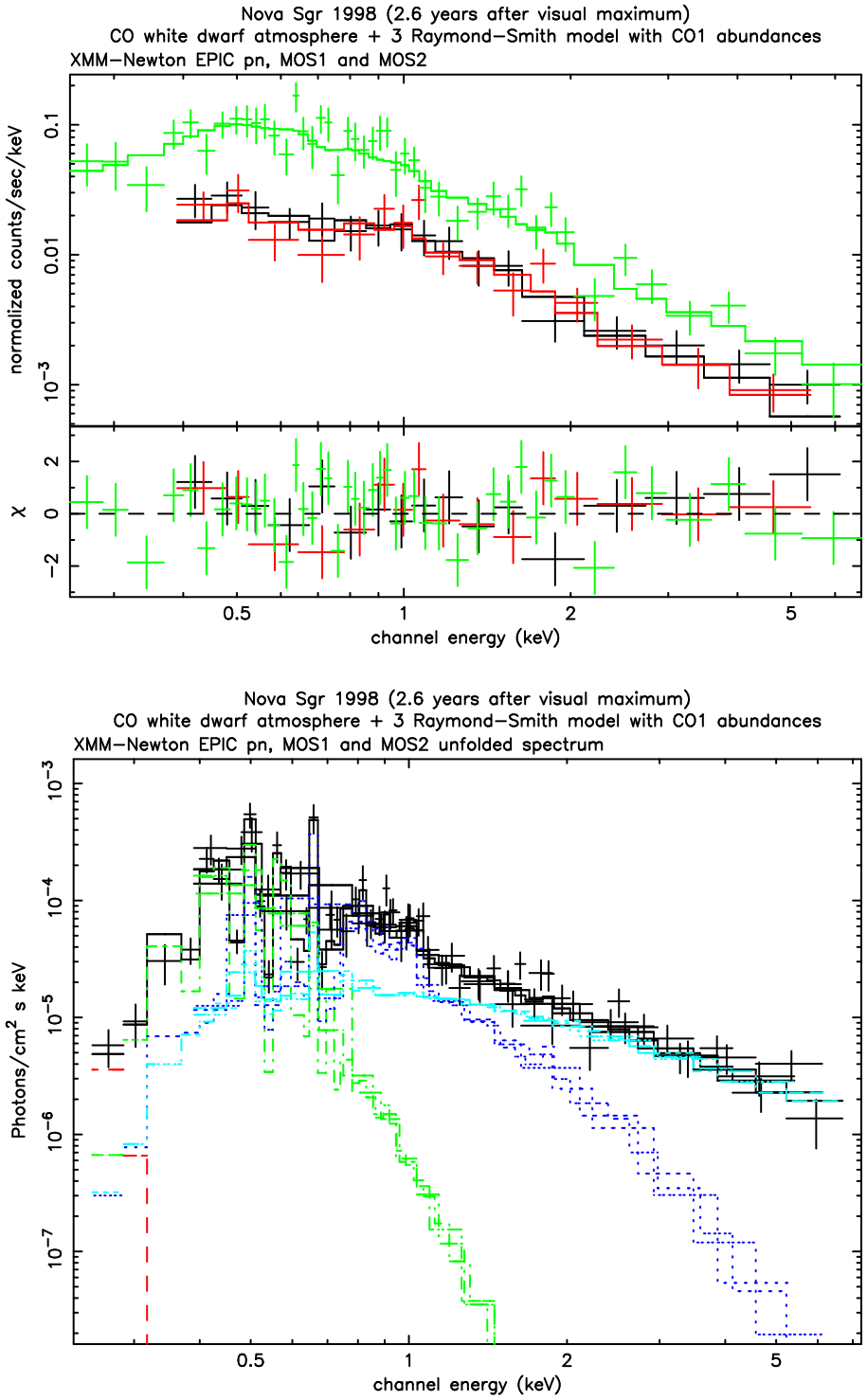

Figure 4.8: V4633 Sgr observed spectrum 2.6 years after outburst and best-fit model with CO1 abundances.

Upper panel: Observed spectrum and residuals (data minus folded model) plotted in terms of sigmas, with error bars of size one. Data from the three EPIC cameras are indicated: pn (green), MOS1 (black) and MOS2 (red). The solid lines indicate the best-fit model with CO white dwarf atmosphere and a 3-temperature Raymond-Smith with abundances form CO1 model in José & Hernanz (1998).

Lower panel: Unfolded spectrum, showing the contribution of each component in thick lines: CO white dwarf atmosphere (red dotted line) and Raymond-Smith models with $kT_1 = 0.11\ keV$ (green dash-dotted), $kT_2 = 0.82\ keV$ (dark blue dotted) and $kT_3 = 37\ keV$ (light blue dash-dotted). The black line plots the total resulting model.

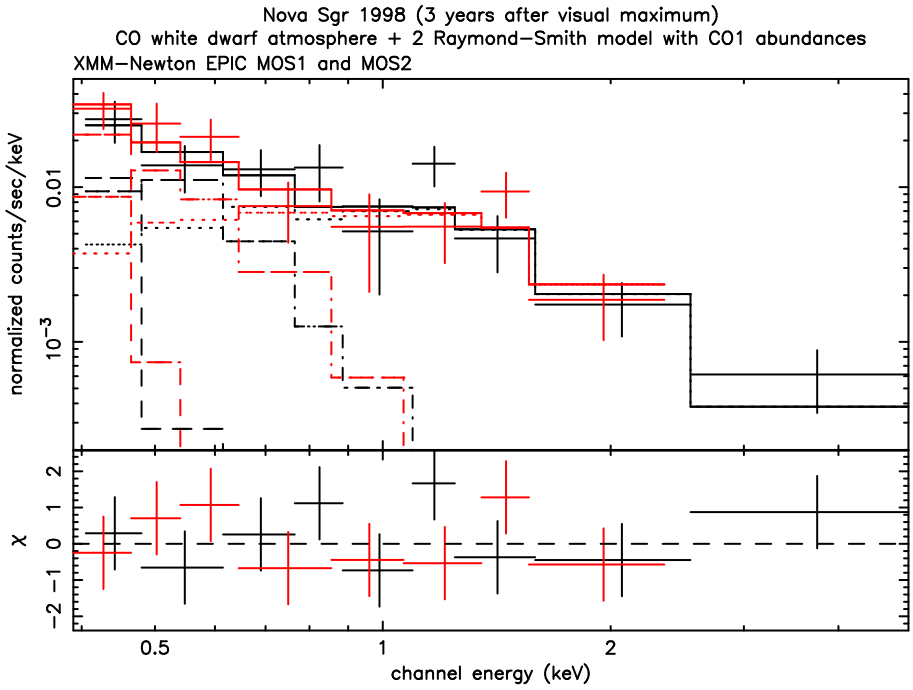

Figure 4.9: V4633 Sgr observed spectra in the second XMM-Newton observation, 3.0 years after outburst. EPIC MOS1 (black) and EPIC MOS2 (red) spectra are shown. Contribution of the various components of the model are displayed; from left to right, CO white dwarf atmosphere (dashed line), and Raymond-Smith model with CO1 abundances, at low temperature (dash-dotted line) and high temperature (dotted line).

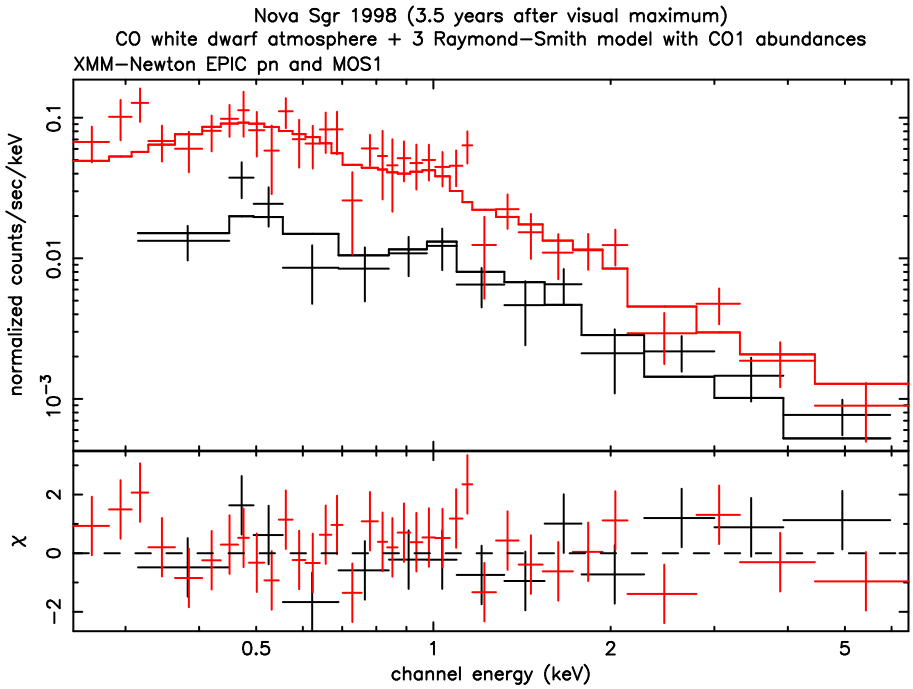

Figure 4.10: V4633 Sgr observed spectra with EPIC pn (red) and MOS1 (black) in the third observation, 3.5 years after outburst, with best fit CO white dwarf plus three-temperature Raymond-Smith model with CO1 abundances, and residuals.

Table 4.9: Solar 3-T Raymond-Smith model best-fit values and 3σ error bars (unless otherwise indicated) for V4633 Sgr.

	1^{st}Observation	2^{nd}Observation	3^{rd}Observation
$kT_{RS1}(keV)$	$0.12^{+0.05}_{-0.03}$	$0.13^{+0.11}_{-0.08}$	$0.09^{+0.04}_{-0.03}$
$kT_{RS2}(keV)$	$0.82^{+0.3}_{-0.2}$	$2^{+8(2\sigma)}_{-1(3\sigma)}$	$0.8^{+0.3}_{-0.6}$
$kT_{RS3}(keV)$	13^{+50}_{-9}	-	10^{+50}_{-7}
$K_{RS1}(\times 10^{-4})$	3^{+8}_{-2}	$2^{+20}_{-1.8}$	8^{+50}_{-6}
$K_{RS2}(\times 10^{-5})$	2^{+2}_{-1}	7 ± 3	2^{+3}_{-1}
$K_{RS3}(\times 10^{-5})$	11^{+6}_{-2}	-	8^{+2}_{-3}
$EM_{RS1}(\times 10^{55} cm^{-3})^{(1)}$	30^{+70}_{-20}	20^{+200}_{-18}	80^{+500}_{-60}
$EM_{RS2}(\times 10^{55} cm^{-3})^{(1)}$	2^{+2}_{-1}	7 ± 3	2^{+2}_{-1}
$EM_{RS3}(\times 10^{55} cm^{-3})^{(1)}$	11^{+6}_{-2}	-	8^{+2}_{-3}
$F^{plasma}_{unabs}\,(erg\,cm^{-2}s^{-1})^{(2)}$	7.2×10^{-13}	4.8×10^{-13}	7.7×10^{-13}
$L^{plasma}_{unabs}\,(\times 10^{33} erg\,s^{-1})^{(3)}$	7^{+4}_{-3}	5^{+3}_{-2}	9^{+6}_{-5}
$F^{total}\,(erg\,cm^{-2}s^{-1})^{(4)}$	2.7×10^{-13}	4.1×10^{-13}	2.1×10^{-13}
χ^2_ν	1.11	0.99	1.05

(1) Emission measure of the thermal plasma components for a distance of d=9 *kpc*. For other distances, factor $\left(\frac{d}{9kpc}\right)^2$ affects these values.

(2) Unabsorbed flux of the multi-temperature thermal plasma best-fit model, in the range 0.2-8.0 *keV*.

(3) Luminosity of the multi-temperature thermal plasma in the range 0.2-8.0 *keV*, for a distance of 8.9 ± 2.5 *kpc*. Error bars in this cases correspond to distance uncertainty, not to the determination of the flux, which is fixed to the best-fit model value.

(4) Total absorbed flux, in the range 0.2-8.0 *keV*.

Atmospheric component

For the white dwarf component, only upper limits are obtained, with the luminosity decreasing for increasing effective temperatures. The exact behaviour of this upper limit can be seen in figure 4.12, where confidence contours are plotted for the effective temperature and the atmosphere normalization, defined as L_{39}/D^2_{10}, where L_{39} is the luminosity in units of $10^{39} erg\,s^{-1}$ and D_{10} is the distance in units of 10 *kpc*. The confidence contours reflect the fact that the quality of the fit does not depend on the contribution of the atmosphere model, since without it, the low temperature thermal plasma can account for the soft X-ray photons. Nevertheless, the presence of this component associated to the hot white dwarf cannot be ruled out.

4.5.2 Discussion

4.5.2.1 Atmospheric component

The broad confidence region of the $T_{atm} - K_{atm}$ parameters for the atmospheric component includes many possible combinations. But a H-burning white dwarf, with $L \sim 10^{38} erg\,s^{-1}$ (which with $d = 9\,kpc$ implies $K_{atm} \sim 0.12$) and $T \geq 3.5 \times 10^5 K \approx 30\,eV$ or even $T \geq 2.3 \times 10^5 K \approx 20\,eV$ (which would imply a very extended envelope) is completely excluded. There are two basic possibilities compatible with the confidence contours shown in figure 4.12: a cool but luminous white dwarf, with a very extended envelope, or a still

Table 4.10: CO1 3-T Raymond-Smith model best-fit values and 3σ error bars (unless otherwise indicated) for V4633 Sgr.

	1^{st}Observation	2^{nd}Observation	3^{rd}Observation
$kT_{RS1}(keV)$	$0.11^{+0.07}_{-0.04}$	$0.16^{+0.19(2\sigma)}_{-0.14(3\sigma)}$	$0.13^{+0.06}_{-0.08}$
$kT_{RS2}(keV)$	0.8 ± 0.2	$1.6^{+10(2\sigma)}_{-0.5(2\sigma)}$	0.9 ± 0.5
$kT_{RS3}(keV)$	$20^{+no\,limit}_{-14}$	-	$31^{+no\,limit}_{-27}$
$K_{RS1}(\times 10^{-6})$	6^{+50}_{-4}	$2.9^{+400(2\sigma)}_{-2.6(3\sigma)}$	5^{+65}_{-3}
$K_{RS2}(\times 10^{-6})$	13^{+9}_{-7}	22^{+20}_{-2}	12^{+12}_{-11}
$K_{RS3}(\times 10^{-6})$	45 ± 20	-	30^{+20}_{-15}
$EM_{RS1}(\times 10^{54} cm^{-3})^{(1)}$	6^{+50}_{-4}	$2.81^{+400(2\sigma)}_{-2.5(3\sigma)}$	4^{+60}_{-2}
$EM_{RS2}(\times 10^{55} cm^{-3})^{(1)}$	$1.3^{+0.9}_{-0.7}$	$2.1^{+2.0}_{-0.2}$	$1.2^{+1.2}_{-1.1}$
$EM_{RS3}(\times 10^{55} cm^{-3})^{(1)}$	4.4 ± 2.0	-	$3.0^{+2.0}_{-1.5}$
$F^{plasma}_{unabs}\ (erg\,cm^{-2}s^{-1})^{(2)}$	4.8×10^{-13}	2.3×10^{-13}	4.3×10^{-13}
$L^{plasma}_{unabs}\ (\times 10^{33} erg\,s^{-1})^{(3)}$	5^{+2}_{-3}	2 ± 1	4^{+3}_{-2}
$F^{total}\ (erg\,cm^{-2}s^{-1})^{(4)}$	2.5×10^{-13}	4.1×10^{-13}	2.0×10^{-13}
χ^2_ν	1.04	0.99	1.10

(1)Emission measure of the thermal plasma components for a distance of d=9 kpc. For other distances, factor $\left(\frac{d}{9kpc}\right)^2$ affects these values.

(2)Unabsorbed flux of the multi-temperature thermal plasma best-fit model, in the range 0.2-8.0 keV.

(3)Luminosity of the multi-temperature thermal plasma in the range 0.2-8.0 keV, for a distance of 8.9 ± 2.5 kpc. Error bars in this cases correspond to distance uncertainty, not to the determination of the flux, which is fixed to the best-fit model value.

(4)Total absorbed flux, in the range 0.2-8.0 keV.

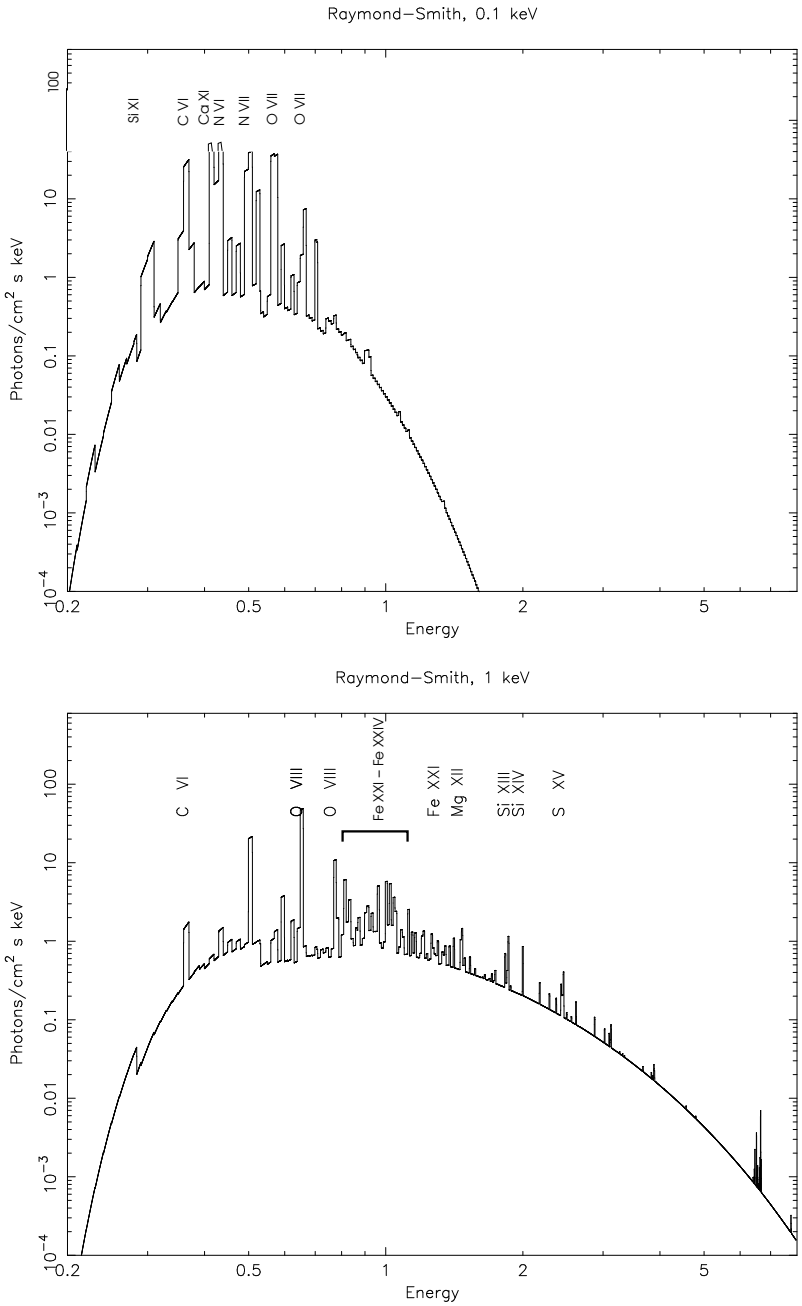

Figure 4.11: Raymond-Smith models with CO1 abundances from José & Hernanz (1998), for kT 0.1 and 1 keV.

hot, though already cooling, dim white dwarf.

The first possibility corresponds to the high luminosity - low temperature (say $< 2 \times 10^5 K$) left end in figure 4.12. For an effective temperature of $2 \times 10^5 K$ ($17\ eV$), the observed spectra is compatible with a white dwarf as luminous as $\sim 10^{39} erg\, s^{-1} \approx 3 \times 10^5 L_\odot$ ($K_{atm} \sim 1$, for $d = 9\, kpc$), with a very extended envelope, $R_{WD} \sim 10^{10} cm$. This upper limit includes luminosities $2 - 5 \times 10^4 L_\odot$ which, for this temperature, would situate the object at the right end of L-kT figures in section 2.4 (figure 2.6), with $R_{WD} = 8 - 13 \times 10^9 cm$. This configuration is indeed possible for a post-outburst nova, but shortly after the nova event. At the time of our observations, ~ 3 years after the outburst, the photosphere cannot be so extended and must have already receded to smaller radius, showing inner and hotter layers of the envelope. It is thus unrealistic for V4633 Sgr white dwarf to have this kind of photosphere.

The second and more realistic possibility is that hydrogen burning had already ceased and the white dwarf is cooling down. In this case, Prialnik (1986) and Kovetz et al. (1988) predict that the luminosity of a post-outburst nova evolves like $L_{nova} = L_{Edd} \times \left(\frac{t}{3 \times 10^6 s}\right)^{-1,14}$, for a 1.25 $M_\odot$ white dwarf nova; for an elapsed time of $\sim$3 years since outburst, $L_{nova} \approx 10^{36} erg\, s^{-1}$, which corresponds to $K_{atm} \approx 10^{-3}$ for a distance of 9 *kpc*. Figure 4.12 indicates that the maximum effective temperature for this luminosity is $\sim 3 \times 10^5 K$ ($\sim 26\ eV$), corresponding to a minimum $R_{WD} = 4 \times 10^8 cm$. This is an unrealistic radius for a still hot white dwarf, but it is a lower limit and includes realistic values for a cooling core, with lower effective temperatures. In other words, cooler and dimer white dwarfs are also compatible with the data, but with the present information, the exact position of V4633 Sgr in the cooling path cannot be determined.

4.5.2.2 Multi-temperature thermal plasma component

Two possible scenarios exist for the emission of the multi-temperature thermal plasma component: the shocked, expanding nova shell, or the resumption of accretion of matter with cosmic abundances from the secondary star. The model with solar abundances would correspond to the accreting flow emission, while CO and ONe models would simulate the emission from the ejecta. As will be seen in the following, the luminosity of the thermal plasma component, the plasma temperatures, and the distribution and evolution of the emission measures can help to decide between the two possibilities.

Luminosity of the thermal plasma component

As listed in tables 4.9 and 4.10, the unabsorbed X-ray (0.22-8.0 keV) luminosity of the multi-temperature plasma component is in the range $10^{33} - 10^{34} erg\, s^{-1}$ in all cases, both for the solar and the CO1 models, for a distance of $8.9 \pm 2.5\ kpc$ (Lipkin et al.(1998)). This X-ray luminosity for the plasma component of V4633 Sgr is too large to be associated to accretion onto a non-magnetic white dwarf, which have typical luminosities $L_X \approx 10^{29} - 10^{32} erg\, s^{-1}$(see, for instance, the review in Kuulkers et al.(2003)). The polar case can be ruled out as well, since typical luminosities are a few times $10^{32} erg\, s^{-1}$(Mukai (2003), Ramsay & Cropper (2004)). But in case accretion had been reestablished, the luminosity of the thermal plasma component of V4633 Sgr indicates that it could belong to the intermediate polar class, with luminosities usually a few times $10^{33} erg\, s^{-1}$ (Mukai (2003)). In fact, as mentioned above, optical observations suggested that V4633 Sgr is a nearly synchronous magnetic system (Lipkin et al.(1998)). In addition, photometric observations of other post-novae cataclysmic variables indicate that some are intermediate polars (i.e., Nova Sco 1941, V697 Sco, Warner & Woudt (2002)).

Regarding the possibility of the thermal plasma emission being originated in the expanding shell, unabsorbed luminosities as large as $10^{34} erg\,s^{-1}$ have been found in post-outburst novae showing hard X-ray emission, although none as late as 2.6 years after outburst. ROSAT observations indicated shocked shell luminosities of $5 \times 10^{33} - 10^{35} erg\,s^{-1}$ for Nova Her 1991 only 5 days after outburst, with a very fast decline (Lloyd et al.(1992), O'Brien et al.(1994)), $(0.8 - 2.0) \times 10^{34} erg\,s^{-1}$ for Nova Cyg 1992 150 days after outburst (Balman et al.(1998)), and $7.5 \times 10^{33} erg\,s^{-1}$ for Nova Pup 1991 16 months after outburst (Orio et al.(1996)). Nova Vel 1999 also reached luminosities as large as $10^{34} erg\,s^{-1}$ in the hard X-ray range (above 0.8 keV) when observed with Beppo-SAX 15 days after maximum, decreasing to a few $10^{33} erg\,s^{-1}$ five and a half months later (Orio et al.(2001a)). The luminosity of the ejected shell was even larger, since emission lines observed below 0.8 keV were also originated in the shell (Orio et al.(2001b)). So the luminosity of the thermal plasma component of V4633 Sgr is fully compatible with those observed from other shock heated nova ejecta. The main difference is that those observations were closer to outburst than XMM-Newton observations of V4633 Sgr, and that most of observed nova shells cooled very fast. Nevertheless, those cooling time-scales were shorter than expected: for an optically thin thermal plasma with electronic densities typically observed in nova ejecta, $n_e < 10^6 cm^{-3}$, the cooling time-scale is larger than 10 years (Brecher et al.(1977),Ögelman et al.(1987)). Therefore, the emission of hard X-rays from shock heated ejecta in Nova Sgr 1998, 3.5 years after the outburst would be fully compatible with theoretical predictions of cooling times. In addition, the flux detected in the third observation is smaller than in the first one. The flux detected in the second observation was also smaller, but as data of the pn camera are lacking and significant flux is detected in a narrower energy band, it can not be compared to the other two. Although given the uncertainties it is not possible to be conclusive, the thermal plasma luminosity is compatible with the emission both of a cooling shell and of an intermediate polar cataclysmic variable.

Plasma temperature, emission measure and electronic density

Both the solar and the CO1 models give similar fluxes and plasma temperatures. The main difference lays in the emission measure, specially of the coolest component. In addition to the luminosity of the plasma discussed above, the possible origin of the thermal emission, that is, reestablished accretion or cooling shell, will be now discussed based on the plasma temperatures, the emission measures and the derived electronic densities.

Expansion velocities around 1800 $km\,s^{-1}$ were indicated by infrared observations performed 525 and 850 days after outburst (Lynch et al.(2001)). Coronal lines, which are a good signature of shocks in the plasma, were also present in those observations. For a shock-heated plasma, temperatures are related to velocity as $kT \propto v^2$ (Brecher et al.(1977)). With the expansion velocities observed by Lynch et al.(2001), the plasma temperature would be $\sim$3 keV, which lays between the upper limit for the second component and the lower limit for the third one, both in the solar and in the CO1 models. The temperatures of the multi-temperature plasma are probably representative of a continuum of temperatures in the plasma, so the 3 keV could be included in this continuum. In other words, the temperature deduced from the expansion velocity observed by Lynch et al.(2001) is compatible with the X-ray emission observed with XMM-Newton.

For an expanding cooling shell, assuming some geometry for the emitting region and taking into account the observed expansion velocities for Nova Sgr 1998, an electronic density can be obtained from the emission measure for each component of the thermal plasma (tables 4.9 and 4.10). If the shell is assumed to be spherical and to expand at the constant velocity, with the expansion velocity observed by Lynch et al.(2001) ($1800 km\,s^{-1}$)

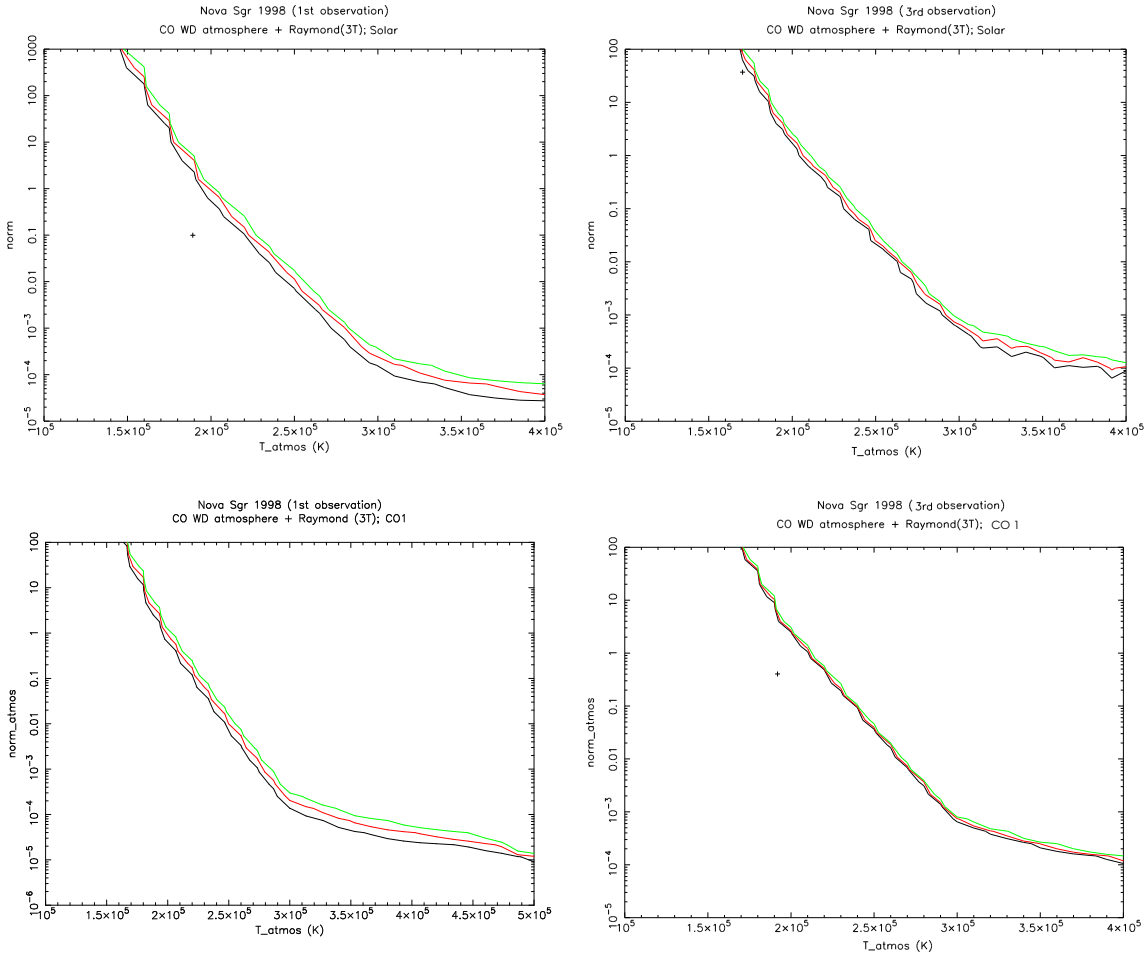

Figure 4.12: Confidence contours (from left to right, 1 -black-, 2 -red-, and 3σ -green-) for the effective temperature (T_atmos) and normalization (norm) of the white dwarf atmosphere component for the models with solar (upper panels) and CO1 (lower panels) abundances for the 1st (left panels) and 3rd (right panels) observations of V4633 Sgr. The cross indicates the best-fit values.

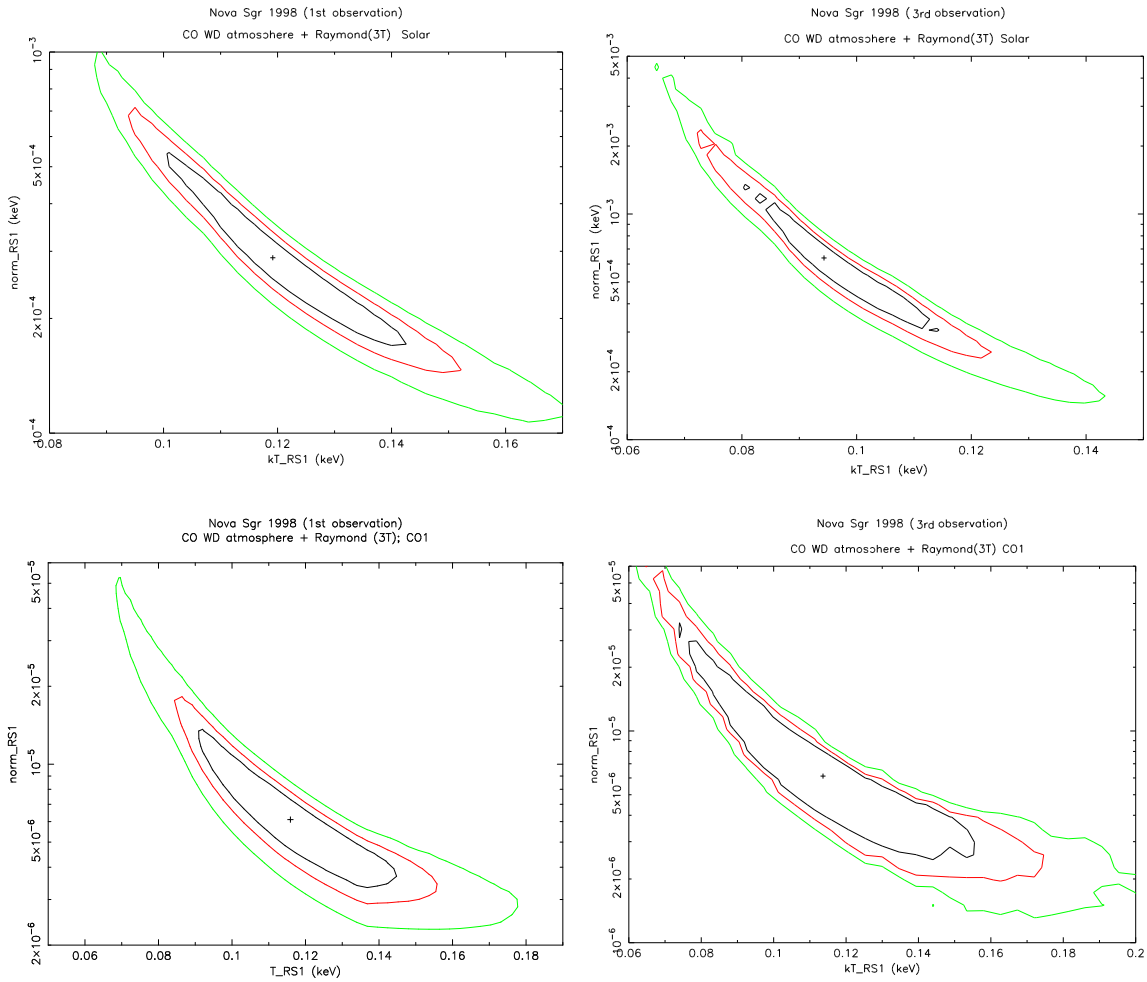

Figure 4.13: Confidence contours (1,2,and 3σ) for the plasma temperature and normalization of the low temperature Raymond-Smith component for the models with three temperatures, with solar (upper panels) and CO1 (lower panels) abundances for the 1st (left panels) and 3rd (right panels) observations of V4633 Sgr. The cross indicates the best-fit values.

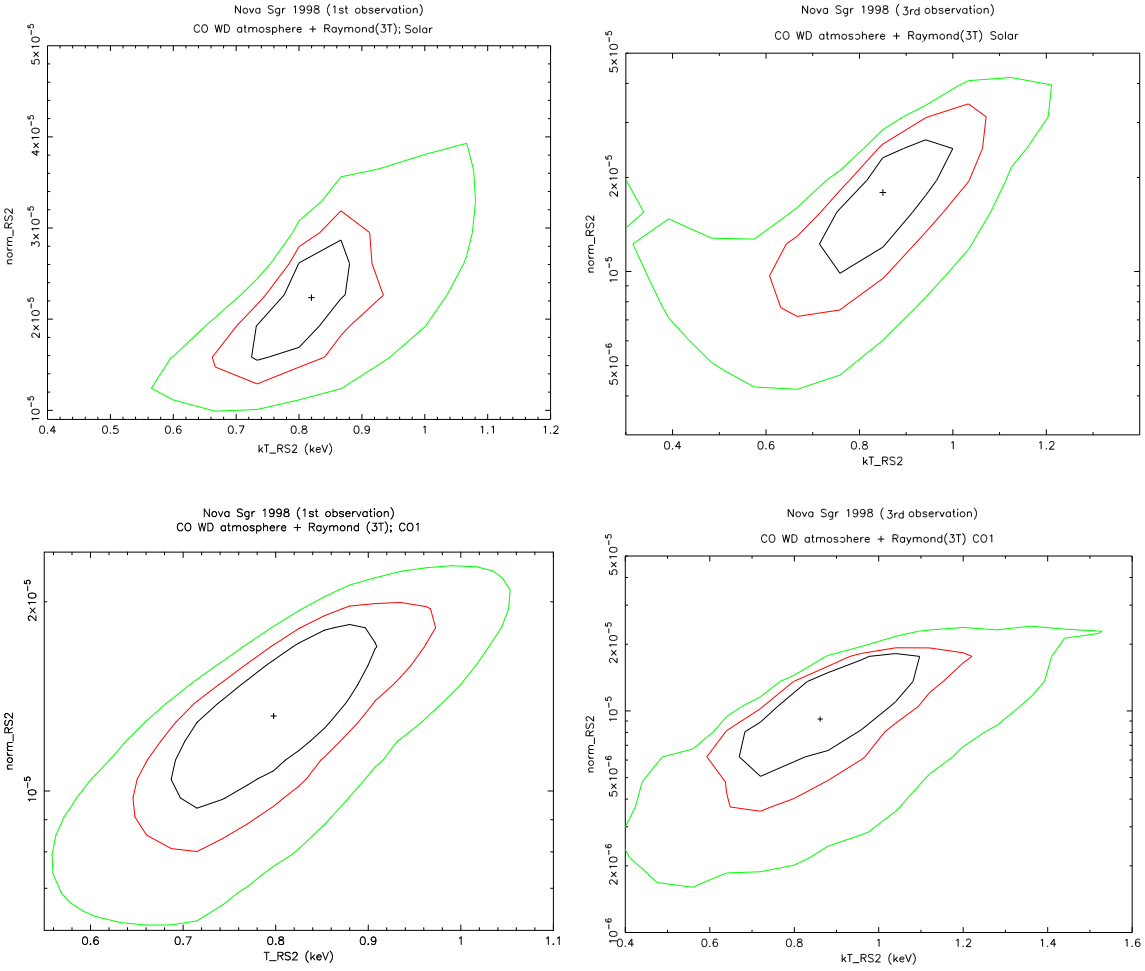

Figure 4.14: Confidence contours (1,2,and 3σ) for the plasma temperature and normalization of the second, intermediate temperature Raymond-Smith component for the models with three temperatures, with solar (upper panels) and CO1 (lower panels) abundances for the 1st (left panels) and 3rd (right panels) observations of V4633 Sgr. The cross indicates the best-fit values.

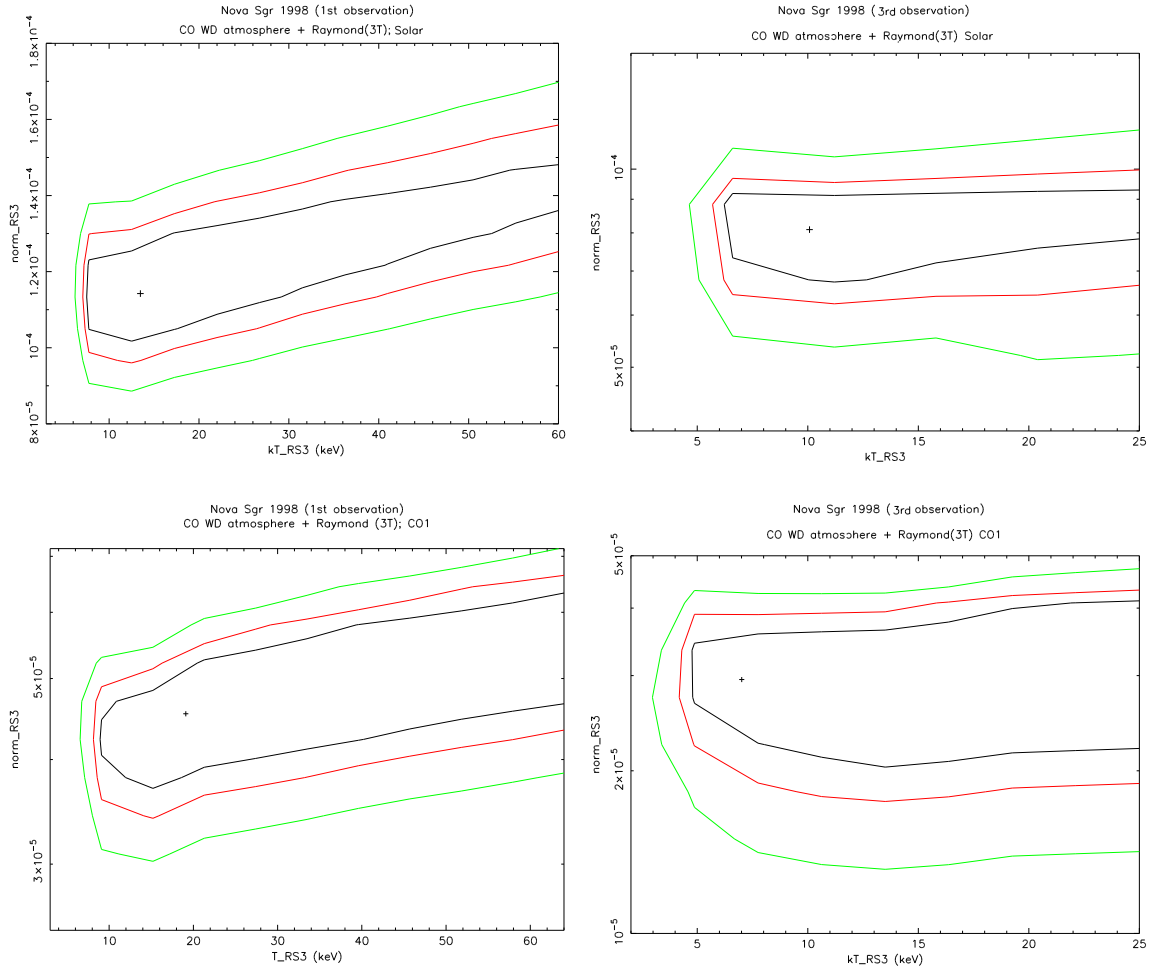

Figure 4.15: Confidence contours (1,2,and 3σ) for the plasma temperature and normalization of the high temperature Raymond-Smith component for the models with three temperatures, with solar (upper panels) and CO1 (lower panels) abundances for the 1st (left panels) and 3rd (right panels) observations of V4633 Sgr. The cross indicates the best-fit values.

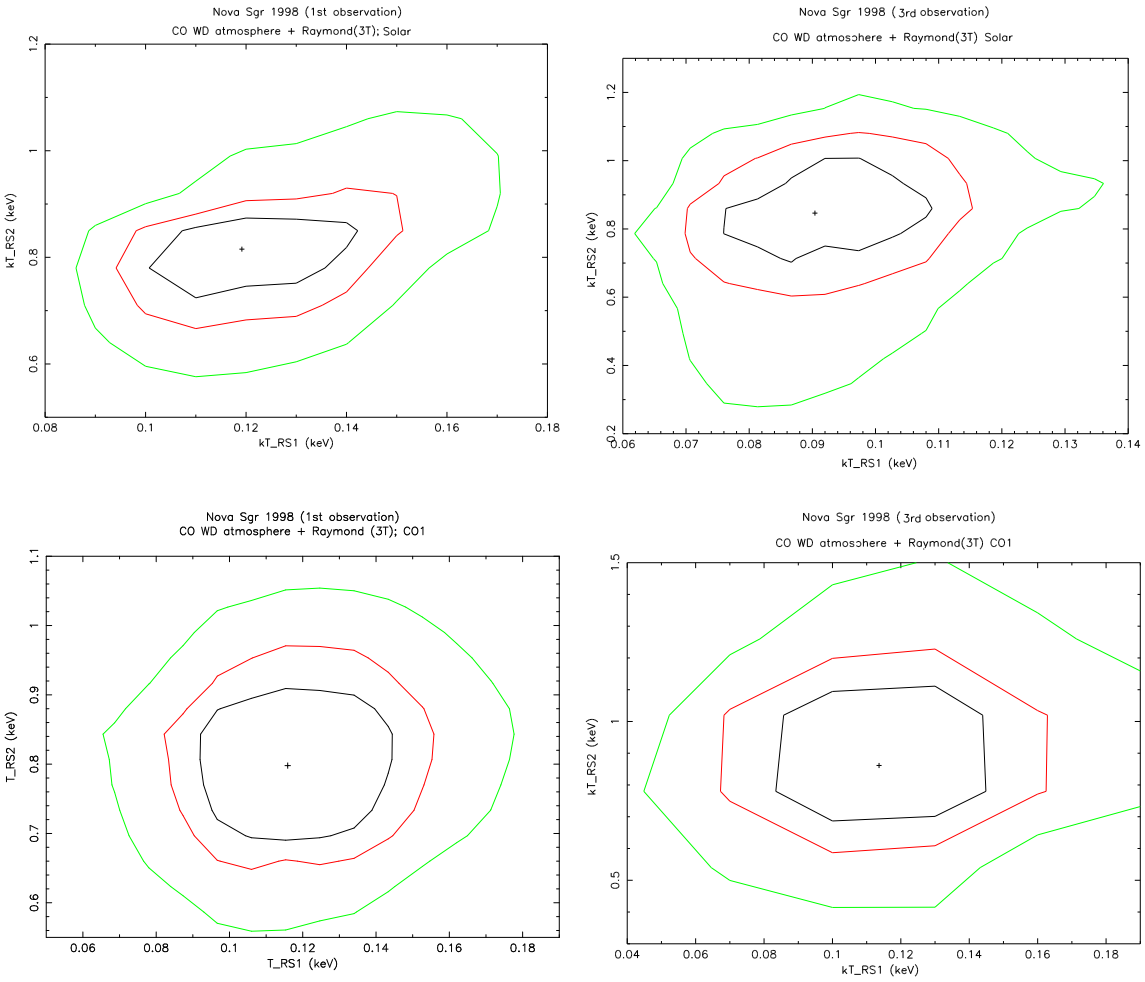

Figure 4.16: Confidence contours (1,2,and 3σ) for the plasma temperatures of the first (coldest) and second (intermediate temperature) Raymond-Smith components for the models with three temperatures, with solar (upper panels) and CO1 (lower panels) abundances for the 1st (left panels) and 3rd (right panels) observations of V4633 Sgr. The cross indicates the best-fit values.

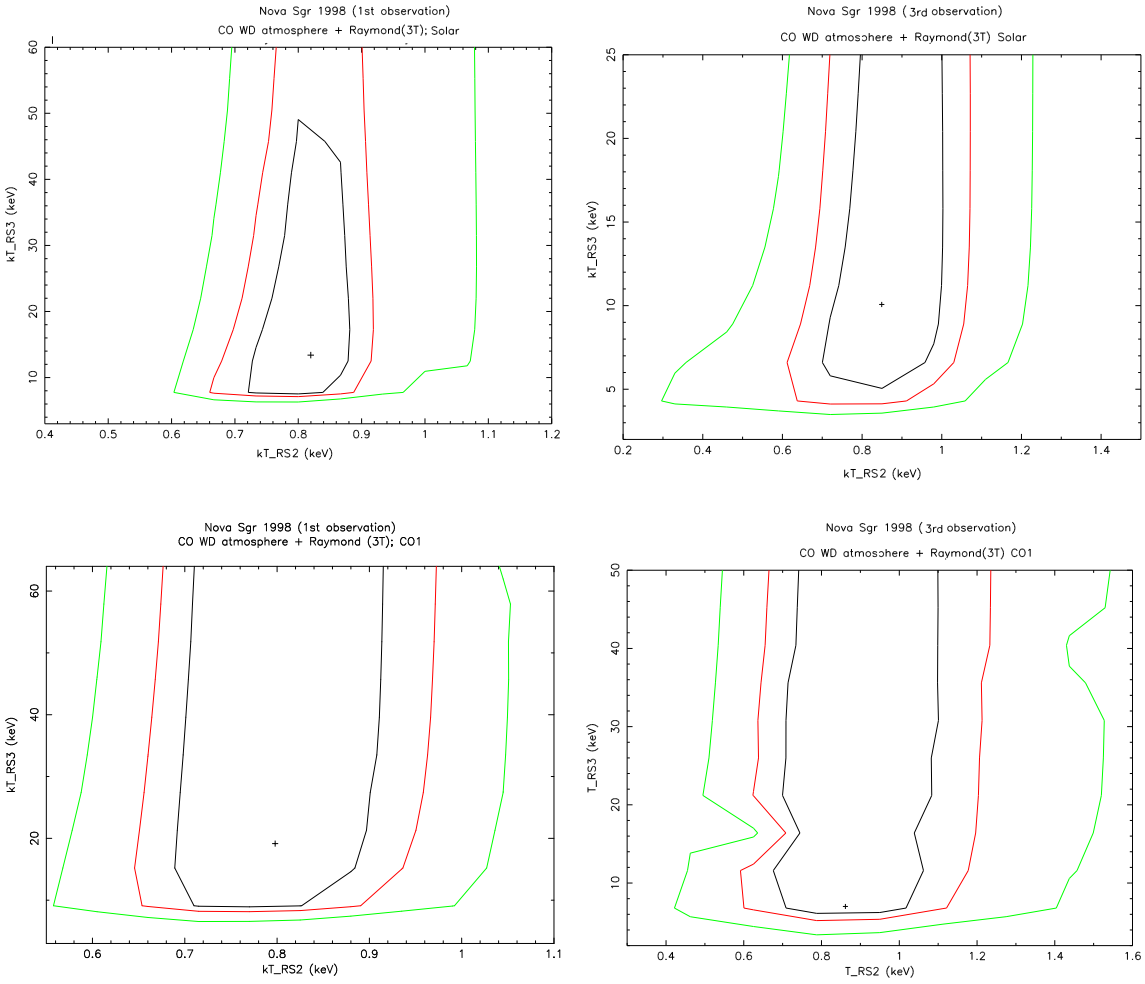

Figure 4.17: Confidence contours (1,2,and 3σ) for the plasma temperatures of the second (intermediate temperature) and third (hottest) Raymond-Smith components for the models with three temperatures, with solar (upper panels) and CO1 (lower panels) abundances for the 1st (left panels) and 3rd (right panels) observations of V4633 Sgr. The cross indicates the best-fit values.

Table 4.11: Electronic densities for the thermal plasma model with solar abundances assuming a constant expansion velocity of 1800 $km\,s^{-1}$.

	1^{st} observation Day 934	2^{nd} observation Day 1083	3^{rd} observation Day 1265	$n_e^{1st.obs}/n_e^{3nd.obs}$
$n_{e,1}(\times 10^3 cm^{-3})$	$4.8^{+4.0}_{-2.0}$	$3.2^{+29(2\sigma)}_{-1.0(3\sigma)}$	$5.0^{+8.5}_{-2.5}$	1.03
$n_{e,2}(\times 10^3 cm^{-3})$	$1.3^{+0.5}_{-0.4}$	$1.0^{+4.0}_{-5.0}$	$0.8^{+0.3}_{-0.2}$	0.63
$n_{e,3}(\times 10^3 cm^{-3})$	$2.9^{+0.7}_{-0.3}$	-	$1.6^{+0.2}_{-0.3}$	0.53

Table 4.12: Electronic densities for the thermal plasma model with CO1 abundances, assuming a constant expansion velocity of 1800 $km\,s^{-1}$.

	1^{st} observation Day 934	2^{nd} observation Day 1083	3^{rd} observation Day 1265	$n_e^{1st.obs}/n_e^{3nd.obs}$
$n_{e,1}(\times 10^3 cm^{-3})$	$0.7^{+1.0}_{-0.3}$	$0.4^{+4.1(2\sigma)}_{-0.3(3\sigma)}$	$0.4^{+1.1}_{-0.1}$	0.5
$n_{e,2}(\times 10^3 cm^{-3})$	1.0 ± 0.3	$1.0^{+4.0}_{-5.0}$	$0.6^{+0.3}_{-0.4}$	0.6
$n_{e,3}(\times 10^3 cm^{-3})$	$1.9^{+0.4}_{-0.5}$	-	1.0 ± 0.3	0.5

since day 850 after outburst, the emission volume at the time of our observations would be $1.3 \times 10^{49} cm^{-3}$ (for day 934), $2.0 \times 10^{49} cm^{-3}$ (for day 1083), and $3.2 \times 10^{49} cm^{-3}$ (for day 1265). With these volumes and the emission measures for the solar and the CO1 models from tables 4.9 and 4.10, electronic densities in the shell are obtained for each component and observation (see tables 4.11 and 4.12). Since the spherical geometry considered gives the maximum volume and it could be smaller (with the shell thickness smaller than the shell radius), the electronic densities listed in tables 4.11 and 4.12 are lower limits. The small electronic density agrees with the thinning of the ejecta found between days 525 and 850 by Lynch et al.(2001), who adopted a density of $10^4 cm^{-3}$ in their analysis.

The electronic density is expected to evolve with time as t^{-3} if a spherical shell is considered and the outer radius expands at constant velocity, or as t^{-2} if the shell thickness remains constant during expansion (Lyke et al.(2003)). With the first expansion picture, a decrease of a factor $\sim$0.55 is expected between the first and the third XMM-Newton observations, while the decay would be in a factor $\sim$0.4 in the second case. As listed in table 4.12, the decrease in the best-fit value of the electronic density for the CO1 model is 0.5 for the coolest thermal plasma component, 0.6 for the middle one and 0.5 for the hottest component, all compatible with the expansion of a spherical shell. For the solar model, the second and third component evolve as an expanding shell, but the density of the coolest component increases instead of decreasing with time. The excess of density in this cold component in the third observation may indicate that the gas is cooling down, and more amount of material is at low temperatures in the last observation than in the first one. Nevertheless, the CO1 model has abundances typical for ejected material in a nova outburst, and it is thus the first candidate to represent the expanding shell responsible for the thermal plasma emission from V4633 Sgr, rather than the model with solar abundances.

If accretion onto the white dwarf had been reestablished, and the emission were originated in the accretion flow, the typical electron densities expected would be larger than those in nova ejecta, with maximum values in the post-shock region of $n_e \sim 10^{15} - 10^{16} cm^{-3}$ (Ishida et al.(1994), Fujimoto & Ishida (1997)). Assuming $n_e \sim 10^{15} cm^{-3}$, our emission

measures indicate a corresponding emitting volume of $10^{24} - 10^{26} cm^{-3}$, which is close to the expected value for a post-shock region on top of an accreting white dwarf, with height $h \sim 3 \times 10^7 cm$ (see Fujimoto & Ishida (1997), where the model by Aizu (1973) is applied to the study of the X-ray emission of the intermediate polar EX Hya). However, the expected profile of temperatures according to Aizu's model is quite steep in the proximity of the white dwarf surface (Fujimoto & Ishida (1997)). Then, for a shock temperature of 10 keV, a temperature 100 times smaller (our lowest temperature, i.e. ~ 0.1 keV) would be confined to a really narrow region (with height $h \ll 3 \times 10^7 cm$), and its corresponding emission measure could not be similar to that of the hottest component. The increase in density expected is only a factor of 10 (Fujimoto & Ishida (1997)), so that it can not compensate the decrease in emitting volume. The shock temperature in the accretion flow obeys the relation $kT_{shock} = \frac{3}{8}\frac{GM\mu m_H h}{R}$ (Frank et al.(1985)), giving 18 keV for a $0.8 M_\odot$ white dwarf and 58 keV for a $1 M_\odot$ white dwarf. Plasma temperatures obtained for Nova Sgr 1998 are smaller than these. Both the values of the emission measures and the fact that they are similar for all temperatures indicate that the origin of the plasma emission is possibly different from accretion, i.e., that the source is the cooling ejected shell.

Table 4.13: EPIC exposure details of XMM-Newton observations of V2487 Oph.

Observation date	Camera	Exposure time (s)	Total counts (0.3-8.0 keV) (cts)	Count rate (0.3-8.0 keV) ($cts\,s^{-1}$)
Feb. 25, 2001	pn	-	-	-
	MOS1	6322	1989	0.301 ± 0.007
	MOS2	7616	2127	0.264 ± 0.006
Sep. 5, 2001	pn	4680	5028	1.06 ± 0.01
	MOS1	7513	2479	0.325 ± 0.007
	MOS2	7514	2511	0.327 ± 0.007
Feb. 26, 2002	pn	2662	2546	0.91 ± 0.02
	MOS1	5150	1533	0.278 ± 0.008
	MOS2	5145	2546	0.290 ± 0.008

4.6 Nova Oph 1998 (V2487 Oph)

Nova Oph 1998 (V2487 Oph) was optically discovered in outburst on 1998 June 15.561 UT (Nakano et al.(1998)), with a visual magnitude of 9.5. Spectral observations on 18 June 1998 confirmed it as a nova (Filippenko et al.(1998)). It was a very fast nova, with $t_2 \approx 6.3$ days and $t_3 \approx 9.5$ days (Liller & Jones (2000)). Lynch et al.(2000) determined the distance to the source to be 27 ± 3 *kpc*. Given the galactic coordinates of the source (6.60 ,+7.77), this would situate V2487 Oph at the other end of the Galaxy and at 3.65 *kpc* over the galactic plane, out of the disk. This distance is unusually large and its determination must be taken with caution. Lynch et al.(2000) used an empirical relation to determine the absolute visual magnitude, M_V^{max}, from t_2, the apparent visual magnitude at discovery and the visual extinction ($A_V = 1.16 \pm 0.24$ mag) derived from the colour excess $E_{B-V} = 0.38 \pm 0.08$, which they obtained from the observed OI λ8446 and λ11287 near-infrared lines. Since the nova was a very fast one and quite faint at discovery, it is possible that the actual maximum had been missed and that the true m_V^{max} had been brighter. Extrapolating the visual light curve back in time to the pre-discovery data using the expression in Harris et al.(1999), the true m_V^{max} can be estimated to be between 6.8 and 9.5. With $M_V^{max} = -8.8$ (derived from the empirical $M_V^{max} - t_2$ relation) and $A_V = 1.16$, V2487 Oph could be somewhere between 8 and 27 *kpc*. Given the large uncertainty in the distance determination, we scale all the magnitudes derived from observations to a distance of 10 *kpc*.

XMM-Newton observed V2487 Oph 2.7, 3.2 and 3.7 years after outburst (see table 4.2). Since around 2000 seconds of the third observation were affected by a flare, a fourth observation was performed 4.3 years after the outburst (still to be analyzed). In all observations, the nova was detected as a bright X-ray source. The main results of the first two observations were reported in Hernanz & Sala (2002).

4.6.1 Spectral analysis

The X-ray spectrum detected with the EPIC cameras (shown in figures 4.18-4.20) spans up to $\sim 8\,keV$ with a higher count rate than V4633 Sgr. The spectrum is dominated by thermal plasma emission, which can be modelled by a two-temperature MEKAL model (Mewe et al.(1995), included in XSPEC, see appendix F). The parameters of the fits are summarized in table 4.14. The best-fit thermal plasma model has a cool component, at 0.2-0.3 *keV,* and a hot component, with temperatures above ~ 64 *keV* for the second and

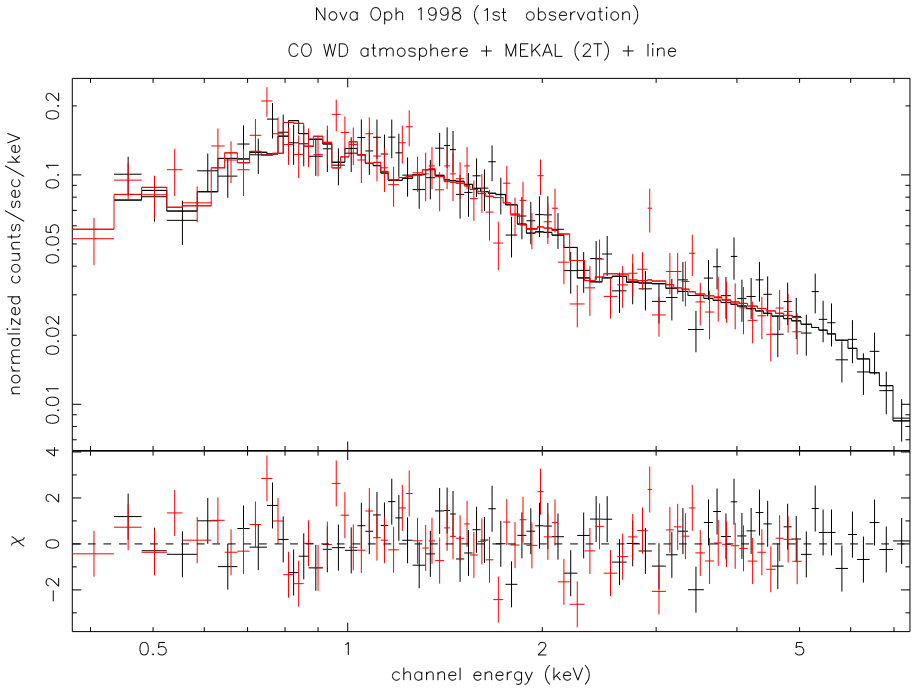

Figure 4.18: V2487 Oph observed spectra 2.7 years after outburst and best fit model. The lower panel indicates residuals (data minus folded model) in terms of sigmas, with error bars of size one. Data from the two EPIC MOS cameras are shown: MOS1 (black) and MOS2 (red).

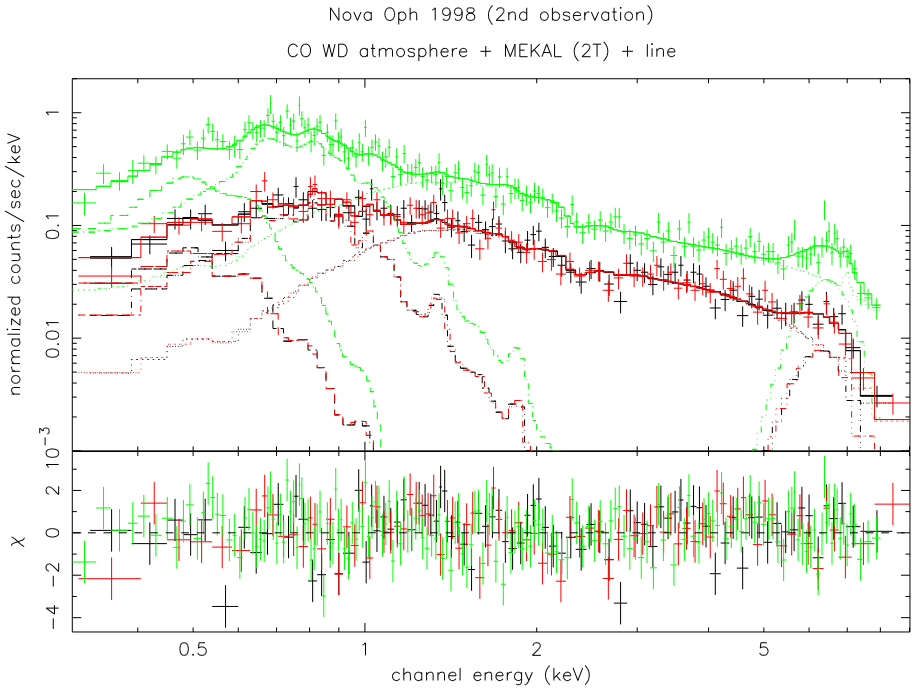

Figure 4.19: V2487 Oph observed spectra 3.2 years after outburst and best fit model. The lower panel indicates residuals (data minus folded model) in terms of sigmas, with error bars of size one. Data from the three EPIC cameras are shown: pn (green, with higher count-rate), MOS1 (black) and MOS2 (red), as well as the contribution of each component of the best-fit model (from left to right, white dwarf atmosphere, low temperature MEKAL, high temperature MEKAL and Gaussian emission line).

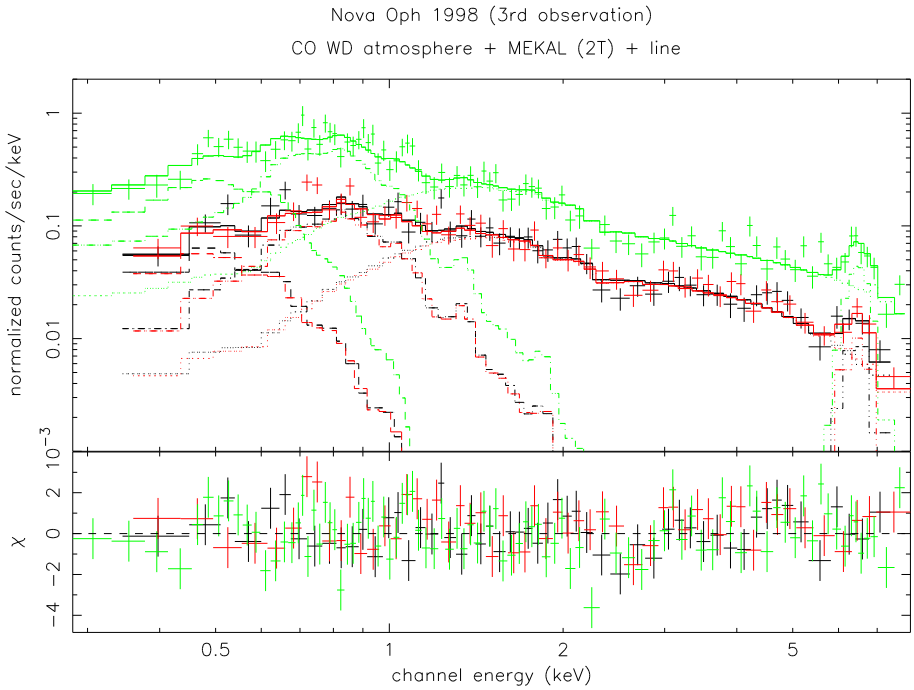

Figure 4.20: V2487 Oph observed spectra 3.7 years after outburst and best fit model. The lower panel indicates residuals (data minus folded model) in terms of sigmas, with error bars of size one. Data from the three EPIC cameras are shown: pn (green, with higher count-rate), MOS1 (black) and MOS2 (red), as well as the contribution of each component of the best-fit model (from left to right, white dwarf atmosphere, low temperature MEKAL, high temperature MEKAL and Gaussian emission line).

third observations (and above $\sim 10\ keV$ in the first one). The plasma spectrum at these high temperatures is very flat, and the temperature is not well constrained. In the case of the first observation, data from the pn camera are missing, and the parameters of the model are in general less constrained than in the second and third observations.

In all observations, with this two-component model, the data show an excess around $\sim 6.4 - 6.5\ keV$. An additional Gaussian line centered at this energy and with a width $\sigma \sim 0.6\ keV$ can account for this excess (see figure 4.21 for the confidence contours of the line energy and its width). The two temperature thermal plasma model can not account neither for the soft part of the spectrum, which is well fitted with a white dwarf atmosphere model (from MacDonald & Vennes (1991), see appendix E), absorbed by a hydrogen column density of $N_H = 4 \times 10^{21} cm^{-2}$, slightly larger than the average interstellar absorption in the direction of the source ($2 \times 10^{21} cm^{-2}$, Dickey & Lockman (1990)). The best fit is obtained with effective temperatures between 64 and 74 eV, depending on the observations, and a bolometric luminosity $\sim 10^{35} erg\, s^{-1}$ (assuming a distance of 10 kpc), which implies a radius of the emitting region of $3 \times 10^7 cm$ for the first observation and of $\sim 1.6 \times 10^7 cm$ in the second and the third ones. This is clearly smaller than the whole white dwarf surface, indicating that it must be associated to a hot emitting region of the star.

Although the spectral model that fits the data is the same in the three observations, the total observed flux decreases with time. Nevertheless, since EPIC pn data are missing in the first observation and the exposure time free from flaring background is much smaller in the third observation, no conclusions regarding the evolution can be safely drawn.

Table 4.14: V2487 Oph best-fit model spectral parameters, with 1σ errors.

	1st obs	2nd obs	3rd obs
$kT_{atm}(eV)$	64±5	72^{+3}_{-7}	74^{+6}_{-5}
$L_{atm}(\times 10^{35} erg\, s^{-1})^{(1)}$	2±1	$1.4^{+0.3}_{-0.2}$	$1.4^{+0.3}_{-0.2}$
$kT_1(keV)$	0.26±0.03	$0.25^{+0.01}_{-0.02}$	$0.27^{+0.02}_{-0.03}$
$kT_2(keV)$	>10	>64	>64
$EM_1(\times 10^{57} cm^{-3})^{(1)}$	1.3±0.8	$1.8^{+0.4}_{-0.2}$	$1.3^{+0.4}_{-0.2}$
$EM_2(\times 10^{57} cm^{-3})^{(1)}$	3.1±0.1	3.4±0.5	3.1±0.6
$E_{line}(keV)$	6.4±0.4	6.49±0.07	6.50±0.05
$\sigma_{line}(keV)$	1.2±0.4	0.61±0.08	0.27±0.05
$F_{line}(\times 10^{-5} phot\, cm^{-2} s^{-1})$	14±8	7±2	4±1
$F^{total}_{absorbed}(\times 10^{-12} erg\, cm^{-2}\, s^{-1})^{(2)}$	4.8	4.6	4.0
$L^{total}_{absorbed}(\times 10^{34} erg\, s^{-1})^{(3)}$	5.7	5.5	4.8
χ^2_ν	1.07	1.13	1.24

(1) White dwarf atmosphere luminosity and emission measures of the thermal plasma components are given for a distance of d=10 kpc. For other distances, a factor $\left(\frac{d}{10kpc}\right)^2$ affects these values.

(2) Total absorbed flux, in the range 0.22-8.0 keV.

(3) Total model luminosity in the range 0.22-8.0 keV, for a distance of 10 kpc. For other distances, a factor $\left(\frac{d}{10kpc}\right)^2$ affects this value.

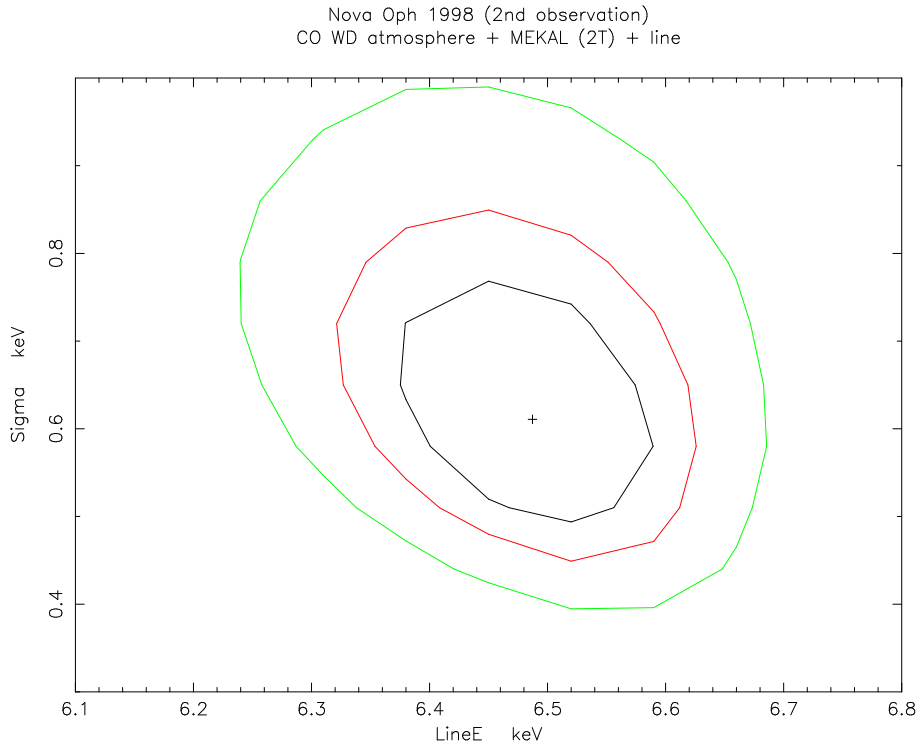

Figure 4.21: 1σ, 2σ and 3σ confidence contours for the energy and width of the emission line added to the thermal plasma model of V2487 Oph for the second observation, 3.2 years after outburst.

4.6.2 Discussion

The most remarkable feature of V2487 Oph X-ray spectrum is the emission line at $\sim 6.4 - 6.5\,keV$. The fact that it must be simulated with an additional Gaussian line, added to the MEKAL model, which already includes the iron emission lines of the thermal plasma, indicates that it must be powered by some extra mechanism. A fluorescent line at 6.41 keV can be produced by cold, neutral iron. Other fluorescent lines can be emitted at higher energies by iron in intermediate states of ionization (Hellier et al. (1998)). The main fluorescent Kα line emitted by cold, neutral iron could thus explain the emission line observed for V2487 Oph, while the blend with other fluorescent lines could explain the width of the line. An emission line at this energy had never been observed before in a post-outburst classical nova, but is a common feature in accreting white dwarfs in cataclysmic variables. The intermediate polars EX Hya and AO Pisc showed this kind of emission (thermal plasma plus fluorescent line), as observed with ASCA (Advanced Satellite for Cosmology and Astrophysics) (Ishida et al.(1994), Hellier et al.(1996), Fujimoto & Ishida (1997)).

The fluorescent Fe K_α line can only be induced by reflection of the X-rays generated in the hot post-shock region of the accretion flow on neutral iron, i.e, on colder material of the disk or the white dwarf. A reflection effect requires therefore that accretion had been reestablished by the time of observations. The thermal plasma emission modelled by the two temperature plasma model would arise then from the shocked gas in the accretion flow (Patterson & Raymond (1985)), and the reflection of its X-rays on the accretion disk or on the white dwarf surface would produce the Fe K_α line.

As mentioned above, the kind of spectra found for V2487 Oph is similar to that observed for the intermediate polars EX Hya and AO Pisc (Ishida et al.(1994), Hellier et al.(1996), Fujimoto & Ishida (1997)). Nevertheless, those cataclysmic variables had thermal plasma spectra steeper than V2487 Oph, indicating cooler plasmas in the accretion stream. The high temperatures in the shocked plasma may be a consequence of accretion onto a massive white dwarf, which would agree with the mass determination of Hachisu et al.(2002), $M_{WD} = 1.35 M_\odot$, from the visual light curve and the numerical model described in Hachisu & Kato (2001).

The parameters of the soft component of the spectrum indicate that it can not be associated to the emission from the whole white dwarf surface, i.e., it can not be produced by hydrogen burning on the star's envelope. Nevertheless, in the absence of residual hydrogen burning, a part of the white dwarf surface can be heated by the hard X-ray radiation from the accretion flow. This kind of emission is common in other accreting systems, specially in polar cataclysmic variables: the white dwarf surface below the shock region of the accretion stream is heated up to temperatures larger than $10^5 K$ by the hard X-rays emitted in the accretion column, and by direct injection of kinetic energy by dense blobs of material (Mukai (2003)). As a result, only a fraction of the white dwarf surface is emitting soft X-rays, as observed for V2487 Oph. The effective temperature of the soft component detected in V2487 Oph is compatible with this process, and similar values are obtained for other cataclysmic variables (Ramsay & Cropper (2003), Ramsay & Cropper (2004)). The presence of this soft component, typical of magnetic cataclysmic variables, also supports the surprisingly fast resumption of accretion, less than 1000 days after the nova event.

The hydrogen column density that affects the soft component is slightly larger than the average interstellar absorption in the direction of the source ($2 \times 10^{21} cm^{-2}$, Dickey & Lockman (1990)). The additional absorption may be also due to the contribution of the accretion column.

The large luminosity of the thermal plasma components, the small slope of the spectrum

and the soft component may indicate that V2487 Oph is a magnetic system. Nevertheless, the large uncertainty in the distance prevents a good determination of the luminosity. In addition, no evident periodicity related to the rotation the white dwarf or the orbital motion has been found in our data. The presence of a magnetic field has been pointed out as a difficulty for the formation of the accretion disk and the development of the thermonuclear runaway that powers the nova outburst (Livio et al.(1988)), but other novae have been found to have exploded on magnetic white dwarfs (as V1500 Cyg, DQ Her and GK Per).

4.6.3 ROSAT detection of the pre-nova cataclysmic variable

At the same position as V2487 Oph, an X-ray source (1RXS J173200.0-1934) was detected by ROSAT during the RASS (ROSAT All-Sky Survey, Voges et al.(1999)), in September 1990, 8 years before the nova event. 1RXS J173200.0-1934 is one of the 18,811 sources included in the ROSAT All-Sky Survey Bright Source Catalogue, which contains all sources detected with a PSPC count-rate larger than 0.05 $cts\,s^{-1}$ in the 0.1-2.4 keV band, with a detection likelihood of at least 15 and at least 15 counts.

At the time of the nova discovery, in 1998, Nakano et al.(1998) already noted that the position of the nova lay in the 16-arcsec ROSAT error box of 1RXS J173200.0-1934, but the indetermination in the RASS source position prevented to identify the X-ray source with the nova. XMM-Newton provided much better spatial resolution, and showed that the positions of V2487 Oph and 1RXS J173200.0-1934 are closer than the EPIC angular resolution, i.e., less than ~ 6 arcsec apart. This indicates that the source detected in the RASS was probably the accretion powered cataclysmic variable prior to the nova explosion. Since the X-ray emission detected by the XMM-Newton instruments is mainly associated to the accretion flow, as was at the time of the ROSAT observation, the fluxes are expected to be similar in both cases. The 1RXS J173200.0-1934 flux detected in September 1990 ($(3.3-8.9)\times10^{-13} erg\,cm^{-2}s^{-1}$, from the RASS Bright Source Catalogue, 1RXS-B, Voges et al.(1999)) is indeed similar to that from XMM-Newton in the same energy range (0.75-2.4 keV, $F = 9.4\times10^{-13} erg\,cm^{-2}s^{-1}$). The short exposure time in the RASS observation, 426.7s, with a total count-rate of $(8.6\pm1.8)\times10^{-2} cts\,s^{-1}$, and the limited spectral range with significant data (0.75-2.4 keV) make impossible a good analysis of the spectral energy distribution. Nevertheless, we have obtained the spectrum for 1RXS J173200.0-1934 and found it to be compatible with a spectral model equivalent to the best-fit for V2487 Oph (see figure 4.22). With this detection, Nova Oph 1998 becomes the first classical nova whose accreting binary system was detected in X-rays before the outburst, supporting the cataclysmic variable scenario for nova explosions.

4.7 Summary

Five recent post-outburst classical novae have been monitored with XMM-Newton, with three observations every six months for each source. Two of the five observed targets are bright X-ray sources, with their X-ray emission spanning the whole energy range of the EPIC cameras, 0.2-8 keV.

The X-ray spectrum of Nova Sgr 1998 (V4633 Sgr) is compatible with the emission from a hot white dwarf plus the thermal plasma emission of the expanding shell, although the possible reestablishment of the accretion flow can not be ruled out. The spectral analysis shows that the white dwarf can not be still burning hydrogen on its surface, and must be already on the cooling path. Regarding the thermal plasma emission that dominates the spectrum detected by the EPIC cameras, the best-fit model is a three-temperature thermal plasma, with temperatures $\sim 0.1\,keV$, $\sim 1\,keV$ and $30-40\,keV$ (although no upper limit

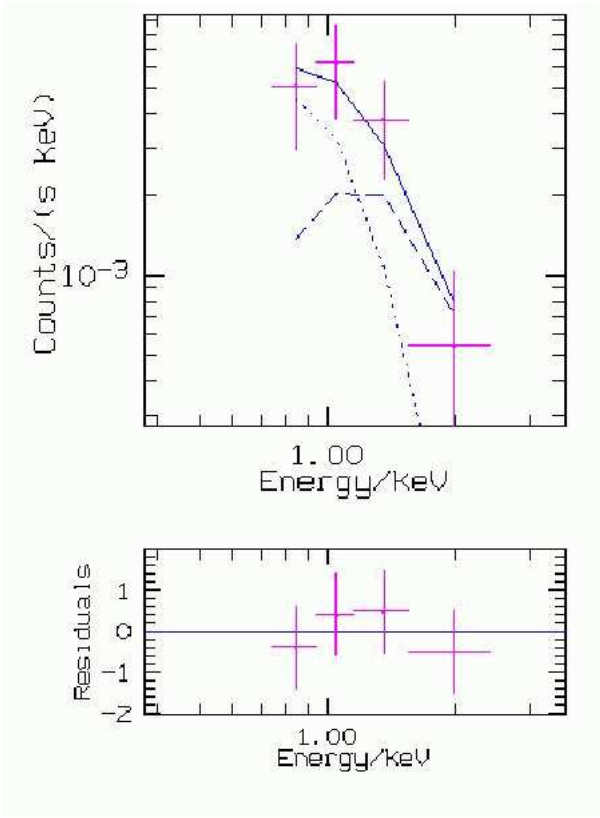

Figure 4.22: 1RXS J173200.0-1934 spectra obtained during the ROSAT All Sky Survey (RASS) on September 1990.
The solid line shows a model equivalent to the best-fit model for V2487 Oph EPIC spectra: two thermal bremsstrahlung models, with kT_1=0.2 keV (dotted line) and kT_2=48 keV (dashed line), both with similar normalization constants (as in the best fit model for V2487 Oph) and with $N_H = 4 \times 10^{21} cm^{-2}$. EXSAS (Zimmerman et al.(1998)) has been used for the data reduction and spectral analysis (see appendix **??** for details on ROSAT data reduction-).

is found for this component) and with either solar or CO enhanced abundances. The temperature range includes the temperature expected from a shocked plasma, both for nova shells or in the accretion flow. The unabsorbed luminosity of the plasma is also compatible with the X-ray emission from other observed nova shells, and also with that observed in intermediate polars. The electronic densities decrease by a factor 0.5-0.6 between the first and the last observation, which is the decrease expected for a spherical expanding shell. This would favour the ejecta as the possible site of the thermal plasma emission, but the reestablishment of accretion can not be ruled out.

XMM-Newton observations of Nova Oph 1998 (V2487 Oph) revealed that accretion had reestablished on the cataclysmic variable less than 1000 days after outburst. When the spectrum is fitted with a two temperature thermal plasma model, an excess around 6.4 keV indicates the presence of an iron K_α fluorescence line, which is a clear signature of accretion. The soft part of the spectrum is incompatible in this case with emission from hydrogen burning on the white dwarf envelope, but must be associated instead to a fraction of the surface heated by the X-ray radiation from the post-shock region of the accretion flow. Interestingly enough, the cataclysmic variable hosting Nova Oph 1998 was detected during the ROSAT All Sky Survey 8 years before the nova outburst, with a flux and an energy distribution compatible with the results obtained by XMM-Newton. With this detection, V2487 Oph becomes the first classical nova whose accretion has been observed in X-rays before and after the outburst.

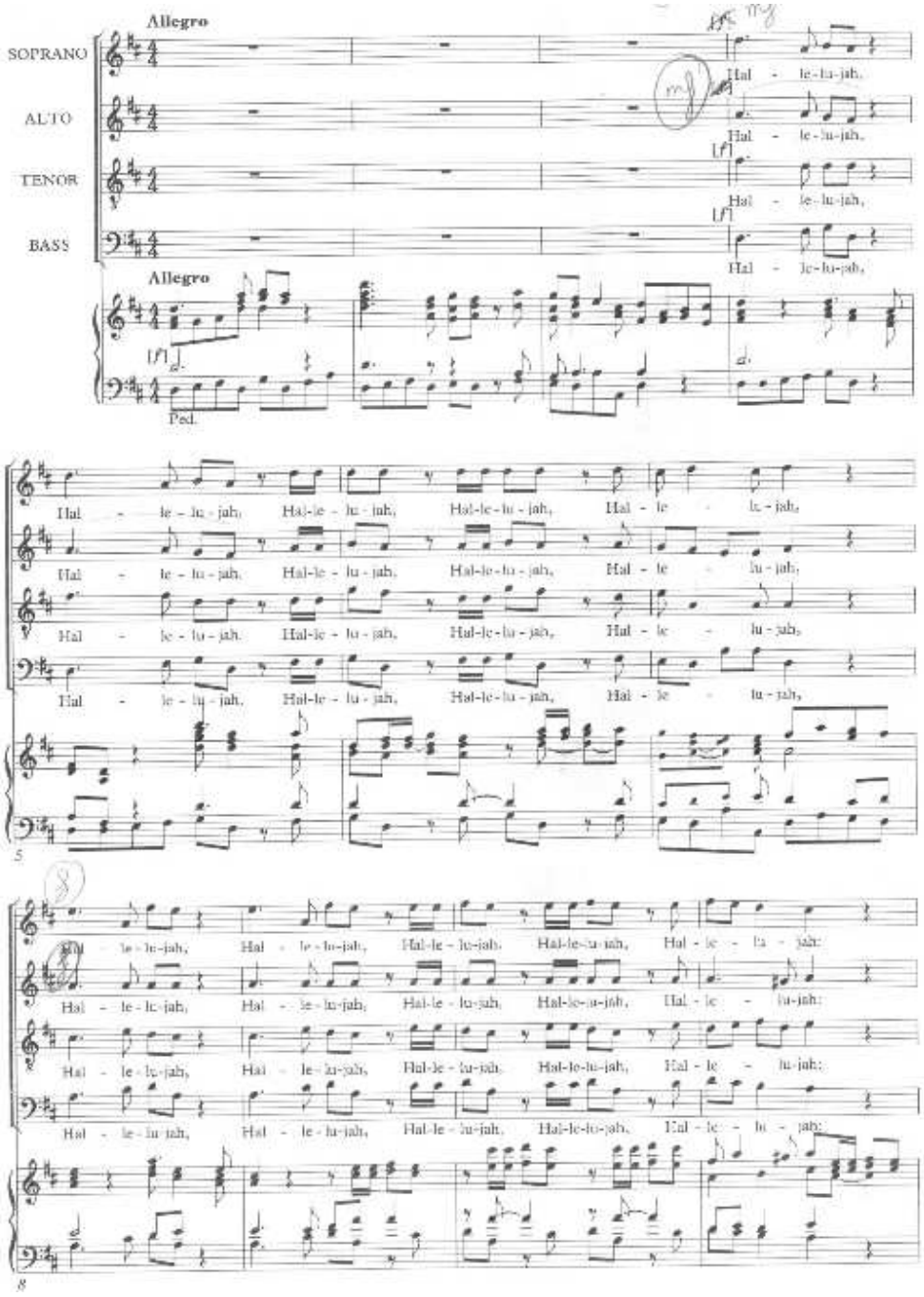

"Hallelujah"

The Messiah,

G. F. Händel

Chapter 5

Conclusions

The problem of the turn-off of classical novae has been studied in this work both from theoretical and observational points of view. A numerical code has been developed to model hot, hydrogen burning white dwarf envelopes and simulate the properties of their X-ray emission. Results have been compared to X-ray observations of classical novae from the ROSAT archival data. In addition, new observations of post-outburst classical novae have been performed with XMM-Newton.

The white dwarf envelope models

White dwarf envelope models with steady hydrogen burning have been calculated for realistic compositions of accreted envelopes in classical novae, and their evolution has been approximated as a sequence of steady states. Results show that, for a given white dwarf mass and composition, the envelope evolves in the HR diagram increasing its effective temperature along a plateau of quasi-constant luminosity, while its mass is slowly reduced due to hydrogen burning. Both the luminosity and the average envelope mass during the plateau depend on the white dwarf mass and hydrogen mass fraction. The linear core-mass luminosity relation found in this work is compatible with previous determinations of this relation for white dwarf envelopes with different compositions (for instance, Iben (1982), Tuchman & Truran (1998)). Envelope masses are smaller than those obtained for studies of hydrogen richer (and metal poorer) envelopes (Iben (1982)).

The envelope masses for which stable hydrogen burning can occur are smaller than the accreted envelope mass needed to trigger the nova outburst. Since hydrodynamic models show that the outburst ejects only a fraction of the accreted material, it seems clear that some extra mass loss mechanism must reduce the envelope mass after the nova outburst. In addition to some mechanisms already suggested (common envelope, MacDonald et al.(1985), and thick wind, Kato & Hachisu (1994)), it would be interesting to study if the hydrodynamical instabilities that could appear in an envelope left with a mass too large for stable hydrogen burning could get rid of some of the mass excess (as first suggested by Tuchman & Truran (1998)).

The constant bolometric luminosity phase lasts until the envelope mass is reduced down to a critical value, below which steady hydrogen burning can not proceed and the source turns off. This minimum envelope mass occurs in the proximity of the maximum effective temperature, which is therefore reached just before the turn off. The maximum effective temperature, which also depends on the white dwarf mass and envelope hydrogen mass fraction, is a useful parameter for comparison with X-ray observations, since it does not depend on the distance determination. Nevertheless, it can only constrain the properties of the nova if monitoring observations are performed and the maximum effective temperature

is not missed.

After the steady hydrogen burning phase, the white dwarf is left with a helium rich layer resulting from hydrogen burning plus a hydrogen rich envelope (with the minimum critical mass for which hydrogen burning stops). When accretion reestablishes in the system, the newly hydrogen-rich accreted envelope will need to overcome this buffer to reach the degenerate core and be enhanced with the CNO nuclei required for the outburst to occur. The results from our envelope models provide the mass of this remaining envelope, which should be taken into account for studies of the mixing processes.

For the envelope masses of our models with compositions typical for classical novae, the nuclear timescales range from some months to a few years. The quasi-static approximation shows indeed that the evolution proceeds at a rate that ranges from a few days to some months for a change of 10 eV of the effective temperature, depending on the white dwarf mass and hydrogen mass fraction. These time scales are compatible with the ROSAT observations of the three novae that showed soft X-ray emission associated to the hydrogen burning envelope. The cases where no soft X-ray emission was detected could correspond to massive white dwarfs, or very hydrogen poor envelopes, for which the duration of the hydrogen burning phase is, according to our models, of only a few days. With a very short duration, the soft X-ray emission was probably missed. It is in fact possible that it never became visible, since the source could have turned off before the ejecta became transparent to X-rays.

Comparison with ROSAT archival data

The results of our white dwarf envelope models have been compared to archival ROSAT observations of the three classical novae that showed soft X-ray emission during the ROSAT operational phase (V1974 Cyg, GQ Mus, N LMC 1995). From this comparison, the white dwarf mass, envelope mass, turn-off times and hydrogen abundances of the observed novae have been constrained. For V1974 Cyg, ROSAT observations followed the whole rise, plateau and decline of its X-ray lightcurve, thus making possible a good comparison with the predicted evolution. Our models show that the evolution of its soft X-ray emission is compatible with the envelope of either an ONe nova of 0.9 $M_{\odot}$ with 50% mixing, or an ONe nova of $1.0 M_{\odot}$ with 25% mixing, with a turn-off time between 8 and 15 months. In the cases of GQ Mus and nova LMC 1995, the evolution was not followed observationally so well as in the case of V1974 Cyg. For GQ Mus, optical and UV observations of the ionized nebula are combined with ROSAT observations to constrain the properties of the central soft X-ray source, indicating that the mass of the white dwarf can be $1.1 \pm 0.1 M_{\odot}$. The two observations of Nova LMC 1995 (the second one with XMM-Newton) show a slow evolution of the soft X-ray source, only compatible with models for hydrogen rich envelopes on a small white dwarf.

In all previous cases, the comparison of observations with the envelope models relies on the values of the effective temperature and its evolution, independent of the distance determination. Since distances to nova are usually very bad constrained, this represents a major improvement and a powerful tool for studies of classical novae. Previous determinations of the white dwarf masses in classical novae relied on core mass-luminosity relations, with all the uncertainty in the distance affecting the luminosity and therefore the mass.

Our envelope models with steady hydrogen burning can also be used in the future for analysis of Supersoft X-ray Sources, whose X-ray emission is powered by steady hydrogen burning on the surface of a white dwarf in a close binary. The accretion rate in these systems equals the rate of mass decrease due to hydrogen burning, and thus keeps the source in a steady state. For long enough accretion phases, the white dwarf can reach the

Chandrasekhar mass, which makes supersoft X-ray sources good candidates for type Ia supernovae.

XMM-Newton observations

Keeping the determination of the turn-off time of classical novae as the main goal, monitoring observations of recent novae have been performed with XMM-Newton. Five novae have been observed between two and four years after the outburst. Two of them are bright X-ray sources, with their X-ray emission spanning the whole energy range of the EPIC cameras, 0.2-8 keV. In both cases, the spectrum indicates that the main origin of the X-rays is not photospheric, and that hydrogen burning has ceased on the white dwarf envelope, thus indicating turn-off times shorter than $\sim$ 3 years.

The X-ray spectrum of Nova Sgr 1998 (V4633 Sgr) is dominated by thermal plasma emission, which can be due to the shock-heated expanding shell, or to the possible reestablishment of the accretion in the system. The best-fit model is a three-temperature thermal plasma, with temperatures between 0.1 keV and 40 keV. Thermal plasma models with different compositions (solar, and several CO and ONe enhanced from realistic nova models) have been tried, and the best-fit is obtained either with a CO enhanced model, or with the solar abundances. The first case would correspond to emission from the expanding nova shell. The unabsorbed luminosity of the thermal plasma component is indeed compatible with the X-ray emission from other observed nova shells, as well as the electronic densities derived from the emission measure. The possibility of accretion being reestablished, which would be simulated by the solar thermal plasma model, can not be ruled out. In this case, the luminosity of the plasma would be compatible with accretion in a intermediate polar cataclysmic variable. Optical observations of V4366 Sgr also support the magnetic character of this nova, indicating that it is a nearly synchronous system (Lipkin et al.(1998)).

XMM-Newton observations of Nova Oph 1998 (V2487 Oph) surprised us showing that accretion had been reestablished on the cataclysmic variable less than 1000 days after outburst (Hernanz & Sala (2002)). The spectrum in this case is also dominated by thermal plasma emission, but an additional excess around 6.4 keV indicates the presence of iron K_α fluorescent lines. Fluorescent lines can only arise from reflection effects, which imply the reestablishment of accretion by the time of observations. The spectrum shows also a soft component associated to a fraction of the white dwarf surface heated by hard X-rays from the accretion shock region, which is another common feature in accreting cataclysmic variables, specially on magnetic systems. The high temperature and large luminosity of the thermal plasma emission also indicate that V2487 Oph probably occurred on a magnetic white dwarf.

V2487 Oph is twice exceptional, since the cataclysmic variable hosting Nova Oph 1998 was also detected eight years before the outburst during the ROSAT All Sky Survey. This detection makes V2487 Oph the first classical nova detected in X-rays before and after the outburst, and supports the cataclysmic variable scenario for classical novae.

Livio et al.(1988) pointed out that the presence of a magnetic field in the cataclysmic variable may prevent the formation of the accretion disk and the development of the thermonuclear runaway. Nevertheless, V2487 Oph has clearly reestablished its accretion onto a magnetic white dwarf in a surprisingly short period of time after the outburst, and other post-novae cataclysmic variables have been found in the past to have magnetic fields (V1500 Cyg, DQ Her, GK Per). The fast recovery of the accretion flow in V2487 Oph may indicate that the outburst does not completely halt the accretion flow, and that the magnetic field does not seem to prevent accretion.

The exceptional spectrum of V2487 Oph deserves a more detailed study, and the nature of the emission observed in V4633 Sgr (accretion or cooling shell) can only be disentangled with longer observations. Our proposal for more observations of V2487 Oph and V4633 Sgr with longer exposure times has been accepted for the present observing cycle of XMM-Newton. The high resolution spectra that could be obtained with these observations would allow us to determine more precisely the abundances in the plasma spectrum. This would make possible to distinguish between the metal enhanced ejecta and the solar-like accreting material, and to determine whether the fluorescent emission observed in V2487 Oph is due to a unique or to multiple lines. It would be possible, in addition, to see the evolution of these sources six years after the outburst.

The results obtained in this work show clearly that the new generation of X-ray observatories provide new insights into the nature of classical novae. It is clear that access to all wavelengths of the spectrum is needed for a full understanding of these objects. The simultaneous flight of Chandra and XMM-Newton offers an exceptional opportunity for these studies, which must be taken advantage of while these missions are still in orbit.

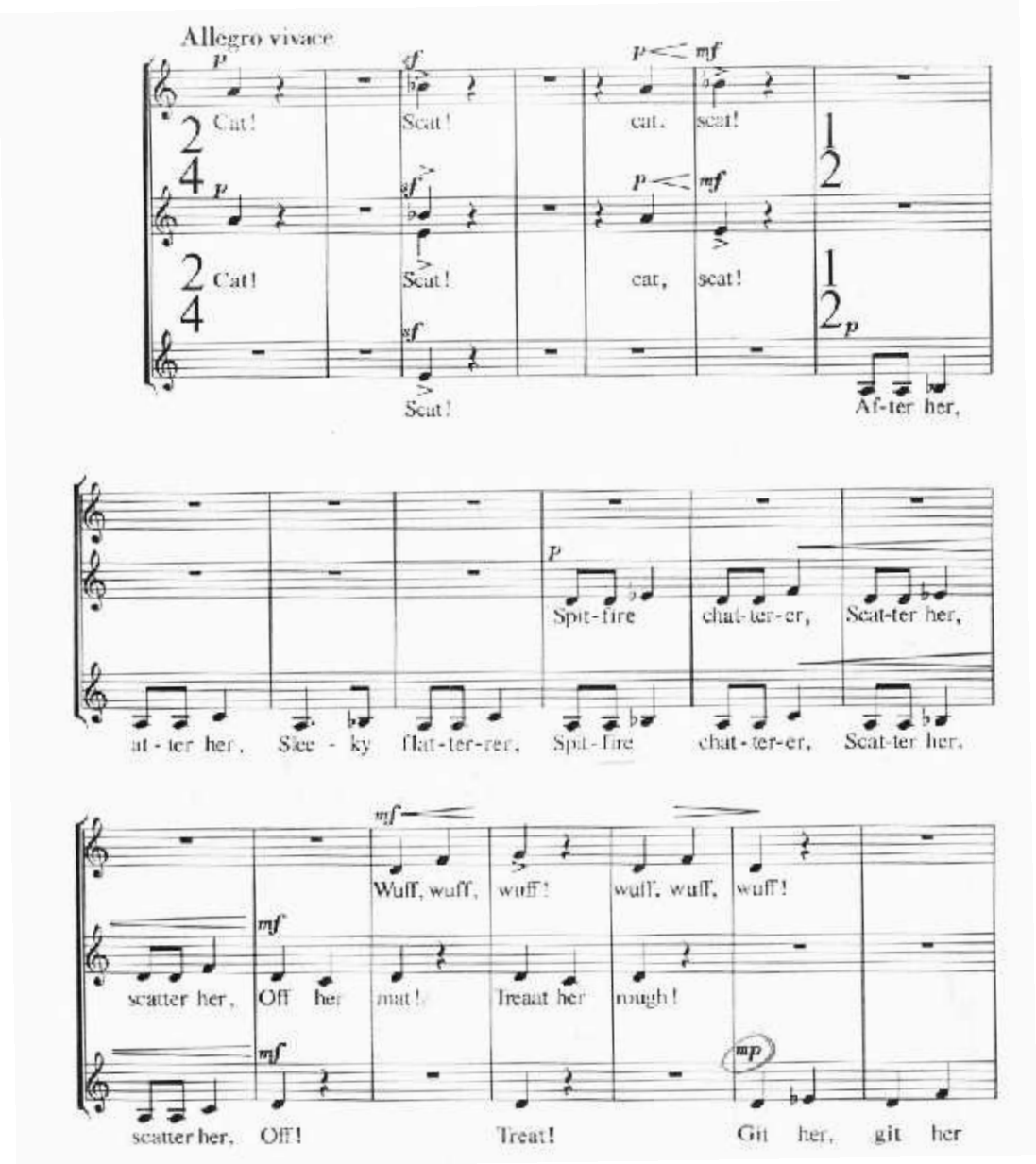

Cat

Miklós Cocksár

(dedicat a la Leina, la Xana i el Taqueta)

Bibliography

Aizu, K. 1973, *Progr.Theor.Phys.*, **49**, 1184

Allen, C.W., **Astrophysical Quantities**, The Athlone Press, 1973.

Arnaud, K.A. 1996, in **Astronomical Data Analysis Software and Systems V**, eds. Jacoby G. and Barnes J., p.17, ASP Conf. Series volume 101. (http://heasarc.gsfc.nasa.gov/ lheasoft/ xanadu/ xspec/ index.html)

Austin, S.J., Wagner, R.M., Starrfield, S., Shore, S. N., Sonneborn, G. & Bertram, R. 1996, *AJ*, **111**, 869

Balman, S., Orio, M. & Ögelman, H. 1995, *ApJ*, **449**, L47

Balman, S., Krautter, J. & Ögelman, H. 1998, *ApJ*, **499**, 395

Balman, S., & Ögelman, H. 1999, ApJ, 518, L111

Balman, S. & Krautter, J. 2001, *MNRAS,* **326**, 1441

Balman, S. 2002, in **Classical Nova Explosions**, eds. M.Hernanz & J.José, AIP Conference Proceedings, vol. 637, p. 365

Beckmann, K. & Collins, P. 1987, *IAU Circ.* 4488

Böhm-Vitense, E. 1958, *Zs. f. Ap.*, **46**, 108.

Bowers, R.L. & Deeming, T., **Astrophysics**, Jones and Bartlett Publishers, Sudbury, MA, 1984.

Brecher, K., Ingham, W.H. & Morrison, P. 1977, *ApJ*, **213**, 492

Briel, U.G. et al. 1997, **ROSAT User's Handbook**, Max-Planck-Insitut für extraterrestrische Physik.

Burwitz, V., Starrfield, S., Krautter, J. & Ness, J.U. 2002 in **Classical Novae Explosions**, eds. M. Hernanz & J. José, AIP Conference Proceedings, vol. 637, p. 386

Camilleri, P. 1992, *IAU Circ.* 5422

Cassatella, A., Lamers, H.J.G.L.M., Rossi, C., Altamore, A., & González-Riestra, R. 2004, *A&A*, **420**, 571

Cash, J.R. & Karp, A.H. 1990, *ACM Transactions on Mathematical Software*, **16**, 201.

Chochol, D., Grygar,J., Pribulla, T., Komzik, R., Hric, L. & Elkin, V. 1997, *A&A*, **318**, 908

Christy, R.F. 1966, *ApJ*, **144**, 108

Clayton, D., **Principles of Stellar Evolution and Nucleosynthesis**, McGraw-Hill, 1968.

Collins, P. 1984, *IAU Circ.* 4023

Collins, P. 1992, *IAU Circ.* 5454

Crawford, J.A. & Kraft, R.P. 1956, *ApJ*, **123**, 44

Cox, J.P. & Stewart, J. 1970a, *ApJS*, **19**, 243

Cox, J.P. & Stewart, J. 1970b, *ApJS*, **19**, 261

Cox, J.P. & Giuli, R.T., **Principles of Stellar Structure**, Gordon & Breach Science Publishers, 1968.

Ehle, M., Breitfellner, M. , Gonzalez-Riestra, R., Guainazzi, M., Rodriguez, P., Santos-Lleo, M., Schartel, N., Tomas, L., Verdugo, E. & Dahlem, M. **XMM-Newton Users' Handbook**, Issue 2.1, 2003

Della Valle M., Pizzella A., Bernardi M., Jones A.F., Kiss L., Hornoch K., Schmeer P. & Trigo J.M. 1998, *IAU Circ.* 6848

den Herder, J.W. et al. 2001, *A&A*, **365**, L7

Dickey, J.M. & Lockman, F.J. 1990, *ARAA*, **28**, p215.

Di Stefano, R. & Kong, A.K.H. 2003, *ApJ*, **592**, 884

Drake, J.J., Wagner, R.M., Starrfield, S., Butt, Y., Krautter, J., Bond, H.E., Della Valle, M., Gehrz, R.D., Woodward, C.E., Evans, A., Orio, M., Hauschildt, P., Hernanz, M., Mukai, K. & Truran, J. 2003, *ApJ*, **584**, 448

Ebisawa, K., Mukai, K., Kotani, T., Asai, K., Dotani, T., Nagase, F., Hartmann, H. W., Heise, J., Kahabka, P., & van Teeseling, A. 2001, *ApJ*, **550**, 1007

Fairbanks, A. 1898, *The First Philosophers of Greece,* K. Paul, Trench, Trubner, London (extracted from the *Hannover Historical Texts Projects,* http://history.hanover.edu/project.html)

Filippenko, A.V., Leonard, D. C., Modjaz, M., Eastman, R. G., Takamizawa, K., Hanzl, D. & Kowalski, R. A. 1998, *IAU Circ.* 6943

Frank, J., King, A.R. & Raine, D.J., **Accretion Power in Astrophysics**, Cambridge University Press, 1985.

Fujimoto, M.Y. 1982, *ApJ*, **257**, 767

Fujimoto, R. & Ishida, M. 1997, *ApJ*, **474**, 774

Fontaine, G. & Van Horn, H.M. 1976, *ApJS*, **31**, 467.

Gallagher, J.S. & Code, A.D. 1973, *BAAS*, **5**, 17

Garradd, G. 1988, *IAU Circ.* 4568

Giannone, P. & Weigert, A. 1967, *Zs. f. Ap.*, **67**, 41

Gil-Pons, P., García-Berro, E., José, J., Hernanz, M. & Truran, J.W. 2003, *A&A*, **407**, 1021

González-Riestra, R., Orio, M., Gallagher, J, 1998, *A&AS*, **129**, 23

Gorenstein, P. 1975, *ApJ*, **198**, 95

Greiner, J., Supper, R. & Magnier, E.A. 1996 in **Supersoft X-ray Sources**, ed. J. Greiner, Springer, p.75

Greiner, J. 2000, *New Astronomy,* **5**, 137

Hachisu, I. & Kato, M. 2001, *ApJ*, **558**, 323

Hachisu, I., Kato, M., Kato, T. & Matsumoto, K. 2002, in **The Physics of Cataclysmic Variables and Related Objects**, eds. B.T.Gänsicke, K.Beuermann & K.Reinsch, AIP Conference Proceedings, vol. 261, p. 629

Halpern, J.P. & Grindlay, J.E. 1980, *ApJ*, **242**, 1041.

Hamada, T. & Salpeter, E. E. 1961, *ApJ*, **264**, 282.

Harris, M.J., Naya, J. E., Teegarden, B. J., Cline, T. L., Gehrels, N., Palmer, D. M., Ramaty, R., Seifert, H. 1999, *ApJ*, **522**, 424

Hartmann, H.W. & Heise, J. 1997, *A&A*, **322**, 591.

Hasinger, G. 1997, *Rev. Mod. Astrophys.*,**7**,129

Hatchett, S., Buff, J. & McCray, R. 1976, *ApJ*, **206**, 847.

Hayward, T.L., Saizar, P., Gehrz, R.D., Benjamin, R.A., Mason, C.G., Houk, J.R., Miles, J.W., Guli, G.E. & Schoenwald, J. 1996, *ApJ*, **469**, 854

Hellier, C., Mukai, K., Ishida, M. & Fujimoto, R. 1996, *MNRAS*, **280**, 877

Hellier, C., Mukai, K. & Osborne, J.P. 1998, *MNRAS*, **297**, 526

Hernanz, M. 2002, in **Classical Nova Explosions**, eds. M.Hernanz & J.José, AIP Conference Proceedings, vol. 637, p. 399

Henyey, L., Vardya, M.S. & Bondenheimer, P. 1965. *ApJ*, **142**, 841.

Hernanz, M. & Sala, G. 2002, *Science*, **298**, 393

Honda, M. 1975, *IAU Circ.* 2826

Hubbard, W.B. & Lampe, M. 1969, *ApJS*, **18**, 279

Iben, I., Jr. 1975, *ApJ*, **196**, 525

Iben, I., Jr. 1977, *ApJ*, **217**, 788

Iben, I., Jr. 1982, *ApJ*, **259**, 244

Iben. I., Jr. & Tutukov, A.V. 1989, *ApJ*, **342**, 430

Iben, I., Jr. & Tutukov, A.V. 1996, *ApJS*, **105**, 145

Iglesias, C.A. & Rogers, F.J. 1996, *ApJ*, **464**, 943 (http://www-phys.llnl.gov/Research/OPAL/)

Ikeda, Y., Kawabata, K.S. & Akitaya, H. 2000, *A&A*, **355**, 256

Ishida, M., Mukai, K. & Osborne, J., *PASP*, **46**, L81 (1994)

Jansen, F. et al. 2001, *A&A*, **365**, L1

José, J. & Hernanz, M. 1998, *ApJ*, **494**, 680

José. J. 2002, in **Classical Nova Explosions**, eds. M.Hernanz & J.José, AIP Conference Proceedings, vol. 637, p. 104

Kaastra, J.S. 1992, *An X-Ray Spectral Code for Optically Thin Plasmas* (Internal SRON-Leiden Report, updated version 2.0)

Kahabka, P., Pietsch, W. & Hasinger,G. 1994, *A&A*, **288**, 538

Kallman, T.R., & McCray, R. 1982, *ApJS*, **50**, 263.

Kallman, T.R., *XSTAR User's Guide Version 2.1*h, NASA GSFC. May 31, 2002.

Karzas, W. J. & Latter, R. 1961, *ApJS*, **6**, 167

Kato, M. & Hachisu, I. 1994, *ApJ*, **437**, 802

Kellogg, E., Baldwin, J. R. & Koch, D. 1975, *ApJ*, **199**, 299

Kippenhahn, R., Weigert, A. & Hofmeister, E. 1967, *Meth. Comp. Phys.*, **7**, 129

Kippenhahn, R. 1981, *A&A*, **102**, 293

Kippenhahn, R. & Weigert, A., **Stellar Structure and Evolution**, Springer-Verlag, Berlin, 1990.

Kirsch, M. 2003, *"XMM-EPIC Status of Callibration and Data Analysis"*, issue 2.1, XMM-SOC-CAL-TN-0018, XMM-Newton Science Operations Centre

Kosai, H. 1984, *IAU Circ.* 3963

Kosai, H. 1986, *IAU Circ.* 4281

Kosai, H. 1987, *IAU Circ.* 4307

Kovetz, A., Prialnik, D. & Shara, M. 1988, *ApJ*, **325**, 828

Kraft, R.P. 1964, *ApJ*, **139**, 457

Krautter, J., Beuerman, K., Leitherer, C., Oliva, E., Moorwood, A.F.M., Deul. E., Wargau, W., Klare, G., Kohoutek, L., van Paradijs, J. & Wolf, B. 1984, *A&A*, **137**, 307

Krautter, J. & Williams, R.E. 1989, *ApJ*, **341**, 968

Krautter, J., Ögelman, H., Starrfield, S., Wichmann, R., & Pfeffermann. E. 1996, *ApJ*, **456**, 788

Kuulkers, E., Norton, A., Schwope, A. & Warner, B. 2003, in *Compact stellar X-ray sources*, eds. W.H.G. Lewin, M. van der Klis, Cambridge University Press (astro-ph/0302351)

Lang, K.R., **Astrophysical Formulae**, Springer- Verlag, 1980.

Latour, J. 1970, *A&A*, **9**, 277.

Liedahl, D.A., Osterheld, A.L. & Goldstein, W.H. 1995, *ApJL*, **438**, 115

Liller, W. 1983, *IAU Circ.* 3764

Liller, W. 1995, *IAU Circ.* 6143

Liller, W. 1998, *IAU Circ.* 6846

Liller, W., & Jones, A.F. 1999, *IBVS*, **4664**, 1

Liller, W., & Jones, A.F. 2000, *IBVS*, **4870**, 1

Lipkin, Y., Leibowitz, E.M., Retter, A. & Shemmer, O. 2001, *MNRAS*, **328**, 1169

Livio, M., Shankar, A. & Truran, J. 1988, *ApJ*, **330**, 264

Livio, M., Shankar, A., Burkert, A. & Truran, J.W. 1990, *ApJ,* **356**, 250

Livio, M. & Truran, J. 1994, *ApJ*, **425**, 797

Lloyd, H. M., O'Brien, T. J., Bode, M. F., Predehl, P., Schmitt, J.H.M.M., Trümper, J., Watson, M.G. & Pounds, K. A. 1992, *Nature*, **356**, 222

Loiseau, N. 2003, *Users' Guide to the XMM-Newton Science Analysis System*, Issue 2.1, (ESA/XMM-Newton Science Operations Centre, VILSPA, Madrid)

Lund, N. & Brandt, S. 1991, *IAU Circ.* 5161

Lynch, D.K., Rudy, R.J., Mazuk, S. & Puetter, R.C. 2000, *ApJ*, **541**, 791

Lynch, D.K., Rudy, R.J., Venturini, C.C. & Makuz, S. 2001, *AJ*, **122**, 2013

Lyke, J.E., Koenig, X. P., Barlow, M. J., Gehrz, R. D., Woodward, C. E., Starrfield, S., Péquignot, D., Evans, A., Salama, A., González-Riestra, R., Greenhouse, M.A., Hjellming, R. M., Jones, T.J., Krautter, J., Ögelman, H. B., Wagner, R. M., Lumsden, S. L., & Williams, R. E. 2003, *AJ*, **126**, 993

MacDonald, J. 1996, in **Cataclysmic Variables and Related Objects**, Kluwer, Dordrecht, p. 281

MacDonald, J., Fujimoto, M.Y. & Truran, J.W. 1985, *ApJ*, **294**, 263

MacDonald, J. & Vennes, S. 1991, *ApJ*, **373,** L51.

Marigo, P. 2000, *A&A*, **360**, 617

Mason, K.O. et al. 2001, *A&A*, **365**, L36

Mathis, J.S, Cohen, D., Finley, J.P. & Krautter, J. 1995, *ApJ*, **449**, 320

Matsuo, S. & Alcock, G. 1991, *IAU Circ.* 5222

McNaught, R.H. 1987, *IAU Circ.* 4453

McNaught, R.H. 1988, *IAU Circ.* 4663

Mewe, R., Gronenschild, E.H.B.M. & van den Oord, G.H.J. 1985, *A&AS*, **62**, 197

Mewe, R., Lemen, J.R. & van den Oord, G.H.J. 1986, *A&AS*, **65**, 511

Mewe, R., Kaastra, J.S. & Liedhal, D.A. 1995, *Legacy* **6**, 16 (available at http:// heasarc.gsfc.nassa.gov / docs / journal / meka6.html)

Mihalas, D. 1965, *ApJ*, **141**, 564

Mukai, K. 2003, *AdSpR*, **32**, 2067 (astro-ph/0112048)

Morisset, C. & Péquignot, D. 1996, *A&A,* **312**, 135

Morisset, C. & Péquignot, D. 1996, *A&A,* **313**, 611

Nakano, S., Takamizawa, K., Kushida, R., Kushida, Y. & Kato, T. 1998, *IAU Circ.* 6941

Ness, J.U., Starrfield, S., Burwitz, V., Wichmann, R., Hauschildt, P., Drake, J.J., Wagner, R.M., Bond, H.E., Krautter, J., Orio, M., Hernanz, M., Gehrz, R.D., Woodward, C.E., Butt, Y., Mukai, K., Balman, S. & Truran, J. 2003, *ApJ*, **594**, L127

O'Brien, T.J.O., Lloyd, H.M. & Bode, M.F. 1994, *MNRAS*, **271**, 155

Ögelman, H., Beuermann, K. & Krautter, J. 1984, *ApJ*, **287**, L31

Ögelman, H., Krautter, J. & Beuermann, K. 1987, *A&A*, **177**, 110

Ögelman, H., Orio, M., Krautter, J. & Starrfield, S. 1993, *Nature*, **361**, 331

Ögelman, H. & Orio, M. 1995, in **Cataclysmic Variables**, ed. Bianchini et al., Kluwer Academic Publishers, The Netherlands, p. 11

Orio, M., Balman, S., Della Valle, M., Gallagher, J. & Ögelman, H. 1996, *ApJ*, **466**, 410

Orio, M., Trussoni, E., Balman, S., Ögelman, H., Gallagher, J., de Martino, D., Della Valle, M., González-Riestra, R. & Selvelli, P. 1997, *IAU Circ.* 6778

Orio, M. 1999, *Physics Reports*, **311**, 419

Orio, M. & Greiner, J. 1999, *A&A*, **344**, L13

Orio, M., Covington, J. & Ögelman, H. 2001a, *A&A*, **373**, 542

Orio, M., Parmar, A.N., Benjamin, R., Amati, L., Frontera, F., Greiner, J., Ögelman, H., Mineo, T., Starrfield, S. & Trussoni, E. 2001b, *MNRAS*, **326**, L13

Orio, M., Greiner, J., Hartmann, W. & Still, M. 2002a, in **Classical Nova Explosions**, eds. M.Hernanz & J.José, AIP Conference Proceedings, vol. 637, p. 355

Orio, M., Parmar, A.N., Greiner, J., Ögelman, H., Starrfield, S., Trussoni, E. 2002b, *MNRAS*, **333**, L11

Orio, M., Hartmann, W., Still, M. & Greiner, J. 2003, *ApJ*, **594**, 435

Orio, M. 2004, in **Compact Binaries in the Galaxy and Beyond**, RevMexAA, Conf. Series (in press, astro-ph/0402035).

Paczyński, B. 1970, *Acta Astr.*, **20**, 47

Paczyński, B. 1983, *ApJ*, **264**, 282.

Paerels, F., Rasmussen, A. P., Hartmann, H. W., Heise, J., Brinkman, A. C., de Vries, C. P. & den Herder, J. W. 2001, *A&A*, **365**, L308

Paresce, F., Livio, M., Hack, W. & Korista, K. 1995, *A&A*, **299**, 823

Patterson, J. & Raymond, J.C. 1985, *ApJ*, **292**, 535

Péquignot, S., Petitjean, P., Boisson, C. & Krautter, J. 1993, *A&A*, **271**, 219

Press, W.H, Teukolsky, S.A., Vetterling, W.T. & Flannery, B.P. **Numerical Recipes in Fortran**, Cambridge University Press, 1992.

Prialnik, D. 1986, *ApJ*, **310**, 222

Prialnik, D., & Kovetz, A. 1995, *ApJ*, **445**, 789

Quirrenbach, A., Elias II, N.M., Mozurkewich, D., Armstrong, J. T, Buscher, D.F. & Hummel, C.A. 1993, *AJ*, **106**, 1118

Ramsay, G. & Cropper, M. 2003, *MNRAS*, **338**, 219

Ramsay, G. & Cropper, M. 2004, *MNRAS*, **347**, 497

Raymond, J. & Smith, B. 1977, *ApJS*, **35**, 419

Reeves, H. 1965, in **Stellar Structure - Stars and Stellar Systems: Compendium of Astronomy and Astrophysics, Vol. VIII**, eds. L.H. Aller & D.B. McLaughlin, University of Chicago Press, 1965, p. 113-194

Refsdal, S. & Weigert, A. 1970, *A&A*, **6**, 426

Ritossa, C., Garcia-Berro, E. & Iben, I., Jr. 1996, *ApJ*, **460**, 489

Saslaw, W.C. 1968, *MNRAS*, **138**, 337

Shanley, L., Ögelman, H., Gallagher, J. S., Orio, M. & Krautter, J. 1995, *ApJ*, **438**, L95

Shore, S. N., Sonneborn, G., Starrfield, S., González-Riestra, R. & Ake, T. B. 1993, *AJ*, **106**, 2408

Shore, S. N., Sonneborn, G., Starrfield, S., González-Riestra, R. & Polidan, R.S. 1994, *ApJ*, **421**, 344

Shore, S. N., Starrfield, S. & Sonneborn, G. 1996, *ApJ*, **463**, L21

Shore, S. 2002, in **Classical Nova Explosions**, eds. M.Hernanz & J.José, AIP Conference Proceedings, vol. 637, p. 175

Shore, S.N., Schwarz, G., Bond, H.E., Downes, R.A., Starrfield, S., Evans, A., Gehrz, R.D., Hauschildt, P.H., Krautter, J. & Woodward, C.E., 2003, *AJ*, **125**, 1507

Snowden, S., Still, M., Harrus, I., Arida, M. & Perry, B. 2002, *An Introduction to XMM-NEWTON Data Analysis*, Version 1.3 (NASA/GSFC XMM-Newton Guest Observer Facility, Greenbelt, MD)

Starrfield, S. 1971, *MNRAS*, **152**, 307

Starrfield, S., Truran, J.W., Sparks, W.M. & Kutter, G. S. 1972, *ApJ*, **176**, 169

Starrfield, S., Sparks, W.M. & Truran, J.W. 1974, *ApJS,* **28**, 247

Starrfield, S. 1989, in **Classical Novae**, eds. M. F. Bode & A. Evans, John Wiley & Sons, New York, p. 39

Starrfield, S., Krautter, J, Shore, S.N., Idan, I., Shaviv, G. & Sonneborn, G. 1996, in **Astrophysics in the Extrem Ultraviolet**, eds. S. Bowyer & R.F. Malina, Kluwer, Dordrect, p. 419

Starrfield, S., Truran, J.W., Wiescher, M.C. & Sparks, W.M. 1998, *MNRAS*, **296**, 502

Starrfield, S. 2002, in **Classical Nova Explosions**, eds. M.Hernanz & J.José, AIP Conference Proceedings, vol. 637, p. 89

Strüder, L.. et al. 2001, *A&A*, **365**, L18

Schwarz, G.J., Shore, S. N., Starrfield, S., Hauschildt, P.H., Della Valle, M. & Baron, E. 2001, *MNRAS*, **320**, 103

A. Swartz, D.A., Ghosh, K.K., Suleimanov, V., Tennant, A.F. & Wu, K. 2002, *ApJ*, 574, 382

Schwarzschild, M., **Structure and Evolution of the Stars**, Dover poublications, Inc., New York, 1958

Tarter, C.B., Tucker, W. & Salpeter, E.E. 1969, *ApJ*, **156**, 943

Tuchman, Y., Glasner, A. & Barkat, Z. 1983, *ApJ*, **268**, 356

Tuchman, Y. & Truran, J., 1998, *ApJ*, **503**, 381

Turner, T.J., George, I. M., Kallman, T., Yaqoob, T. & Zycki, P.T. 1996, *ApJ*, **472**, 571

Turner, M.J.L. et al., 2001, *A&A*, **365**, L27

Vanlandingham, K.M., Schwarz, G.J., Shore, S.N., Starrfield, S. 2001, *ApJ*, **121**, 1126

Voges, W. et al. 1999, *A&A*, **349**, 389

Walker, M.F. 1954, *PASP*, **66**, 230

Warner, B. & Woudt, P. 2002, *PASP*, **114**, 1222

Wild, P. 1989, *IAU Circ.* 4861

Williams, R. 1992, *AJ*, **104**, 725

Zimmerman, H.U., Boese, G., Becker, W., Belloni, T., Döbereiner, S., Izzo, C., Kahabka, P. & Schwentker, O. 1998, EXSAS User's Guide, MPE report, ROSAT Scientific Data Center, Garching (http://wave.xray.mpe.mpg.de/exsas)

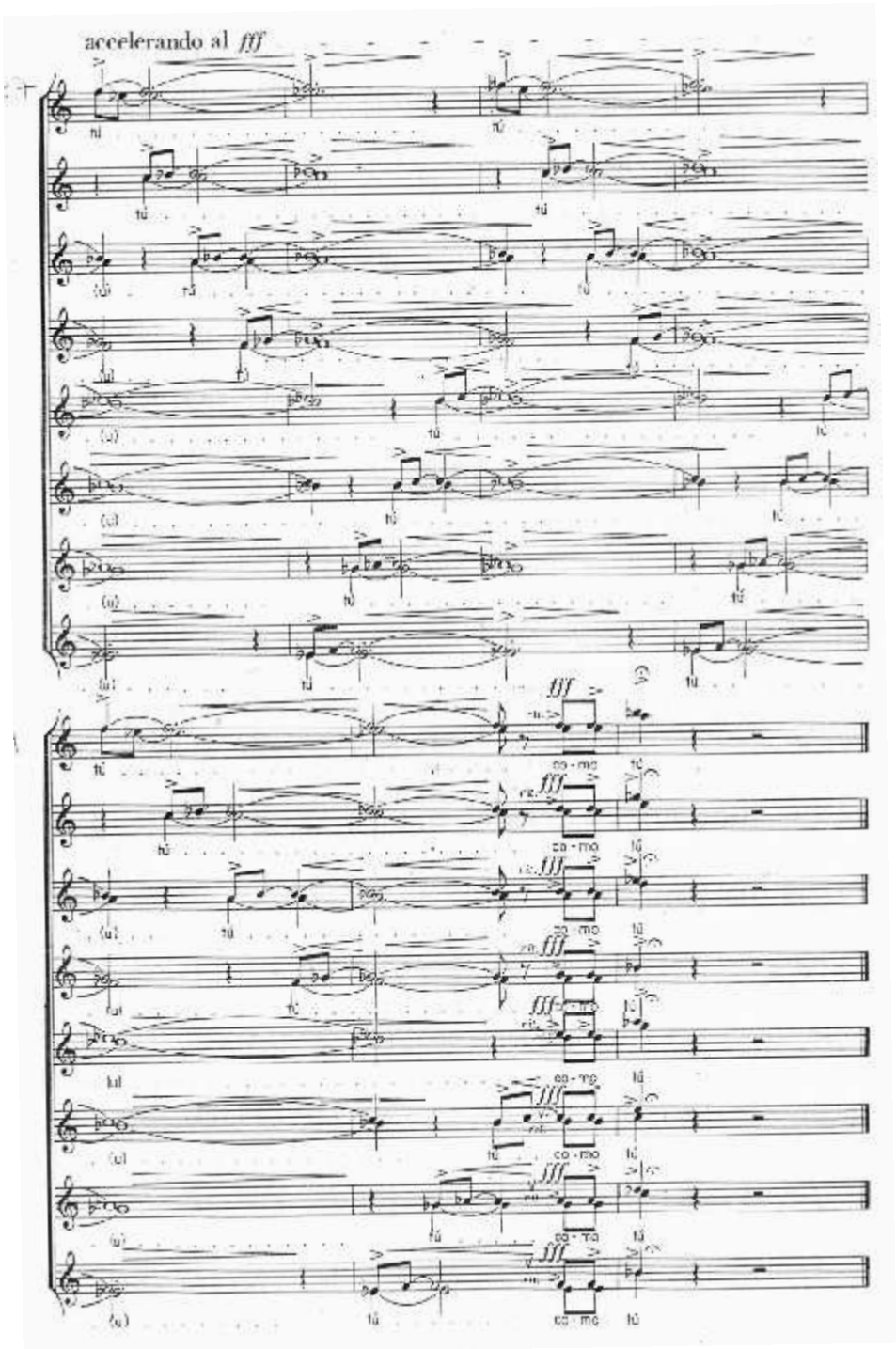

Como tú

Poesia de Ruben Dario, música de Alberto Grau

Appendix A

Analytical Approximation for the White Dwarf Envelopes

In the outer envelope of any star in complete thermal and hydrostatic equilibrium, there is an analytical solution for the system of stellar equilibrium equations. Except for the innermost layers, temperatures are too low for nuclear energy production to be significant, so that luminosity L is constant for wide ranges of the radius r, and equal to the total luminosity L_{tot} of the star. Density is small, so that the mass M varies very slowly with increasing radius, and can be considered to be approximately constant in the stellar envelope and equal to the mass of the degenerate core, M_c.

A.1 The Pressure-Temperature Relation

In the conditions mentioned for an outer stellar envelope, the four stellar equilibrium equations are reduced to a power law relation between the pressure and the temperature, as shown in Schwarzschild (1958) or in Kippenhahn & Weigert (1990). For a stellar envelope with constant values of luminosity, $L = L_{tot}$, and mass, $M = M_c$, the four stellar equilibrium equations, in case of radiative transport of energy, are reduced to

$$\frac{dP}{dr} = -\frac{GM_c}{r^2}\rho \tag{A.1.1}$$

$$\frac{dT}{dr} = -\frac{3\kappa\rho}{64\pi\sigma}\frac{L_{tot}}{r^2T^3} \tag{A.1.2}$$

Dividing (A.1.2) by (A.1.1),

$$\frac{dT}{dP} = \frac{3}{64\pi\sigma G}\frac{\kappa L}{T^3 M_c}. \tag{A.1.3}$$

With an approximation for the opacity as a power law of pressure and temperature,

$$\kappa = \kappa_0 P^a T^b \tag{A.1.4}$$

with κ_0 constant, and typically $a > 0$ and $b < 0$,

$$\frac{T^{3-b}}{P^a}\frac{dT}{dP} = \frac{3\kappa_0}{64\pi\sigma G}\frac{L}{M_c}. \tag{A.1.5}$$

Equation A.1.5 can be integrated by separation of the variables, and then

$$T^{4-b} = B\left(P^{1+a} + C\right) \tag{A.1.6}$$

where

$$B = \frac{4-b}{1+a}\frac{3\kappa_0}{64\pi\sigma G}\frac{L}{M_c}$$

and C is a constant of integration. For $a = 1$ and b = -4.5, (A.1.4) is the Kramers opacity, and with this,

$$P^2 = \frac{T^{8.5}}{B} - C \tag{A.1.7}$$

For zero outer boundary conditions, $T = 0$ when $P = 0$, and then $C = 0$. In this case,

$$P = AT^{4.25} \tag{A.1.8}$$

with

$$A = \left(\frac{1}{B}\right)^{\frac{1}{2}} = \left(\frac{32\pi acG}{25.5\kappa_o}\frac{M_c}{L}\right)^{\frac{1}{2}}.$$

In case of convection, if the transport of energy is assumed to be adiabatic, equation (A.1.2) is substituted by

$$\frac{dT}{dr} = \left(1 - \frac{1}{\gamma}\right)\frac{T}{P}\frac{dP}{dr} \tag{A.1.9}$$

$$\frac{\mathrm{d}\ln T}{\mathrm{d}\ln P} = \left(1 - \frac{1}{\gamma}\right) = \frac{\gamma - 1}{\gamma} \Rightarrow P \sim T^{\frac{\gamma}{\gamma-1}} \tag{A.1.10}$$

where $\gamma = \frac{c_p}{c_v}$ is the adiabatic exponent. For a completely ionized ideal monoatomic gas, $\gamma = \frac{5}{3}$, and $P \sim T^{\frac{5}{2}}$.

Taking into account equations (A.1.8) and (A.1.10), the general solution for the analytic model with zero outer boundary conditions can be written as

$$P = KT^n \tag{A.1.11}$$

where, in case of radiative transport with an opacity given by (A.1.4),

$$K = K_{rad} = \left(\frac{4-b}{1+a}\frac{3\kappa_0}{64\pi\sigma G}\frac{L}{M_c}\right)^{-\frac{1}{1+a}}, \; n = \frac{4-b}{1+a} \tag{A.1.12}$$

and in case of convection,

$$K = K_{conv}, \; n = \frac{\gamma}{\gamma - 1}.$$

Figure A.1 shows the $logP - logT$ profile resulting from numerical integration of the four stellar equilibrium equations (2.1, 2.2, 2.5, 2.4) for an ideal gas with Kramers opacity, with several boundary conditions at the bottom (P_b and T_b) (similar figures can be found in Schwarzschild (1958) and in Kippenhahn & Weigert (1990)). Except for the most internal regions, energy production is unimportant and the analytical model, with no energy generation (i.e. with constant luminosity), is recovered. The effect of the different boundary conditions is equivalent to different values of the constant of integration C in (A.1.7). Positive values of C cause the temperature to reach a finite value as the pressure goes to zero. For increasing temperatures, the high exponent of the temperature in (A.1.7) makes the value of the constant C negligible. All solutions converge strongly to the zero outer boundary conditions case, thus indicating the small effect of different outer boundary conditions in the interior solution. For negative values of C, the temperature will be lower for each value of pressure than the corresponding temperature in the case of zero outer boundary conditions. The temperature gradient is then, for a given pressure gradient, steeper than in the zero outer boundary conditions case. The Schwarzschild criterion (C.1.1) is violated, the envelope becomes dynamically unstable and convection appears.

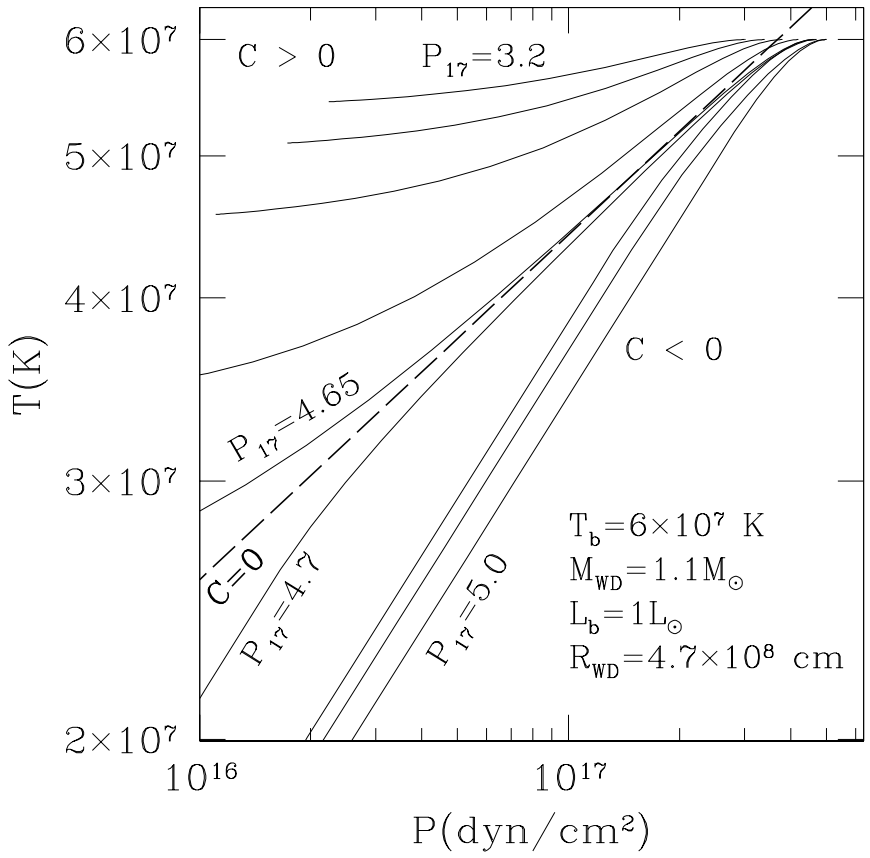

Figure A.1: $logP - logT$ diagram for several values of pressure at the bottom of the envelope for a $1.1M_{\odot}$ white dwarf.
Temperature and luminosity at the base of the envelope are fixed to $T_b = 6 \times 10^7 K$ and $L_b = 1L_{\odot}$. P_{17} indicates pressure in units of $10^{17} dyn\, cm^{-2}$. Different conditions at the bottom of the envelope are equivalent to different values of C in (A.1.7). The dashed line indicates $P^2 \sim T^{8.5}$ (case with $C = 0$, $P_{out} = 0$, $T_{out} = 0$, zero outer boundary conditions). The solid lines show the result of the integration of the four stellar equilibrium equations for an ideal gas with Kramers opacity, for several values of pressure at the bottom of the envelope. The effect of the luminosity and mass not being constant is only significant for the deepest shells of the envelope, i.e., those with the highest values for T and P. When convection appears (for $C < 0$), temperature gradient is assumed to be adiabatic, with $P \sim T^{\frac{5}{2}}$ (which can be expressed as $\nabla_{ad} = \frac{\mathrm{d} \ln T}{\mathrm{d} \ln P}\big|_{ad} = \frac{1}{n} = \frac{\gamma - 1}{\gamma} = \frac{2}{5} = 0.4$).

Temperature, pressure and density distributions

In the case of zero outer boundary conditions, equation (A.1.11) can be used to rewrite the pressure gradient as,

$$\frac{dP}{dr} = \frac{dP}{dT}\frac{dT}{dr} = KnT^{n-1}\frac{dT}{dr}. \tag{A.1.13}$$

The right-hand side of (A.1.1) and of (A.1.13) must be equal,

$$-\frac{GM_c}{r^2}\rho = KnT^{n-1}\frac{dT}{dr}. \tag{A.1.14}$$

Using equation (A.1.11) and the equation of state of ideal gas (B.1.1), density can be written as a function only of the temperature,

$$\rho = \frac{\mu}{\Re}\frac{P}{T} = \frac{\mu}{\Re}K\frac{T^n}{T} = \frac{\mu}{\Re}KT^{n-1}. \tag{A.1.15}$$

In case of radiative transport of energy with Kramers opacity ($K = K_{rad} \propto \left(\frac{L_{tot}}{M_c}\right)^{-\frac{1}{2}}$ and $n = 4.25$), $\rho \propto T^{3.25}\sqrt{\frac{M_c}{L_{tot}}}$.

Introducing (A.1.15) into (A.1.14),

$$-\frac{GM}{r^2}\frac{\mu}{\Re}KT^{n-1} = KnT^{n-1}\frac{dT}{dr}$$

$$\frac{dT}{dr} = -\frac{\mu GM_c}{n\Re}\frac{1}{r^2} \tag{A.1.16}$$

which can be integrated,

$$T = \frac{\mu GM_c}{n\Re}\frac{1}{r} + C' \tag{A.1.17}$$

where C' is a constant of integration. If temperature at the bottom of the envelope, where $r = R_c$, is $T = T_b$,

$$T = T_b + \frac{\mu GM_c}{n\Re}\left(\frac{1}{r} - \frac{1}{R_c}\right). \tag{A.1.18}$$

It is worth noticing that, for an ideal gas, the temperature distribution, unlike the pressure and the density, is independent of the luminosity of the envelope. The pressure distribution is obtained introducing (A.1.18) into (A.1.11).

Figure A.2 shows temperature, pressure and density distributions for the analytical model with zero outer boundary conditions and Kramers opacity. It can be observed that, as a consequence of (A.1.18), the outer radius of the envelope (or the envelope thickness) increases for increasing bottom temperatures. In fact, (A.1.18) indicates that, given a chemical composition, the temperature distribution only depends on the mass (M_c) and the radius (R_c) of the degenerate core,

$$T \sim \frac{M_c}{R_c}\left(\frac{R_c}{r} - 1\right)$$

A.2 Homology relations

Refsdal & Weigert (1970) showed that the physical variables (ρ, T, P, L) in shell source burning stars with degenerate cores verify homology relations of the form

$$\rho(r/R_c) \sim M_c^{\varphi_1} R_c^{\varphi_2} \tag{A.2.19}$$

$$T(r/R_c) \sim M_c^{\psi_1} R_c^{\psi_2} \tag{A.2.20}$$

$$P(r/R_c) \sim M_c^{\tau_1} R_c^{\tau_2} \tag{A.2.21}$$

$$L(r/R_c) \sim M_c^{\sigma_1} R_c^{\sigma_2} \tag{A.2.22}$$

These relations mean that, for two stars with masses M_c and M_c', and radius R_c and R_c', the physical quantities taken at homologous points ($r/R_c = r'/R_c'$) are connected by relations (A.2.19-A.2.22). Expression (A.1.18) shows that this shell source hommology also exists for the temperature in the envelope with

$$\psi_1 = 1, \quad \psi_2 = -1$$

From (A.1.11) it is clear that, taking into account that L is constant in the whole the envelope, the pressure also verifies an homology relation with

$$\tau_1 = \psi_1 n = n, \quad \tau_2 = \psi_2 n = -n$$

and finally, the equation of state of ideal gas indicates that for the density,

$$\varphi_1 = \tau_1 - \psi_1 = n - 1, \quad \varphi_2 = \tau_2 - \psi_2 = 1 - n$$

A.3 Luminosity of the degenerate core

In the interior of the white dwarf core, degenerate electrons provide a high thermal conductivity which does not allow strong temperature gradients and cause the degenerate core to be isothermal, with temperature T_c. As shown in Schwarzschild (1958) or in Kippenhahn & Weigert (1990), the analytical approximation for the envelope provides an estimation for the relation between the core temperature T_c and the degenerate core luminosity L_c. Let us assume that the transition from the degenerate core to the envelope occurs at the base of the envelope, where $T = T_b = T_c$, and that it is also the transition point in the equation of state from the degenerate electron gas to the ideal gas, where (see appendix B, expression B.1.15)

$$T = \frac{1}{\Re}\frac{1}{20}\left(\frac{3}{\pi}\right)^{2/3}\frac{h^2}{m_e m_u^{5/3}}\frac{\mu}{\mu_e}\rho^{2/3} = 1.207\times 10^5\frac{\mu}{\mu_e}\rho^{2/3} \qquad (cgs) \tag{A.3.23}$$

Introducing now the expression for the density in the radiative envelope with Kramers' opacity (A.1.15),

$$T_c = 6.3\times 10^7\left(\frac{L_c/L_\odot}{M_c/M_\odot}\right)^{2/7} \quad (K) \tag{A.3.24}$$

For a $1M_\odot$ white dwarf with $L_c = 1L_\odot$, the core temperature is $6.3\times 10^7 K$. Temperature at the base of the numerical envelope models lays between $\sim 6\times 10^7 K$ and $\sim 10^8 K$ (see for instance figure 2.26). With these temperatures, (A.3.24) indicates that the luminosity of a $1M_\odot$ degenerate core would be between 0.8 and 5 $L_\odot$. In the numerical calculation, the luminosity core is assumed to be $1L_\odot$. The exact value of this core luminosity is unimportant, since the solutions are insensitive to its exact value, as long as it is kept within this order of magnitude.

A.4 Estimation of the envelope thickness, luminosity and mass

A rough estimation of the envelope outer radius R_{out} can be obtained from (A.1.18), just setting $T = T_{out} = 0$,

$$\frac{1}{R_{out}} = \frac{1}{R_c} - \frac{n\Re}{\mu G M_c}T_b \tag{A.4.25}$$

$$\frac{\Delta R}{R_{out}} = \frac{R_{out}-R_c}{R_{out}} = \frac{n\Re}{\mu G M_c}R_c T_b. \tag{A.4.26}$$

In case of radiative transfer with Kramers opacity ($n = 4.25$), for the chemical composition corresponding to an envelope of a CO $1.1M_\odot$ white dwarf, with $R_c = 4.7\times 10^8 cm$ (Hamada & Salpeter (1961)), formed by accreted solar material mixed at 50% with the core material ($X = 0.35$, $Y = 0.15$ and $Z = 0.5$, $\mu = 0.94$), $\frac{n\Re}{\mu G M_c} = 2.58\times 10^{-18} cm^{-1}K^{-1}$, and then

$$\frac{\Delta R}{R_{out}} = 0.12\left(\frac{T_b}{10^8 K}\right) \tag{A.4.27}$$

which indicates that with $T_b = 10^8 K$, the envelope is a 12% of the total radius of the star. It is worth noticing that ΔR indicates an approximation for the total envelope, but only the deepest layers of it will have temperatures high enough for the energy production to be

significant and the hydrogen production layer will be much smaller. Taking into account that $R_{out} = R_c + \Delta R$, (A.4.27) can be rewritten as

$$\frac{\Delta R}{R_c} = \frac{\left(\frac{T_b}{10^8 K}\right)}{8.3 - \left(\frac{T_b}{10^8 K}\right)}$$

For a $1.1 M_\odot$ white dwarf and a typical base temperature of $T_b = 10^8 K$, $\Delta R = 6.4 \times 10^7 cm$.

The analytical model provides also an approximate relation between the total envelope luminosity, the temperature and the mass of the energy generation layer. If temperature and density, and consequently the energy generation rate ε, are assumed to be constant thorough the energy production layer,

$$L \simeq \varepsilon \, \Delta M \tag{A.4.28}$$

A first rough estimation of the mass in the energy generation shell can be deduced using the energy generation rates (B.2.19-B.2.20). With radiative transport of energy, for a $1.1 M_\odot$ white dwarf with a luminosity $10 L_\odot$, with $X = 0.35$, $Z = 0.5$, and a temperature $10^7 K$, equation (A.1.15) indicates a density $\rho \simeq 32 \, g \, cm^{-3}$ and thus a pressure $P = 3 \times 10^{16} dyn \, cm^{-2}$. For this temperature and density, the pp chain dominates the energy production and equation (B.2.19) indicates $\varepsilon = 0.25 \, erg \, g^{-1} s^{-1}$. With this, the necessary mass for a luminosity of $10 L_\odot$ is $\Delta M \sim 80 M_\odot$, which is completely unrealistic. This indicates that the temperature of the energy production layer will always be higher than $10^7 K$ and the CNO cycle will dominate the energy production.

Using equation (A.1.15) to relate temperature and density at any point of the envelope, also at the base of it, just above the energy production layer, it is possible to write the energy generation rate for the CNO cycle (B.2.20) as a function only of temperature, luminosity and mass of the star. For radiative transport with Kramers opacity

$$\varepsilon_{CNO} = 1.41 \times 10^{31} \left(\frac{32 \pi a c G}{25.5 \kappa_o}\right)^{\frac{1}{2}} X \, X_{CNO} \, \mu^{\frac{1}{2}} \left(\frac{M_c}{L_{tot}}\right)^{\frac{1}{2}} T_6^{\frac{31}{12}} \exp\left(-152.313 T_6^{-\frac{2}{3}}\right) \, erg \, g^{-1} s^{-1}$$

With the parameters of the example described above ($X = 0.35$, $Z = 0.5$ ($X_{CNO} = Z/3$), $\mu = 0.94$),

$$\varepsilon_{CNO} = 1.6 \times 10^{42} L_c^{-\frac{1}{2}} T_6^{\frac{31}{12}} \exp\left(-152.313 T_6^{-\frac{2}{3}}\right) \, erg \, g^{-1} s^{-1}$$

which combined with (A.4.28) gives

$$L^{\frac{3}{2}} = 1.6 \times 10^{42} \Delta M T_6^{\frac{31}{12}} \exp\left(-152.313 T_6^{-\frac{2}{3}}\right) \, erg \, g^{-1} s^{-1}$$

Figure A.3 plots the relation $L(T, \Delta M)$ for $X = 0.35$ and $Z = 0.5$, for values of the mass of the energy production layer ΔM between $10^{-9} M_\odot$ (which with $\rho = 10 \, g \, cm^{-1}$ corresponds to a minimum thickness of 1 km) and $10^{-3} M_\odot$ (corresponding to a maximum of 100 km, for $\rho = 10^5 g \, cm^{-3}$, although for this extreme case the equation of state would not be an ideal gas and the analytical approximation would not be valid).

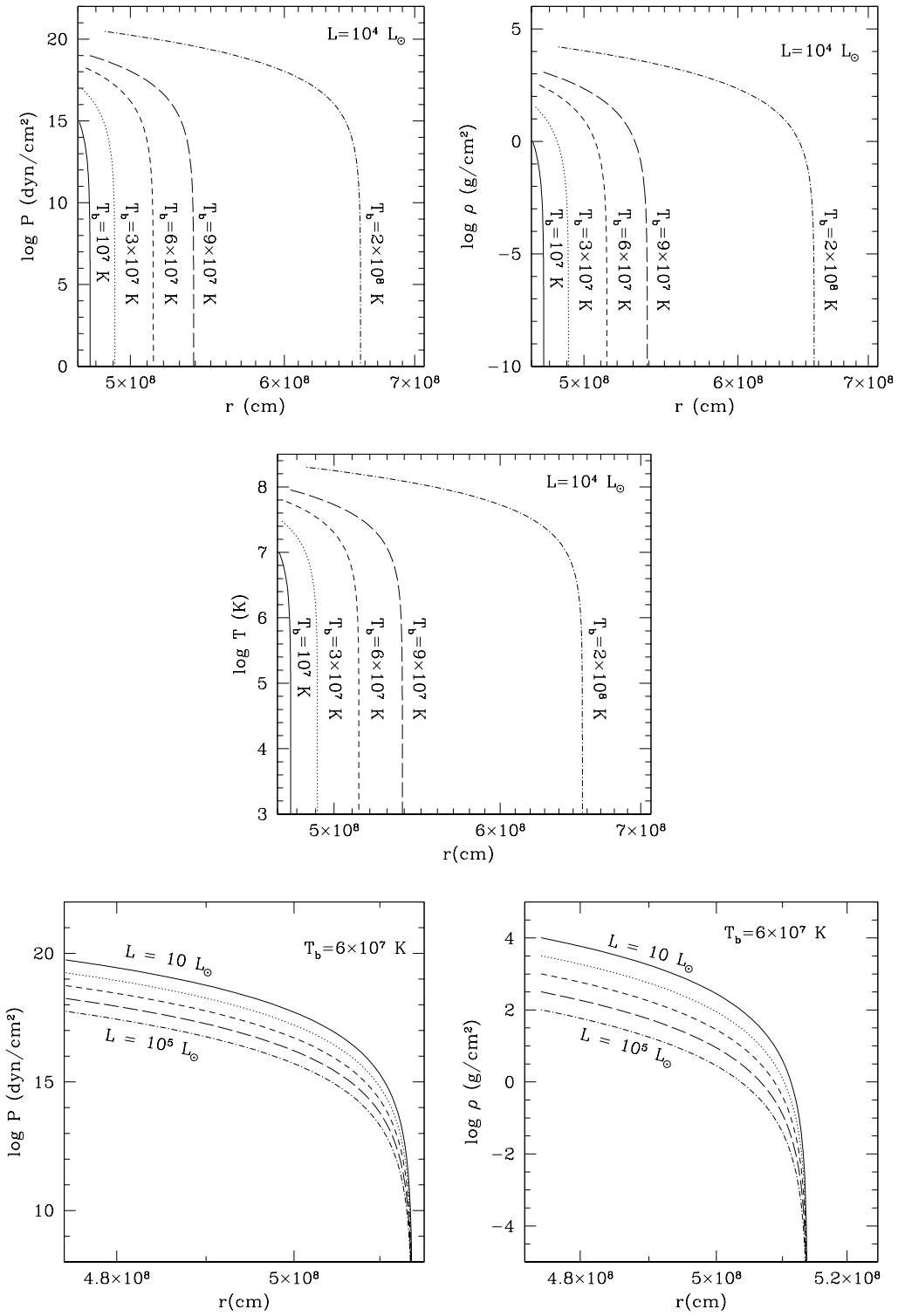

Figure A.2: Pressure, temperature and density distribution in the radiative analytical model for Kramers opacity and zero outer boundary conditions.
Results for several values of bottom temperature (T_b: (1, 3, 6, 9, 20)$\times 10^7 K$) and for several luminosities (L: 10, 10^2, 10^3, 10^4, 10^5 $L_\odot$) are plotted. Note that pressure at the base of the envelope is automatically determined as a function only of temperature by the analytical approximation. The envelope temperature distribution does not depend on the luminosity. The degenerate core has mass and radius $M_c = 1.1 M_\odot$ and $R_c = 4.7 \times 10^8 cm$.

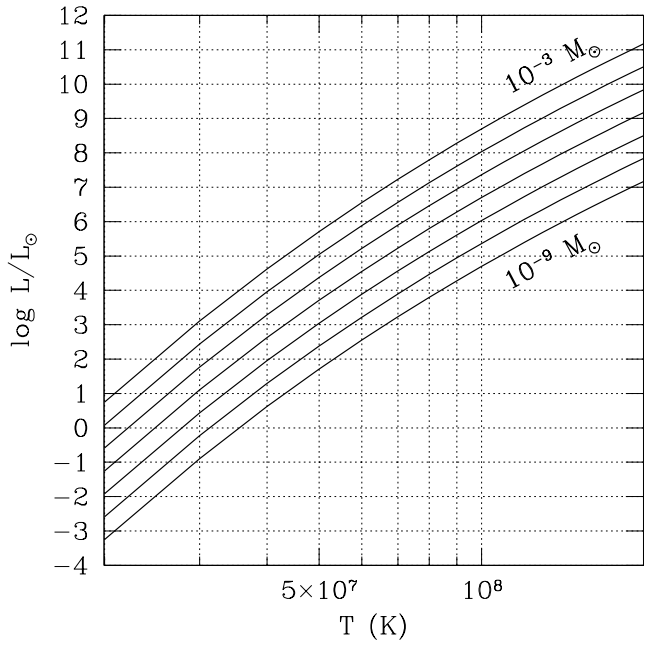

Figure A.3: Temperature and luminosity of the hydrogen burning layer for several values of its mass.

Appendix B

Input Physics

B.1 Equation of State: Ideal gas with radiation pressure

The equation of state of the matter in the present white dwarf envelope models is that of ideal gas with radiation pressure. We have tested that for the conditions of the gas in the present models, no significant effects due to degeneration (at the base of the envelope) or partial ionization (at the outermost layers) need to be taken into account.

The equation of state of an ideal gas is

$$P_{id} = P_{id,ions} + P_{id,e} = \rho \Re T \left(\frac{1}{\mu_{ions}} + \frac{1}{\mu_e} \right) = \frac{\rho \Re T}{\mu} \tag{B.1.1}$$

where P is the pressure, ρ the mass density, T the temperature, μ the mean molecular weight and $\Re = 8.31 \times 10^7 erg\, K^{-1} g^{-1}$ is the universal gas constant. For a completely ionized gas,

$$\mu = \left(\sum_i \frac{X_i \left(1 + Z_i\right)}{A_i} \right)^{-1} \tag{B.1.2}$$

with X_i, Z_i and A_i being the mass fraction, atomic number and mass number of nuclei of type i. In the conditions found in the envelope models of this work, gas is completely ionized, and carbon and oxygen or oxygen and neon, in CO and ONe white dwarf envelope models respectively, are enhanced with respect to solar composition. Their contribution to the mean molecular weight is separated from other metals. Then, for CO white dwarf envelopes

$$\mu = \left(2X + \frac{3}{4}Y + \frac{7}{12}X_C + \frac{9}{16}X_O + \sum_{i(Z>8)} \frac{X_i \left(1 + Z_i\right)}{A_i} \right)^{-1}$$

where $X = X_H$ and $Y = X_{He}$ as usual. For most elements heavier than helium $A_i/Z_i \simeq 2$, so that

$$\mu = \left(2X + \frac{3}{4}Y + \frac{7}{12}X_C + \frac{9}{16}X_O + \sum_{i(Z>8)} X_i \left(\frac{1}{A_i} + \frac{1}{2} \right) \right)^{-1}$$

Since for elements heavier than oxygen, $A_i > 16 \Rightarrow \frac{1}{A_i} + \frac{1}{2} \simeq \frac{1}{2}$, and then

$$\mu = \left(2X + \frac{3}{4}Y + \frac{7}{12}X_C + \frac{9}{16}X_O + \frac{1}{2}\left(1 - X - Y - X_C - X_O\right) \right)^{-1} \tag{B.1.3}$$

In the case of ONe white dwarf envelopes,

$$\mu = \left(2X + \frac{3}{4}Y + \frac{9}{16}X_O + \frac{11}{20}X_{Ne} + \frac{1}{2}\left(1 - X - Y - X_O - X_{Ne}\right)\right)^{-1} \tag{B.1.4}$$

The contribution to pressure due to radiation is

$$P_{rad} = \frac{1}{3}aT^4 \tag{B.1.5}$$

where $a = \frac{4\sigma}{c} = 7.565 \times 10^{-15} erg\, cm^{-3} K^{-4}$. The equation of state for ideal gas with radiation pressure is then

$$P = \frac{\rho \Re T}{\mu} + \frac{1}{3}aT^4 \tag{B.1.6}$$

from where

$$\rho = \frac{\mu}{\Re}\frac{1}{T}\left(P - \frac{a}{3}T^4\right) = \frac{\mu}{\Re}\frac{1}{T}\left(P - P_{rad}\right)$$

For this equation of state, it is common to define the parameter β as

$$\beta = \frac{P_{gas}}{P_{total}}$$

$$1 - \beta = \frac{P_{rad}}{P_{total}}$$

It can be easily seen that

$$\left.\frac{\partial \ln \beta}{\partial \ln \rho}\right|_T = 1 - \beta$$

$$\left.\frac{\partial \ln \beta}{\partial \ln T}\right|_\rho = -3\left(1 - \beta\right)$$

so that

$$\beta \sim \rho^{1-\beta} T^{-3(1-\beta)} \tag{B.1.7}$$

With this, in the neighborhood of given ρ and T, the equation of state can be expressed as

$$P \sim \rho^{\beta} T^{4-3\beta} \tag{B.1.8}$$

Thermodynamic quantities of the ideal gas with radiation

The equation of state being ideal gas plus radiation pressure, the thermodynamic quantities can be expressed in terms of the parameter β:

$$\alpha \equiv \left.\frac{\partial \ln \rho}{\partial \ln P}\right|_T = \frac{1}{\beta}$$

$$\delta \equiv -\left.\frac{\partial \ln \rho}{\partial \ln T}\right|_P = \frac{4 - 3\beta}{\beta} \tag{B.1.9}$$

$$u = \frac{3}{2}\frac{\Re}{\mu}T + \frac{aT^4}{\rho} = \frac{\Re T}{\mu}\left(\frac{3}{2} + \frac{3(1-\beta)}{\beta}\right) \tag{B.1.10}$$

$$c_p \equiv \left.\frac{dq}{dT}\right|_P = \left.\frac{\partial u}{\partial T}\right|_P + P\left.\frac{\partial v}{\partial T}\right|_P = \frac{\Re}{\mu}\left(\frac{3}{2} + \frac{4 - 3\beta}{\beta^2} + \frac{3(4+\beta)(1-\beta)}{\beta^2}\right) \tag{B.1.11}$$

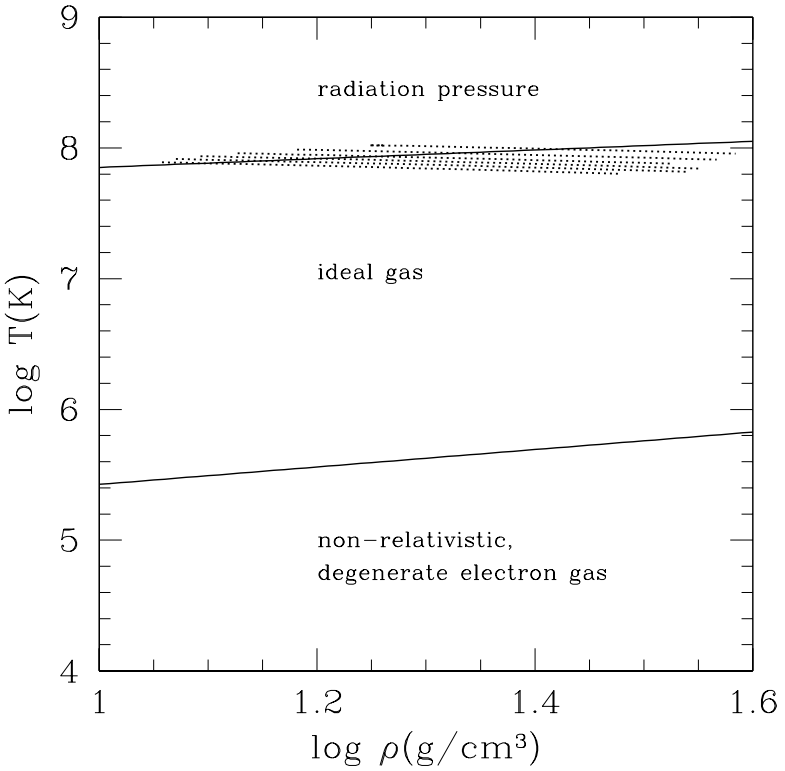

Figure B.1: Sketch of the regions in the ρ-T plane, where the equation of state is dominated by radiation pressure, ideal gas and non-relativistic degenerate electron gas.
Thin dotted lines indicate the conditions at the bottom of the envelopes of all CO50 stable models.

$$c_v = c_p - \frac{P\delta^2}{\rho T \alpha} \tag{B.1.12}$$

$$\nabla_{ad} = \left.\frac{d\ln T}{d\ln P}\right|_{ad} = \frac{\Re\delta}{\beta\mu c_p} = \frac{1+\frac{(1-\beta)(4+\beta)}{\beta^2}}{\frac{5}{2}+\frac{4(1-\beta)(4+\beta)}{\beta^2}} \tag{B.1.13}$$

where dq and u are heat and internal energy per unit mass, and and $v = \frac{1}{\rho}$. In case of no radiation pressure, for $\beta \to 1$, $\nabla_{ad} = \frac{2}{5}$ (ideal monoatomic gas).

Do we need to include degeneracy?

Dealing with white dwarf envelopes, it is necessary to consider the possible degeneracy of the gas in the deepest layers of the envelope. We will see that, for the regime of temperatures and densities found in our models in chapter 2, no degeneracy needs to be taken into account.

The equation of state for a completely degenerate non-relativistic electron gas can be written as (see for instance Kippenhahn & Weigert (1990)),

$$P_e = \frac{1}{20}\left(\frac{3}{\pi}\right)^{2/3}\frac{h^2}{m_e}\left(\frac{\rho}{m_u\mu_e}\right)^{5/3} \tag{B.1.14}$$

where m_u is the atomic mass unit ($m_u = 1\,amu = 1.66\times10^{-24}g$), m_e is the mass of the electron ($m_e = 9.11\times10^{-28}g$) and h is the Planck constant ($h = 6.63\times10^{-27}erg\,s$). The

border between the region of degeneracy and ideal gas regimes can be defined as the region where (B.1.14) and (B.1.1) give the same pressure,

$$T = \frac{1}{\Re}\frac{1}{20}\left(\frac{3}{\pi}\right)^{2/3}\frac{h^2}{m_e m_u^{5/3}}\frac{\mu}{\mu_e}\rho^{2/3} = 1.207\times 10^5\frac{\mu}{\mu_e}\rho^{2/3} \qquad (cgs) \tag{B.1.15}$$

In a similar way, the borderline between the ideal gas and radiation pressure regimes can be defined equating (B.1.1) and (B.1.5),

$$T = \left(\frac{3\Re}{a\mu}\right)^{1/3}\rho^{1/3} = \frac{3.2\times 10^7}{\mu^{1/3}}\rho^{1/3} \qquad (cgs) \tag{B.1.16}$$

The regions defined by these two borderlines are shown in figure B.1 (similar figures can be found in stellar physics text books, for instance, Cox & Giuli (1968) or Kippenhahn (1981)). In the same figure, thin dotted lines indicate the conditions at the deepest layer of all the CO50 stable envelope models from chapter 2 for all masses. It is clear that the equation of state is dominated by ideal gas and radiation pressure, and that no degeneracy effects need to be included.

Partial ionization?

At the gas conditions of white dwarf envelopes in this work, hydrogen and helium are completely ionized, and their recombinations, which determine in many cases stellar envelope structures, do not need to be taken into account. However, C and O, which are abundant elements in our models, could be partially ionized. To control this effect, the ionization states of C and O at the densities and temperatures of some of our envelopes have been computed a posteriori, to test if the effects of their recombination need to be taken into account.

For a gas at temperature T and electron pressure P_e, the number density of atoms in the ionization state r+1 (atoms which have lost r+1 electrons), n_{r+1}, with respect to the number density of atoms in the ionization state r, n_r, is given by the Saha equation:

$$\frac{n_{r+1}}{n_r}P_e = \frac{u_{r+1}}{u_r}2\frac{(2\pi m_e)^{3/2}}{h^3}(kT)^{5/2}\exp^{-\chi_r/kT} \tag{B.1.17}$$

where χ_r is the energy necessary to take away an electron in the ground state of an atom r-times ionized (which has lost r electrons), $u_r = u_r(T)$ and $u_{r+1} = u_{r+1}(T)$ are the partition functions of the r and r+1 ionization states, and the other parameters have their usual meaning ($k = 1.305\times 10^{-16} erg\, K^{-1}$, Boltzmann constant). For an atom in the r ionization state, the partition function u_r is defined as

$$u_r \equiv g_{r,0} + g_{r,1}\exp^{-\psi_{r,1}/kT} + g_{r,2}\exp^{-\psi_{r,2}/kT} + g_{r,3}\exp^{-\psi_{r,3}/kT} + ... \tag{B.1.18}$$

where the summation extends over all excitation states of the ion, $g_{r,i}$ is the statistical weight of the ith excitation state and $\psi_{r,i}$ is the the ith state excitation energy. In general, since higher excitation states contribute little to the partition function, it can be approximated to the statistical weight of the ground state, $u_r \approx g_{r,0}$.

In this work, a program has been developed to solve the Saha equation, based on a routine gently provided by Frederic Daigne from the Institut d'Astrophysique de Paris. The program solves the Saha equations plus the normalization equations ($\sum_{r=0}^{6} n_r^C = 1$ and $\sum_{r=0}^{8} n_r^O = 1$) for all ionization states of a mixture of carbon and oxygen, as a function of temperature and density. The number concentrations of all ionization states,

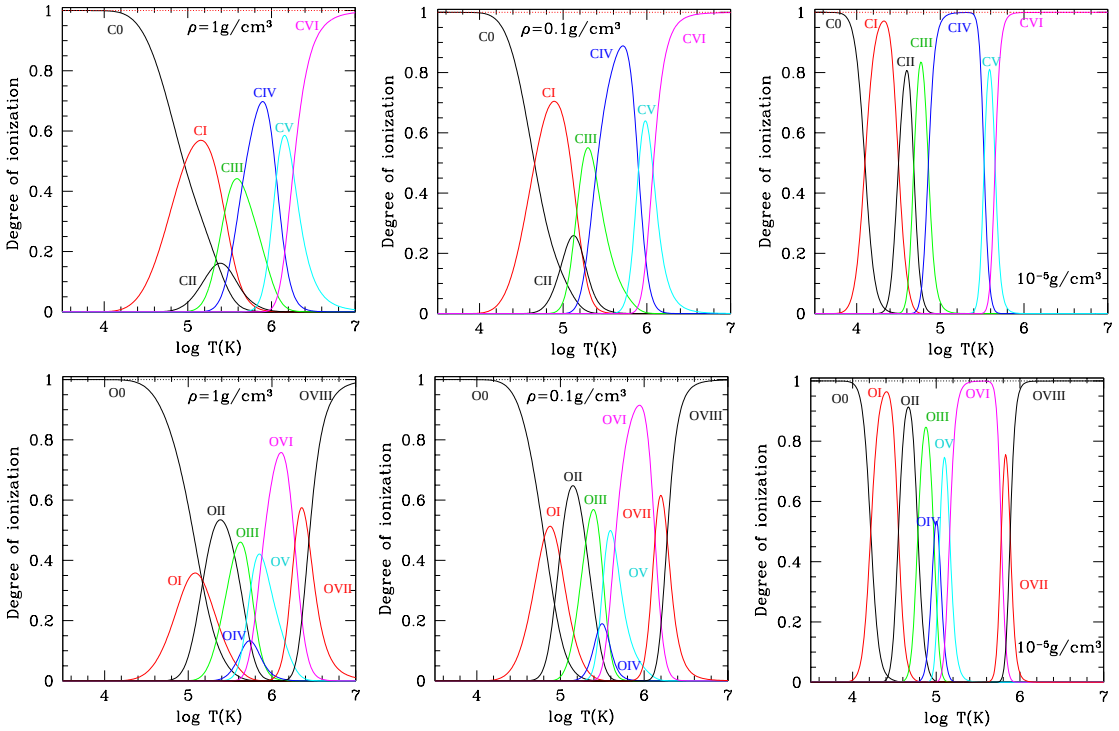

Figure B.2: C and O ionization fractions in a gas with $X_C = 0.5$ and $X_O = 0.5$, as a function of temperature, for three different values of density. In dotted line, the sum of the ionization fractions is also shown as a test.

the electronic number density and the electron pressure are the principal output parameters of the program, as well as the radiation, gas and total pressures, the molecular weight and the ionization, gas and radiation contributions to the internal energy.

Figure B.2 shows the ionization fractions of C and O for several values of density and temperature. Partial ionization affects the equation of state in two ways: changing the mean molecular weight, μ (shown in Figure B.3), and adding the contribution of the energy released in recombinations to the total internal energy, U (shown in figure B.4).

Ionization fractions of C and O in a gas with $X_C = 0.5$ and $X_O = 0.5$ have been computed for the gas conditions obtained in three sample CO white dwarf envelope models of chapter 2, and it has been checked that the ionization effects can be neglected.

B.2 Energy Generation Rates

The energy generation rates taken for the envelope models are (Reeves (1965), Paczyński (1983))

$$\varepsilon_{pp} = 2 \times 10^6 X^2 \rho T_6^{-\frac{2}{3}} \exp\left(-33.81 T_6^{-\frac{1}{3}}\right) erg\, g^{-1} s^{-1} \tag{B.2.19}$$

$$\varepsilon_{CNO} = 8 \times 10^{27} X X_{CNO} \rho T_6^{-\frac{2}{3}} \exp\left(-152.313 T_6^{-\frac{1}{3}}\right) erg\, g^{-1} s^{-1} \tag{B.2.20}$$

where T_6 is the temperature in units of $10^6 K$ and the mass abundance of C, N and O nuclei is approximated as $X_{CNO} = Z/3$. At the temperatures of the burning layers of white dwarf envelopes in this work (around $10^8 K$), the CNO cycle dominates the energy production

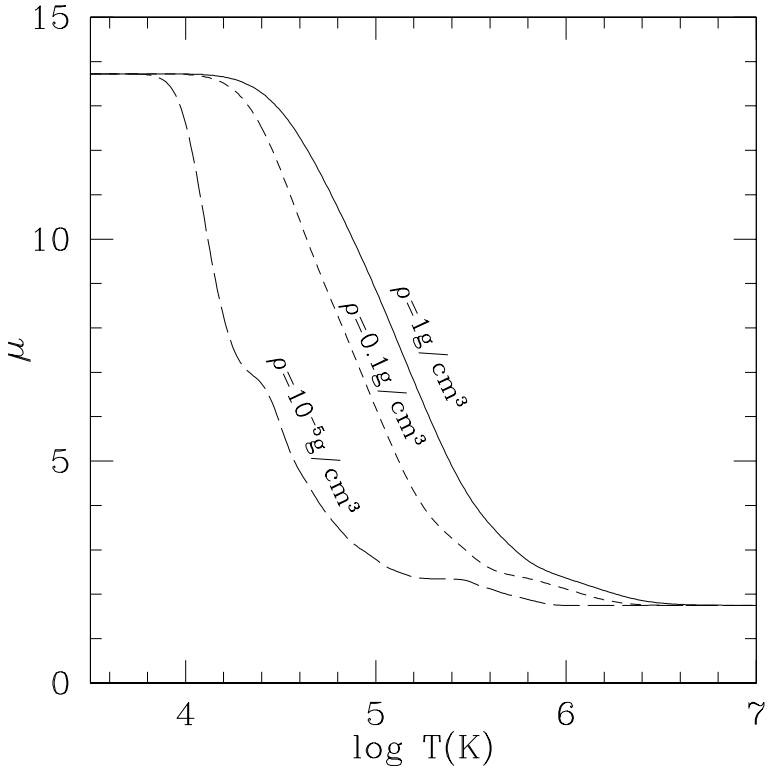

Figure B.3: Change of molecular weight due to recombinations of C and O as a function of temperature, for three different values of density. Gas composition is $X_C = 0.5$ and $X_O = 0.5$.

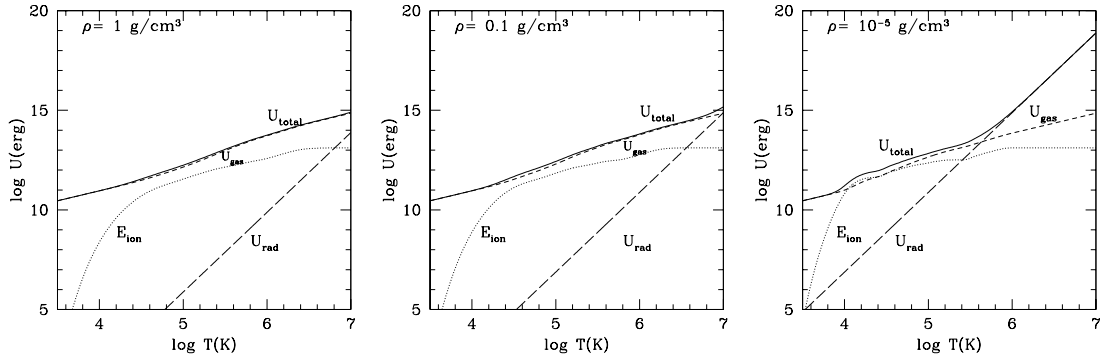

Figure B.4: Contribution to total internal energy, U_{total} (solid line) of the C and O recombinations, E_{ions}(dotted line), as a function of temperature, for three different values of density.
Energy contribution from gas, U_{gas}(short-dashed line), and radiation, U_{rad}(long-dashed line), are also shown. Gas composition is $X_C = 0.5$ and $X_O = 0.5$. Recombination energy contribution is larger for smaller densities.

and the contribution of helium burning through the triple alpha reaction can be neglected (see Figure B.5).

Several expressions similar to (B.2.20) for the CNO cycle energy generation rate are found in the literature. They differ between them in the numerical factors and in the X_{CNO} fraction, which in some cases includes oxygen (Kippenhahn & Weigert (1990), Allen (1973)) and in some other does not (Reeves (1965), Clayton (1968), Cox & Giuli (1968), Paczyński (1983)). Excluding this X_{CNO} factor, for the temperatures and densities of the present

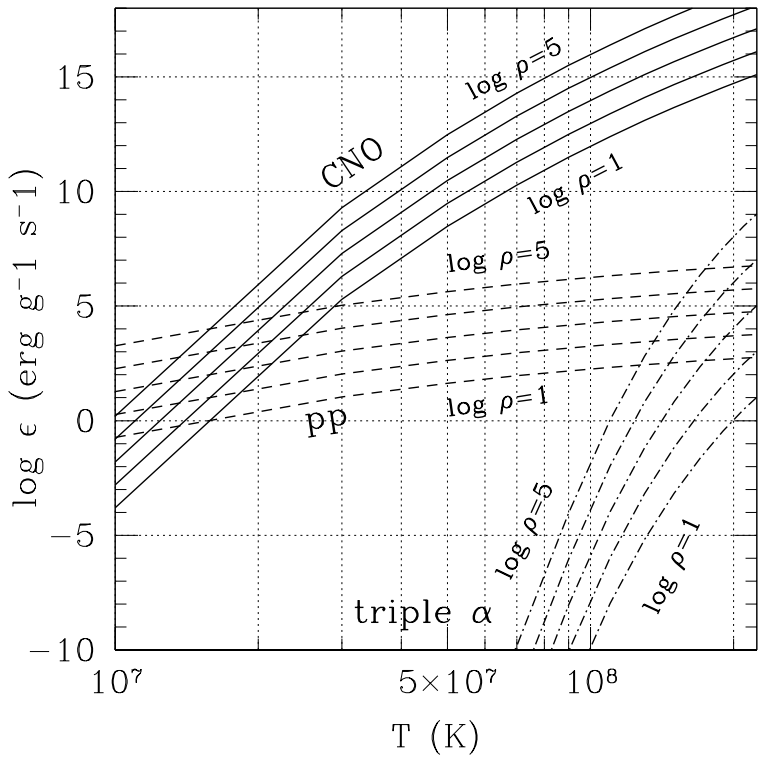

Figure B.5: Energy generation rates as a function of temperature, for the pp chain (dashed line), CNO cycle (solid line), and triple alpha reaction (dot-dashed line), for $X = 0.53$, $Y = 0.21$ and $Z = 0.26$, and densities 10, 10^2, 10^3, 10^4 and $10^5\, g\, cm^{-3}$.

models, the different expressions yield energy generation rates with differences up to a ∼13%. The differences are larger when they are compared to the tabulated values from Allen (1973), which differ from the analytical expressions up to a 20%. Nevertheless, these differences lay in the uncertainity range for these approximations, which, according to Clayton (1968), is ±20%. Regarding the X_{CNO} factor, since these elements are strongly enhanced in our envelopes, the X_{CNO} can vary in a factor ∼10 for the same composition, depending on the inclusion of oxygen or not (see table B.1). As a unified criterium, the approximation used in Paczyński (1983), $X_{CNO} = \frac{Z}{3}$, has been adopted, which yields an intermediate value for the ONe models. For CO50 and I82 models, this approximation underestimates the X_{CN} term by a 30% and the X_{CNO} by a factor 3. The uncertainty introduced by this approximation is therefore maximum for the ONe models, and has been evaluated for some ONe25 $1.1 M_\odot$ models in chapter 2, which have been reintegrated with the X_{CN} and X_{CNO} values from table B.1.

B.3 Opacity

In numerical integration of the envelope model, OPAL Rosseland mean opacity tables (Iglesias & Rogers (1996)) have been used. A specific set of opacity tables has been generated for each one of the six compositions considered in this work using the on-line OPAL opacity table generator. OPAL tables list the logarithm of the Rosseland mean opacity as a function of the logarithm of temperature, logT, for columns of constant logR, where $R = \rho T_6^3$ and $T_6 = 10^{-6} T$, for 70 values of logT between 3.75 and 8.70, and 19

Table B.1: Variations of the X_{CNO} factor involved the energy generation rates.

Model	X_{CN}	X_{CNO}	$\frac{Z}{3}$
ONe75	0.03	0.38	0.25
ONe50	0.02	0.25	0.17
ONe25	0.01	0.13	0.09
ONe09	0.007	0.05	0.04
CO50	0.25	0.5	0.17
I82	0.005	0.01	0.003

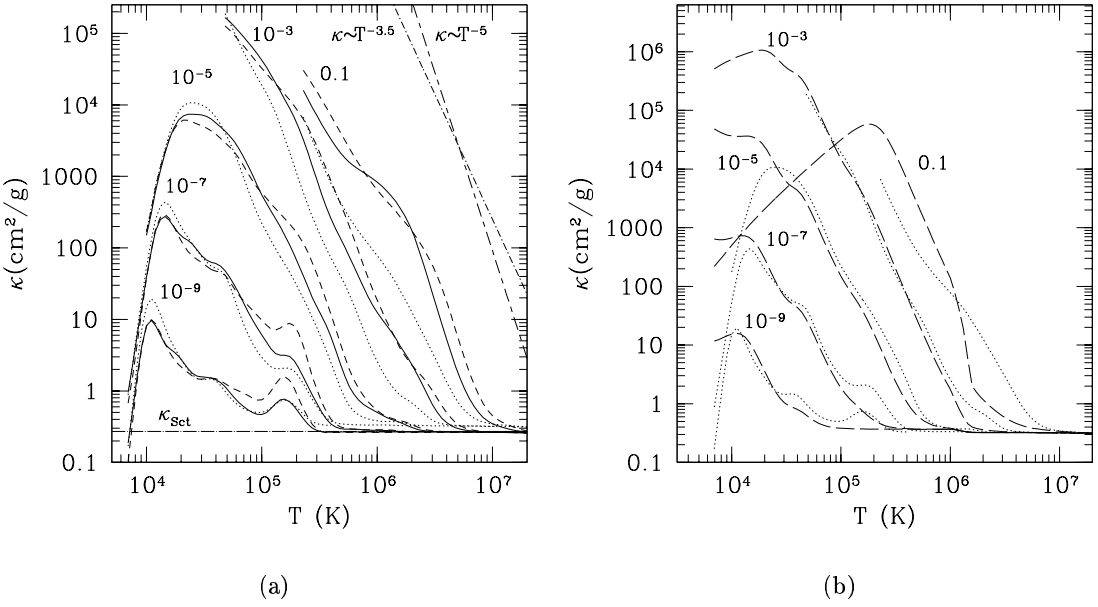

Figure B.6: (a) OPAL opacities as a function of temperature, for several values of the density, for chemical composition of CO50 (solid line), ONe50 (dashed line) and I82 (dotted line) envelope models. (b) OPAL opacities for I82 models (dotted line) and opacities used by Iben (1982) (long-dashed).
In panel (a), for comparison, the Kramers opacity behaviour, $\kappa \sim T^{-3.5}$(short dash-dotted line), and a line with slope $\kappa \sim T^{-5}$ are indicated (short dash-long dash), as well as the approximate value of opacity due to scattering Thompson for $X = 0.35$ (as in ONe50 and CO50 models), $k_{Sct} = 0.2(1 + X) = 0.27$ (long dash-dotted line).

values of logR from -8.0 to 1.0. The OPAL opacity table generator creates a set of tables for a fixed Z and variable values of X and two enhanced elements (say C and O, or O and Ne in our models). Each set of opacity tables consists of five files, for X: 0.0, 0.03, 0.1, 0.35 and 0.7, each of them containing tables for several values of the enhanced elements. The routine xcotrin21, also available at the OPAL site, is used for interpolation between tables. Figure B.6a shows the OPAL opacities used for the CO50, ONe50 and I82 models as a function of temperature, for several values of density. In figure B.6b, OPAL opacities for I82 models are compared to the opacities used by Iben (1982). He used Iben (1975) analytic expressions, which fit the electron conductivity given by Hubbard & Lampe (1969) and the radiative opacities given by Cox & Stewart (1970a,b), for $T > 1.5 \times 10^6 K$; for $T < 1 \times 10^6 K$, he used Christy's (1966) analytic expression, and for temperatures in the range $(1 - 1.5) \times 10^6 K$ he interpolated the two analytic approximations.

For the study of the analytical solution in the case of no energy generation and constant

mass (in appendix A), Kramers opacity is used,

$$\kappa = \kappa_0 \rho T^{-3.5} \tag{B.3.21}$$

where

$$\kappa_0 = 3.8 \times 10^{22} \, (1 + X) \, [(X + Y) + B]$$

$$B = \sum_{i(Z>2)} \frac{X_i Z_i^2}{A_i}.$$

Kramers opacity is often also written as

$$\kappa = \kappa_0' P T^{-4.5} \tag{B.3.22}$$

with $\kappa_0' = \kappa_0 \mu / \Re$.

Appendix C

Mixing Length Theory of Convection

When stellar material is dynamically unstable, convection appears and material is carried upwards by convective bubbles. In a first approximation, it can be assumed that convective bubbles move adiabatically, and that the temperature gradient of the convective layer is simply the adiabatic gradient of the material. But in a more realistic approach, it is necessary to take into account that, in general, convective bubbles do not move adiabatically, but experiment energy losses during their way by radiation to the surrounding medium. In this case, the resulting temperature gradient will differ from adiabatic. The Mixing Length Theory of convection developed by Böhm-Vitense (1958) provides an approximate way to calculate this resulting temperature gradient. The following development of the Mixing Length Theory is extracted mainly from Kippenhahn & Weigert (1990).

C.1 Transport of Energy and Dynamical Stability

The condition for dynamical stability is established in the code using the Schwarzschild criterion:

$$\left|\frac{dT}{dr}\right|_{rad} < \left|\frac{dT}{dr}\right|_{ad} \tag{C.1.1}$$

that for negative temperature gradients

$$\left.\frac{dT}{dr}\right|_{rad} > \left.\frac{dT}{dr}\right|_{ad} \tag{C.1.2}$$

with

$$\left.\frac{dT}{dr}\right|_{ad} = \left.\frac{dT}{dP}\right|_{ad}\left.\frac{dP}{dr}\right|_{ad} = \nabla_{ad}\frac{T}{P}\frac{dP}{dr} \tag{C.1.3}$$

In this work, the envelope is tested at each step for convective instability according to the Schwarzschild criterion. When convection appears, the temperature gradient is calculated using the standard mixing-length theory of Böhm-Vitense (1958).

C.2 Temperature gradients in case of non-adiabatic convection

In case of non-adiabatic convection, it can be seen that

$$\nabla_{rad} > \nabla > \nabla_e > \nabla_{ad} \tag{C.2.4}$$

where $\nabla_{ad} = \frac{d\ln T}{d\ln P}\big|_{ad}$ is the adiabatic gradient, $\nabla_e = \frac{d\ln T}{d\ln P}\big|_e$ is the temperature gradient suffered by the moving volume element (bubble), $\nabla = \frac{d\ln T}{d\ln P}$ is the actual temperature gradient of the medium, and $\nabla_{rad} = \frac{d\ln T}{d\ln P}\big|_{rad}$, defined as

$$F_{rad} + F_{conv} = \frac{L}{4\pi r^2} = \frac{4acG}{3}\frac{T^4 M}{\kappa P r^2}\nabla_{rad} \tag{C.2.5}$$

is the temperature gradient needed to carry all flux by radiation. It must be noticed that, as (C.2.4) indicates, even if convection is not adiabatic, the Schwarzschild criterion for the dynamical stability still holds and only ∇_{ad} and ∇_{rad} need to be compared.

The order in (C.2.4) can be argued as follows: a moving elements reaches the maximum efficiency in energy transport when it moves adiabatically; in this case, the difference of temperature between the bottom and the top of the convective layer is minimum, as well as the temperature gradient ∇_{ad}; if this moving element loses energy during its way, the difference of temperatures for the moving element will be larger than if it had moved adiabatically, and thus $\nabla_e > \nabla_{ad}$. A moving element that starts its way upwards at an initial temperature equal to the medium temperature, will continue its movement if, once it has moved, the surrounding gas is cooler than the bubble, which means that temperature changes faster outside than inside the bubble, $\nabla > \nabla_e$. And finally, if there are convective elements, a larger amount of energy is carried upwards, and the difference of temperature is smaller than in a purely radiative case, $\nabla_{rad} > \nabla$.

C.3 Energy flux in case of non-adiabatic convection

In case of convection, the total energy flux F_{total} results from the addition of convective and radiative fluxes,

$$F_{total} = F_{conv} + F_{rad}$$

which can be rewritten as

$$\frac{L}{4\pi r^2} = F_{conv} + \frac{4acG}{3}\frac{T^4 M}{\kappa P r^2}\nabla \tag{C.3.6}$$

where F_{conv} is the flux due to convective moving elements, the second term in the right is the flux carried by radiation, given the temperature gradient of the medium, ∇, and L is the total luminosity (other variables and constants have their usual meaning). In the construction of a stellar model, L, M, T, P, κ and r are known for each layer or appear in another of the differential equations. It is thus only necessary to evaluate the flux carried by convection, F_{conv}, in order to obtain the temperature gradient of the medium, ∇. The mixing length theory of convection evaluates F_{conv} assuming that volume elements move upwards a mean distance, or *mixing length* l_m, before dissolving in the surrounding medium.

Average convective flux, F_{conv}

The flux carried by a convective bubble of density ρ, moving at speed v and with a temperature difference with respect to the surrounding material (at temperature T) $DT = T_e - T_{surr} = T_e - T$, where T_e is the temperature of the gas inside the bubble, can be written as

$$F_{conv} = \rho v c_p DT \tag{C.3.7}$$

We now need to find an expression for DT and for v to evaluate the convective flux.

Assuming that bubbles dissolve in the medium after moving, on the average, half of the mixing length, l_m, we can write

$$\frac{DT}{T} = \frac{1}{T}\frac{\partial(DT)}{\partial r}\frac{l_m}{2} \tag{C.3.8}$$

$$\frac{DT}{T} = \frac{1}{T}\left(\frac{\partial T_e}{\partial r} - \frac{\partial T}{\partial r}\right)\frac{l_m}{2} = \left(\frac{\partial \ln T_e}{\partial r} - \frac{\partial \ln T}{\partial r}\right)\frac{l_m}{2}$$

$$\frac{DT}{T} = \left(\frac{\partial \ln T_e}{\partial \ln P} - \frac{\partial \ln T}{\partial \ln P}\right)\frac{\partial \ln P}{\partial r}\frac{l_m}{2}$$

$$\frac{DT}{T} = (\nabla_e - \nabla)\frac{\partial \ln P}{\partial r}\frac{l_m}{2} \tag{C.3.9}$$

It will be useful to use here the *pressure scale-height* H_p, defined as

$$H_p \equiv -P\frac{\partial r}{\partial P} = -\frac{\partial r}{\partial \ln P} \tag{C.3.10}$$

which with the hydrostatic equilibrium equation

$$\frac{\partial P}{\partial r} = -\frac{GM}{r^2}\rho = -g\rho \tag{C.3.11}$$

can be written as

$$H_p = \frac{P}{\rho g}.$$

Using the definition of H_p , we can write (C.3.9) as

$$\frac{DT}{T} = (\nabla - \nabla_e)\frac{1}{H_p}\frac{l_m}{2} \tag{C.3.12}$$

In order to evaluate the speed of the bubble in the medium, we need to estimate its kinetic energy after moving $\frac{l_m}{2}$ under the effect of the buoyancy force. The buoyancy force per unit mass acting on a bubble with a difference of density with respect to the surrounding medium of $D\rho$ can be written as

$$k_r = -g\frac{D\rho}{\rho}$$

The bubble is supposed to be in mechanical equilibrium with its surroundings, so that $DP = 0$, and the medium is chemically homogeneous, so that $D\mu = 0$. In these conditions, using the definition of δ,

$$\delta \equiv -\left.\frac{\partial \ln \rho}{\partial \ln T}\right|_P$$

which in the case of equation of state of ideal gas plus radiation pressure can be written as $\delta = \frac{4-3\beta}{\beta}$, with $\beta = \frac{P_{gas}}{P_{total}}$, the density difference is

$$\frac{D\rho}{\rho} = -\delta\frac{DT}{T} \tag{C.3.13}$$

We assume that, on average, half of k_r has acted during the movement of the element, so that using (C.3.12) and (C.3.13) the work done by the buoyancy force is

$$\frac{1}{2}k_r\frac{l_m}{2} = g\delta\left(\nabla - \nabla_e\right)\frac{l_m^2}{8H_P} \tag{C.3.14}$$

Assuming that half of this work is converted into kinetic energy ($v^2/2$ per unit mass), while the other half is lost by transfer to the surrounding medium, we obtain the average velocity v of the ascending bubbles

$$v^2 = g\delta\left(\nabla - \nabla_e\right)\frac{l_m^2}{8H_P} \tag{C.3.15}$$

Using (C.3.12) and (C.3.15) in (C.3.7), we have for the average convective flux

$$F_{conv} = \frac{\rho c_p}{4\sqrt{2}}l_m^2 T\sqrt{g\delta}\left(\frac{\nabla - \nabla_e}{H_P}\right)^{3/2} \tag{C.3.16}$$

which depends on the properties of the medium (ρ, T, g, H_P, c_P), the free parameter l_m, the temperature gradient that suffers the material inside the moving element, ∇_e, and the surrounding temperature gradient ∇, which is the final result that we need to incorporate in the energy transportation equation. If we are able to express ∇_e as a function of known variables, it will be possible to calculate the temperature gradient ∇ as a function of known parameters or variables introducing (C.3.16) in (C.3.6).

The change of temperature of a convective moving element is caused by the radiation of energy to the surroundings and the adiabatic expansion or compression.

Losses of energy of the bubble by radiation to the surroundings

The flux radiated through the surface of the convective element, can be expressed as

$$F = \frac{4ac}{3}\frac{T^3}{\kappa\rho}\frac{\partial T}{\partial n}$$

where $\frac{\partial}{\partial n}$ indicates the differentiation in the direction perpendicular to the surface. For a spherical bubble of diameter d, surface S and volume V, with a difference of temperature with respect to the surrounding of DT, the temperature gradient in the normal direction can be approximated by $\frac{\partial T}{\partial n} \approx \frac{2DT}{d}$. With this, the energy loss per unit time λ due to radiation through the whole bubble surface is

$$\lambda = SF = \frac{8acT^3}{3\kappa\rho}DT\frac{S}{d} \tag{C.3.17}$$

This energy lost by radiation to the surrounding medium will cause a temperature change of the bubble, $\Delta T_{e,rad}$

$$\lambda = \rho V c_p \Delta T_{e,rad}$$

Temperature gradient of the convective volume element, ∇_e

The total change of temperature of the bubble per unit length traveled in its convective movement will be given by the change of temperature due to radiative losses to the medium per unit length, $\frac{\Delta T_{e,rad}}{v}$, plus the adiabatic gradient,

$$\left(\frac{dT}{dr}\right)_e = \left(\frac{dT}{dr}\right)_{ad} - \frac{\lambda}{\rho V c_p v}$$

Here we can use again the pressure scale-height (C.3.10) and multiply the previous expression by H_P/T to write

$$\nabla_e - \nabla_{ad} = \frac{\lambda H_P}{\rho V c_p v T}$$

Substituting λ by its expression in (C.3.17) and using (C.3.12) for DT,

$$\nabla_e - \nabla_{ad} = \frac{8acT^3}{3\kappa\rho}(\nabla - \nabla_e)\frac{1}{H_p}\frac{l_m}{2}T\frac{S}{d}\frac{H_P}{\rho V c_p v T}$$

$$\nabla_e - \nabla_{ad} = \frac{4acT^3}{3\kappa\rho^2 c_p v}(\nabla - \nabla_e)\frac{l_m}{V}\frac{S}{d} \tag{C.3.18}$$

The "form factor" $\frac{l_m}{V}\frac{S}{d}$ in the previous expression depends on the geometry of the moving element. If we assumed the bubbles to be spheres of diameter l_m, the "form factor" would be $6/l_m$. Usually, the form factor used in the literature is

$$\frac{l_m S}{V d} \approx \frac{9}{2l_m}$$

which introduced in (C.3.18) gives

$$\frac{\nabla_e - \nabla_{ad}}{\nabla - \nabla_e} = \frac{6acT^3}{\kappa\rho^2 c_p v l_m} \tag{C.3.19}$$

and using (C.3.15) for the average velocity

$$\frac{\nabla_e - \nabla_{ad}}{\nabla - \nabla_e} = \frac{6acT^3}{\kappa\rho^2 c_p l_m^2}\sqrt{\frac{8H_P}{g\delta}}(\nabla - \nabla_e)^{-1/2} \tag{C.3.20}$$

which relates the actual temperature gradient of the medium, ∇, to the change of temperature of the moving element, ∇_e (the other quantities are known in the problem).

C.4 Dimensionless equations for the temperature gradient

We define now two dimensionless quantities, U and W, that will make simpler the equations:

$$U \equiv \frac{3acT^3}{\kappa\rho^2 c_p l_m^2}\sqrt{\frac{8H_P}{g\delta}} \tag{C.4.21}$$

$$W \equiv \nabla_{rad} - \nabla_{ad} \tag{C.4.22}$$

With this new quantities, we can rewrite (C.3.20) as

$$\frac{\nabla_e - \nabla_{ad}}{\nabla - \nabla_e} = 2U(\nabla - \nabla_e)^{-1/2}$$

$$\nabla_e - \nabla_{ad} = 2U\sqrt{\nabla - \nabla_e} \tag{C.4.23}$$

We can find a second, independent relation between ∇ and ∇_e, which will make possible to find a solution for ∇. Combining (C.3.6) with the definition of ∇_{rad} in (C.2.5), we have

$$\frac{4acG}{3}\frac{T^4 M}{\kappa P r^2}\nabla_{rad} = F_{conv} + \frac{4acG}{3}\frac{T^4 M}{\kappa P r^2}\nabla$$

and using the expression for F_{conv} found above, (C.3.16),

$$\frac{4acG}{3}\frac{T^4M}{\kappa Pr^2}\left(\nabla_{rad}-\nabla\right)=\frac{\rho c_p}{4\sqrt{2}}l_m^2T\sqrt{g\delta}\left(\frac{\nabla-\nabla_e}{H_P}\right)^{3/2}$$

$$\left(\nabla-\nabla_e\right)^{3/2}=\frac{4acG}{3}\frac{T^3M}{\kappa Pr^2}\frac{2\sqrt{8}}{l_m^2}\frac{H_P^{3/2}}{\rho c_p\sqrt{g\delta}}\left(\nabla_{rad}-\nabla\right)$$

$$\left(\nabla-\nabla_e\right)^{3/2}=\frac{8}{9}\left(\frac{3acT^3}{\kappa\rho c_pl_m^2}\sqrt{\frac{8H_P}{g\delta}}\right)\frac{GM}{Pr^2}\rho H_P\left(\nabla_{rad}-\nabla\right)$$

Using now (C.4.21) and (C.3.11)

$$\left(\nabla-\nabla_e\right)^{3/2}=\frac{8}{9}U\left(-\frac{dP}{dr}\right)\frac{1}{P}H_P\left(\nabla_{rad}-\nabla\right)$$

which with (C.3.10) becomes

$$\left(\nabla-\nabla_e\right)^{3/2}=\frac{8}{9}U\left(\nabla_{rad}-\nabla\right) \tag{C.4.24}$$

We have now two equations, (C.4.23) and (C.4.24), relating ∇ and ∇_e, which can be reduced to only one. Equation C.4.23 can be rewritten as

$$\left(\nabla-\nabla_{ad}\right)-\left(\nabla-\nabla_e\right)=2U\sqrt{\nabla-\nabla_e} \tag{C.4.25}$$

which is a quadratic equation for $x=\sqrt{\nabla-\nabla_e}$,

$$x^2+2Ux-\left(\nabla-\nabla_{ad}\right)=0$$

with the solution $x=-U\pm\sqrt{\nabla-\nabla_{ad}+U^2}$. We define a new variable ξ as the positive root of

$$\xi^2\equiv\nabla-\nabla_{ad}+U^2 \tag{C.4.26}$$

to write the solution of (C.4.25) as

$$\sqrt{\nabla-\nabla_e}=\xi-U \tag{C.4.27}$$

We introduce this into (C.4.24) and use (C.4.26) and (C.4.22) to obtain a cubic equation for ξ, independent of ∇_e

$$\left(\xi-U\right)^3=\frac{8U}{9}\left(\nabla_{rad}-\nabla\right)=\frac{8U}{9}\left(\nabla_{rad}-\nabla_{ad}-\xi^2+U^2\right)$$

$$\left(\xi-U\right)^3+\frac{8U}{9}\left(\xi^2-U^2-W\right)=0 \tag{C.4.28}$$

which expanded becomes

$$\xi^3-\left(\frac{19U}{9}\right)\xi^2+\left(3U^2\right)\xi-\frac{U}{9}\left(8W+17U^2\right)=0$$

This cubic equation has only one real solution. In general, the solution of a cubic equation of the form $x^3+ax^2+bx+c=0$ with only one real solution is Press et al.(1992)

$$x=A+B-\frac{a}{3}$$

where

$$A = -sgn(R)\left|\left(|R| + \sqrt{R^2 - Q^3}\right)^{1/3}\right|$$

$$B = \frac{Q}{A}\, for\, A \neq 0,\ and\, B = 0\, if\, A = 0$$

$$Q = \frac{a^2 - 3b}{p},\quad R = \frac{2a^3 - 9ab + 27c}{54}$$

For our cubic equation,

$$\xi = A + B + \frac{19}{27}U \tag{C.4.29}$$

$$Q = -\frac{368}{729}U^2$$

$$R = -\frac{4672}{19683}U^3 - \frac{4}{9}WU$$

Taking into account the definition of dimensionless quantities U and W (C.4.21,C.4.22), we find that U is always positive and different from zero, and that in case of convection, as (C.2.4) verifies, W>0. In this case, R is positive, and then $A = \left(|R| + \sqrt{R^2 - Q^3}\right)^{1/3}$, and $B = Q/A$.

Once we have obtained the value of ξ, the temperature gradient is easily computed from (C.4.26) as

$$\nabla = \xi^2 + \nabla_{ad} - U^2$$

Appendix D

Computational Method

As most of stellar structure and evolution problems, the construction of a white dwarf envelope model involves the resolution of a system of differential equations with boundary conditions fixed at the two boundaries of the integration interval. The integration of the envelope has been performed using an embedded (adaptative stepsize controlled) Runge-Kutta method, and to solve the two point boundary problem, a shooting method has been used.

D.1 Embedded Runge-Kutta method

Given a set of N first-order coupled differential equations for the functions y_i,

$$\frac{dy_i(x)}{dx} = f_i(x, y_1, ..., y_N) \quad i = 1, ..., N$$

the embedded Runge-Kutta formulas, invented by Fehlberg, provide a method to solve numerically the system with a stepsize adjustment algorithm based on a fifth-order Runge-Kutta method.

For a given stepsize h, the Runge-Kutta method advances the solution from x_n to $x_{n+1} = x_n + h$, evaluating the functions f_i once at the initial point of the interval, once at a trial end point, and twice or more times at trial midpoints, the number of these midpoints depending on the order of the Runge-Kutta method (two midpoints for the popular fourth-order Runge-Kutta). The Fehlberg method is based on the use of six function evaluations combined in two different ways that give a fifth-order and a fourth-order Runge-Kutta methods. The stepsize is adjusted using the difference between the two solutions of $y(x + h)$ as an estimation of the truncation error.

The general form of a fifth-order Runge -Kutta formula is

$$k_1 = hf(x_n, y_n)$$

$$k_2 = hf(x_n + a_2 h, y_n + b_{21} k_1)$$

$$\cdots$$

$$k_6 = hf(x_n + a_6 h, y_n + b_{61} k_1 + \cdots + b_{65} k_5)$$

$$y_{n+1} = y_n + c_1 k_1 + c_2 k_2 + c_3 k_3 + c_4 k_4 + c_5 k_5 + c_6 k_6 + O\left(h^6\right) \tag{D.1.1}$$

The embedded fourth-order formula is

$$y^*_{n+1} = y_n + c^*_1 k_1 + c^*_2 k_2 + c^*_3 k_3 + c^*_4 k_4 + c^*_5 k_5 + c^*_6 k_6 + O\left(h^5\right) \tag{D.1.2}$$

In the previous formulae, a_i, b_{ij}, c_i and $c_i^*$are constants, for which the routine we use takes the values found by Cash & Karp (1990), and y_n indicates the value of the vector of dependent variables, $y = (y_1, ..., y_N)$ at the n step of the integration. The truncation error estimate is then

$$\Delta = y_{n+1} - y^*_{n+1} = \sum_{i=1}^{6} (c_i - c_i^*)\, k_i \tag{D.1.3}$$

The stepsize control will be imposed demanding Δ to be smaller than a given accuracy value at each step. It is convenient to set the accuracy value for each element of the vector Δ independently, using a vector argument, *yscal(1:N)*, and a tolerance level called *eps,* so that $\Delta(i) = eps \times yscal(i)$. In this work, we set $yscal(i) = |y(i)| \times |h \times f(i)|$, which gives constant fractional errors except very near zero points.

Once the desired accuracy Δ is determined, some relation between Δ and the stepsize h is needed to impose this control. As seen from (D.1.1-D.1.3), Δ scales as h^5. If we denote by h_1 a stepsize that gives an error Δ_1, the stepsize h_0 that would give the desired accuracy Δ_0 can be estimated as

$$h_0 = h_1 \left| \frac{\Delta_0}{\Delta_1} \right|^{\frac{1}{5}} \tag{D.1.4}$$

If the accuracy of the previous step, Δ_1, is larger than the desired accuracy, the same step will be recalculated using the new stepsize h_1; otherwise, if Δ_0 is good enough, h_0 will be the stepsize used in the next integration step (see Figure D.1).

In this work, the routines *rkqs* and *rkck* from Press et al.(1992), which apply the embedded Runge-Kutta method with Cash-Karp coefficients, have been used. The tolerance level *eps* has been fixed to 10^{-9}, which results in a stepsize of $\Delta M \sim 10^{-9} - 10^{-10} M_\odot$.

D.2 The Shooting Method

The basic principle of the shooting method is similar to a shooting game: an integration is 'shut' with trial initial parameters from one of the boundaries of the integration interval, and after reaching the end of the interval, the functions values obtained are compared with the desired 'target' values; the 'shooting' initial parameters are accordingly changed to obtain in the next 'shoot' a result closer to the 'target'.

The shooting method (see flow chart in Figure D.2) makes possible the integration of the four stellar structure equations in chapter 2 for the four variables *M, P, L* and *T* with two of the four boundary conditions fixed at the photosphere (say $L_{ph} = L$ and $T_{ph} = T_{eff}$) and the other two at the base of the envelope ($M_{base} = 0$ and $R_{base} = R_{WD}$) . The integration starts at the top of the envelope, with L_{out} and T_{eff} fixed (the determination of this outer boundary conditions is explained in chapter 2) and trial values for $M_{photos} = M_{env}$ and R_{photos}, and proceeds inwards, with decreasing values of the radius R (though the actual integration variable is the geometrical depth as defined in chapter 2), from the photosphere to the base of the envelope or surface of the degenerate core. When the base of the envelope is reached, the values of M_{base} and R_{base} are compared with the required surface conditions, $M_{base} = 0$ and $R_{base} = R_{WD}$. If the differences of the conditions are larger than a required accuracy, the integration re-starts from the photosphere with new trial values for M_{env} and R_{photos}. The problem consists actually in finding the roots of a vector of functions: the method has to find the roots of two functions, f_1 and f_2, which can be the differences between the desired and the obtained values, or some convenient combination of these, at the end of the integration interval (conditions on M_{base} and R_{base} at the base of the envelope in this case). These functions to be zeroed are in fact functions of the trial outer

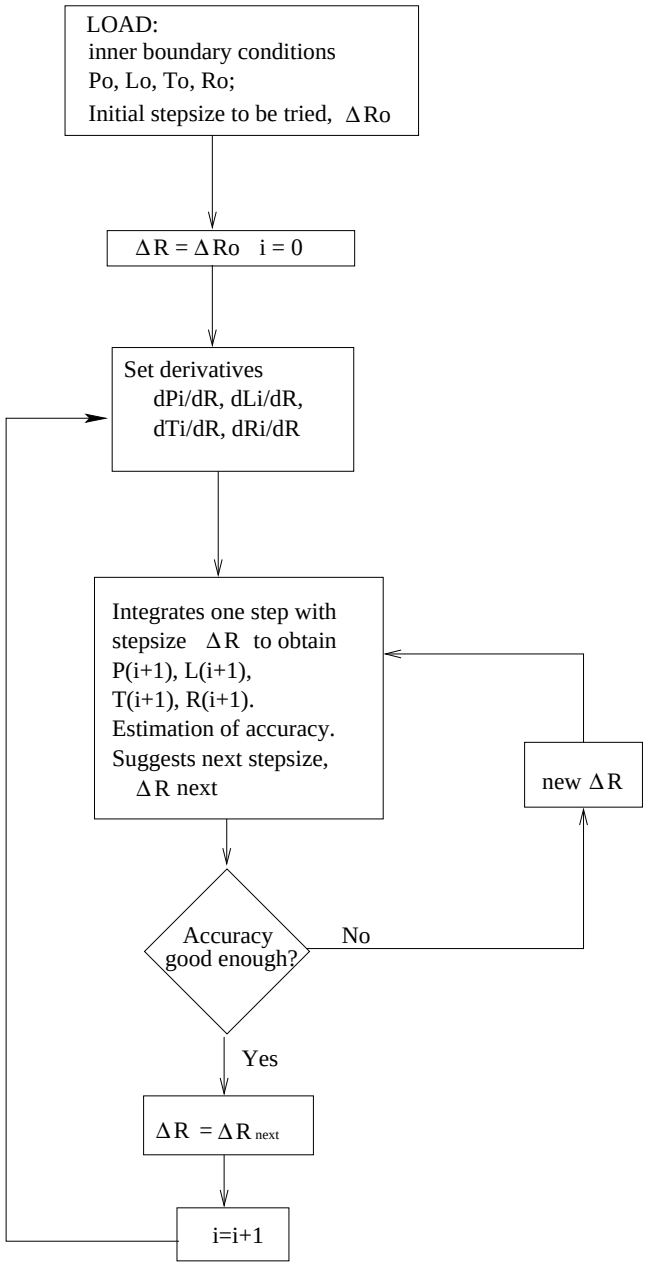

Figure D.1: Flow chart for the integration process with adaptative stepsize.

boundary conditions (here, M_{env} and R_{ph} at the photosphere), since the obtained values at the end of the integration interval depend on these boundary conditions.

The shooting method procedure used in this work, obtained from Press et al.(1992) (routines *shoot, newt, fdjac, fmin, lnsrch, lubksb, ludcmp*), implements a multidimensional, globally convergent Newton-Raphson method to seek to zero the functions of boundary conditions obtained after integration. This routine requires the variables in the functions to have values approximately in the range 0-1, which can be achieved by scaling the photospheric boundary conditions with proper parameters. The Newton-Raphson routine used in the envelope models seeks to zero the functions f_1 and f_2 of the variables v_1 and v_2, where the functions and variables are defined as

$$v_1 = \sqrt{R_{ph}} \tag{D.2.5}$$

$$v_2 = \sqrt{\frac{(M_{env} - M_{WD})}{M_\odot}} \tag{D.2.6}$$

$$f_1 = 10^{13} \frac{M_{env}(M_{env},\, R_{ph})}{M_\odot} \tag{D.2.7}$$

$$f_2 = 10^5 \left| \frac{R_{base}(M_{env},\, R_{ph}) - R_{WD}}{R_{WD}} \right| \tag{D.2.8}$$

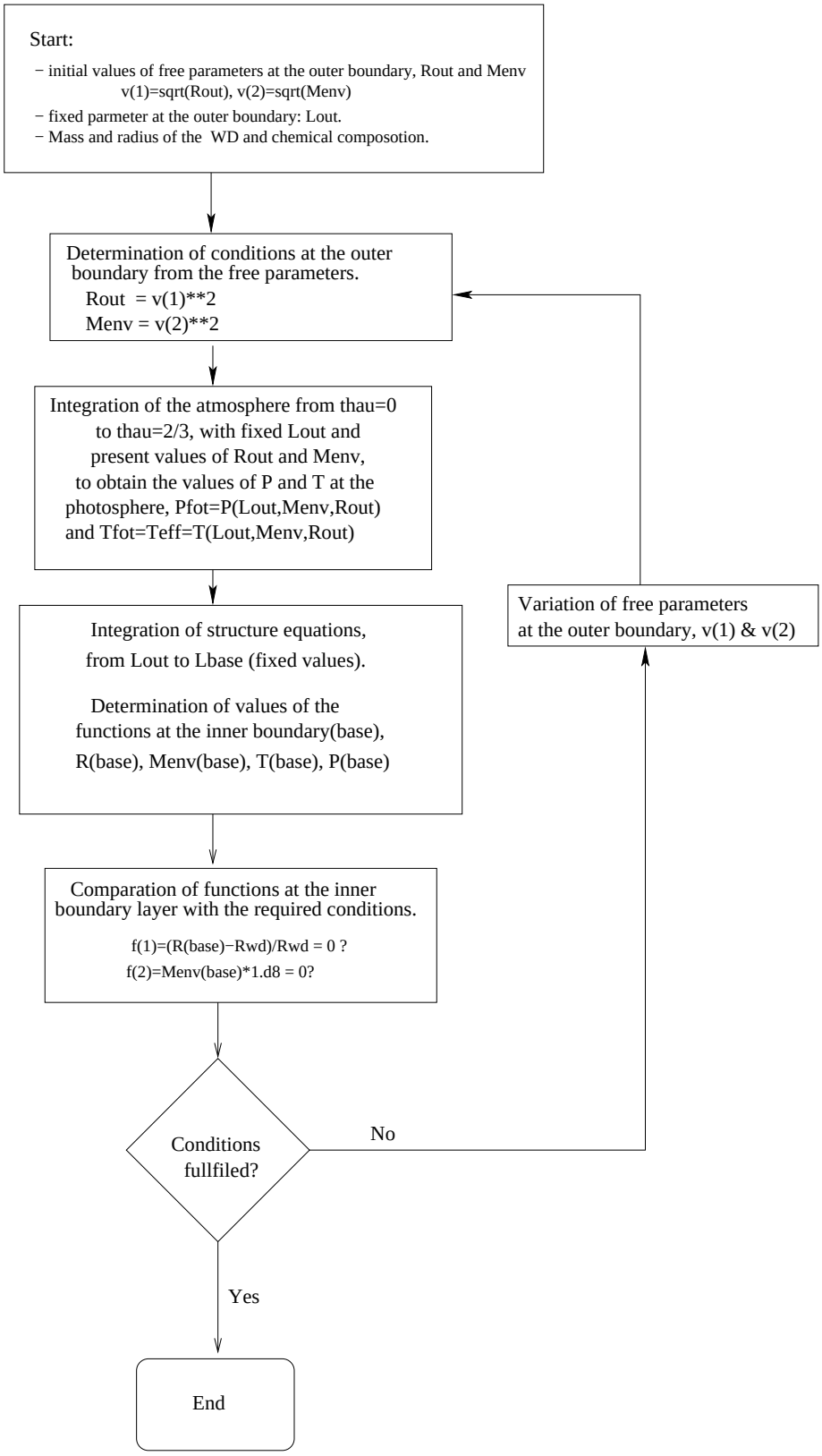

Figure D.2: Shooting method.

Appendix E

White Dwarf Atmosphere Models

The white dwarf atmosphere models used in this work were kindly provided by Jim MacDonald and are hydrostatic LTE atmosphere models for CO and ONe white dwarfs(MacDonald & Vennes (1991)). The white dwarf mass and luminosity are fixed to $1.2 M_{\odot}$ and $4.2 \times 10^4 L_{\odot}$, and two representative compositions are considered: CO atmosphere models, with $C/C_{\odot} \sim 15$, $O/O_{\odot} \sim 15$ and $Ne/Ne_{\odot} \sim 7$, and ONe models, with $C/C_{\odot} \sim 1.2$, $O/O_{\odot} \sim 14$ and $Ne/Ne_{\odot} \sim 81$. H, He and N are also included, with N enhanced with respect to solar abundances (see table E.1 for detailed composition). For each composition, a grid of eleven white dwarf atmosphere spectrum models (for energies between 0.4 eV and 6.2 keV) is included, for the effective temperatures T_{eff}: (1, 2, 3, 3.5, 4, 5, 6, 7, 8, 9, 10)$\times 10^5 K$. As the luminosity and the white dwarf mass are fixed, for a given effective temperature, the photospheric radius and the surface gravity are determined as

$$R_{ph} = 4.75 \times 10^{10} \left(\frac{10^5 K}{T_{eff}} \right)^2 cm$$

$$g = 7.06 \times 10^4 \left(\frac{T_{eff}}{10^5 K} \right)^4 cm\, s^{-2}$$

Figure E.1 shows a CO and an ONe white dwarf atmosphere models, with $T_{eff} = 10^5 K$, as well as a blackbody of the same temperature for comparison. It can be observed that for the same effective temperature, the total flux is larger for the blackbody model. The white dwarf atmosphere models emits a larger flux only between 0.5 and 1.0 keV, the energy band where the maximum emission of H-burning white dwarfs is found. The blackbody model has a harder tail than the atmosphere models, and a larger flux for the same effective temperature. As a result, the fits with blackbody models to X-ray observational data in the spectral band of the ROSAT/PSPC or the EPIC cameras (above 0.1 keV) give lower effective temperatures and larger fluxes than white dwarf atmosphere models. Absorption edges are specially evident for CO models. CO white dwarf atmosphere models are shown for five different effective temperatures in figure E.2. For effective temperatures larger than $4 \times 10^5 K$, the increasing depth of the absorption edges represents a cut-off for the spectrum.

To fit the observational data with the white dwarf atmosphere models, it as been necessary to build table models for use with XSPEC spectral fitting program. When XSPEC fits a table model to observational data, it multiplies the model by a normalization constant. The meaning of this constant depends on the construction of the model tables. We have normalized the atmosphere models so that the normalization constant introduced by XSPEC has the same interpretation as the normalization constant of the blackbody

Table E.1: Chemical compositions (in mass fractions) of the atmosphere models.

Model	H	He	C	N	O	Ne
CO White Dwarf	0.47	0.22	0.059	0.11	0.13	0.015
ONe White Dwarf	0.31	0.31	0.0046	0.08	0.12	0.17

models incuded in the XSPEC distribution. In fact, there are two blackbody models in XSPEC: in one of them, *bbodyrad*, the normalization constant is proportional to the squared photospheric radius,

$$K_R = \left(\frac{R_{km}}{D_{10}}\right)^2$$

(where R_{km} is the photospheric radius in units of *km* and D_{10} is the distance to the source in units of *10 kpc*), while in the other, *bbody*, it is proportional to the source luminosity,

$$K_L = \frac{L_{39}}{D_{10}^2}$$

(where L_{39} is the source luminosity in units of $10^{39} ergs/s$). In this work, two series of table models have been generated for each composition: the first one, scaled to a source of a radius of *1km* located at a distance of *10 kpc*, so that the XSPEC normalization constant can be interpreted as in the *bbodyrad* XSPEC model; in the second one, atmosphere models are scaled to a luminosity of $10^{39} ergs/s$ and the same distance, and the XSPEC normalization constant is equivalent to that in *bbody* XSPEC model.

There is a certain inconsistency in the previous scaling of the white dwarf atmosphere models: as mentioned above, the models are calculated for certain luminosity, $L = 4.2 \times 10^4 L_\odot$, and thus have a fixed photospheric radius for each effective temperature. By allowing the spectra to be scaled with a normalization constant as XSPEC does, we assume that the same shape of the spectrum is valid for different values of the luminosity. To be entirely consistent, it would be necessary to fix the normalization constant to the value corresponding to $L = 4.2 \times 10^4 L_\odot$ and the distance to the source, or to understand a different normalization constant as due to a different distance to the source. Of course, it is unrealistic to expect all white dwarfs in post-outburst classical novae to have this precise value of the luminosity; in fact, they are expected to have luminosities not very different from $4.2 \times 10^4 L_\odot$. When fitting data with white dwarf atmosphere models, it is assumed that for similar (but not exactly equal) luminosities, the shape of the spectrum is not very different.

Some works have compared LTE and non-LTE atmosphere models (see Hartmann & Heise (1997)), to find that both kind of spectra differ little for *log g* > 9 (i.e for $M_{WD} \geq 0.6 M_\odot$). At these high gravities, the density is high enough for collisional ionizations to dominate over photoionization. The radiation field is strongly coupled to the atmosphere local temperature and LTE determines the degree of ionization and the atomic level occupation. Thus for white dwarfs in classical novae, which are always more massive than $0.6 M_\odot$, the error in using LTE atmosphere models must be small. White dwarf atmosphere models in this work have been previously used for analysis of post-outburst classical novae with supersoft X-ray emission (Balman et al.(1998), Balman et al.(2001), Orio & Greiner (1999) for Nova Cygni 1992, Nova Mus 1983 and Nova LMC 1995, respectively).

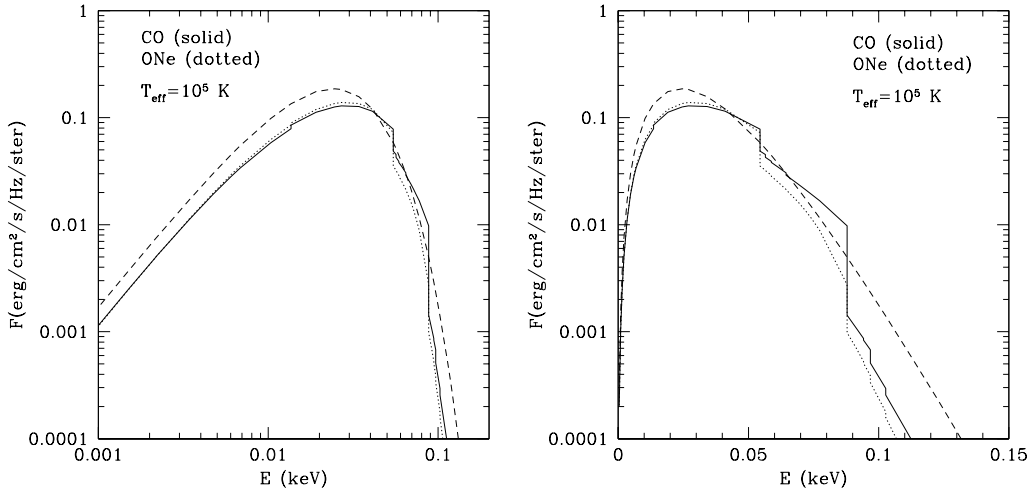

Figure E.1: CO (solid line) and ONe (dotted line) white dwarf atmosphere models at $T_{eff} = 10^5 K$. A blackbody of the same temperature (dashed line) is shown for comparison.

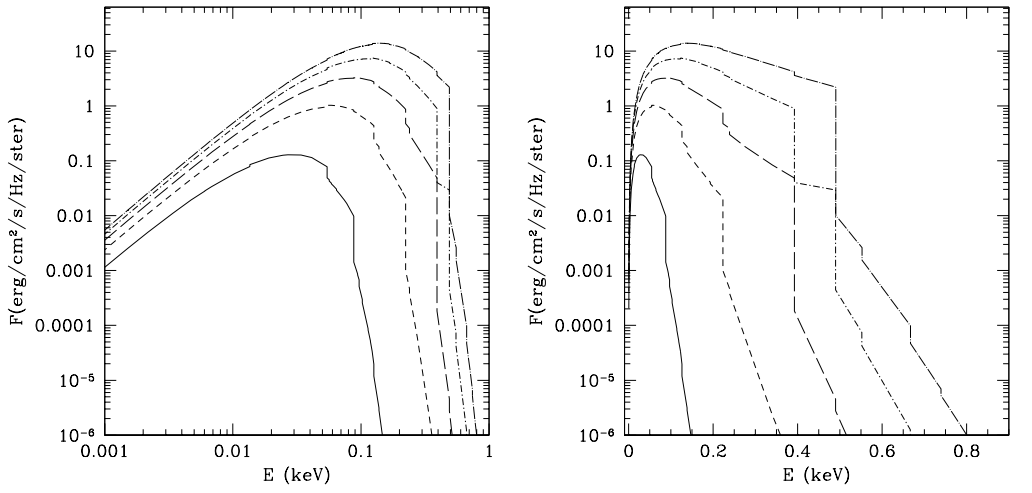

Figure E.2: CO white dwarf atmosphere models at $T_{eff} = 10^5 K$ (solid line), $T_{eff} = 2 \times 10^5 K$ (short dashed), $T_{eff} = 3 \times 10^5 K$ (long dashed), $T_{eff} = 4 \times 10^5 K$ (dot - short dash) and $T_{eff} = 5 \times 10^5 K$ (dot - long dash).

Appendix F

X-ray data analysis

F.1 Data reduction

F.1.1 ROSAT/PSPC data reduction

ROSAT/PSPC data reduction has been performed using EXSAS/MIDAS (Extended Scientific Analysis Software, Zimmerman et al.(1998)). For each exposure, an image of the detector plane is obtained, with a field of view of 2 degrees. Previous to the extraction of the source count-rate and spectrum, the background needs to be evaluated in a region close to the source of interest and free from other sources in the field of view. The region of the image containing the source is selected and the background is subtracted from the source image, using the necessary correction factors for the different areas of the two regions. As the source flux is time dependent, both the extraction region of source photons and the background estimation region have been selected for each exposure independently. The source photons have been extracted from a circle with different radius for each exposure, while the background has been determined in an annular region centered on the position of V1974 Cyg for the observations with a low count rate (figure F.1). For the days with the highest flux, an extended X-ray halo caused by dust scattering of low energy photons appears around the source (Mathis et al.(1995)). In these cases, the background has been extracted from a box in a region with no halo and no detector structure pattern, in order to estimate a background free from dust scattering effect (figure F.2). Individual sources different from V1974 Cyg have been removed from both the source and the background extraction regions. They have been detected using a source detection algorithm developed by Dr. Jochen Greiner (Max-Planck-Institut für extraterrestrische Physik) and those with a count-rate higher than 0.05 cts s^{-1} have been removed from the image.

For the spectral analysis, channels from 1 to 10 (corresponding to energies below 0.11 keV) have been removed because of their very low statistics. The remaining channels have been binned using a constant signal to noise ratio of 3σ. All data have been corrected for vignetting and dead time.

F.1.2 XMM-Newton data reduction

For the analysis of XMM-Newton data, the pipeline products (calibrated and concatenated event lists) delivered by the XMM-Newton Science Survey Centre (SSC) have been taken as starting point. The XMM-Newton Science Analysis System (SAS, Loiseau (2003)) has been used for data reduction, which has been performed following the recommendations from Snowden et al. (2002) for point-like sources. EPIC images have been filtered, removing bad pixels and selecting only events with pattern $\leq$12 for MOS cameras, and $\leq$4 for the

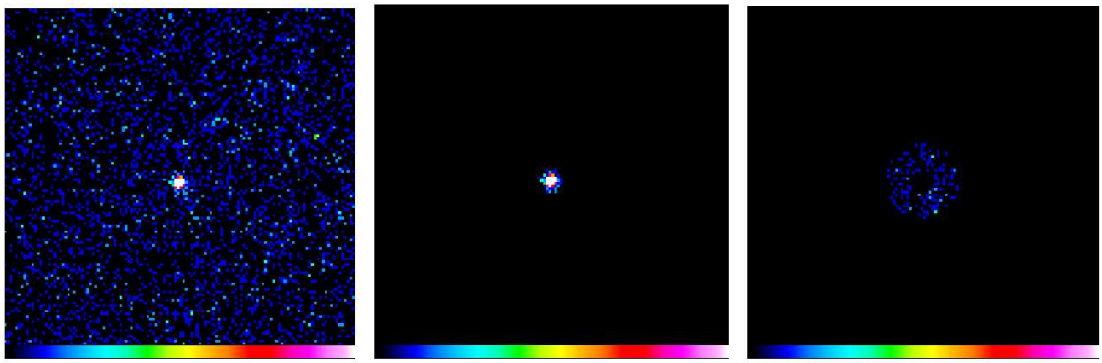

(a) (b) (c)

Figure F.1: (a) Central region of the ROSAT/PSPC image of V1974 Cyg area on day 97 (FOV $\sim$ 0.5 degrees). (b) Extraction region containing the source. (c) Extraction region for background evaluation.

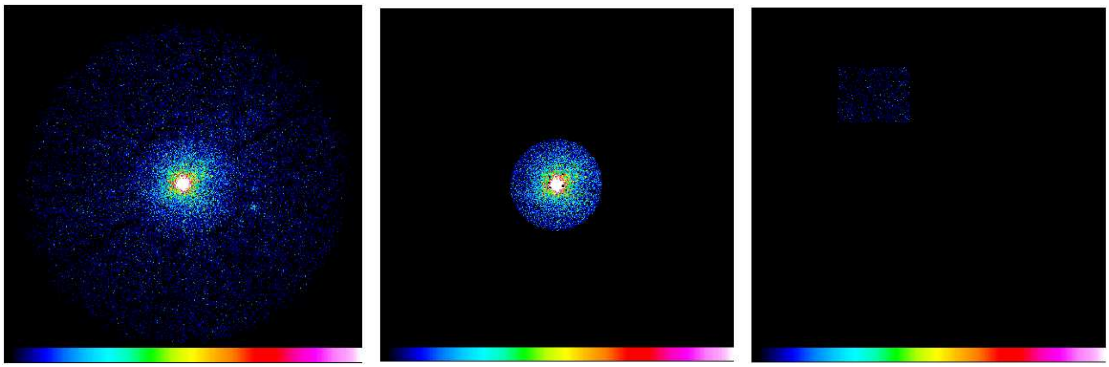

(a) (b) (c)

Figure F.2: (a) ROSAT/PSPC image of V1974 Cyg area on day 434 after outburst (2 degrees FOV). An extended X-ray halo appears around the source. (b) Extraction region containing the source. (c) Extraction region for background evaluation.

pn camera. In general, source photons have been extracted from a circle of $\sim$30". Since no extended halo like the one for V1974 Cyg was present in our XMM-Newton observations, the background has been extracted from an annulus around the source of inner and outer radius 30" and 60". As in the case of ROSAT, background is scaled according to the extraction region.

For spectral analysis, response matrices and anciliary region files have been created with SAS for each observation. The spectra have been binned with the *grppha* ftool to include 25 counts per bin for V2487 Oph and 15 counts per bin for V4633 Sgr.

Regarding the energy range included in our spectral analysis, we have taken into account the fact that the low energy resolution of the MOS cameras have been observed to degrade with time. The most recent "XMM-EPIC Status of Callibration and Data Analysis" document (Kirsch (2003)) reports a gradual change in the response of MOS cameras starting from around revolution 200, and causing the greatest changes from revolution 450. According to Kirsch (2003), the reason for the low energy resolution degradation may be

an increase in the surface charge loss property of the CCDs. The *Science Operation Center* is working to develop epoch-dependent matrices to take into account this degradation, but for the time being, the recommendation for observations between orbits 200 and 450 (when our observations were preformed) is to suspect from calibration below $\sim$0.35 keV. For this reason, channels below 0.35 keV have been ingored for EPIC MOS cameras. For the EPIC pn camera, channels down to 0.2 keV are included.

F.2 Spectral Analysis with XSPEC

The XSPEC package (Arnaud et al.(1996)) has been used for spectral fitting. XSPEC is an X-ray spectral-fitting program designed to be completely detector-independent and can be used for any spectrometer. The observed spectrum is introduced as a table of photon counts (C) within specific instrument channels (I). XSPEC contains spectral models and can also fit user-defined spectra. The chosen model spectrum, f(E), is described in terms of a few parameters that the program can change to find the "best fit" model for a certain observed spectrum. To fit theoretical spectral models to observational data, XSPEC predicts the count rate of the model in each channel, $C_p(I)$, and compares to the observed data, $C(I)$. To find the "best fit" parameters that define the "best fit" model, the program changes the model parameters until it finds the minimum χ^2 defined as

$$\chi^2 = \sum (C(I) - C_p(I))^2/(\sigma(I))^2$$

where $\sigma(I)$ is the error for each channel I (usually estimated as $\sqrt{C(I)}$). The χ^2 statistic provides a well-known goodness-of-fit criterion. For a given number of degrees of freedom ν (calculated as the number of channels minus the number of parameters), a good fit has $\chi^2 \sim \nu$, i.e., $\chi^2_\nu \simeq 1$, with χ^2_ν defined as χ^2/ν.

With XSPEC it is possible to study the behavior of the fitting statistics in a two parameter space. The model is computed for different values of two of the parameters, keeping the others at their best fit value. The fitting statistics χ^2 is computed for each pair of the studied model parameters, as well as the $\Delta\chi^2$ from the minimum fitting statistics of the best fit model. A *confidence contour* plot is then built, plotting the contours that join the model parameter pairs with $\Delta\chi^2$ at 1σ, 2σ and 3σ of the best-fit model, corresponding to an increase of $\Delta\chi^2$ of 2.3, 4.61 and 9.21 .

Spectral models

In our analysis, in addition to user defined table spectral models, some models included in the standard distribution of XSPEC have been used. Multi-component spectra, built by adding or multiplying models, have been generally used. The program uses normalization constants for every additive component as parameters to fit the data. Here a brief description of the models used in this work is given.

Blackbody For a temperature T_{eff}, the intensity of the radiation, I, at energy E, is given by

$$I(E, T_{eff}) = \frac{2E^3}{h^2c^2\left(e^{E/kT_{eff}} - 1\right)}$$

where k is Boltzmann's constant, h is Planck's constant and c is the speed of light. The temperature of the "best fit" blackbody model defines the "effective temperature" (T_{eff}) of

a spectrum. Very often the value of kT_{eff} is given (in eV) instead of the temperature in Kelvin. For the blackbody, the normalization constant in XSPEC can is

$$K_{bb} = \frac{L_{39}}{D_{10}^2}$$

for the *bbody* XSPEC model, where L_{39} is the source luminosity in units of $10^{39} erg\, s^{-1}$and D_{10} is the distance to the source in units of 10 *kpc*, and

$$K_R = \left(\frac{R_{km}}{D_{10}}\right)^2$$

for the *bbodyrad* XSPEC model, where R_{km} is the photospheric radius in units of *km* and D_{10} is the distance to the source in units of *10 kpc*.

Thermal Bremsstrahlung A thermal bremsstrahlung spectrum based on the Kellogg et al. (1975) polynomial fits to the Karzas & Latter (1961) numerical values. He abundance is assumed to be 8.5% of H by number. Fit parameters are the plasma temperature (*kT)* in keV and the normalization constant,

$$K_{br} = \frac{3.02 \times 10^{-15}}{4\pi D^2} EM$$

where D is the distance to the source in cm and EM is the emission measure, $EM = \int n_e n_i dV$; n_e and n_i are the electron and ion densities, in units of cm^{-3}, and V is the volume of emitting plasma.

Raymond-Smith Emission model of hot, diffuse gas by Raymond & Smith (1977), including thermal bremsstrahlung and recombination continua, and line emissions from several elements. Input parameters are the plasma temperature (kT) in keV, element abundances of He, C, N, O, Ne, Mg, Si, S, Ar, Ca, Fe and Ni by number relative to H relative to solar, and the normalization constant

$$K_{RS} = \frac{10^{-14}}{4\pi (D_A(1+z))^2} EM$$

where D_A is the angular distance to the source in *cm, z* is the redshift, and EM is the emission measure.

MEKAL Emission model of hot, diffuse gas based on model calculations of Mewe and Kaastra (Mewe et al.(1985), Mewe et al.(1986), Kaastra (1992), Mewe et al.(1995)), with Fe L calculations by Liedahl et al.(1995), including thermal bremsstrahlung and recombination continua, and line emissions from several elements. Input parameters are the plasma temperature (kT) in keV, element abundances of He, C, N, O, Ne, Na, Mg, Al, Si, S, Ar, Ca, Fe and Ni, and the normalization constant

$$K_{RS} = \frac{10^{-14}}{4\pi (D_A(1+z))^2} EM$$

where D_A is the angular distance to the source in *cm, z* is the redshift, and EM is the emission measure.

Photoelectric absorption To evaluate the absorption affecting the emission, in all cases a multiplicative model for the photoelectric-absorption available in XSPEC has been added,

$$M(E) = e^{-N_h \sigma(E)}$$

where N_h is the equivalent hydrogen column density ($atoms/cm^2$) between the source and the observer, and $\sigma(E)$ is the photo-electric cross-section (Arnaud et al.(1996)).

Appendix G

XSTAR photoionization code

G.1 The XSTAR photoionization code

XSTAR calculates the physical conditions and the outgoing spectrum of a spherical gas shell photoionized by the X-ray emission of a central source. The numerical code determines simultaneously the state of the gas and the radiation field as a function of the distance to the central source. For a detailed description of the code see Kallman & McCray (1982) and the XSTAR User's Guide, Kallman (2002).

Assumptions in XSTAR:

- stationary local balance between heating-cooling and between the various rates connecting atomic levels.
- not large optical depths (all points coupled to the rest of the gas).
- complete redistribution in the scattering in the cores of resonance lines of abundant ions, transfer of line photons in a close region around the emitting point.
- *either* constant density *or* constant pressure.
- spherical symmetry

Elementary considerations:

- if the gas is *optically thin*, the state of the gas only depends on the *photoionization parameter* $\xi = L/nR^2$, as shown in Tarter et al.(1969); with this scaling law, one calculation is valid for a wide variety of applications.
- if the gas is *optically thick*, the state of the gas can be parameterized with an additional parameter (see Hatchett et al.(1976)). In the case of constant density n, this second parameter is $\sqrt{Ln}$.

Algorithm: Simultaneous determination of the state of the gas and the radiation field as a function of the distance from the source. The state of the gas is determined by its temperature and by the *ionic level populations*, which are computed taking into account:

Ionization processes: photoionization (including the effects of the Auger process and secondary ionization by Auger electrons), charge transfer and collisional ionization.

Table G.1: Elements included in the XSTAR models and their solar abundance by number relative to solar as taken in XSTAR.

Element	Solar abundance relative to H
H	1.
He	0.1
C	$0.354 \cdot 10^{-3}$
N	$0.933 \cdot 10^{-4}$
O	$0.74 \cdot 10^{-3}$
Ne	$0.12 \cdot 10^{-3}$
Mg	$0.38\ 10^{-4}$
Si	$0.355 \cdot 10^{-4}$
S	$0.214 \cdot 10^{-4}$
Ar	$0.331 \cdot 10^{-5}$
Ca	$0.229 \cdot 10^{-5}$
Fe	$0.316 \cdot 10^{-4}$
Ni	$0.178 \cdot 10^{-5}$

Recombination processes: radiative recombination, dielectric recombination and charge transfer.

Level populations are determined taking into account the *excitation* and *de-excitation* processes for each ion, including in the calculation collisional and radiative transitions, photoionization, collisional ionization, photoionization excitation and recombination rates for all the levels of every ion.

G.2 Using XSTAR

Input to XSTAR

The input to the program includes:

Luminosity and spectrum of the ionizing radiation. The spectrum can be a black body, a thermal bremsstrahlung, a power law or can be read from a text file.

Chemical composition of the gas in the shell. The abundances must be given by number relative to solar $\left(\frac{(N_i)_{Nova}}{(N_i)_{\odot}}\right)$. The default value (1) means solar abundance. Table G.1 lists the elements included in the code and their solar abundance by number relative to solar as taken in XSTAR.

Temperature of the gas in units of 10^4 K.

Density of the gas in cm^{-3} ; this is actually the hydrogen nucleus density. If the constant pressure switch (**lcpres**) is 0, density is kept constant.

Pressure of the gas in dyn/cm^2. If the constant pressure switch (lcpres) is 1, pressure is kept constant. In other case, this value is used as an initial guess. The program can only run keeping constant density or pressure.

Geometry can be controlled through three parameters:

covering factor: determines which fraction of the sphere is illuminated by the ionizing source.

column density: the program divides the gas in concentric shells. The calculation starts at the innermost shell, and goes on integrating shells until the required column density is reached. So the column density determines the thickness of the shell.

log of the ionization parameter: the user input define the initial value of the ionization parameter. If the density is held constant, this parameter has the form $\xi = L/nR^2$, while if model runs with constant pressure, $\Xi = L/(4\pi R^2 P)$.

XSTAR output

XSTAR output files are in FITS format.

xout_spect1.fits contains the *incident*, the *transmitted* and the *emitted* (outwards and inwards) *spectra*, sorted by energy (eV). The *emitted* spectrum includes continuum emission by bremsstrahlung and recombination as well as line emission (Turner et al.(1996)). The actual spectrum an observer would see coming out from the gas shell will be the addition of the transmitted plus the emitted spectra.

xout_step.log prints input parameters and some parameters for each shell. In addition, a list of the luminosities of the 100 strongest lines is printed at the end.

xout_cont1.fits contains the *incident*, the *transmitted* and the *emitted* (outwards and inwards) *continuum spectra*, sorted by energy (eV). In this file, emission lines are not added to the continuum.

xout_lines1.fits contains the following information about the 1000 strongest emission lines: line index, ion, lower and upper levels involved in the transition, wavelength, luminosity and optical depth.

xout_rrc1.fits contains the list of RRC contributing to the continuum spectrum.

xout_abund1.fits print ion abundances and cooling rates for each shell.

xout_detail.fits is only printed when the hidden parameter *write_switch* is set to 1. Contains all level populations and continuum emissivities for all spatial zones.

xout_detal2.fits is only printed if the hidden parameter *write_switch* is set to 1. Print all line emissivities for all spatial zones.

G.3 XSTAR2XSPEC

XSTAR2SPEC runs XSTAR for a grid of different input parameter and generates a table model suitable for model fitting with XSPEC spectral fitting program.

Input to XSTAR2XSPEC

It is necessary to define the grid of parameters that XSTAR2XSPEC must use to run XSTAR. For each XSTAR parameter, the following values must be given: the maximum and minimum value, the type of variation (0=constant; 1=additive; 2=interpolated), the type of interpolation if the type of variation is 2 (0=linear, 1=logarithmic) and the number

of steps. It must be taken into account that XSPEC can fit table models with a maximum of 5 free parameters, making a grid for more than 5 changing parameters quite useless. The running time of XSTAR2XSPEC depends on the times XSTAR is called, which depends on the number of additive and interpolated parameters and the steps for each of them.

XSTAR2XSPEC output: table models for XSPEC

XSTAR2XSPEC generates two model tables which can be used for fitting with XSPEC:

xout_aout.fits (and xout ain.fits) contains the outwards and inwards emitted spectra in the form of an additive XSPEC model table. This FITS file has 2 extensions or tables: the first one defines the bins of energy of each spectrum, and the second one contains the luminosity (in *erg/s/erg*) of each bin for all spectra generated by the multiple runs of XSTAR.

xout_mtable.fits contains the transmitted spectrum divided by the incident spectrum in the form of a multiplicative table.

These tables can be defined as table models for XSPEC to fit observational spectra. The format of the files generated for XSTAR2XSPEC is understood by XSPEC, so that when the table model is read from the file, XSPEC identifes which are the free parameters and their maximum and minimum values. When fitting, XSPEC will interpolate between the available spectra in the table grid to obtain the best fit.

G.4 Differences between versions

New versions of the XSTAR code appear at least once a year. When we started working with XSTAR, we used version 2.0. There are some small differences in the output spectra of versions 2.0 and 2.1d (see Figure G.1). In the example shown in the figure, the gas temperature (computed by XSTAR) is higher for version 2.1d ($log\,T = 4.52$) than for version 2.0 ($log\,T = 3.88$), which can explain the larger width of the Radiative Recombination Continua observed in the emitted spectrum from version 2.1d (bottom right panel in figure G.1). There are also important differences in the incident blackbody spectrum. But both the 2.0 and the 2.1d versions contain an error that was corrected only in version 2.1h. This error caused the appearance of false emission features for energies above 2 keV (see figures G.2 and G.3), which could account for the hard excess on ROSAT spectra of Nova Cyg 1992, Nova Pup 1991 and Nova Her 1991. But when the error was corrected, XSTAR showed that the photoionization could not contribute to the X-ray spectrum at energies higher than the ionizing soft X-ray source, and that it could not account for the hard X-ray component observed in novae.

According to Tim Kallman (private communication), the narrow emission features above about 600 eV in figures G.2 and G.3 are recombination emission onto iron ions, both the L shell and the K shell. But for these spectra, the iron ions are 6-7 times ionized, which means that the inner L (L1, L2, L3) sub-shells and the K shell are full. So the recombination features that appear above 1 keV in version 2.1d should not occur, because the final state of the electron is already occupied. The recombination emission features in version 2.1h, which are only due to the outermost shell, which is not completely full, are correct. But the ones that stick out at high energies in 2.1d are due to an accounting error. There is absorption at these energies, but negligible emission.

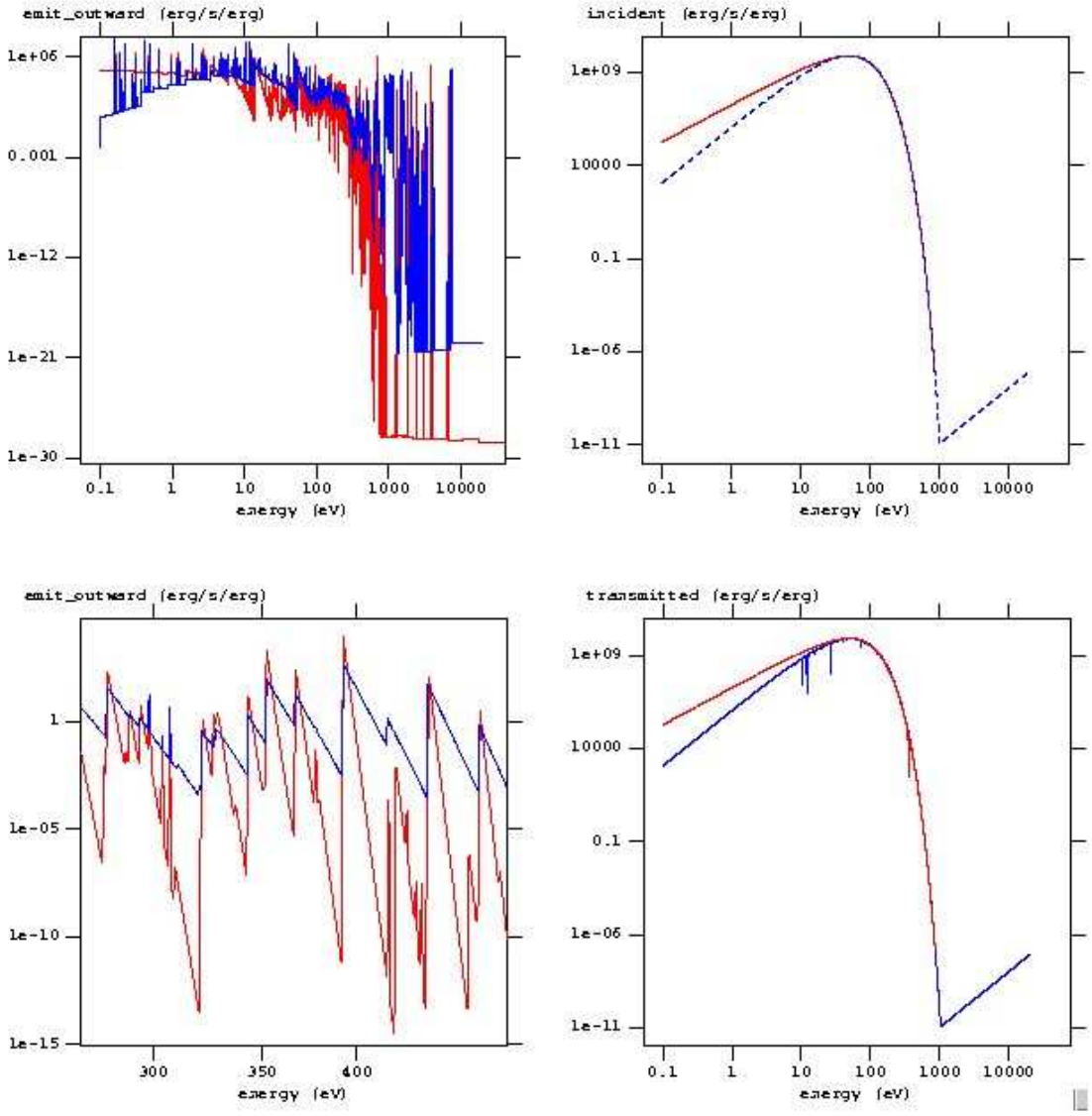

Figure G.1: XSTAR versions 2.0 (red) and 2.1d (blue).
Model parameters: solar abundances, $kT_{bb} = 20eV$, $L_{bb} = 10^{38} erg\, s^{-1}$, $n = 3000\, cm^{-3}$, $N_H = 10^{18} cm^{-2}$ and $log\, \xi = 1.5$. Left panels show the emitted spectrum (bottom panel is a detail); right upper panel plots the incident spectrum, while right lower panel shows the spectrum of the radiation transmitted through the shell.

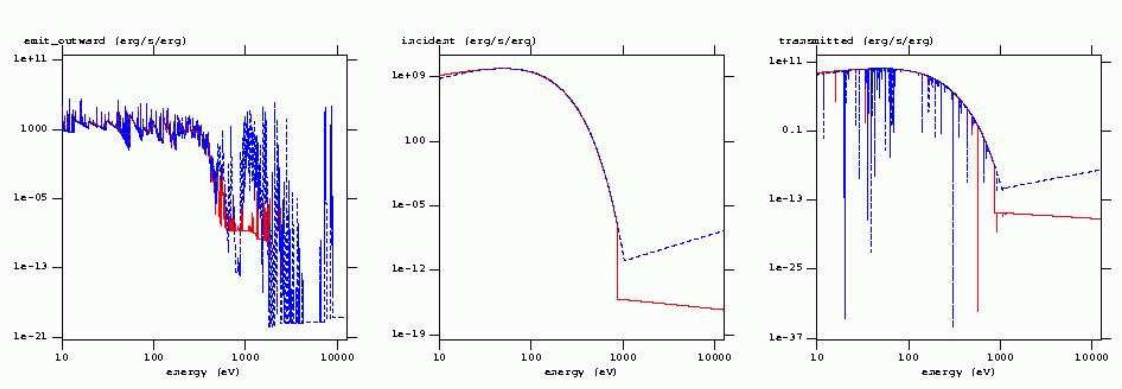

Figure G.2: XSTAR versions 2.1d (blue dashed line) and 2.1h (red solid line). Model parameters: V1974 Cyg abundances, $kT_{bb} = 20eV$, $L_{bb} = 10^{38} erg\, s^{-1}$, $n = 10000\, cm^{-3}$, $N_H = 10^{19} cm^{-2}$ and $log\, \xi = 7$.

.

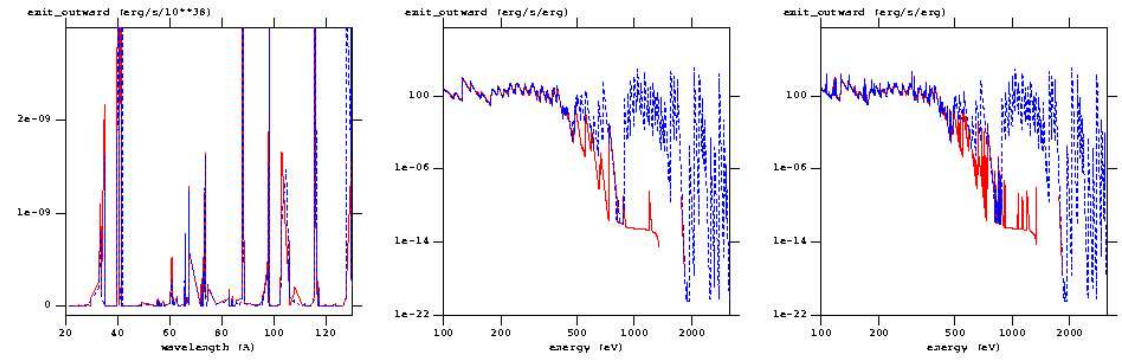

Figure G.3: XSTAR versions 2.1d and 2.1h compared in a model with solar abundances. Model parameters: solar abundances, $kT_{bb} = 34eV$, $L_{bb} = 10^{38} erg\, s^{-1}$, $n = 3000\, cm^{-3}$, $N_H = 10^{18} cm^{-2}$ and $log\, \xi = 1.5$. Contribution from emission lines (left) and Radiative Recombination Continua (central) to the total spectrum (right) is shown for versions 2.1d (blue dashed) and 2.1h (red solid line).

Apèndix H

Resum en català

Emissió en raigs X de noves clàssiques

"Segons alguns savis, uns cossos tan grans haurien de produir necessàriament algun so degut al seu desplaçament, ja que els cossos del nostre entorn en produeixen igualment, per bé que les seves masses no són pas com les dels astres, i que la velocitat del seu moviment no és tan gran. I del Sol, la Lluna, i les estrelles, tan nombroses i tan grans, i que es mouen amb tanta rapidesa, ha de néixer necessàriament un so d'una intensitat extraordinària. Tenint en compte tot això, i el fet que per la raó de les distàncies, les velocitats mantenen els mateixos intervals que les notes d'un acord musical, diuen que el cant produit pels moviments circulars dels astres és harmoniós. I com que lògicament sembla inexplicable que nosaltres no sentim aquest cant, diuen que el motiu és que és un so present a la mateixa natura de totes les coses, i que per tant no tenim ocasió de distingir-lo per contrast amb el silenci. Diuen que igual que els ferrers, que semblen indiferents al soroll que fan pel fet d'estar-hi acostumats, els homes hem esdevingut també insensibles, per la mateixa raó."

Aristòtil, *De caelo,* II.9; 290 b 15 (referint-se als pitagòrics)

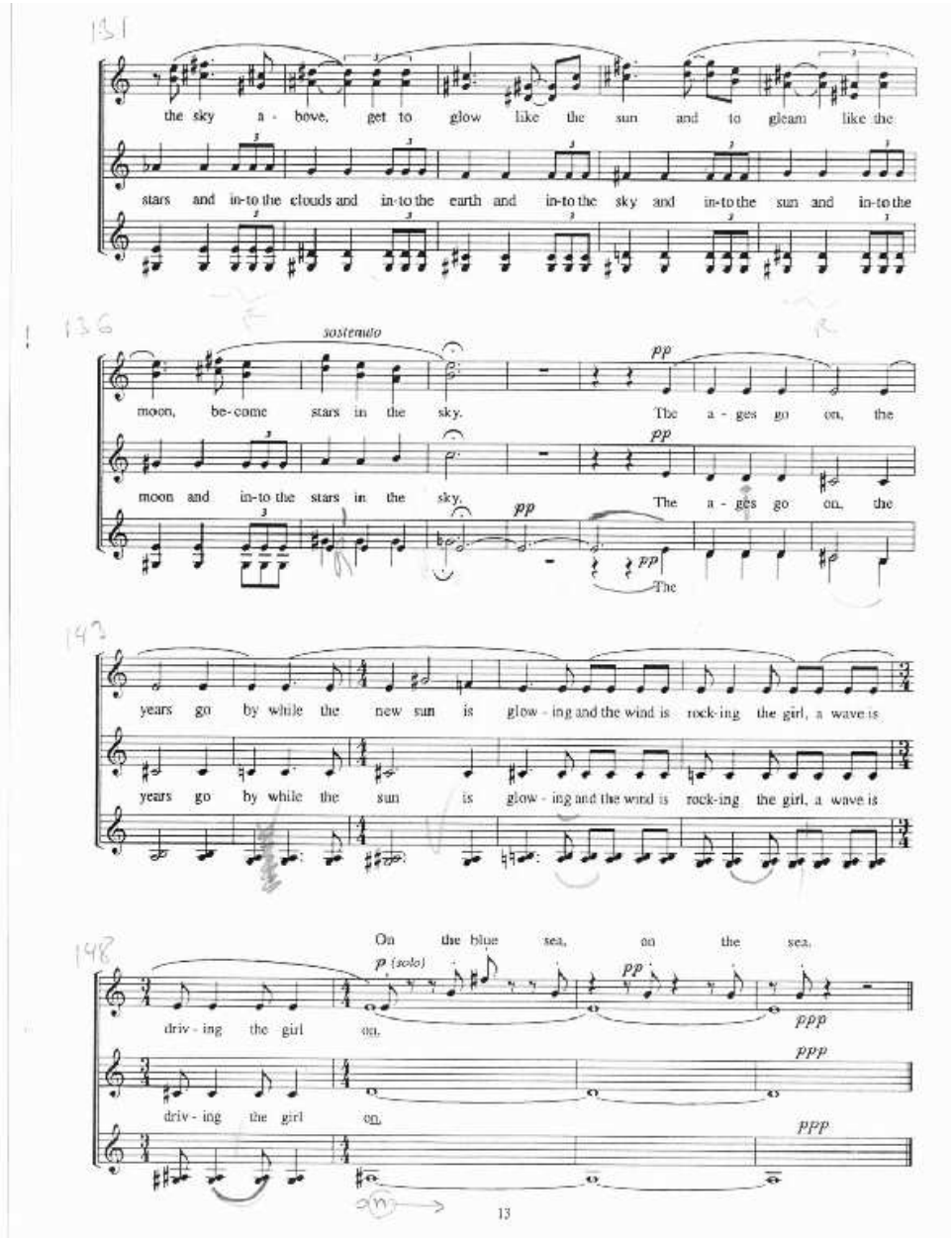

"The bits turn (...) into the clouds and into the earth and

into the sky and into the sun and

into the moon and into the stars in the sky"

The First Runo

Einojuhani Rautavara

H.1 Introducció

En l'aparent imperturbabil·litat del cel estrellat, les variables cataclísmiques, incloses les noves clàssiques, es troben entre els pocs objectes astronòmics privilegiats que viuen en una escala de temps "humana". Si sou prou afortunats com per ser a l'hemisferi correcte quan una nova brillant exploti (en promig, n'hi ha una més brillant que $m_v = 3$ per dècada), veureu que durant unes nits hi ha una nova estrella allí on abans no hi havia res. La magnitud d'aquesta *nova stella* anirà minvant amb el pas dels dies, durant un període que pot durar entre uns pocs dies i uns quants mesos. Es calcula que cada any exploten unes 35 noves a la nostra gal·làxia, però sols se'n decobreixen unes cinc, degut a l'alta absorció del medi interestel·lar. Malgrat el seu nom, les noves clàssiques no són pas noves estrelles, sino remanents d'estels morts que tornen a viure durant un temps.

Les explosions de noves clàssiques són produides per la combustió explosiva d'hidrogen a la superfície d'una nana blanca en una variable cataclísmica, un sistema binari proper en el qual l'estrella de la seqüència principal transfereix material ric en hidrogen a la nana blanca. Quan ja s'han acumular uns $10^{-5} - 10^{-4} M_\odot$ de material ric en hidrogen, té lloc la ignició de l'hidrogen en condicions degenerades i s'inicia un allau termonuclear en l'embolcall acretat (veure José & Hernanz (1998), Starrfield et al.(1998), Prialnik & Kovetz (1995), i Starrfield (2002) per una revisió recent). Els models indiquen que el fenòmen explosiu sols és possible si el material acretat, de composició solar, és enriquit amb material del nucli degenerat de la nana blanca, mitjançant algun mecanisme de barreja. Com a conseqüència de l'allau termonuclear, l'embolcall s'expaneix i la lluminositat de l'estrella arriva a $\sim 10^5 L_\odot$, augmentant fins a 10 magnituds. Una fracció de l'embolcall és expulsada a grans velocitats, mentre que la resta roman a la superficie de la nana blanca, cremant hidrogen en equil·libri hidrostàtic amb una lluminositat bolomètrica constant propera al límit d'Eddington de l'estel. La clofolla formada pel material ejectat processa la radiació generada a la superfície de la nana blanca, i en modifica l'espectre a mida que s'expandeix, tot mantenint una lluminositat bolomètrica constant: a mida que l'embolcall s'expandeix, la fotosfera retrocedeix i l'emissió que s'observa prové de capes més internes i calentes, movent amb el temps el màxim de l'emissió de l'òptic, l'ultraviolat, ultraviolat extrem i finalment als raigs X. L'emissió de raigs X tous és doncs un indicador directe de la combustió termonuclear d'hidrogen a la superficie de la nana blanca. És d'esperar que totes les noves experimentin aquesta fase, emetent raigs X amb un espectre corresponent a l'atmosfera d'una nana blanca calenta (MacDonald & Vennes (1991)), amb temperatures efectives de $10^5 - 10^6 K$ i lluminositat properes al límit d'Eddington. Tenint en compte la massa de l'embolcall necessària per produir l'explosió de nova i suposant que la massa de l'embolcall remanent és del mateix ordre de magnitud, aquesta fase hauria de durar centenars d'anys.

A més de l'emissió fotosfèrica de raigs X tous, les noves clàssiques tenen altres mecanismes d'emissió de raigs X. Durant l'explosió i poc després d'aquesta, el material ejectat, escalfat per xocs interns entre components ejectades a diferents velocitats, o per xocs externs amb el medi circumestel·lar, assoleix temperatures prou altes com per emetre raigs X durs, amb un espectre de plasma calent. Finalment, quan es restableix l'accreció sobre la nana blanca, el sistema emet com una variable cataclísmica, degut al frenat i escalfament del material del disc i accretat sobre la superfície de la nana blanca.

La primera nova detectada en raigs X tous fou la Nova Muscae 1983 (GQ Mus), observada pel satèl·lit EXOSAT el 1983, 460 dies després del màxim visual. Però els avenços més important en l'astronomia X en general els va proporcionar ROSAT. En el cas de les noves clàssiques, ROSAT va mostrar que no totes les noves emetien raigs X tous després de l'explosió, ans el contrari: de 39 noves clàssiques observades menys de 10 anys després

de l'explosió, sols en va trobar tres amb emissió associada a la combustió d'hidrogen a la superfície de la nana blanca: GQ Mus, ja descoberta per EXOSAT, la Nova Cygni 1992 (V1974 Cyg) i la Nova LMC 1995 (Orio et al.(2001a)). A més, excepte en aquest últim cas, encara brillant en una observació del 2000 realitzada pel satèl·lit XMM-Newton, les altres dues es van apagar en una escala de temps molt inferior als centenars d'anys predits (9 anys en el cas de GQ Mus i sols 18 mesos en el cas de V1974 Cyg). Aquests resultats van posar en evidència que la massa de l'embolcall remanent a la superfície de la nana blanca havia de ser molt inferior a la que es necessita per que la nova exploti, indicant la presència d'algun mecanisme extra de pèrdua de massa (embolcall comú o vents òpticament gruixuts). De totes maneres, no es disposava de cap model que simulés les condicions de l'embolcall després de l'explosió i la seva evolució. A més, és clar que per confirmar els resultats de ROSAT caldrien observacions de més noves recents amb instruments més sensibles.

El principal objectiu d'aquesta tesi és suplir aquestes dues mancances. En la vessant teòrica, s'ha desenvolupat un model per embolcalls calents de nana blanca, amb combustió estacionària d'hidrogen, i s'ha simulat l'evolució com una successió d'estats estacionaris. Els resultats del model s'han comparat amb observacions d'arxiu de ROSAT de les tres noves amb emissió de raigs X tous (V1974 Cyg, GQ Mus, N LMC 1995). Finalment, s'ha ampliat la mostra de noves post-explosives amb noves observacions de noves recents amb el satèl·lit XMM-Newton.

H.2 Embolcalls de nana blanca amb combustió estacionària d'hidrogen

En aquesta secció es presenta un model numèric per embolcalls de nanes blanques amb combustió estacionària d'hidrogen. El model simula les condicions del material ric en hidrogen que roman a la superfície de la nana blanca després de l'explosió de nova. L'evolució temporal s'estudia com una seqüència d'estats estacionaris.

Després d'una presentació del model a la secció H.2.1, els principals resultats del model per diferents masses de la nana blanca i composicions de l'embolcall es presenten a la secció H.2.2. L'evolució com a succesió d'estats estacionaris es presenta a la secció H.2.3.

A més a més del que s'inclou en aquest resum, en el text en anglès s'hi pot trobar un estudi dels resultats de la integració de les equacions d'estructura de l'embolcall en funció de les condicions de contorn a la base (secció 2.3), una avaluació de l'error comès en l'aproximació de l'evolució com a seqüencia d'estats estacionaris (secció 2.5) i un comentari sobre la solució analítica per embolcalls estel·lars amb lluminositat i massa constant (apèndix A).

H.2.1 El model d'embolcall

En aquesta tesi, s'han calcul·lat models d'embolcall per sis masses diferents de la nana blanca (de 0.8 a 1.3 $M_{\odot}$) i sis composicions químiques diferents, que coincideixen amb les composicions del material accretat dels models de José & Hernanz (1998). Quatre d'ells corresponen a embolcalls de nanes blanques d'ONe amb un 9.3%, un 25%, un 50% i un 75% de grau de barreja entre el material del nucli degenerat i el material accretat amb abundàncies solars (models que anomenem ONe09, ONe25, ONe50 i ONe75). També s'ha inclòs un cas d'embolcall de nana blanca de CO amb un grau de barreja d'un 50% (models CO50). Les composicions químiques dels nuclis degenerats s'han tret de Ritossa et al.(1996) per les nanes blanques d'ONe, i és un 50% d'oxigen i un 50% de carboni per les

Table H.1: Composicó dels embolcalls de nana blanca, en fraccions en massa. $X = X_H$, $Y = X_{He}$. Z conté els metalls (tots els elements excepte H i He) en fraccions solars. δX_i indica l'excés de fracció en massa per sobre del valor solar inclòs a Z per l'element i. L'abundància total de metalls és Z_{total}.

Nucli	Barreja	Nom	X	Y	Z			Z_{total}
						δX_O	δX_{Ne}	
ONe	75%	ONe75	0.18	0.08	0.12	0.38	0.24	0.74
ONe	50%	ONe50	0.35	0.15	0.09	0.25	0.16	0.5
ONe	25%	ONe25	0.53	0.2	0.06	0.13	0.08	0.27
ONe	9.3%	ONe09	0.6378	0.25	0.03	0.05	0.03	0.11
						δX_C	δX_O	
CO	50%	CO50	0.35	0.14	0.02	0.245	0.245	0.51
					δX_C	δX_N	δX_O	
-	-	I82	0.6378	0.35	0.0016	0.0033	0.0073	0.01

nanes blanques de CO. La composició detallada es pot trobar a la taula H.1. Finalment, s'ha calculat una sèrie extra de models amb abundàncies similars a les usades per Iben (1982) (models I82). La fracció en massa d'hidrogen en aquest cas és la mateixa que pels models de ONe amb un 9.3% de barreja (ONe09), els quals tenen un grau de barreja triat expressament per tal que tinguin la mateixa fracció d'hidrogen en massa que els models I82.

El model d'embolcall de nana blanca es construeix integrant les equacions d'equilibri estel·lar:

$$\frac{dM}{dr} = 4\pi r^2 \rho \tag{H.2.1}$$

$$\frac{dP}{dr} = -\frac{GM}{r^2}\rho \tag{H.2.2}$$

$$\frac{dL}{dr} = 4\pi r^2 \rho \left(\varepsilon + T\frac{ds}{dt}\right) \tag{H.2.3}$$

$$\frac{dT}{dr} = -\frac{3\overline{\kappa}\rho}{64\pi\sigma}\frac{L}{r^2 T^3}, \tag{H.2.4}$$

on r és el radi des del centre de l'estrella, M és la massa total inclosa a l'esfera de radi r , P, ρ i T són pressió, densitat i temperatura, L és la lluminositat i s és l'entropia per unitat de massa; G és la constant de la gravitació, $G = 6.673 \times 10^{-8} dyn\, cm^2\, g^{-2}$; $\sigma = \frac{ac}{4}$, amb $a = 7.65 \times 10^{-15} erg\, cm^{-3}\, K^{-4}$, la constant de radiació-densitat, i $c = 2.9979 \times 10^{10} cm\, s^{-1}$, la velocitat de la llum; $\varepsilon_r = \varepsilon_n - \varepsilon_\nu$, amb $\varepsilon_n = \varepsilon_n(\rho_r, T_r)$ el ritme de generació d'energia nuclear i ε_ν les pèrdues degudes als neutrins; i κ és l'opacitat mitjana de Rosseland. L'equació H.2.4 sols és vàlida si el transport d'energia és radiatiu. En aquest treball, els embolcalls estudiats són estacionaris i les pèrdues per neutrins són negligibles, de manera que en comptes de (H.2.3) tenim

$$\frac{\partial L_r}{\partial r} = 4\pi r^2 \rho_r \varepsilon_n \tag{H.2.5}$$

En la integració numèrica, a cada pas d'integració es comprova l'estabilitat dinàmica de l'embocall segons el criteri de Schwarzschild. Quan la capa és inestable enfront la convecció, l'equació H.2.4 ja no és vàlida i el gradient de temperatura es calcula mitjançant la teòria estàndard de longitud de barreja (standard mixing-length theory, Böhm-Vitense

(1958); veure apèndix C per més detalls). Pel gradient radiatiu, es fan servir les opacitats radiatives del codi OPAL (Iglesias & Rogers (1996)). Les approximacions usades pels ritmes de producció d'energia són les de Reeves (1965) i Paczyński (1983). L'equació d'estat és la del gas ideal amb pressió de radiació. Com es mostra a la secció 2.4.3 del text en anglès i a l'apèndix B, per les condicions del gas als embolcalls d'aquest treball, els efectes d'ionització parcial són negligibles, el gas mai no es troba en condicions degenerades i la generació d'energia per combustió de l'heli es negligible. A l'apèndix B es donen més detalls sobre la física del model.

Les quatre equacions d'equilibri (H.2.1-H.2.4) s'integren de la fotosfera cap a la base de l'embocall utilitzant un mètode Runge-Kutta amb control adaptatiu del pas d'integració amb parametres de Cash-Karp (Cash & Karp (1990), Press et al.(1992)). El problema de les condicions de contorn als dos extrems de l'interval d'integració es resol amb un mètode de "shooting" (Press et al.(1992), a l'apèndix D es dónen més detalls)

La integració comença a la fotosfera, amb un valor fixat per la lluminositat L_{tot} i valors de prova per la massa de l'embolcall, M_{env}, i el radi fotosfèric, R_{fotos}. Les altres condicions de contorn a la fotosfera (temperatura i pressió) s'obtenen integrant cada vegada un model d'atmosfera gris pels valors de L_{tot}, M_{env} i R_{fotos} triats. Les equacions d'equil·libri s'integren des de la fotosfera, amb radis decreixents, fins que la lluminositat és prou petita com per considerar que estem per sota de la capa de producció d'energia. En aquest punt, es comprova si el resultat de la integració verifica les condicions de contorn requerides a la base de l'embolcall: la massa de l'embolcall ha de ser quasi zero (imposem que sigui més petita que $10^{-13} M_{\odot}$) i el radi R_{base} ha de ser el radi del nucli degenerat R_c (exactament, es requereix que el factor $\left|\frac{R_{base}-R_c}{R_c}\right|$ sigui més petit que 10^{-5}, i R_c s'obté de la relació radi-massa per nanes blanques de Hamada & Salpeter (1961)). Si aquestes condicions no es verifiquen, la integració torna a començar des de la fotosfera, per nous valors de R_{fotos} i M_{env}.

H.2.2 Resultats

Els principals resultats del model es mostren a les figures H.1, H.2 i H.3, on es representen la lluminositat, el radi fotosfèric i la massa de l'embolcall en funció de la temperatura efectiva per tots els models. S'observa que per cada composició i massa de la nana blanca, existeix una lluminositat màxima i una temperatura efectiva màxima. El màxim de temperatura efectiva divideix els models en dues branques: una branca de lluminositat alta i quasi constant, i una segona branca de lluminositat més baixa i radi fotosfèric constant. Els models d'alta lluminositat tenen sempre una zona convectiva sota la fotosfera, mentre que el transport és purament radiatiu en els models de la branca de baixa lluminositat. Quant a la massa de l'embolcall, hi ha una massa mínima perque l'embolcall sigui encara estable, que es dóna a prop del màxim de temperatura efectiva. La massa de l'embolcall és pràcticament constant al llarg de la branca d'alta lluminositat, però creix ràpidament per temperatures decreixents a la branca de baixa lluminositat.

Una anàlisi d'estabilitat de la combustió en capa mostra que, mentre les solucions de la branca d'alta lluminositat són estables, la branca de baixa lluminositat no representa solucions estables per un embolcall amb combustió estacionària. Aquesta anàlisi es pot trobar al capítol 2.4.2 del text en anglès, però l'estabilitat de les branques es pot veure també de manera qualitativa. L'evolució de l'embolcall es pot aproximar com una successió d'estats estacionaris, amb masses decreixents degut a la combustió termonuclear de l'hidrogen. Si considerem la possible evolució al llarg de la branca de baixa lluminositat, les figures H.1, H.2 i H.3 ens mostren que a mida que la massa decreix, augmenten la

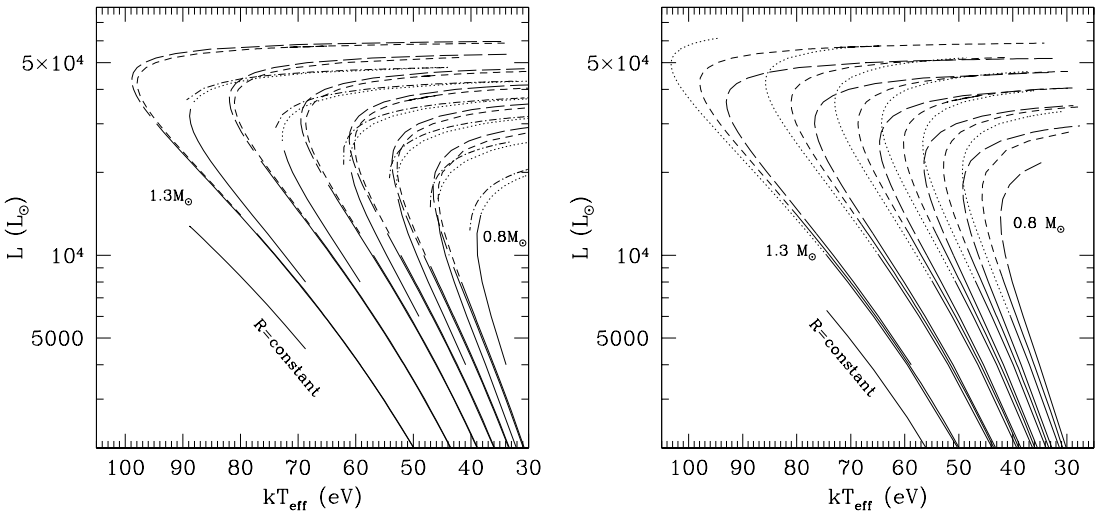

Figure H.1: Lluminositat total versus temperatura efectiva per tots els models.
(a) CO50 (ratlles llargues), ONe50 (ratlles curtes), ONe09 (punt-ratlla) i I82 (linia puntejada); les línies contínues indiquen les els embolcalls sense zones convectives (pels models ONe09, la branca radiativa no està representada). (b) ONe25 (ratlles llargues pels models convectius, ratlla llarga-punt per models radiatius), ONe50 (ratlla curta per convectius, ratlla curta-punt pels radiatius) i ONe75 (linia puntejada pels convectius, contínua pels radiatius). Per cada composició, es representen sis series de models, corresponents a les masses 0.8, 0.9, 1.0, 1.1, 1.2 i 1.3 $M_\odot$.

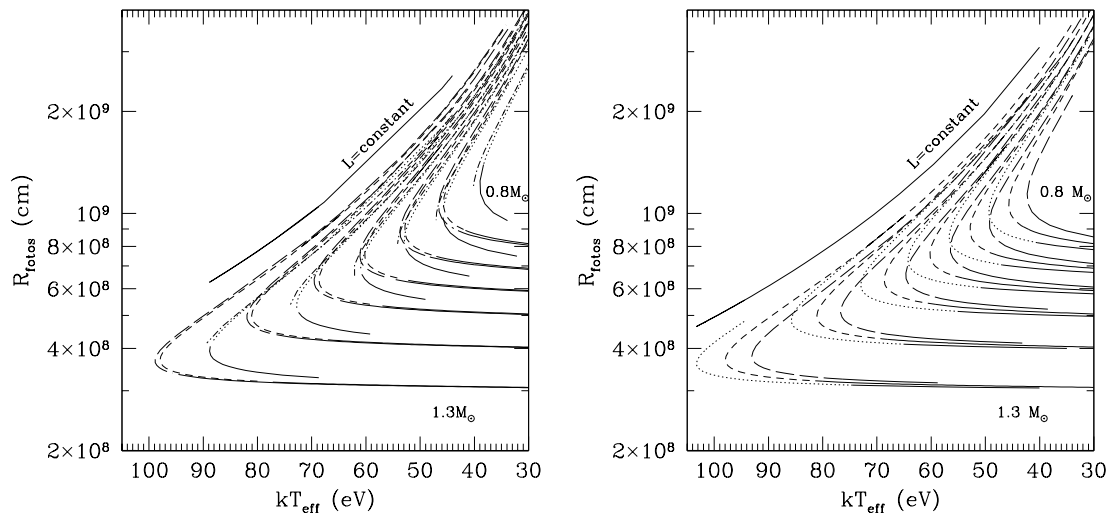

Figure H.2: Radi fotosfèric versus temperatura efectiva pels mateixos models que a la figura H.1

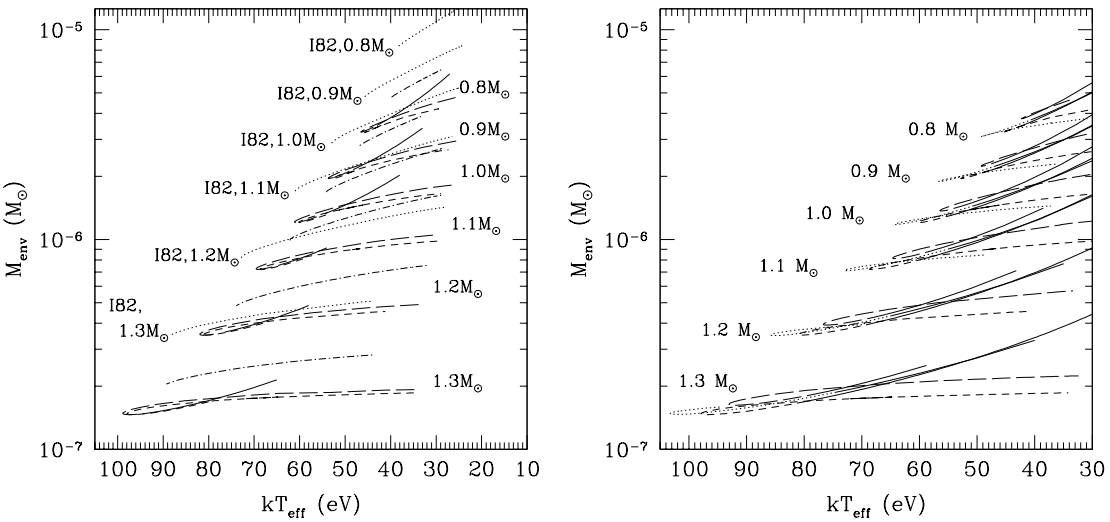

(a) (b)

Figure H.3: Massa de l'embolcall versus temperatura efectiva pels mateixos models que a la figura H.1

temperatura efectiva i la lluminositat, mantenint-se constant el radi fotosfèric. Això està relacionat amb un augment de la temperatura a la base de l'embolcall, tal com es mostra a la figura H.4. Sense cap font extra d'energia, l'evolució en aquest sentit no és possible. En canvi, si considerem l'evolució al llarg de la branca d'alta lluminositat, a mida que la massa de l'embolcall es redueix, el radi fotosferic decreix i la fotosfera es desplaça cap a capes més internes i calentes de l'embolcall, incrementant la temperatura efectiva. Malgrat tot, la temperatura a la base de l'embolcall va decreixent amb el temps (figura H.4), així com la lluminositat (figura H.1). La temperatura efectiva augmenta sols com a conseqüència del desplaçament de la fotosfera cap a capes més profundes. L'evolució procedirà cap a masses decreixents fins arribar a la massa mínima (i temperatura efectiva màxima); després, l'embolcall no tindrà prou massa per mantenir la combustió d'hidrogen en condicions estacionàries. Les reaccions nuclears s'aturaran i la nana blanca començarà a refredar-se, mantenint un embolcall de massa i radi constant.

Tal com es veu a la figura H.1, la lluminositat a la branca estable es pràcticament constant, i els seu valor depèn de la massa de l'estrella, M_c, i de la composició de l'embolcall. La dependència amb la massa es pot aproximar per

$$L(L_\odot) \simeq 5.95 \times 10^4 \left(\frac{M_c}{M_\odot} - m_0 \right) \tag{H.2.6}$$

on, pels models CO50 $m_0^{CO50} = 0.3$, pels models ONe75 $m_0^{ONe75} = 0.24$, pels models ONe50 $m_0^{ONe50} = 0.32$, pels models ONe25 $m_0^{ONe25} = 0.42$, i pels models ONe09 i I82, $m_0^{ONe09} = m_0^{I82} = 0.48$. Aquesta dependència lineal de la lluminositat amb la massa es pot justificar analíticament, tal com va fer Kippenhahn (1981) (veure també Kippenhahn & Weigert (1990)) i es pot trobar al text en anglès. A partir de les relacions homòlogues per la combustió en capa obtingudes per Refsdal & Weigert (1970), es pot veure que, quan la pressió de radiació contribueix en gran part a l'equació d'estat (cosa que succeeix en els embolcalls de la capa estable), $L \sim M_c$ i no depèn del radi de l'estrella.

Aquesta relació lineal va ser trobada per primer cop per Paczyński (1970), qui trobà amb

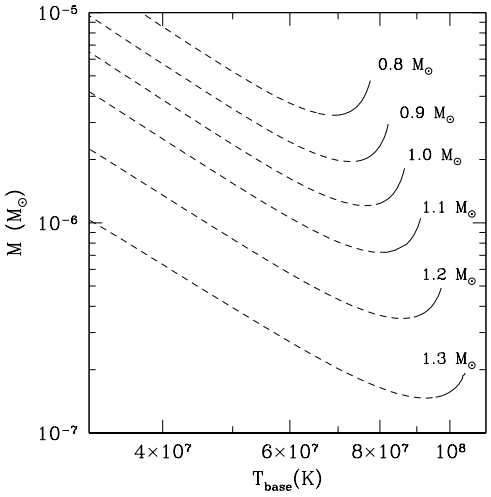

Figure H.4: Massa de l'embolcall versus temperatura a la base pels models CO50. Les línies contínues indiquen embolcalls amb regions convectives.

els seus models evolutius que la lluminositat dels estels després de la branca assimptòtica de les gegants (post-AGB), amb una doble capa de combustió (H, He) sobre un nucli de CO quasi completament degenerat, dependia de la massa com

$$L(L_\odot) = a\left(\frac{M_c}{M_\odot} - b\right)$$

amb $a = 59{,}250$ i $b = 0.522$. Treballs posteriors van trobar relacions semblants, amb petites diferències en els paràmetres. Concretament, Iben (1982), que estudià nanes blanques calentes amb accreció i combustió estacionària d'hidrogen a la superfície, trobà $a = 59{,}500$ and $b = 0.5$, valors molt propers als nostres pels models amb la mateixa composició que els seus.

Pels models d'ONe, podem trobar una expressió més general, tenint en compte la dependència de la lluminositat amb la fracció d'hidrogen en massa,

$$L(L_\odot) \simeq 5.95 \times 10^4 \left(\frac{M_c}{M_\odot} - 0.536X_H - 0.14\right) \tag{H.2.7}$$

A la figura H.3 és clar que la massa de l'embolcall a la branca estable decreix sols lentament per temperatures efectives creixents.Iben (1982) va trobar que la massa dels embolcalls en aquest 'plateau' depenia sols de la massa de l'estrella com $log\, M^{Iben82}_{plateau} \simeq -4.38 - 4.96\left(\frac{M_c}{M_\odot} - 1\right)$. Els nostres resultats no es poden aproximar per cap relació lineal com aquesta. Sols es pot trobar una relació general entre la massa de l'embolcall, la massa total i la composició pels models ONe25, ONe50 i ONe75, pels quals

$$\log M^{ONe}_{plateau} \simeq 0.42X_H - \left(\frac{M_c}{M_\odot} - 0.13\right)^3 - 5.26 \tag{H.2.8}$$

De manera semblant, per aquest models trobem que per la massa mínima de l'embocall

$$\log M^{ONe}_{min} \simeq 0.13X_H - \left(\frac{M_c}{M_\odot} - 0.13\right)^3 - 5.26 \tag{H.2.9}$$

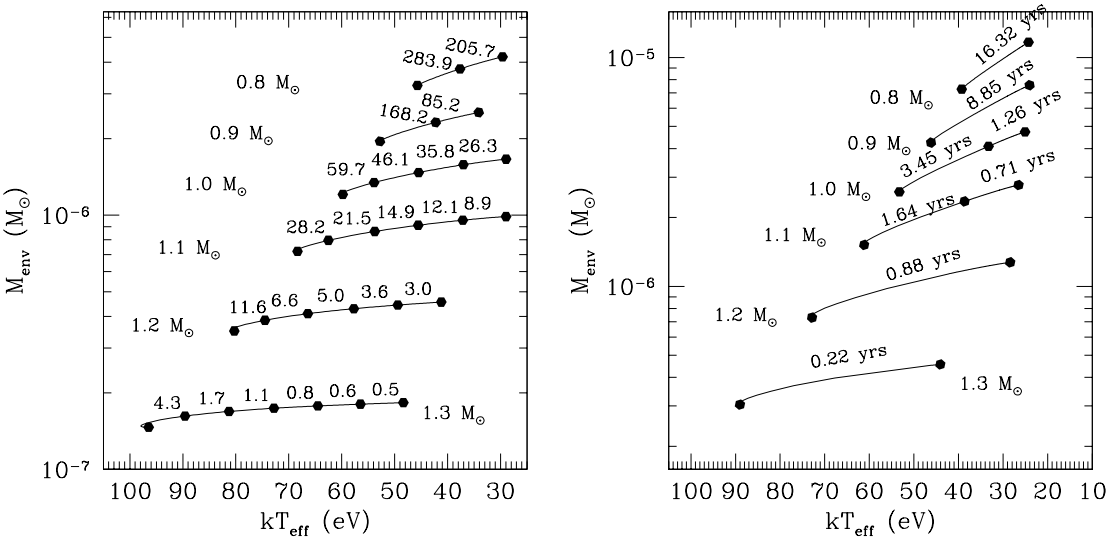

(a) (b)

Figure H.5: Massa de l'embolcall en funció de la temperatura efectiva pels models ONe50 (a) i I82 (b). El temps emprat per l'embolcall per evolucionar d'un punt a un altre s'indica en dies pels models ONe50 i en anys pels models I82.

H.2.3 Evolució quasi-estacionària

L'evolució d'un embolcall de nana blanca amb combustió d'hidrogen es pot aproximar com una successió d'estats estacionaris. Les capes més internes de l'embolcall per les quals l'hidrogen ja s'ha consumit, s'assimilen al nucli (l'increment en massa del nucli és negligible), de manera que la massa de l'embolcall es va reduint. El temps Δt necessari perque la massa de l'embolcall es redueixi en ΔM_{env} degut únicament a la combustió d'hidrogen es pot estimar com

$$\Delta t = \epsilon \frac{\Delta M_{env} X_H}{L} \tag{H.2.10}$$

on X_H és la fracció en massa d'hidrogen, L és la lluminositat mitjana durant el periode considerat (la qual es manté quasi constant) i ϵ és l'energia alliberada per gram d'hidrogen processat ($\epsilon = 5.98 \times 10^{18} erg\, g^{-1}$). Les figures H.5-H.6 mostren la massa de l'embolcall en funció de la temperatura efectiva per alguns models (ONe50, I82, One25 i One75). El temps necesari perque l'embolcall experimenti un cert canvi de massa s'indica en dies (pels models ONe i CO) o en anys (pels models I82). L'evolució és més lenta per les nanes blanques de massa més petita, ja que la lluminositat és menor en aquests casos. Els intervals de temps són també més llargs pels embolcalls més rics en hidrogen.

Els temps característics dels nostres models es poden comparar amb els temps característics nuclears que es troben a la literatura pels remanents de noves clàssiques. A Starrfield (1989), aquest temps s'estima com

$$\tau_{nuc} = 400 \left(\frac{M_H}{10^{-4} M_\odot} \right) \left(\frac{L}{2 \times 10^4 L_\odot} \right)^{-1} yr \tag{H.2.11}$$

on M_H és la massa d'hidrogen i L és la lluminositat. Per les masses d'embolcalls necessàries per produir l'allau tèrmic que provoca l'explosió de nova, uns $10^{-4} M_\odot$, el temps caracterís-

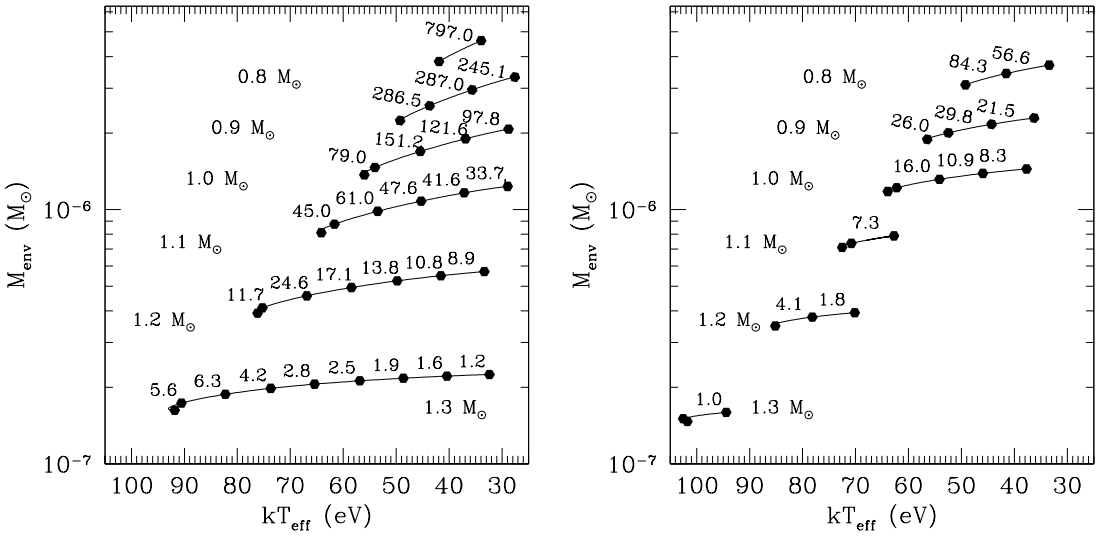

Figure H.6: El mateix que la figura H.5 pels models ONe25 i One75. Els intervals de temps s'indiquen en dies.

tic és de centenars d'anys. La fracció de material accretat que s'ejecta segons els models hidrodinàmics d'explosions de noves no és prou gran com per reduir la massa de l'embolcall remanent a $\sim 10^{-6} M_{\odot}$. Però en aquesta tesi hem trobat que els embolcalls de nanes blanques amb combustió estacionària sols estan enequilibri per masses d'aquest ordre. Si reescrivim l'expressió (H.2.11) pels valors típics dels nostres models ($M_{env} = 10^{-6} M_{\odot}$, $L = 4 \times 10^4 L_{\odot}$) tenim

$$\tau_{nuc} = 2 X_H \left(\frac{M_{env}}{10^{-6} M_{\odot}} \right) \left(\frac{L}{4 \times 10^4 L_{\odot}} \right)^{-1} yr \qquad \text{(H.2.12)}$$

Per X=0.35 (com en els models ONe50 i CO50), $\tau_{nuc} \simeq 255$ dies; pels models I82, amb X=0.64, $\tau_{nuc} \simeq 9$ anys.

H.3 Observacions del satèl·lit ROSAT de noves clàssiques

El satèl·lit ROSAT (*Röntgensatellit*, Briel et al.(1997)), posat en òrbita el 1990, obrí una nova era per l'astronomia X. Obtingué resultats millors que les missions anteriors gràcies a una àrea efectiva més gran, unes millors ressolucions angular i espectral, i un doble programa d'observacions, incloent un mapejat complet del cel en raigs X, i observacions més detallades de fonts sel·lecionades. Els resultats més remarcables sobre noves clàssiques i altres objectes estel·lars foren obtinguts amb els PSPCs (*Position Sensitive Proportional Counters,* contadors proporcionals sensibles a la posició), que permetien obtenir imatges i espectres entre 0.1 i 2.4 keV amb una resolució espectral moderada, però molt millor que la de les missions anteriors ($\frac{\Delta E}{E}$ ~50%).

Les observacions de noves clàssiques realitzades per ROSAT mostraren que la duració de l'emissio de raigs X tous deguda a la combustió d'hidrogen en l'embolcall de la nana blanca després de l'explosió era molt menys comú i curta del que s'esperava. Sols tres de les 39 noves clàssiques observades menys de 10 anys després de l'explosió van mostrar aquesta emissió, i amb una duració màxima de 9 anys. En aquest capítol, es comparen els models d'embolcall de nana blanca desenvolupats en el capítol anterior amb les observacions de ROSAT de les tres noves amb emissió de raigs X tous: V1974 Cyg (Nova Cygni 1992), GQ Mus (Nova Muscae 1983) i la Nova LMC 1995.

H.3.1 Nova Cygni 1992 (V1974 Cyg)

La Nova Cygni 1992 (V1974Cyg) es va descobrir el 19 de Febrer de 1992 UT (Collins (1992)). Va ser la nova més brillant des de la Nova Cyg 1975 (V1500 Cyg), assolint una magnitud màxima de V = 4.4 el 21 de Febrer de 1992, i fou classificada com una nova de ONe (Austin et al.(1996),Shore et al.(1993),Shore et al.(1994)). V1974 Cyg fou la primera nova clàssica observada en totes les longituts d'ona, de ràdio als raigs gamma. El ROSAT l'observà en raigs X de l'Abril del 1992 al Desembre de 1993 (Krautter et al.(1996)).

La corva de llum en raigs X mostrà tres fases ben diferenciades: una pujada inicial del flux del dia 63 al dia 255 després de l'explosió, deguda a la disminució de l'absorció de la clofolla de material ejectat deguda a la seva pròpia expansió; una fase de lluminositat constant, del dia 255 al 511; i una fase final de caiguda del flux a partir del dia 511 després del descobriment. L'emissió durant la fase de lluminositat constant estava centrada en la banda tova de l'espectre X, i fou ajustada amb els models d'emissió d'atmosfera de nana blanca de MacDonald & Vennes (1991) (veure apèndix E) per Balman et al.(1998). Com a resultat de l'ajust, obtingueren, per cada observació, la temperatura efectiva i el radi fotosfèric de la nana blanca.

Per comparar els seus resultats observacionals amb els nostres models d'embolcall, hem superposat els valors obtinugts per Balman et al.(1998) en el pla de radi fotosfèric - temperatura efectiva dels nostres models a les figures H.7-H.9. Donat que els ajustos de Balman et al.(1998) no donen directament el radi fotosfèric, sino una constant de normalització proporcional al quadrat d'aquest i inversament proporcional al quadrat de la distància, la determinació del radi fotosfèric depèn de la distànica. A les figures H.7-H.9, tota la indeterminació introduïda per la distància està tinguda en compte. A més de comparar els valors observacionals i del model, és molt útil comparar els intervals de temps transcorreguts entre les observacions i l'evolució predita pels models. Per això, en els panels inferiors de les figures H.7-H.9, es mostra la massa de l'embolcall i el temps en dies necessaris per passar d'una tempertura efectiva a una altra segons els nostres models.

La gran incertesa en la determinació de la distància a la font, un problema comú per les noves clàssiques, fa impossible una comparació directa del radi fotosfèric. Però la

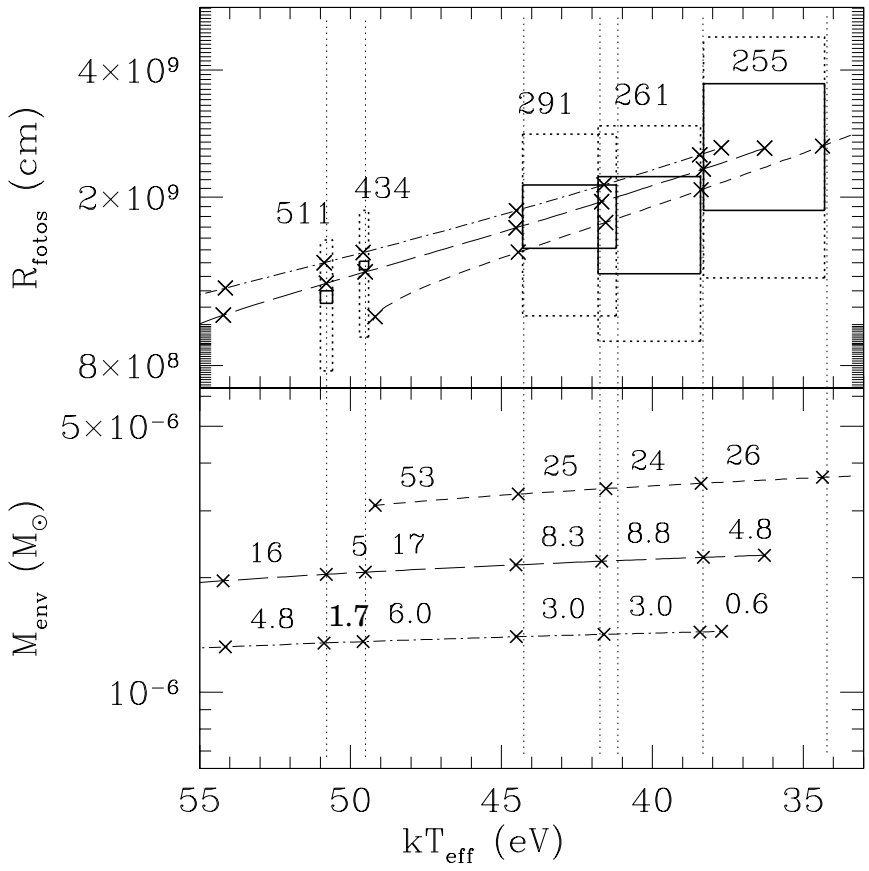

Figura H.7: Resultats per V1974 Cyg obtinguts per Balman et al.(1998) en el pla $R_{fotos} - kT_{eff}$ comparats amb els models d'embolcall de nana blanca ONe75.
Panell superior: Contorns de confiança de 3σ obtinguts per Balman et al.(1998) pels models d'tmosfera de nana blanca ajustats a V1974 Cyg. Els contorns en linia continua indiquen els resultats per una distànica de 2.45 *kpc*, mentre que els contorns en línia puntejada inclouen tota l'error en la determinació de la distànica, 1.7-3.2 *kpc*. Els nombres indiquen el dia després de l'explosió en que es realitzà l'observació. Els models d'emblcall que es mostren són per $0.8M_{\odot}$ (ratlles curtes), $0.9M_{\odot}$ (ratlles llargues) i $1.0M_{\odot}$ (ratlla-puntt). Les linies puntejades verticals son orientatives per comparar amb el panell inferior.
Panell inferior: Masses dels embolcalls mostrats al panell superior. Els nombres entre marques indiquen els dies necessaris perque l'embolcall evolucioni d'un punt al següent degut purament a la combustió estacionària d'hidrogen.

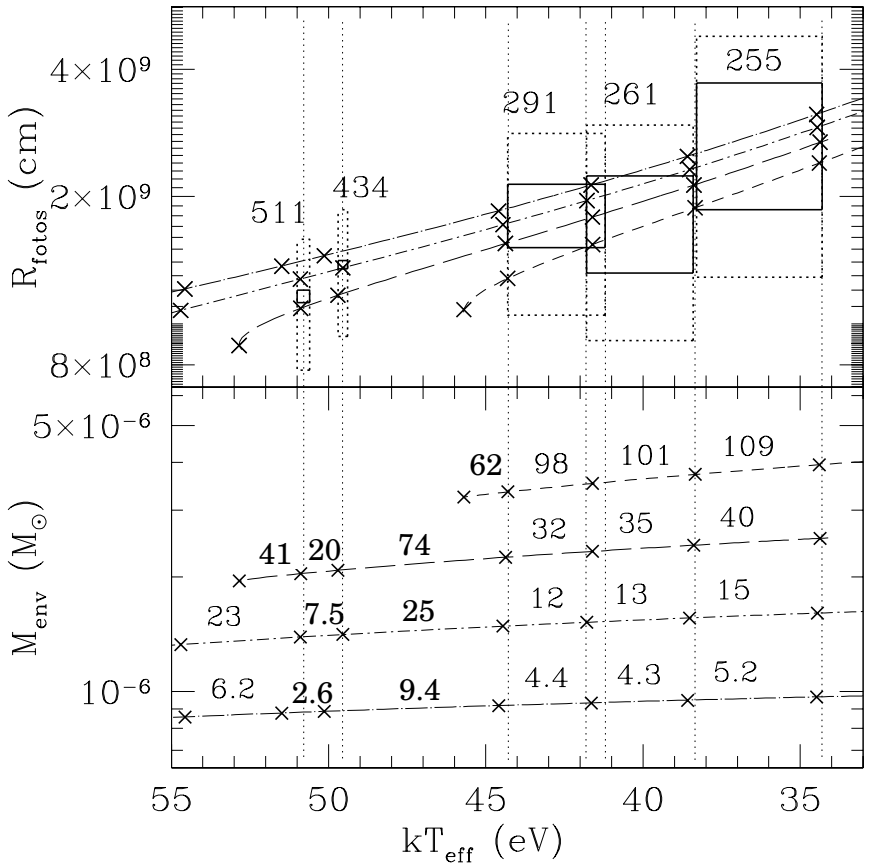

Figura H.8: Resultats per V1974 Cyg obtinguts per en el pla R_{fotos}-kT_{eff} comparats amb els models d'embolcall de nana blanca ONe50.

Panell superior: Contorns de confiança de 3σ obtinguts per pels models d'tmosfera de nana blanca ajustats a V1974 Cyg. Els contorns en linia continua indiquen els resultats per una distànica de 2.45 kpc, mentre que els contorns en línia puntejada inclouen tota l'error en la determinació de la distànica, 1.7-3.2 kpc. Els nombres indiquen el dia després de l'explosió en que es realitzà l'observació. Els models d'emblcall que es mostren són per $0.8M_{\odot}$ (ratlles curtes), $0.9M_{\odot}$ (ratlles llargues), $1.0M_{\odot}$ (ratlla curta -puntt) i 1.1 $M_{\odot}$ (ratlla llarga-punt). Les linies puntejades verticals son orientatives per comparar amb el panell inferior.

Panell inferior: Masses dels embolcalls mostrats al panell superior. Els nombres entre marques indiquen els dies necessaris perque l'embolcall evolucioni d'un punt al següent degut purament a la combustió estacionària d'hidrogen.

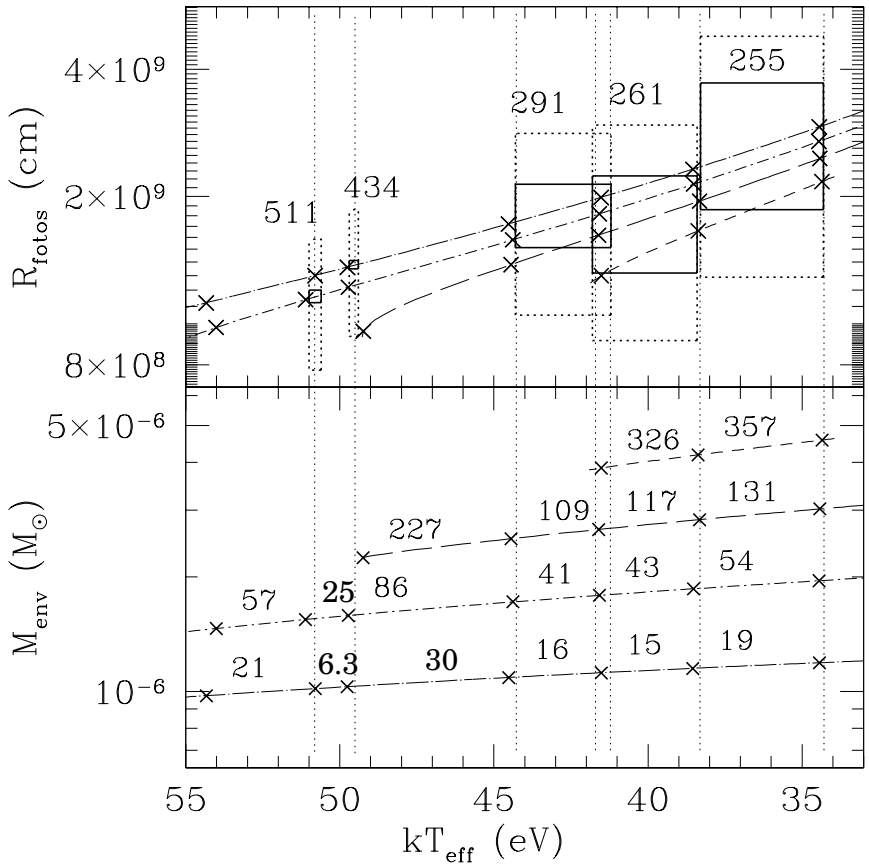

Figura H.9: Resultats per V1974 Cyg obtinguts per en el pla R_{fotos}-kT_{eff} comparats amb els models d'embolcall de nana blanca ONe25.

Panell superior: Contorns de confiança de 3σ obtinguts per pels models d'tmosfera de nana blanca ajustats a V1974 Cyg. Els contorns en linia continua indiquen els resultats per una distànica de 2.45 kpc, mentre que els contorns en línia puntejada inclouen tota l'error en la determinació de la distànica, 1.7-3.2 kpc. Els nombres indiquen el dia després de l'explosió en que es realitzà l'observació. Els models d'emblcall que es mostren són per $0.8M_{\odot}$ (ratlles curtes), $0.9M_{\odot}$ (ratlles llargues), $1.0M_{\odot}$ (ratlla curta -puntt) i 1.1 $M_{\odot}$ (ratlla llarga-punt). Les linies puntejades verticals son orientatives per comparar amb el panell inferior.

Panell inferior: Masses dels embolcalls mostrats al panell superior. Els nombres entre marques indiquen els dies necessaris perque l'embolcall evolucioni d'un punt al següent degut purament a la combustió estacionària d'hidrogen.

comparació de la temperatura efectiva i la seva evolució són suficients per determinar el model d'embolcall que pot explicar les observacions.

D'una banda, els models mostren que, per cada massa i composició, l'embolcall assoleix una temperatura efectiva màxima, just abans d'apagar-se. El primer element de comparació entre observacions i model és doncs la temperatura efectiva màxima. D'altra banda, els intervals de temps transcorreguts entre dos temperatures efectives en els models d'embolcall depenen també de la massa de la nana blanca i la fracció en massa d'hidrogen a l'embolcall. Per tant, la comparació de l'evolució de la temperatura efectiva observada amb la dels models limita encara més els parametres del model.

Tenint en compte la temperatura efectiva màxima de cada model i l'observada, i els temps d'evolució del model i els passos de temps entre observacions, la comparació mostrada a les figures H.7-H.9 indica que sols dos models d'embolcall poden explicar les observacions: el de ONe50 amb una nana blanca de 0.9 $M_{\odot}$, o el de ONe25 amb una massa de $1.0 M_{\odot}$. Determinacions observacionals de la fracció en massa d'hidrogen en el material ejectat indiquen que és d'entre el 0.1 i el 0.4 (Austin et al.(1996), Hayward et al.(1996)), compatible per tant amb l'abuncància d'hidrogen dels models ONe50. En qualsevol els dos casos, la massa de l'embolcall és $\sim (2-3) \times 10^{-6} M_{\odot}$, un ordre més petita que la massa accretada necessària per que es produeixi l'explosió de nova. Tenint en compte que la fracció que s'ejecta , segons els models hydrodinàmics, no és prou gran com per reduir la massa de l'embolcall a aquests valors, sembla necessària l'existència d'algun mecanisme extra de pèrdua de massa després de l'explosió (vents òpticament gruixits o embolcall comú).

H.3.2 Nova Muscae 1983 (GQ Mus)

La Nova Mus 1983 (GQ Mus), descoberta el 18 de Gener de 1983 (Liller (1983)), fou l'única nova detectada durant el ROSAT All-Sky Survey (RASS), d'entre un total de 26 noves classical observades menys de 10 anys després de l'explosió. Observacions més detallades realitzades el Febrer de 1992 amb el PSPC mostraren un espectre X molt tou (Ögelman et al.(1993)). Balman et al.(2001) va ajustar els resultats de ROSAT amb els models d'atmosferes de MacDonald & Vennes (1991), i va determinar que el Febrer de 1992 ja no hi havia combustió d'hidrogen a la superfície de la nana blanca. Onze mesos més tard, ROSAT va confirmar que la font s'havia apagat (Shanley et al.(1995)).

Com en el cas de V1974 Cyg, hem comparat els resultats observacionals amb els nostres models d'embolcall. La comparació indica que la nana blanca de la nova Muscae 1983 té probablement una massa de $1.1 \pm 0.1 M_{\odot}$. Les relacions dels nostres models indiquen que la corresponent massa de l'embolcall és $\sim 10^{-6} M_{\odot}$. Però tenint en compte que la combustió d'hidrogen a l'embolcall va durar entre 5 i 9 anys (segons indiquen observacions en X i en òptic), i donada la lluminositat de la font, la massa cremada durant aquest periode seria de $7.6 \times 10^{-6} M_{\odot}$, més gran que la massa per la qual l'embolcall amb combustió estacionària d'hidrogen és estable.

H.3.3 Nova LMC 1995

La Nova LMC 1995, descoberta el 2 de Març de 1995 (Liller (1995)), fou observada amb l'instrument PSPC de ROSAT una sola vegada, el Febrer de 1998, durant una observació d'altres fonts de LMC properes a la nova. Orio & Greiner (1999) va ajustar satisfactòriament l'espectre de la nova amb els models d'atmosfera de MacDonald & Vennes (1991), amb una temperatura de 31 eV ($\sim 3.6 \times 10^5 K$).

La nova LMC 1995 va ser observada posteriorment amb el satèl·lit XMM-Newton, el Desembre del 2000 (Orio et al.(2003)). En aquest cas, es van provar diferents models d'at-

mosfera, amb abundàncies i masses variades. El millor ajust s'obtingué amb abundàncies típiques del LMC, amb una massa de $0.9M_{\odot}$ i una lluminositat de $2.3 \times 10^{37} erg\, s^{-1}$. L'evolució d'aquesta nova sols és compatible amb els models d'embolcall més 'lents', que són els més pobres en hidrogen (els models I82) amb una nana blanca petita, de 0.8-$0.9M_{\odot}$ (compatible per tant amb el resultat de Orio et al.(2003)). Segons aquests models, la font s'hauria d'apagar l'agost del 2004.

H.4 Observacions de noves realitzades amb el satèl·lit XMM-Newton

Al mateix temps que el satèl·lit ROSAT acabava la seva missió, començava una nova era en l'astronomia de raigs X amb el llençament l'any 1999 dels satèl·lits Chandra (de la NASA) i XMM-Newton (de la ESA). Aquesta nova generació de satèl·lits, amb telescopis molt més potents, detectors més sensibles i una alta resolució espectral, proporcionen una magnífica oportunitat per l'estudi de les noves clàssiques.

Amb la idea d'estudiar l'emissió de raigs X tous de les noves i la durada de la fase de lluminositat bolomètrica constant, vam proposar l'observació de cinc noves clàssiques durant el primer cicle d'observació de XMM-Newton. Les fonts sel·leccionades van ser noves descobertes durant l'any anterior a la data de la proposta (abril 1999), amb l'excepció de la nova Sco 1997, inclosa a la proposta per la seva aparent detecció amb el satèl·lit italià Beppo SAX (Orio et al.(1997)). Cada nova es va observar en tres ocasions, en intervals de sis mesos (veure taula H.2).

La nova Sco 1997 (V1141 Sco) no va ser detectada en cap de les observacions. Però això no és sorprenent, donat que la identificació de la font en l'observació amb Beppo SAX descrita a Orio et al.(1997) no va poder ser confirmada un temps després (Orio (1999)). La Nova Sco 1998 (V1142 Sco) i la nova Mus 1998 (LZ Mus) van ser detectades a les últimes observacions realitzades amb XMM-Newton, però l'algorisme de detecció de fonts no les va identificar en les primeres observacions. L'anàlisi espectral detallat s'ha realitzat per les dues noves més brillants de la nostra mostra: Nova Sgr 1998 (V4633 Sgr) i Nova Oph 1998 (V2487 Oph).

H.4.1 Nova Sgr 1998 (V4633 Sgr)

V4633 Sgr fou observada per XMM-Newton en tres ocasions, 2.6, 3.0 i 3.5 anys després de l'explosió (veure taula H.3). Com es pot observar a la figura H.10, els espectres obtinguts per les càmeres EPIC mostren que l'emissió de raigs X s'estén per tot el rang d'energies de les càmeres, fins als $\sim$ 8 keV. L'anàlisi espectral realitzat amb XSPEC (Arnaud et al.(1996), veure apèndix F) mostra que l'espectre està dominat per emissió de plasma tèrmic, simulada per un model Raymond-Smith (Raymond & Smith (1977), veure apèndix F) amb tres components a diferent temperatura. A més, la banda d'energia més baixa de l'espectre és compatible amb la presència d'una atmosfera de nana blanca (simulada pels models de MacDonald & Vennes (1991), veure apèndix E).

Mantenint sempre la presència de l'atmosfera de nana blanca, s'ha provat l'ajust del model de plasma amb abundàncies solars i amb 14 abundàncies típiques del material ejectat per una nova, corresponents als resultats dels models hidrodinàmics de José & Hernanz (1998). Els millors ajustos es troben per abundàncies solars o per abundàncies corresponents a noves de CO, concretament, pels models CO1 i CO4 de José & Hernanz (1998) (que tenen abundàncies molt semblants). Els resultats amb abundàncies solars i amb CO1 (que prenem com a representatiu de CO1 i CO4) es mostren a les taules H.4 i H.5.

Table H.2: Observacions de noves recents amb XMM-Newton

Nova	Data del descobriment	Data d'observació amb XMM-Newton	Temps des del descobriment	Detectada amb EPIC?
N Sco 1997 (V1141 Sco)	5 Jun. 1997	Oct. 11, 2000	1224 d, 3.4 anys	NO
		Mar. 24, 2001	1388 d, 3.8 anys	NO
		Sep. 7, 2001	1555 d, 4.3 anys	NO
N Sgr 1998 (V4633 Sgr)	22 Mar. 1998	Oct 11, 2000	934 d, 2.6 anys	SI
		Mar. 9, 2001	1083 d, 3.0 anys	SI
		Sep. 7, 2001	1265 d, 3.5 anys	SI
N Oph 1998 (V2487 Oph)	15 Jun.1998	Feb. 25, 2001	986 d, 2.7 anys	SI
		Sep. 5, 2001	1178 d, 3.2 anys	SI
		Feb. 26, 2002	1352 d, 3.7 anys	SI
		Sep. 24,2002	1562 d, 4.3 anys	SI
N Sco 1998 (V1142 Sco)	21 Oct. 1998	Oct. 11, 2000	721 d, 2.0 anys	NO?
		Mar. 24, 2001	885 d, 2.4 anys	NO?
		Sep. 7, 2001	1052 d, 2.9 anys	SI?
N Mus 1998 (LZ Mus)	29 Des. 1998	Dec. 18, 2000	730 d, 2.0 anys	SI?
		Jun. 26, 2001	910 d, 2.5 anys	SI?
		Dec. 26, 2001	1093 d, 3.0 anys	SI?

Table H.3: Detalls de les observacions de V4633 Sgr.

Data	Càmera	Temps d'exposició (s)	Contes totals (0.2-8.0 keV) (cts)	Count rate (0.2-8.0 keV) ($\times 10^{-2}$cts s^{-1})
Oct 11, 2000	pn	6782	723	9.7 ± 0.4
	MOS1	8862	267	2.6 ± 0.2
	MOS2	9000	261	2.4 ± 0.2
Mar. 9, 2001	pn	...	...	...
	MOS1	6463	136	1.5 ± 0.2
	MOS2	6382	144	1.4 ± 0.2
Set. 7, 2001	pn	5684	561	8.1 ± 0.4
	MOS1	8962	219	2.0 ± 0.2
	MOS2	...	...	...

Table H.4: Paràmetres del millor ajust obtingut amb un model de Raymond-Smith de tres temperatures per V4633 Sgr, amb barres d'error de 3σ (si no s'indica altra cosa), amb abundàncies solars.

	1^aObservació	2^aObservació	3^aObservació
$kT_{RS1}(keV)$	$0.12^{+0.05}_{-0.03}$	$0.13^{+0.11}_{-0.08}$	$0.09^{+0.04}_{-0.03}$
$kT_{RS2}(keV)$	$0.82^{+0.3}_{-0.2}$	$2^{+8(2\sigma)}_{-1(3\sigma)}$	$0.8^{+0.3}_{-0.6}$
$kT_{RS3}(keV)$	13^{+50}_{-9}	-	10^{+50}_{-7}
$K_{RS1}(\times 10^{-4})$	3^{+8}_{-2}	$2^{+20}_{-1.8}$	8^{+50}_{-6}
$K_{RS2}(\times 10^{-5})$	2^{+2}_{-1}	7 ± 3	2^{+3}_{-1}
$K_{RS3}(\times 10^{-5})$	11^{+6}_{-2}	-	8^{+2}_{-3}
$EM_{RS1}(\times 10^{55} cm^{-3})^{(1)}$	30^{+70}_{-20}	20^{+200}_{-18}	80^{+500}_{-60}
$EM_{RS2}(\times 10^{55} cm^{-3})^{(1)}$	2^{+2}_{-1}	7 ± 3	2^{+2}_{-1}
$EM_{RS3}(\times 10^{55} cm^{-3})^{(1)}$	11^{+6}_{-2}	-	8^{+2}_{-3}
$F^{plasma}_{unabs}\,(erg\,cm^{-2}s^{-1})^{(2)}$	7.2×10^{-13}	4.8×10^{-13}	7.7×10^{-13}
$L^{plasma}_{unabs}\,(\times 10^{33} erg\,s^{-1})^{(3)}$	7^{+4}_{-3}	5^{+3}_{-2}	9^{+6}_{-5}
$F^{total}\,(erg\,cm^{-2}s^{-1})^{(4)}$	2.7×10^{-13}	4.1×10^{-13}	2.1×10^{-13}
χ^2_ν	1.11	0.99	1.05

(1) Mesura d'emissió per les components del plasma tèrmic per una distància de 9 *kpc*. Per altres distàncies, un factor $\left(\frac{d}{9kpc}\right)^2$ afecta aquests resultats.

(2) Flux sense absorció del model de plasma tèrmic en el rang 0.22-8.0 *keV*.

(3) Lluminositat del plasma tèrmic en el rang 0.22-8.0 *keV*, per una distància 8.9 ± 2.5 *kpc*.

(4) Flux total (amb absorció) en el rang 0.22-8.0 *keV*.

Les dues possibles abundàncies (solar i CO) corresponen a dos possibles escenaris per l'emissió del tipus plasma tèrmic. El model amb abundàncies riques en CO, típica del material ejectat en una nova, correspondria a l'emissió de la clofolla de material ejectat en expansió, escalfat per xocs interns o externs amb el medi circumestel·lar. En canvi, el model amb abundàncies solars estaria associat al reestabliment de l'acreció sobre la nana blanca. En ambdós casos, els parametres de l'emissió són semblants. La temperatura del plasma, la mesura d'emissió observada i les densitats que se'n deriven, així com l'evolució observada entre la primera i la tercera observació, indiquen que es podria tractar de la clofolla de material en expansió. Però la determinació dels paràmetres no és prou precisa com per descartar que l'acrecció s'hagi reestablert.

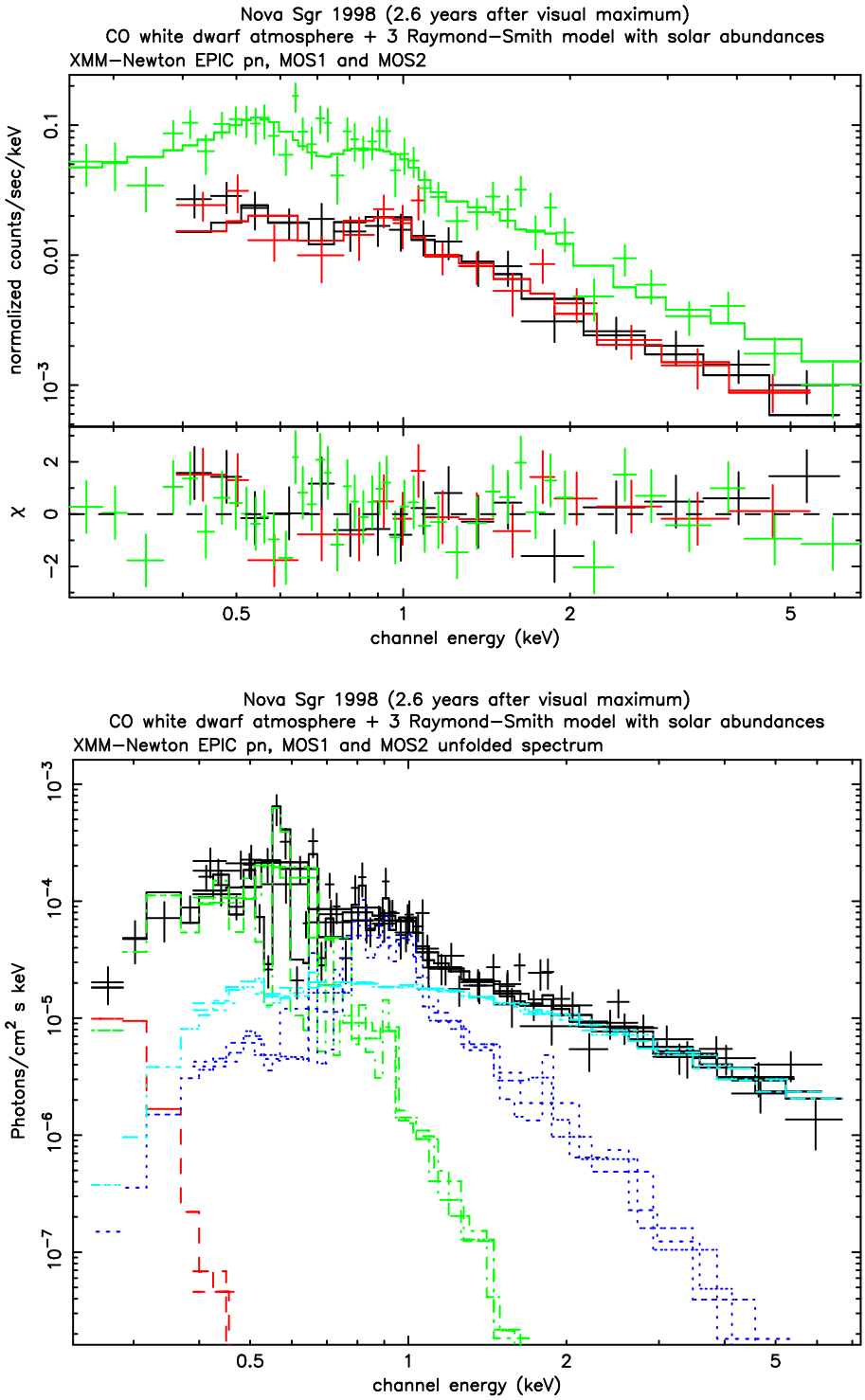

Figure H.10: Espectre de V4633 Sgr obtingut per XMM-Newton 2.6 anys després de l'explosió i millor ajust amb el model d'abundàncies solars.
Panell superior: Espectre observat amb model i residus (dades menys model convolucionat amb la resposta de l'instrument) representat en termes de sigmes, amb barres d'error de mida unitat. Es representen les dades de les tres càmeres EPIC: pn (amb més contes), MOS1 i MOS2. Les línies continues indiquen el millor ajust del model.
Panell inferior: Espectre i model deconvolucionats, mostrant la contribució de cada component del model. D'esquerra a dreta, model d'atmosfera de nana blanca de CO i models de Raymond-Smith amb $kT_1 = 0.11\ keV$, $kT_2 = 0.82\ keV$ i $kT_3 = 37\ keV$.

Table H.5: Paràmetres del millor ajust obtingut amb un model de Raymond-Smith de tres temperatures per V4633 Sgr, amb barres d'error de 3σ (si no s'indica altra cosa), amb abundàncies CO1.

	1^{st}Observation	2^{nd}Observation	3^{rd}Observation
$kT_{RS1}(keV)$	$0.11^{+0.07}_{-0.04}$	$0.16^{+0.19(2\sigma)}_{-0.14(3\sigma)}$	$0.13^{+0.06}_{-0.08}$
$kT_{RS2}(keV)$	0.8 ± 0.2	$1.6^{+10(2\sigma)}_{-0.5(2\sigma)}$	0.9 ± 0.5
$kT_{RS3}(keV)$	$20^{+no\,limit}_{-14}$	-	$31^{+no\,limit}_{-27}$
$K_{RS1}(\times 10^{-6})$	6^{+50}_{-4}	$2.9^{+400(2\sigma)}_{-2.6(3\sigma)}$	5^{+65}_{-3}
$K_{RS2}(\times 10^{-6})$	13^{+9}_{-7}	22^{+20}_{-2}	12^{+12}_{-11}
$K_{RS3}(\times 10^{-6})$	45 ± 20	-	30^{+20}_{-15}
$EM_{RS1}(\times 10^{54} cm^{-3})^{(1)}$	6^{+50}_{-4}	$2.81^{+400(2\sigma)}_{-2.5(3\sigma)}$	4^{+60}_{-2}
$EM_{RS2}(\times 10^{55} cm^{-3})^{(1)}$	$1.3^{+0.9}_{-0.7}$	$2.1^{+2.0}_{-0.2}$	$1.2^{+1.2}_{-1.1}$
$EM_{RS3}(\times 10^{55} cm^{-3})^{(1)}$	4.4 ± 2.0	-	$3.0^{+2.0}_{-1.5}$
$F^{plasma}_{unabs}\,(erg\,cm^{-2}s^{-1})^{(2)}$	4.8×10^{-13}	2.3×10^{-13}	4.3×10^{-13}
$L^{plasma}_{unabs}\,(\times 10^{33} erg\,s^{-1})^{(3)}$	5^{+2}_{-3}	2 ± 1	4^{+3}_{-2}
$F^{total}\,(erg\,cm^{-2}s^{-1})^{(4)}$	2.5×10^{-13}	4.1×10^{-13}	2.0×10^{-13}
χ^2_ν	1.04	0.99	1.10

(1) Mesura d'emissió per les components del plasma tèrmic per una distància de 9 *kpc*. Per altres distàncies, un factor $\left(\frac{d}{9kpc}\right)^2$ afecta aquests resultats.

(2) Flux sense absorció del model de plasma tèrmic en el rang 0.22-8.0 *keV*.

(3) Lluminositat del plasma tèrmic en el rang 0.22-8.0 *keV*, per una distància 8.9 ± 2.5 *kpc*.

(4) Flux total (amb absorció) en el rang 0.22-8.0 *keV*.

Table H.6: Detalls de les observacions de V2487 Oph.

Data d'observació	Càmera	Temps d'exposició (s)	Contes totals (0.3-8.0 keV) (cts)	Contes per segon (0.3-8.0 keV) (cts s^{-1})
Feb. 25, 2001	pn	-	-	-
	MOS1	6322	1989	0.301 ± 0.007
	MOS2	7616	2127	0.264 ± 0.006
Sep. 5, 2001	pn	4680	5028	1.056 ± 0.01
	MOS1	7513	2479	0.325 ± 0.007
	MOS2	7514	2511	0.327 ± 0.007
Feb. 26, 2002	pn	2662	2546	0.91 ± 0.02
	MOS1	5150	1533	0.278 ± 0.008
	MOS2	5145	2546	0.290 ± 0.008

H.4.2 Nova Oph 1998 (V2487 Oph)

La Nova Oph 1998 (V2487 Oph) fou observada amb XMM-Newton 2.7, 3.2 i 3.7 anys després de l'explosió (veure taula H.2). L'espectre observat per les càmeres EPIC té un flux més gran que en el cas de V4633 Sgr i també s'extén fins a ~ 8 keV (veure figura H.11). L'espectre està dominat per emissió de plasma tèrmic, que es pot modelar amb un model MEKAL (Mewe et al.(1995)) de dues temperatures. Els paràmetres de l'ajust es resumeixen a la taula H.7. El millor ajust correspon a una component de baixa temperatura, 0.2 keV, i una d'alta temperatura $kT \geq 64$ keV. Però amb aquest model, les dades mostren un excés a $\sim 6.4-6.5$ keV. Una línia Gaussiana adicional centrada a aquesta energia amb una amplada de $\sigma = 0.6$ keV ajusta correctament aquest excés. El model de plasma tèrmic tampoc pot explicar la component de més baixa energia, que s'ajusta correctament amb una atmosfera de nana blanca. En aquest cas, però, l'emissió no pot ser deguda a la combustió d'hidrogen a l'embolcall de la nana blanca, ja que la lluminositat observada correspon a una superfície emissora més petita que l'estrella sencera. Emissions com aquesta s'han observat sovint en variables cataclísmiques, en les quals la superfície de la nana blanca s'escalfa degut a la incidència dels raigs X de més alta energia procedents de la regió de xoc del flux d'acreció.

El més remarcable de l'espectre de raigs X de V2487 Oph és, sens dubte, la línia d'emissió a $\sim 6.4 - 6.5\,keV$ (Hernanz & Sala (2002)). Una emissió d'aquest tipus no ha estat mai observada en cap nova clàssica, però és un tret comú de l'espectre de raigs X de variables cataclísmiques (per exemple, EX Hya i AO Pisc, Ishida et al.(1994), Hellier et al.(1996), Fujimoto & Ishida (1997)). Per temperatures del plasma tèrmic d'uns pocs keV, el ferro es troba en l'estat d'ionització Fe XXV, que té una línia d'emissió Kα a 6.7 keV. Aquesta línia, com totes les que corresponen a l'emissió del plasma calent, ja estan simulades pel model MEKAL. El fet que calgui afegir una component gaussiana per ajustar l'emissió a 6.4-6.5 keV indica que aquesta línia ha de ser produida per un mecanisme diferent del plasma tèrmic. El ferro neutre té una línia de fluorescència a 6.41 keV, i altres línies de fluorescència d'estats intermitjos es troben entre aquestes dues energies. Per tant, la línia observada a 6.4-6.5 keV ha de correspondre a l'emissió del ferro fred per fluorescència.

Aquestes línies de fluorescència sols poden ésser generades per reflexió de raigs X més energétics (generats en la regió post-xoc del fluxe d'acreció i corresponents a les components de plasma tèrmic de l'espectre) en regions més fredes, que pot ser el disc d'acreció o la mateixa nana blanca. En altres paraules, que hi hagi reflexió indica que l'acreció de material de l'estrella secundària sobre la nana blanca s'ha reestablert.

Table H.7: Paràmetres del model espectral per V2487 Oph (amb errors a 1σ de confiança).

	1a obs	2a obs	3a obs
$kT_{atm}(eV)$	64±5	72^{+3}_{-7}	74^{+6}_{-5}
$L_{atm}(\times 10^{35} erg\, s^{-1})^{(1)}$	2±1	$1.4^{+0.3}_{-0.2}$	$1.4^{+0.3}_{-0.2}$
$kT_1(keV)$	0.26±0.03	$0.25^{+0.01}_{-0.02}$	$0.27^{+0.02}_{-0.03}$
$kT_2(keV)$	>10	>64	>64
$EM_1(\times 10^{57} cm^{-3})^{(1)}$	1.3±0.8	$1.8^{+0.4}_{-0.2}$	$1.3^{+0.4}_{-0.2}$
$EM_2(\times 10^{57} cm^{-3})^{(1)}$	3.1±0.1	3.4±0.5	3.1±0.6
$E_{linia}(keV)$	6.4±0.4	6.49±0.07	6.50±0.05
$\sigma_{linia}(keV)$	1.2±0.4	0.61±0.08	0.27±0.05
$F_{linia}(\times 10^{-5} fotons\, cm^{-2} s^{-1})$	14±8	7±2	4±1
$F^{total}_{absorvit}(\times 10^{-12} erg\, cm^{-2}\, s^{-1})^{(2)}$	4.8	4.6	4.0
$L^{total}_{absorvit}(\times 10^{34} erg\, s^{-1})^{(3)}$	5.7	5.5	4.8
χ^2_ν	1.07	1.13	1.24

(1) La lluminositat de l'atmosfera de nana blanca i les mesures d'emissió de les components del plasma tèrmic es donen per una distància de 10 *kpc*. Per altres distàncies, un factor $\left(\frac{d}{10kpc}\right)^2$ afecta aquests valors.

(2) Flux total del model en el rang 0.22-8.0 *keV*.

(3) Lluminositat total del model en el rang 0.22-8.0 *keV*, per una distància de 10 *kpc*. Per altres distàncies, un factor $\left(\frac{d}{10kpc}\right)^2$ afecta aquests valors.

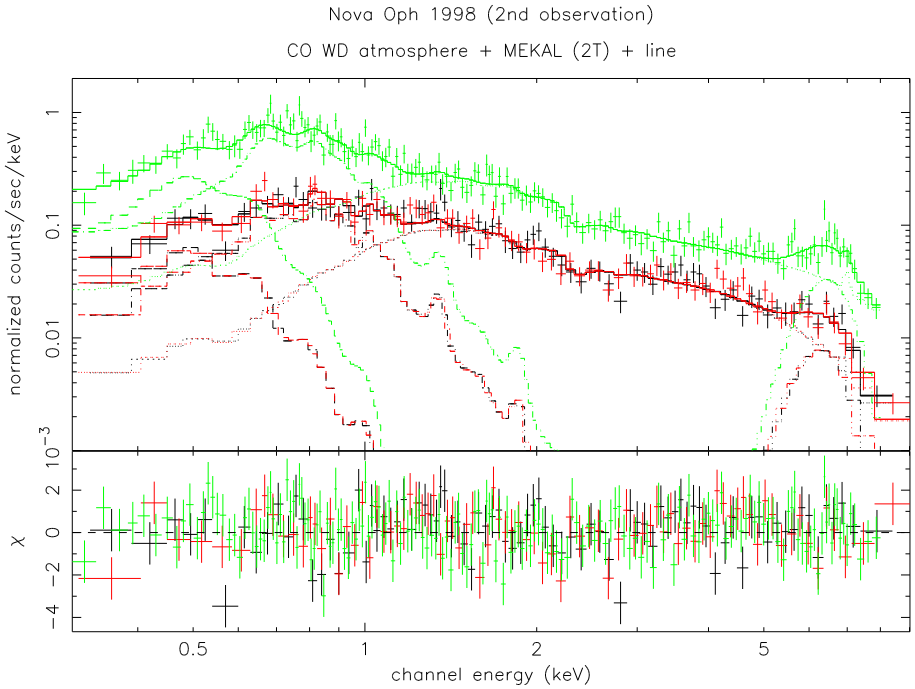

Figure H.11: Espectre de V2487 Oph observat per XMM-Newton 3.2 anys després de l'explosió, i millor ajust del model. El panell inferior indica els residus (dades menys model convolucionat) en termes de sigmes, amb barres d'error unitat. Es mostren dades de les tres càmeres EPIC (pn -amb més contes-, MOS1 i MOS2). Es mostra també la contribució de cada componen del modelt: atmosfera (en el rang 0.2-0.8 *keV*), plasma tèrmic a baixa temperatura (a 2.5 *keV*), plasma tèrmic a alta temperatura (a partir de 0.5 *keV*), i línia Gaussiana (centrada a 6.4 *keV*).

A més de ser la primera nova en la que s'ha observat el reestabliment de l'acreció en menys de 1000 dies, V2487 Oph té una altra peculiaritat. La variable cataclísmica que va allotjar l'explosió de la nova Oph 1998 va ser detectada per ROSAT 8 anys abans de l'explosió, durant el ROSAT All Sky Survey. Quan va explotar la nova, Nakano et al.(1998) ja va fer notar que aquesta es trobava dins la caixa d'error de 16" de la posició de la font de raigs X descoberta per ROSAT i catalogada com 1RXS J173200.0-1934. Les observacions amb XMM-Newton, amb una millor resolució espacial, mostren que 1RXS J173200.0-1934 i V2487 Oph són la mateixa font. A més, el flux i l'espectre d'aquella detecció són compatibles amb les nostres observacions amb XMM-Newton. Aquesta detecció de ROSAT converteix la Nova Oph 1998 en la primera nova clàssica en la que l'acreció en la variable cataclísmica ha estat detectada abans i després de l'explosió.